A new understanding of luminescence processes in feldspar using novel site-selective spectroscopic techniques

Raju Kumar

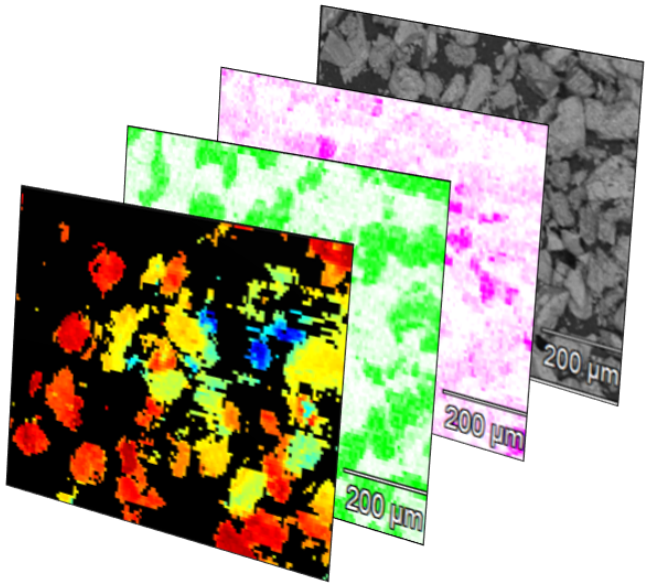

Ph.D. Thesis
December 2019

DTU Nutech
Center for Nuclear Technologies

Center for Nuclear Technologies
Technical University of Denmark
Risø Campus, Frederiksborgvej 399
4000, Roskilde, Denmark
Phone + 45 4677 4900
www.nutech.dtu.dk/english

Dedicated to my beloved parents

PREFACE

This dissertation is submitted in partial fulfillment of the requirements for the Ph.D. degree in Physics, at the Technical University of Denmark (DTU). The Ph.D. project started on 15th December 2016 and completed by 14th December 2019. The majority of work was conducted at the Luminescence Physics Laboratory, Center of Nuclear Technologies (DTU Nutech), Risø, under the supervision of Senior Scientist Mayank Jain, Ph.D. (Main supervisor), and Senior R & D Engineer Myungho Kook, Ph.D. (Co-supervisor). The aim of this work is to advance our current understanding of defect-related luminescence processes in a naturally occurring wide bandgap aluminosilicate (feldspar).

Acknowledgments

It is my pleasure to acknowledge the roles of several individuals who were means of pursuing my aim.

First and foremost, I would like to express my deep and sincere gratitude to my research advisor, Dr. Mayank Jain, Ph.D., Head of section, Luminescence Physics Laboratory, DTU Nutech, for giving me this opportunity to pursue doctoral studies, for his continuous support, for his patience, motivation, enthusiasm, and immense knowledge. I am highly indebted to him for his constant supervision in completing this endeavor.

Besides my main advisor, I am extremely thankful to my co-advisor, Dr. Myungho Kook, Ph.D., for his guidance and encouragement throughout this research project. It is my pleasure to thank Dr. Amit Kumar

Prasad for teaching me experimental skills at the beginning of my Ph.D.

I am pleased to thank Dr. Jens-Peter Lynov and Dr. Bent Lauritzen for their support and encouragement. I would like to thank Ms. Pia Elhauge and Ms. Merete Holmegaard Larsen for their support on official matters. I also thank the DTU administrative staff for their support.

It is my pleasure to thank Dr. Marine Frouin, Dr. Reza Sohbati, Dr. Eike F. Rades, Elaine Sellwood and Svenja Riedesel for their help and proofreading. My special thanks to Martin Autzen for his help and valuable suggestions. My sincere thanks to Dr. Jan-Pieter Buylaert, Prof. Andrew Murray and Dr. Kristina Thomsen for their support and encouragement.

It is my pleasure to thank Mr. Karsten Bracht Nielsen for his help with software; Mr. Søren Vig Dalsgaard for his help in mechanical related issues; Mr. Jørgen Hesselbjerg Jakobsen, Mr. Lars Peter Pirtzel, Mr. Per Günther Sørensen and Mr. Bo Dalbjerg for their help in electronic related issues; Mr. Finn Jørgensen for his help in computer related issues; Dr. Minqiang Bu for general support. It is my pleasure to thank Ms. Louise Maria Helsted, Ms. Vicki Hansen, and Mr. Henrik Olesen for their help.

My special thanks to Dr. Per Roos for his support and encouragement. It is my pleasure to thank Dr. Claus Andersen, Dr. Mark Bailey, Dr. Lars Lindvold, Dr. Erik Nonbøl, Prof. Arne Miller, Ms. Nina Jensen, and Ms. Linda Bohn for their support and encouragement. My sincere thanks to all the researchers who I met in the conferences for their time and encouragement.

Thanks to my officemates Jeppe, Nicolo, Ashkhen, Claire, Xiao Xiao, Mads, and Frederik for their great company, to my housemates Warren and Oscar for being nice neighbors, to Eren, Alastair, Trine, Grichar, Magdalena, Tim, Jacobus and everybody who made my stay at DTU Nutech and in Denmark memorable.

It is my pleasure to thank Prof. Dirk Poelman for providing his supervision and lab facilities at the University of Ghent (UGhent). I would like to thank Lisa Martin for her support in the experiments at the UGhent. I would like to thank Prof. Philippe Smet, UGhent, for providing sketch for cathodoluminescene system. I would like to thank Ewoud Cosaert, David Van Der Heggen, Andreas Sousanis, Jiaren Du, Simon Michels, Reinert Verstraete, Nasrin Karimi, Simon Nachtergaele for their help and support at UGhent.

It is my pleasure to thank Prof. Dr. Johan De Grave and Dr. Dimitri

Vandenberghe for their help and support that made my stay at UGhent pleasant. I would also like to thank Ann-Eline Debeer for her help in sample preparation at UGhent.

I am pleased to thank Prof. Nicolas Stenger for providing lab facilities at the Department of Photonics Engineering, and Moritz Fischer for his help in experiments. My sincere thanks to Prof. D.J. Huntley for giving us all his feldspar samples.

I would like to extend my sincere thanks to my teachers and mentors Prof. V. P. N. Nampoori, Prof. C. P. Grijavallabhan, Prof. P. Radhakrishnan, Dr. Sheenu Thomas, Dr. Kailasnath, and Prof. John McInerney for their support and encouragement.

I must express my very profound gratitude to my parents, family, and friends for their love, support, and continuous encouragement throughout my studies.

Last but not least, I would like to thank all the people who I have forgotten to mention here.

Raju Kumar
Risø, December 14, 2019

ABSTRACT

Metastable states in solids are widely used for dosimetry and photonic applications. Feldspar, a ubiquitous naturally occurring aluminosilicate, consists of many defects and impurities; some of these transform into metastable states by capturing electrons or holes, when exposed to ionizing radiation. These metastable states can have lifetimes of millions of years rendering feldspar useful for luminescence geochronology. In this dating technique, the dose-dependent concentration of the metastable states (generated by ionizing radiation) is measured via optically stimulated luminescence (OSL) or infrared stimulated luminescence (IRSL) signals. These signals are generated by charge transfer across the metastable states, followed by electron-hole recombination resulting in the emission of light.

Despite many decades of research, the luminescence mechanisms and the associated defect system in feldspar are poorly understood; for example, the defect responsible for the main dosimetric trap (i.e. principal trap) and its physical characteristics are still unknown. This lack of knowledge may largely be attributed to the inherent physical processes involved in OSL and IRSL generation. The OSL/IRSL technique is not ideal for characterizing the principal trap (e.g. optical trap depth, electronic states, number of defects and their concentration, etc.) as it involves both electron and hole sites as well as the charge transport dynamics, making any interpretation of the electron-trapping state ambiguous. Therefore, it is desirable to use site-selective methods that can directly probe the principal trap without involving any hole sites in the

emission process. The main purpose of this Ph.D. research is to advance our current understanding of the luminescence processes in feldspar and the associated defect system using site-selective multi-spectroscopic techniques.

This work shows that there are two principal traps in K-Na feldspar. These traps emit Stokes-shifted infrared photoluminescence (IRPL) bands centered at 1.41 eV (880 nm) and 1.30 eV (955 nm). The two trapping centers have similar electron capture cross-sections and excited-to-ground state relaxation lifetimes, but different trap depths and excited-state energies. These results suggest that the 1.41 eV and 1.30 eV emission centers consist of the same defect that resides in two different sites and, thus, experiences different crystal fields. Cathodoluminescence (CL) microscopy explores the question on the spatial variability of the two principal traps and their link to feldspar composition. CL investigations suggest that the two emission centers (i.e. the two traps) vary spatially even within a single-grain of feldspar and their relative emission peak intensity (1.30 eV vs. 1.41 eV) shows a correlation with the K-Na content. This work sheds new light on the long-standing issues of estimation of trap depth in feldspar, and whether there are single or multiple traps giving rise to the OSL/IRSL signals.

This Ph.D. research also establishes a link between the IRPL emission bands (1.41 eV and 1.30 eV) and the OSL/IRSL phenomenon. Tracking of changes in IRPL (i.e. trapped electron population) due to IRSL (i.e. electron and hole populations) shows that a) both the 1.41 eV and 1.30 eV centers participate in IRSL, and b) only a fraction of the principal trap population participates in the IRSL at a given measurement temperature. A comparison of thermal depletion of IRSL and IRPL signals suggests that the trapped electrons in the principal trap are quite stable up to about 400 °C. The decrease in IRSL because of preheating to 300-400 °C occurs due to the depletion of holes; the holes are used up during the TL measurement (i.e., preheating) prior to the IRSL measurement. Furthermore, it is observed that the electron trapping probability in the principal trap is both a function of its electron capture cross-section and its distance to the nearest hole. This new understanding is anticipated to play a crucial role in the development of mathematical models of luminescence phenomena involving metastable states.

Finally, the test of the potential of IRPL in sediment dating suggests that IRPL can be successfully adapted to a SAR protocol; it recovers

accurate equivalent doses from 100 to 300 Gy (age range 20-128 ka) without a fading correction.

In terms of practical utility, a new measurement facility for detecting infrared photoluminescence (IRPL) at 1.41 eV (880 nm) and 1.30 eV (955 nm) for routine dosimetric measurements has been developed. Furthermore, a dose measurement protocol, i.e. coupled IRPL-IRSL SAR protocol, is developed to measure natural doses in feldspar using IRPL. This work establishes a fundamentally different dating technique based only on trapped electrons, compared to the existing OSL and IRSL dating techniques.

DANSK RESUMÉ

Metastabile tilstande i faste stoffer bruges ofte i dosimetriske and fotonske anvendelser. Feldspat, et hyppigt forekommende naturligt aluminosilikat, består af mange defekter og urenheder; nogle af disse omdannes til metastabile tilstande ved indfangelse af elektroner eller huller når de udsættes for ioniserende stråling. Disse metastabile tilstande kan have levetider af millioner af år, hvilket gør feldspat brugbart til luminescence geokronologi. I denne daterings teknik, måles den dosisafhængige koncentration af de metastabile tilstande (dannet via ioniserende stråling) via Optisk Stimuleret Luminescence (OSL) eller Infrarødt Stimuleret Luminescence (IRSL) signaler. Disse signaler genereres af ladnings transport over de metastabile tilstande, efterfulgt af elektron-hul rekombination der resulterer i udsendelsen af lys.

På trods af mange årtiers forskning, er der stadig en dårlig forståelse af luminescence mekanismerne og det tilhørende defekt system i feldspat; for eksempel er den ansvarlige defekt for den primære dosimetriske fælde (i.e. primær fælden) og dens fysiske karakteristiker stadig ukendt. Denne manglende viden kan fortrinsvis tilskrives at den fysiske process der er involveret i genereringen af OSL og IRSL. OSL/IRSL teknikken ikke er ideel til at karakteriserer primær fælden (f.x optisk fælde dybde, elektroniske tilstande, antallet af defekter og deres koncentration m.v.) da den involverer både elektron og hul lokaliteter såvel som ladnings transpot dynamikkerne, hvilket gør enhver fortolkning af elektron-fælde tilstanden tvetydig. Derfor er det attraktivt at bruge lokalitetsspecifikke metoder der direkte kan undersøge primær fælden uden at in-

volverer hul lokaliteterne i udstrålingsprocessen. Hovedformålet med denne Ph.D. forskning er at advancere vores nuværende forståelse af luminesence processerne i feldspat og det associerede defekt system ved brug af lokalitetsspecifikke multispektroskopiske teknikker.

Denne afhandling viser at der finds to primær fælder i K-Na feldspat. Disse fælder udstråler Stokes-forskudt Infrarødt Photoluminescence (IRPL) bånd centreret på 1.41 eV (880 nm) og 1.30 eV (955 nm). De to fælde centre har sammenlignlige elektron-indfangelses tværsnit og eksiteret-til-grundtilstands overgangs levetider, men forskellige fælde dybder og energi for den eksiterede tilstand. Disse resultater antyder at 1.41 eV og 1.31 eV udstrålingscentrene består af den samme defekt der forekommer på to forskellige lokaliteter og dermed oplever forskellige krystalfelter. Katodeluminescence (CL) mikroskopi udforsker spørgsmålet om rumlige variabilitet af de to primær fælder og deres forbindelse til sammensætningen af feldspat. CL undersøgelser antyder at de to udstrålingscentre (i.e. de to fælder) har en rumlig variation, selv indenfor et enkelt feldspat korn og deres relative udstrålingstop intensiteter (1.30 eV mod 1.41 eV) viser en korrelation med K-Na indhold. Dette kaster nyt lys på på veletablerede problemer med estimering af fælde dybde i feldspat og om der er én eller flere fælder der giver anledning til OSL/IRSL signalerne.

Denne Ph.D forsking etablerer også en forbindelse mellem IRPL udstrålingsbpnd (1.41 eV og 1.30 eV) og OSL/IRSL fænomenet. Ved at undersøge ændringer i IRPL (i.e. den fangede elektron population) pga. IRSL (i.e. elektron og hul populationer) viser det sig at a) både 1.41 eV og 1.30 eV centrene deltager i IRSL og b) kun en brøkdel af primær fælde populationen deltager i IRSL ved en given målingstemperatur. En sammenligning af den termiske reduction af IRSL og IRPL signalerne antyder at den fangede elektron population er ganske stabil op til omkring 400 °C. Reduktionen i IRSL ved preheating til 300-400 °C sker pga. en reduktion af huller; huller bruges under TL måling (i.e. preheating) inden IRSL målingen. Endvidere observeres det at sandsynligheden for eletronindfangelse i primær fælden både er en funktion af dens elektron-indfangelsestværsnint og dens afstand til nærmeste hul. Det antages at denne nye forståelse kommer til at spille en vigtig rolle i udviklingen af matematiske modeller for luminescence fænomener der involverer metastabile tilstande.

Afsluttende viser testen af IRPL's potentiale in sediment datering at IRPL kan successfuldt tilpasses en SAR protocol; IRPL er i stand til at

måle præcise dosis fra 100 til 300 Gy (ca. 20-128 ka) uden korrektion for fading.

I forhold til praktisk brugbarhed, er et nyt målingsfacilitet for detektion af Infrarødt Photoluminescence (IRPL) ved 1.41 eV (880 nm) og 1.30 eV (955 nm) til rutine dosimetriske målinger blevet udviklet. Ydermere er en protokol til måling af dosis, i.e. en koblet IRPL-IRSL protokol blevet udviklet til måling af naturlige doser i feldspat ved brug af IRPL. Denne afhandling etablerer en fundamental anderledes dateringsmetode baseret udelukkede på fangede elektroner, sammenlignet med eksiterende OSL og IRSL daterings teknikker.

LIST OF PUBLICATIONS

Publications as the first author:

1. **Kumar, R.**, Kook, M., Murray, A. S., & Jain, M. (2018). Towards direct measurement of electrons in metastable states in K-feldspar: Do infrared-photoluminescence and radioluminescence probe the same trap? Radiation Measurements, 12, 7–13.

2. **Kumar, R.**, Kook, M., & Jain, M. (Submitted). Characterization of electron-trapping centers in feldspar by low-temperature photoluminescence excitation-emission spectroscopy.

3. **Kumar, R.**, Martin, L.I.D.J., Poelman, D., Vandenberghe, V., Grave, J.De., Kook, M., & Jain, M. (Under review). Site-selective mapping of metastable states using electron-beam induced luminescence microscopy.

4. **Kumar, R.**, Kook, M., & Jain, M. (Under review). Sediment dating using Infrared photoluminescence (IRPL).

Presentations at conferences:

1. **Kumar, R.**, Prasad, A. K., Kook, M., Murray, A. S., & Jain, M. (2017). New insights into the electron trapping centers in feldspar. Oral presentation at the 15th International Conference on Luminescence and

Electron Spin Resonance (LED), Cape Town, South Africa.

2. **Kumar, R.**, Kook, M., & Jain, M. (2018). Insights into the stability of trapped electrons in feldspar from infrared photoluminescence (IRPL). Oral presentation at the Conference on Luminescence and Electron Spin Resonance (UK LED), Sheffield, United Kingdom.

3. **Kumar, R.**, Antoine, G., Murray, A. S., Sahiner, E., Sellwood, E., Kook, M., & Jain, M. (2019). Understanding the dynamics of electron de-trapping using ΔIRPL. Oral presentation at the Conference on Luminescence and Electron Spin Resonance (UK LED), Denmark.

4. **Kumar, R.**, Kook, M., & Jain, M. (2019). Sediment dating using infra-red photoluminescence. Poster presentation at the Conference on Luminescence and Electron Spin Resonance (UK LED), Denmark.

5. **Kumar, R.**, Kook, M., & Jain, M. (2019). Characterization of electron traps in a natural aluminosilicate (feldspar) by low-temperature photoluminescence excitation-emission spectroscopy. Oral presentation at the 19th International Conference on Solid-State Dosimetry (SSD), Japan.

Co-authored publications:

1. Kook, M., **Kumar, R.**, Murray, A. S., Thomsen, K. J., & Jain, M. (2018). Instrumentation for the non-destructive optical measurement of trapped electrons in feldspar. Radiation Measurements, 120, 247-252.

2. Riedesel, S., King, G. E., Prasad, A. K., **Kumar, R.**, Finch, A. A., & Jain, M. (2019). Optical determination of the width of the band-tail states, and the excited and ground state energies of the principal dosimetric trap in feldspar. Radiation Measurements, 125, 40-51.

3. Jain, M., **Kumar, R.**, Kook, M., (To be submitted). A coupled PL-OSL system to probe dynamics of the metastable states.

Co-authored presentations:

1. Kook, M., **Kumar, R.**, Murray, A. S., Thomsen, K. J., & Jain, M. (2017). A measurement system for direct probing of trapped electrons in feldspar. 15th International Conference on Luminescence and Electron Spin Resonance (LED), Cape Town, South Africa.

2. Jain, M., **Kumar, R.**, Prasad, A. K., Kook, M., & Murray, A. S. (2017). OSL meets ESR: luminescence dating based on direct probing of trapped electrons. 15th International Conference on Luminescence and Electron Spin Resonance (LED), Cape Town, South Africa.

3. Riedesel, S., King, G. E., Prasad, A. K., **Kumar, R.**, Lambert, R., Finch, A. A., Brückner1, H., & Jain, M. (2017). Constraining the band-tail width of feldspar: implications for luminescence thermochronometry. 15th International Conference on Luminescence and Electron Spin Resonance (LED), Cape Town, South Africa.

4. Jain, M., **Kumar, R.**, & Kook, M.(2018). Preliminary investigations on the application of infrared photoluminescence (IRPL) to sediment dating. Conference on Luminescence and Electron Spin Resonance (UK LED), Sheffield, United Kingdom.

5. Riedesel, S., King, G. E., Prasad, A. K., **Kumar, R.**, Finch, A. A., & Jain, M. (2018). Optical measurement of band-tail width, depth and excited-state energies of the IRSL trap in feldspar. Conference on Luminescence and Electron Spin Resonance (UK LED), Sheffield, United Kingdom.

6. Jain, M., **Kumar, R.**, & Kook, M.(2018). Novel dating methods using Infrared photoluminescence (IRPL). The 5th Asia Pacific Conference on Luminescence and Electron Spin Resonance Dating (APLED2018), Beijing, China.

7. Kook, M., **Kumar, R.**, Murray, A. S., Thomsen, K. J., & Jain, M. (2019). Infrared photoluminescence (IRPL) attachment to the Risø TL/OSL reader. Conference on Luminescence and Electron Spin Resonance (UK LED), Denmark.

8. Şahiner,E., **Kumar, R.**, Kook, M., Polymeris, G.S., Meriç, N., & Jain, M. (2019). Thermal behaviour of the Infra-Red Photoluminescence (IRPL) in feldspar. Conference on Luminescence and Electron Spin Resonance (UK LED), Denmark.

9. Jain, M., **Kumar, R.**, Sellwood, E., Şahiner, E., & Kook, M.(2019). Infrared photoluminescence, a step change in trapped charge dating. Oral presentation at the 19th international conference on solid-state dosimetry (SSD), Japan.

10. Frouin, M., **Kumar, R.**, Kook, M., Buylaert, J-P., & Jain, M. (2019). Further investigations on IRRF and IRPL. German Luminescence and Electron Spin Resonance Meeting (DLED), Bingen, Germany.

Awards:

I received two awards during my Ph.D.:

1. The Peter Townsend Award for most innovative idea in instrumentation/methodology at the 15th International Conference on Luminescence and Electron Spin Resonance (LED) 2017, Cape Town, South Africa.
2. Scientific Excellence Award for the best science at the Conference on Luminescence and Electron Spin Resonance (UK LED) 2019, Denmark.

LIST OF ABBREVIATIONS

3D	Three Dimensional
Al_2O_3	Aluminum Oxide
APh	After Preheat
Ag	Silver
BSE	Backscattered Electrons
$Blue_{290}$	Blue light exposure at 290 °C
BPh	Before Preheat
Ca	Calcium
C	Carbon
CW	Continuous Wave
CB	Conduction Band
CCD	Charge Coupled Device
CL	Cathodoluminescence
COLUR	CryOgenic LUminescence Research
DRC	Dose Response Curve
D_e	Equivalent Dose
EDX	Energy-Dispersive X-ray Spectroscopy
EMCCD	Electron-Multiplying Charge Coupled Device
ESR	Electron Spin Resonance
FWHM	Full Width Half Maximum
Fe	Iron

ICPMS	Inductively Coupled Plasma Mass Spectrometry
IR	Infrared
IRPL	Infrared Photoluminescence
$IRPL_{1.30}$	Infrared Photoluminescence emission at 1.30 eV
$IRPL_{1.41}$	Infrared Photoluminescence emission at 1.41 eV
$IRPL_{955}$	Infrared Photoluminescence emission at 955 nm
$IRPL_{880}$	Infrared Photoluminescence emission at 880 nm
IRRF	Infrared Radiofluorescence
IRRL	Infrared Radioluminescence
IRCL	Infrared Cathodoluminescence
IRSL	Infrared Stimulated Luminescence
IR_{290}	Infrared light exposure at 290 °C
K	Potassium
LED	Light Emitting Diode
Mg	Magnesium
MET-pIRIR	Multiple Elevated Temperature post Infrared Infrared
NIR	Near-Infrared
Na	Sodium
OSL	Optically Stimulated Luminescence
PID	Proportional Integral Derivative
pIRIR	Post Infrared Infrared luminescence
pIR_TIRSL_T	Post Infrared Infrared stimulated luminescence T: Measurement temperature
pIRSL	Pulsed Infrared Stimulated Luminescence
Pb	Lead
PL	Photoluminescence
PMT	Photomultiplier Tube
RC	Recombination Centre
RL	Radioluminescence
SE	Secondary Electrons
SAR	Single Aliquot Regenerative
SEM-CL	Scanning Electron Microscope-Cathodoluminescence
TL	Thermoluminescence
TCSPC	Time-Correlated Single Photon Counting
T	Temperature
UV_{RT}	Ultra-Violet light exposure at room temperature
UV	Ultra-Violet
VB	Valence Band
XEOL	X-ray Excited Optical Luminescence
XRF	X-ray Fluorescence
YPO_4:Ce,Sm	Yttrium Phosphate co-doped with Cerium and Samarium

CONTENTS

CHAPTER 1

INTRODUCTION AND OVERVIEW

1.1 Motivation and purpose

Understanding past climates, environments, and landscapes is important for modeling their future response. This understanding is critical for dealing with, for example, the challenges posed by global warming. Luminescence dating has played a vital role in providing such an understanding by estimating ages of the past geological and geo-archaeological events up to last 0.5 million years (e.g., see Duller, 1997; Aitken, 1998; Wallinga, 2002; Buylaert et al., 2008; Singhvi and Porat, 2008; Rhodes, 2011; Buylaert et al., 2012b; Liritzis et al., 2013; Roberts et al., 2015).

Luminescence dating techniques make use of quartz or feldspar, the most abundant minerals in the Earth's crust (∼60%). Deep-lying defects in the bandgap of these materials can store charges for millions of years at ambient temperatures; these can be measured via luminescence, which is eventually calibrated into age. The most commonly used luminescence dating technique is Optically Stimulated Luminescence (OSL) (Huntley et al., 1985). While the OSL dating technique is well established, some inherent limitations restrict its application over the entire Quaternary period. For example, traps in quartz saturate early thereby prohibiting its use for estimating ages above 0.1 million years. With feldspar, it is possible to date events up to 0.5 million years; however, the OSL signal in feldspar shows instability. The signal undergoes an athermal loss over laboratory and geological time scales by a process known as anomalous

fading, leading to incorrect age estimates (Spooner 1994; Huntley and Lamothe, 2001).

The main research areas in the OSL dating technique include increasing the accuracy and precision in ages, extending the age range above 0.5 million years, solving the problem of partial bleaching, developing new applications (e.g. rock surface dating), and obtaining a better understanding of luminescence processes. Understanding the physics of luminescent traps and the associated charge transfer processes may lead to the development of new methods to address all these research areas. Furthermore, a better understanding of luminescence processes is necessary to establish emerging applications such as thermochronometry (Guralnik et al., 2015; King et al., 2016) and rock surface exposure dating (Sohbati et al., 2012, 2015) on a firm ground; here, physical parameters of the system, e.g. trap depth, distribution of the traps, energy structure, photoionization cross-section, trapping cross-section, competitions, etc., must be known accurately.

As a student of optics and photonics, I have always been interested in understanding light-matter interaction and studying the optical properties of solids. This Ph.D. gave me an outstanding opportunity to explore different experimental methods and put my knowledge acquired during bachelor's and master's to practice. It has been motivating to work on a Ph.D. project, which involves interdisciplinary methods/applications but utilizes optical methods extensively. The OSL dating method is based on electron-hole (e-h) recombination that makes exact trap characterization ambiguous. Recently, it has become possible to directly probe the electron-trapping center in feldspar, also called the principal trap, by using optical method (Prasad et al., 2017). This method called infrared photoluminescence (IRPL) is a powerful site-selective (i.e. allows examination of a single defect type) method for tracking changes in the concentration of occupied electron traps in feldspar. A complimentary site-selective method called infrared radioluminescence (IRRL; Trautmann et al., 1998) can track the concentration of unoccupied electron traps during exposure to ionizing radiation. ***The purpose of this Ph.D. is to understand luminescence processes in feldspar using multi-spectroscopic techniques based on these site-selective methods, i.e. IRPL and IRRL, and to test the potential of IRPL as an alternative dating technique.*** These investigations have required both new experimental measurements as well as an upgrade/refinement of the

existing measurement facilities. My research has implications not just for the field of luminescence dating but also for methodological developments towards understanding luminescence from the metastable states. I hope that the techniques used in this thesis will inspire researchers in solid-state dosimetry and luminescence geochronology.

1.2 Defect induced luminescence

Defects or impurities in a host material can act as luminescent centers. The electronic states of a luminescent center are localized and are strongly coupled to the lattice vibrations of the host crystal through the electron-phonon interaction. Similarly, the electronic states can be influenced by the crystal field. A particular energy level may take the form of several discrete levels or a continuous distribution of levels. Thus, the shape of absorption and emission spectra (because of electronic transitions across these levels) can be strongly affected by the host crystal. Figure 1.1 shows electronic states of an atom (or a luminescence center) in an isolated state and after it is doped in a host material (Fox, 2002).

Luminescence spectroscopy is a powerful tool to understand defects in semiconductors or insulators. These defects interact with electromagnetic (EM) radiations by absorption and emission of photons. The spontaneous emission of photons is referred to as luminescence in soft or condensed matter physics. Luminescence can have different forms depending on the measurement method. The luminescence signals used in this work are 1) radio-luminescence: excitation with ionizing radiation of energy $E > E_g$ (bandgap), 2) optically stimulated luminescence (OSL) based on photoionization of the metastable state of a defect, 3) thermoluminescence (TL) based on thermal-ionization of the metastable state of a defect, and 4) photoluminescence (PL) based on photo-excitation of the metastable state of a defect. These techniques are briefly discussed as follows.

1.2.1 Radioluminescence (RL)

Radioluminescence (RL) is emitted when a sample is exposed to high energy radiations such as electron-beam, x-rays, γ-rays, and α and β particles. A high energy excitation ionizes the lattice thereby creating electrons and holes in the conduction band and the valence band, respectively. Relaxation via different routes results in RL (see Figure 1.2) (Pagel et al., 2000; Baele et al., 2019):

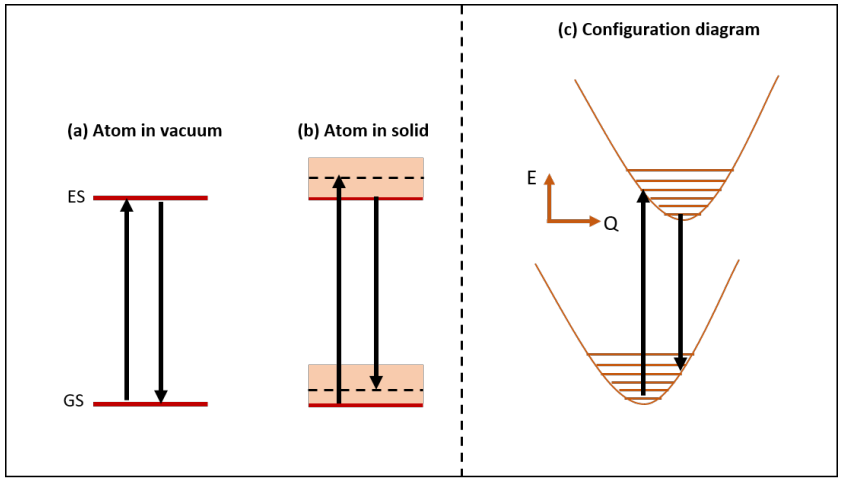

Figure 1.1: (a) The electronic states (GS: ground state and ES: excited state) of a luminescent center are discrete, similar to an atom in a vacuum. (b) Electronic states of a luminescence center in a solid are strongly coupled to the lattice vibrations of the host crystal (through electron-phonon interaction) and influenced by the crystal field. These effects lead to a continuum of states. (c) Energy, E, diagram of the electronic transitions (GS $\Leftrightarrow$ ES) along the configurational coordinate Q.

1. Band-to-band transition: free electrons in the conduction band return to the valence band and recombine, radiatively, with the holes.

2. Band-to-defect transitions i.e. trapping of charge by defects.

3. Trap-assisted band-to-band transitions: free electrons return to the valence band via defect/traps in the bandgap.

4. Intra-defect transitions: electronic transitions within the defect/trap.

The spectral distribution of the emitted luminescence (RL emission spectrum) provides information on the defects or sites participating in the emission process. Depending on the type of the excitation source, RL is referred to as x-ray excited optical luminescence (XEOL) if the x-ray is used, or cathodoluminescence (CL) if an electron-beam is used (Götze, 2012). Luminescence produced using γ-rays, or α and β particles is generally referred to as RL itself. The main differences lie in the penetration depth of the different radiations and particles. The CL technique typically samples the near-surface volume of the material (1-5 µm), while RL samples a full volume. The penetration depth of the x-ray depends on its mean energy.

1.2.2 Optically stimulated luminescence (OSL)

An electron in a trap can be excited to its excited state (T^*, an excited state of the electron trap T) or to the conduction band using optical stimulation. The de-trapped electron can then recombine with a hole at a recombination center ($RC + h^+$), via conduction-band or sub-conduction-band transport. Equally, the electron can recombine with the hole via excited-state tunneling. This recombination may lead to the emission of a photon via the relaxation of excited state RC^* of the recombination center ($RC^* \rightarrow RC$). The resulting signal is called optically stimulated luminescence (OSL). An OSL emission spectrum provides information on the energy levels of the recombination center/site while the OSL excitation spectrum provides information on the energy levels of the electron-trapping site. OSL technique is not site-specific since it involves both the electron and hole sites. Therefore, it becomes challenging to study the physical characteristics of the electron traps (for e.g. trap depth, energy structure, distribution, etc.). The generation mechanism of OSL can be seen in Figure 1.2.

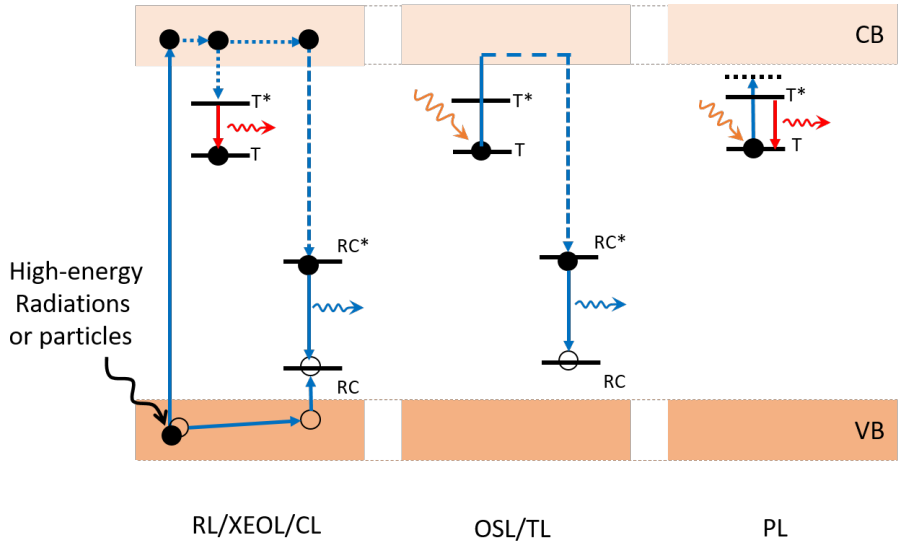

Figure 1.2: Band model of defects participating in different optical transitions. CB: conduction band; VB: valence band; T: electron trap; T^*: excited state of T; RC: recombination center or hole trapping center; RC^*: excited state of RC. RL/XEOL/CL: radioluminescence emission due to trapping of free electrons and holes, created by exposure of high energy radiations or particles ($T^* \rightarrow T$ or $RC^* \rightarrow RC$). Depending on the excitation source, RL is called x-ray excited optical luminescence (XEOL) and cathodoluminescence (CL) when x-rays and an electron-beam are used, respectively. Other transitions, for e.g. intra-band recombination, are possible but not shown here for simplicity; refer to Section 1.2.1 for more details. OSL/TL: optically stimulated luminescence or thermoluminescence results when optically or thermally excited electrons recombine with holes at the recombination center via conduction band transport. PL: photoluminescence emission results from internal transitions within the luminescence center ($T^* \rightarrow T$) subsequent to photoexcitation.

1.2.3 Photoluminescence (PL) and Radiophotoluminescence (RPL)

Electrons in the trap can be optically excited to the higher electronic states from its ground state ($T \rightarrow T^*$). Subsequent relaxation to the ground state ($T^* \rightarrow T$) may occur through spontaneous emission of light, referred to as photoluminescence (PL) (see Figure 1.2). The emitted light is generally longer in wavelength (lower in energy) than that of the excitation light (Stokes-shifted emission). Unlike OSL, which requires prior exposure to ionizing radiation, PL does not require prior irradiation.

A variant of PL called radio-photoluminescence (RPL; Schulman et al., 1951) is based on measuring luminescence from the metastable states created by exposure to ionizing radiation. In contrast to OSL, the RPL emission spectrum provides information on those energy levels of the metastable state that allow electronic transitions to the ground state by radiative relaxation. Similarly, the RPL excitation spectrum provides information on the higher electronic (energy) levels of the metastable state. Thus, RPL is a powerful tool to study luminescence characteristics of a single defect or site by selectively targeting it with appropriate excitation energy.

1.2.4 Thermoluminescence (TL)

Electrons in the trap can also be thermally excited. TL is emitted when thermally excited electrons recombine with the holes at the recombination center via transport through the delocalized band (CB) and band-tail states, or through excited-state tunneling. The TL generation mechanism is very similar to that of OSL (see Figure 1.2); however, the former uses heat while the latter light for stimulating electrons in the traps. For the production of OSL and TL, it is important that the material has previously absorbed energy by exposure to ionizing radiation. TL is a commonly used technique in determining the thermal trap depth in semiconductors or insulators (Bos et al., 2006, 2017).

1.3 Luminescence dating

Luminescence dating is based on estimating the amount of energy absorbed from ionizing radiation by mineral grains during burial. Minerals, such as quartz and feldspar, are exposed to ionizing radiation such as

cosmic rays, alpha and beta particles or gamma rays emitted during the decay of Uranium (U), Thorium (Th), and Potassium (K) radioisotopes in the ground. During this exposure, free electrons and holes are created in the crystal. A fraction of these free charges is trapped in the lattice defects creating metastable states; the net concentration of these states is a function of burial time, plus the fraction that was inherited (i.e. residual charge after exposure to daylight) at the time of burial (Huntley et al., 1985; Wintle, 2008). The trapped electrons can be released using heat or light; the resulting luminescence reflects the concentration of trapped charges and thus the absorbed dose (Gray, Gy = $\mathrm{J\,kg^{-1}}$) from ionizing radiation. If the luminescence signal was fully reset before burial, e.g. by heating or exposure to daylight, then the ratio of the measured dose and the annual environmental dose rate ($\mathrm{J\,kg^{-1}a^{-1}}$) gives an age estimate (Aitken, 1985, 1994):

$$Age\ (years) = \frac{Equivalent\ dose\ (D_e)}{Dose\ rate\ (\dot{D})}, \tag{1.1}$$

where the equivalent dose (D_e) represents the dose absorbed from the beta or gamma source that results in the same luminescence intensity as that from the dose absorbed in nature. The dose rate ($\dot{D}$) is the dose absorbed per unit time, typically reported in years (a) or thousands of years (ka). The principle of luminescence dating is depicted in Figure 1.3a. Complete bleaching of the sample (zeroing) or a sub-sample prior to burial is essential in order to estimate an accurate D_e. The dose rate is calculated by the measurement of radioactive isotopes or radioactivity in and around the sample. TL and OSL (Huntley et al., 1985) are two widely used signals in luminescence dating.

1.4 Luminescence processes in feldspar

Feldspar, a natural crystalline aluminosilicate, is the most abundant mineral in the Earth's crust (>50%). It occurs as the alkali series ($K_xNa_{1-x}AlSi_3O_8$) or the plagioclase series ($Na_{1-x}Ca_xAl_{1+x}Si_{3-x}O_8$) (Figure 1.3b) and has a bandgap of about 7.7 eV (Malins et al., 2004). The defect responsible for electron capture in feldspar also called the principal trap is the main source of dosimetric signal used in OSL dating. The dosimetric signal from this defect can be measured using optically stimulated luminescence (OSL; blue or green light stimulation) or

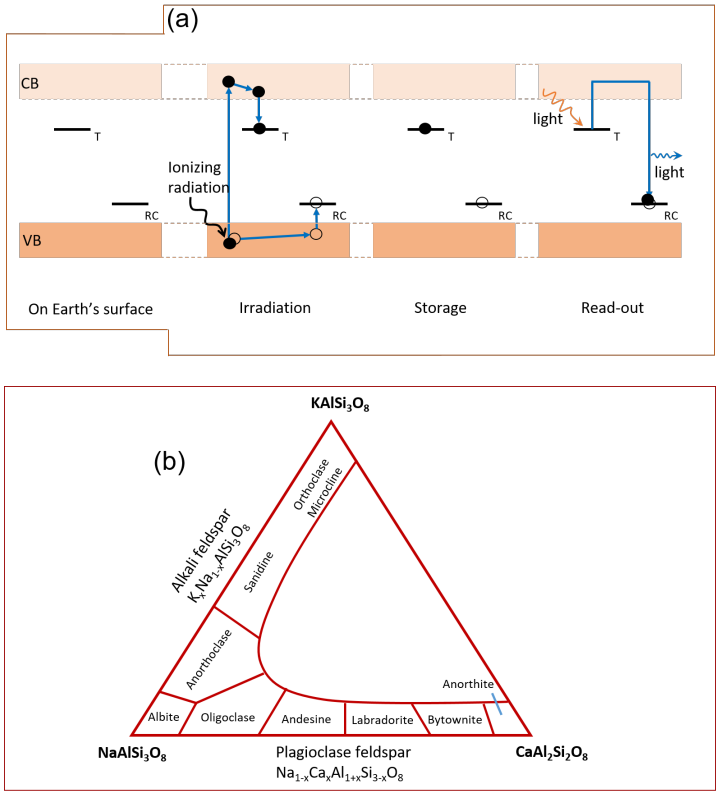

Figure 1.3: (a) Basic principle of luminescence dating. On Earth's surface: electrons in the dosimetric trap are emptied by exposure to sunlight. Irradiation: during burial, ionizing radiation creates free electron and holes, some of these get trapped in the dosimetric trap. Storage: electrons and holes in their respective centers keep accumulating on a geological time scale. Read-out: electrons in the trap are measured via luminescence to estimate the amount of energy absorbed by sample during its burial. (b) Ternary diagram of feldspar. Feldspar occurs as the alkali series ($K_xNa_{1-x}AlSi_3O_8$) or the plagioclase series ($Na_{1-x}Ca_xAl_{1+x}Si_{3-x}O_8$) with $KAlSi_3O_8$ (sanidine, orthoclase, and microcline), $NaAlSi_3O_8$ (albite), or $CaAl_2Si_2O_8$ (anorthite) end members.

IR stimulated luminescence (IRSL).

1.4.1 Feldspar crystal structure and luminescent defects

Feldspar crystallizes in monoclinic or triclinic systems and the crystal structure consists of a three-dimensional framework that is made up of AlO_4 and SiO_4 tetrahedrons, both connected through a shared oxygen atom. In the framework, Si and Al sites are called 'T' sites while interstices (normally occupied by larger cations K, Na, or Ca) are called 'M sites'. Furthermore, there exist T_1 and T_2 sites because of two distinct Si or Al sites lying in a different environment (Götze, 2012). As a natural material, feldspar comprises many defects or impurities (vacancies and impurity atoms). The impurity based defects such as Ce^{3+}, Eu^{2+}, Cu^{2+}, Al-O^{-}-Al, Ga^{3+}, Sm^{3+}, Dy^{3+}, Eu^{3+}, Tb^{3+}, Nd^{3+}, Pb^{+}, etc. have been identified using different spectroscopic techniques (Pagel et al., 2000; Götze, 2012). However, there remain many unidentified defects. The main dosimetric trap (i.e. principal trap), which is used for OSL dating, is one such unidentified defect. The different luminescence emission bands in feldspar and their origins are summarized in Table 1.1.

Unlike OSL (see Section 1.2), the IRSL (Hütt et al., 1988) emission process proceeds through sub-conduction band transport of the detrapped electrons. Hütt et al. (1988) used a two-stage excitation model to explain the IRSL emission process since their estimated trap depth (∼2.50 eV) was significantly greater than the excitation energy (∼1.40 eV). They proposed that IR excitation results in the ground to excited state transition, which is then followed by phonon interaction to release the electrons from the excited state into the conduction band. Later work has demonstrated that there exist localized states below the conduction band edge because of the random distribution of impurities, structural disorder, thermal vibrations, and varying bond angles. The density of these states ρ, known as the band-tail states, falls exponentially below the band edge following equation 1.2.

$$\rho(E) \propto exp(-\frac{E}{E_B}), \tag{1.2}$$

where E is the energy of the state measured away from the band edge, E_B is the band-tail width at which the density of states falls by e^{-1}.

The current luminescence model of the IRSL generation mechanism is based on the active participation of the band-tail states. Electrons

Table 1.1: Emission bands observed in feldspars and their origin, obtained from Prasad (2017) and Götze et al. (2002). TL stands for thermoluminescence, IRSL for infrared stimulated luminescence, CL for cathodoluminescence, RL for radioluminescence, TR-OSL for time-resolved optically stimulated luminescence, and PL for photoluminescence.

Emission band (eV)	Technique	Possible origin	Reference
~3.80-4.40 (280-320 nm)	TL	Strain	Garcia-Guinea et al., 1999
	PL	Ti^{+}	Gorobets et al., 1995
	IRSL	-	Baril and Huntley, 2003
	TR-OSL	-	Clark and Bailiff, 1998
~340-450 nm	CL	O paramagnetic center	Finch and Klein, 1999
	IRSL	-	Rieser et al., 1997
	IRSL	-	Baril and Huntley, 2003
~2.95 (420 nm)	CL	Eu^{2+}	Mariano and Ring, 1975
~2.48 (500 nm)	CL	Ga^{3+}	De St. Jorre and Smith, 1988
~2.20 (560 nm)	IRSL	Mn^{2+}	Rieser et al., 1997,
	IRSL		Baril and Huntley, 2003
	CL		Geake et al., 1977
	TR-OSL		Clark and Bailiff, 1998
	CL		Telfer and Walker, 1978
~1.70 (680-750 nm)	PL	Fe^{3+}	Telfer and Walker, 1975
	IRSL		Krbetschek et al., 1996
	PL		Poolton et al., 1996, 1995, 2006
~1.45 (855 nm)	RL	Pb^{2+}	Erfurt, 2003
~1.36 (910 nm)			

from the excited state diffuse out into the band-tail states by phonon-assisted transport to recombine with the trapped holes (Poolton et al., 2009). The presence of band-tail states greatly influences the thermal stability of trapped electrons and introduces several recombination pathways affecting the OSL or IRSL efficiency (Jain and Ankjærgaard, 2011; Li & Li, 2011b). Thus, band-tail states play a critical role during the measurement of trap properties such as the optical trap depth, excited energy states, etc.

1.4.2 The principal trap

The defect participating in the OSL or IRSL is known as the main dosimetric trap or the principal trap. Despite many decades of research, the exact defect forming the principal trap is not yet identified (Short, 2003). Using OSL, which is a convolution of different processes, such as electron eviction, transport, and recombination, several trap characteristics such as optical trap depth, excited state energies, and the number of traps and their distribution are partially known. Previous work investigating the excited states of the principal trap using OSL excitation spectroscopy indicates that there exist a single or multiple excited states. Hütt et al. (1988) initially reported the excited state energies to be ∼1.40, ∼1.29, ∼1.33 and ∼2.25 eV. In subsequent studies, the excitation resonances, excluding the NIR resonance ∼1.40 eV, were proved to be experimental artifacts (Bailiff and Barnett 1994; Barnett and Bailiff 1997). Baril and Huntley (2003) reported two more resonances ∼1.57 eV and ∼2.0 eV including the main resonance ∼1.44 eV. Poolton et al. (2009) reported an additional resonance ∼1.24 eV in a K-feldspar apart from the main resonance ∼1.44 eV. Andersen et al. (2012) reported three overlapping resonances ∼1.36, ∼1.45, and ∼1.55 eV in the IRSL excitation spectra at room temperature. Recently, Prasad et al. (2017) reported two overlapping resonances ∼1.45 and ∼1.56 eV in the OSL excitation spectrum at room temperature. Whilst there exist a number of investigations and a number of reported resonances, the resonance peak ∼1.44 eV and an exponential rise of OSL intensity at higher excitation energies are universally present in different types of feldspars (Baril and Huntley, 2003; Riedesel et al., 2019). Since the OSL excitation spectrum is a combination of detrapping, transport, and recombination, the efficiencies of which change with the energy of the band-tail states (Jain and Ankjærgaard, 2011), it is not clear what the ideal mathematical form of an OSL

resonance peak should be; therefore, one may question identification of sub-peaks based on deconvolution analysis.

One of the main trap properties, the optical trap depth of the principal trap, has been explored rigorously using OSL/IRSL. The trap depth has been assigned a number of values ranging from 1.9 to 2.5 eV (Hütt et al., 1988; Clark and Sanderson, 1994; Poolton et al., 1995, 2002, 2009; Jain and ankjægaard, 2011; Kars et al., 2013; Riedesel et al., 2019). Hütt et al. (1988) reported an optical trap depth (referred to as optical activation energy in their article) of about 2.5 eV based on the relationship between optical and thermal activation energies. Using OSL excitation spectra, Clark and Sanderson (1994) suggested the optical trap depth to be smaller than 2.5 eV. Poolton et al. (1995, 2002) derived a value of about 2.0 eV using a hydrogenic model. Baril and Huntley (2003) suggested this value to be greater than 2.5 eV using OSL excitation spectroscopic technique. Poolton et al. (2009) applied a different method, photo-transferred TL measurements at 10 K, and suggested the depth to be in the range of 2.0-2.5 eV. Based on the time-resolved OSL, Jain and Ankjægaard (2011) suggested the optical trap depth to be greater than 2.4 eV. Kars et al. (2013) fitted their excitation spectra measured at a low temperature (10 K) using an equation for the photoionization cross-section of a single level defect (Bøtter-Jensen et al., 2003) and derived a value of ∼2.5 eV (or greater) for K-feldspar and ∼2.1 eV for Na-feldspar. Using the same method, Riedesel et al. (2019) obtained trap depths of about 2.04 eV on many feldspar samples irrespective of their chemical composition.

It has been widely debated whether OSL or IRSL in feldspar results from a single trap or multiple traps (e.g., Duller and Bøtter-Jensen, 1993; Jain and Singhvi, 2001; Baril and Huntley, 2003; Jain and Ankjærgaard, 2011; Andersen et al., 2012). Initially, OSL and IRSL were suggested to emit from two different traps; however, the invariance of the shape of the resonance peak after different thermal treatments, and the constancy of the OSL decay rate over the excitation range 1.24-2.40 eV suggest that IRSL and OSL arise from a single trap (Baril and Huntley, 2003; Andersen et al., 2012). It has been demonstrated that the IRSL signal intensity increases with an increase in the measurement temperature. This interesting characteristic of IRSL can be explained both in terms of a single trap (Thomsen et al., 2008; Jain and Ankjærgaard, 2011) or a multiple trap model (Li and Li, 2011a).

1.4.3 Anomalous fading

Infrared stimulated luminescence (IRSL) signal in feldspar suffers from anomalous fading, i.e. unwanted loss of signal on laboratory or geological time scales, which leads to an age under-estimation (Spooner, 1994; Huntley and Lamothe, 2001). Tunneling of electrons to the nearby site (recombination center) has been suggested to be the main reason for this loss (Visocekas et al., 1985; Huntley and Lian, 2006). This problem has been tackled to a satisfactory extent by correcting for the fading loss (Huntley and Lamothe, 2001) or utilizing the novel methods that preferentially select stable signals. The latter methods are based on elevated temperature signals such as post IR-IRSL (pIR_TIRSL_T, where T is the temperature of IR stimulation), and on pulsed IRSL (pIRSL) signals (Thomsen et al., 2008; Buylaert et al., 2012b; Li and Li, 2011a; Tsukamoto et al., 2006, 2017; Jain and Ankjærgaard, 2011; Jain et al., 2015b). The fading correction can only be applied for the low-dose, linear portion of the dose response (Huntley and Lamothe, 2001; Morthekai et al., 2008). The pIR_TIRSL_T methods are generally successful in isolating non-fading signals, but they suffer from problems like slow bleaching, thermal transfer and poor dose recovery (Yi et al., 2016; Roberts et al., 2012; Lowick et al., 2012; Kars et al., 2014). The pIRSL method has low signal sensitivity since the signal during the on-time of the pulse is not considered for the data analysis. Moreover, the pIRSL method may not be completely free from fading (Jain and Ankjærgaard, 2011; Jain et al., 2015b; Tsukamoto et al., 2017).

An alternative dating method based on the infrared radioluminescence (IRRL; Trautmann et al., 1998, 1999 a, b; Frouin et al., 2017) has been suggested to be immune from anomalous fading (Erfurt and Krbetschek, 2003a,b; Degering and Krbetschek, 2007). The IRRL signal (centered at 865 nm) arises in response to the exposure to ionizing radiation (e.g., β particles), and is suggested to emit when an electron is trapped into the principal trap (Trautmann et al., 2000; Erfurt and Krbetschek, 2003a). A test of IRRL signal on a variety of feldspar samples suggests that it suffers from sensitivity change which could potentially result in under- or overestimation of the palaeodose (Buylaert et al., 2012a).

1.5 Site-selective techniques

In Section 1.4, I explained that the physical parameters of the principal trap, e.g. trap depth, excited state energies, number of defects and their concentration are not fully known. This lack of knowledge may be attributed to:

1. Inherent complexities and uncertainties involved in dealing with luminescence production in natural minerals (many unknowns).
2. OSL or IRSL technique is not site-specific. OSL/IRSL processes involve both electron and hole sites and the transport mechanism (many variables).
3. Band-tail states provide alternative routes of charge transport and recombination pathways.
4. Traps other than the principal trap may also get photoionized during optical stimulation and contribute to the OSL/IRSL signal.

Since the width and density of band-tail states change from sample to sample (Poolton et al., 2009; Prasad and Jain, 2018), any measurements on the principal trap made using OSL and IRSL methods lead to ambiguous interpretations. Therefore, it is desirable to use site-specific techniques that can directly probe the electron-trapping site. In this context, the two site-selective signals that result from an electronic transition within the principal trap, radioluminescence (RL) and photoluminescence (PL), are highly promising for understanding luminescence production in feldspar. These signals are briefly described below.

1.5.1 Infrared radioluminescence (IRRL)

RL in feldspar shows a broad emission band centered at 865 nm when exposed to the high energy radiation (for e.g. beta particles; Trautmann et al., 1998). This signal is referred to as infrared radiofluorescence (IRRF) or infrared radioluminescence (IRRL). The origin of the IRRL signal is suggested to be from the principal trap, based on the comparison of the OSL/IRSL excitation spectrum (excitation peak ~860 nm) and IRRL emission spectrum (emission peak ~865 nm) at room temperature. IRRL in feldspar has been suggested to arise from the trapping of free electrons in the conduction band into the principal trap (Krbetschek et al., 2000;

Erfurt and Krbetschek, 2003a; Trautmann et al., 1999 a, b; Trautmann et al., 2000; Erfurt, 2003). The broad IRRL emission band can be deconvoluted into two IRRL emission bands centered at 865 nm (1.43 eV) and 910 nm (1.36 eV) (Erfurt, 2003; Erfurt & Krbetschek, 2003a); these two emissions are suggested to arise from the different excited states of Pb^+ by Erfurt (2003).

1.5.2 Infrared photoluminescence (IRPL)

Prasad et al. (2017) demonstrated that electrons captured in the principal trap after exposure to ionizing radiation can be measured non-destructively using the photoluminescence (PL) technique. PL results from the intra-defect electronic transitions within the trap. Prasad et al. (2017) used an 885 nm (1.40 eV) laser to excite the trap and observed a Stokes-shifted emission at 955 nm (1.30 eV), which they termed as infrared photoluminescence (IRPL). The similarity between the OSL and PL excitation spectra in the energy range 1.30-1.80 eV and the Stokes shift of the order of 0.10 eV between the PL excitation and emission spectra led these authors to conclude that the IRPL originates from the principal trap. As expected from a metastable state, the IRPL signal showed an increase in signal intensity with a dose. Prasad et al. (2017) measured a lifetime of the IRPL signal about 40 and 30 µs at low temperature (7 K) and room temperature (295 K), respectively.

IRPL is a site-selective technique because one can closely tune measurement set up to match the excitation, emission and luminescence lifetime of the principal trap. Furthermore, given the low energy of excitation, fluorescence is not active from other defects in the crystal. According to Prasad et al. (2017), IRPL possess the following features: 1) non-destructive read-out of the dosimetric information at low temperature (7 K) because of inactive transport through the band-tail states, 2) high signal sensitivity because of the repeated measurement of same trapped electrons, and 3) signal stability on geological time scales. These authors also suggested that both the IRSL and the IRPL compete at room temperature; the former process reflects detrapping efficiency (electrons leave the trap) and the later reflects the re-trapping efficiency. Prasad et al. (2017) also demonstrated that the IRPL can be used in optical dating and is amenable to both the additive and the regenerative dose methods (Duller 1991, 1995, 1999).

One advantage of IRPL over IRRL is that it is based on optical exci-

tation after beta irradiation. Thus, it becomes possible to perform all the pre-treatments used in OSL/IRSL (e.g., preheat, optical cleanout, etc.) to IRPL. Furthermore, in comparison to IRSL, one can measure the IRPL signal with high sensitivity, by increasing the measurement time, since IRPL behaves almost like a steady-state signal at room temperature. All the tests to check the internal consistency, such as recuperation, recycling, preheat plateau and dose recovery, of the SAR method (Murray & Wintle, 2000; Murray et al., 2003; Wintle and Murray, 2006) can also be employed in sediment dating using IRPL.

1.6 Objectives of this Ph.D. research

Despite rapid advances in OSL/IRSL dating and many decades of research, the luminescence mechanisms in feldspar are still not fully understood. Several questions that are yet to be answered are:

1. What is the trap depth of the principal trap?
2. What are the excited states of the principal trap?
3. What fraction of the electrons in the principal trap participate in the IRSL process?
4. Whether single or multiple traps are involved in the OSL/IRSL emission process?
5. Does the thermal depletion of OSL/IRSL reflect the thermal stability of the electron population?
6. What is the exact nature of the defects (crystal defects or atom impurities) associated with the OSL/IRSL emission?
7. Why is the signal sensitivity different for different feldspar types (K-F, Na-F and Ca-F)?
8. Can signal fading be described completely by quantum mechanical tunneling?

Detailed knowledge of physics underlying luminescence production is not necessarily required for sediment dating, except for the fading correction method (Visocekas, 1985; Visocekas, 2002; Huntley and Lamothe,

2001). However, new applications of feldspar such as thermochronometry (Guralnik et al., 2015; King et al., 2016), and rock surface dating (Sohbati et al., 2012, 2015) demand better understanding of physical parameters of the system (for e.g. trap depth, energy structure, distribution of the defects, etc.) in order to establish a robust feldspar model. Additionally, advancing our knowledge about the principal trap and the luminescence processes in feldspar will help us designing new dating methods/protocols to improve accuracy and precision (e.g., robust fading correction methods), and extending the age range.

The purpose of this Ph.D. is to use the novel IRPL signal to enhance our knowledge of the principal trap and its response to ionizing radiation in feldspar. The specific objectives of this Ph.D. are **1) to advance our understanding of luminescence processes and the associated defect system in feldspar using site-selective spectroscopic techniques based on infrared photoluminescence (IRPL) and infrared radioluminescence (IRRL), and 2) to test the potential of IRPL for sediment dating.** Achieving these objectives here successfully addresses questions 1, 2, 3, 4 and 5, and paves a way to address questions 6, 7 and 8 in future.

1.7 Thesis outline

This Ph.D. thesis contains nine chapters: Introduction (Chapter 1), Instrumentation and samples (Chapter 2), two published research articles (Chapters 3 and 4), four manuscripts ready for submission (Chapters 5, 6, 7 and 8), and finally a Summary and conclusion (Chapter 9).

During my research, I have investigated several aspects associated with the principal trap such as the electronic structure (energy levels), trap depth, single or multiple traps, spatial distribution, and correlation between emission bands and geochemistry. Furthermore, I have tried to understand the relationship between different signals (IRPL, IRRL, and OSL) originating from the principal trap(s). Finally, I have developed a SAR protocol based on IRPL to use it as an alternative to OSL dating. The outline of this thesis is as follows.

Chapter 1: Introduction and overview

This is the current chapter. Here, the background and objectives of my

research work including the outline of this thesis are presented.

Chapter 2: Instrumentation and samples

In this chapter, a brief summary of the instrumentation, methods, and samples used in this research is given. I have used three main research facilities: 1) Risø station for CryOgenic LUminescence Research (COLUR) at DTU Nutech, Denmark, 2) Risø TL/OSL reader with IRPL attachment, and 3) Scanning Electron Microscope-Cathodoluminescence (SEM-CL) facility at LumiLab, University of Ghent, Belgium. The main spectroscopic techniques used in this work are photoluminescence (PL), radioluminescence (XEOL and CL), and optically stimulated luminescence (OSL). The materials used in this research are natural aluminosilicates (feldspars) of different chemical composition.

Chapter 3: Towards direct measurement of electrons in metastable states in K-feldspar: Do infrared-photoluminescence and radioluminescence probe the same trap?

This chapter is the main building block of this thesis. It reports that there exists another IRPL emission in addition to that reported by Prasad et al. (2017). It then makes a comparative analysis of the infrared photoluminescence (IRPL) and infrared radioluminescence (IRRL or XEOL) signals by examining their spectral response to different measurement conditions.

Chapter 4: Instrumentation for the non-destructive optical measurement of trapped electrons in feldspar

This chapter includes details on the development of the IRPL measurement system for routine sediment dating.

Chapter 5: Characterization of electron-trapping centers in feldspar by low-temperature photoluminescence excitation-emission spectroscopy

This chapter presents a detailed investigation of the origin of optically stimulated luminescence (OSL), and infrared photoluminescence (IRPL)

signals arising from the principal trap. The site-selective technique based on IRPL is extensively used to draw conclusions. It reports parameters such as trap depth, excited-state energies, and the excited-state relaxation lifetime of the principal trap, and provides unambiguous evidence for the existence of two principal traps in feldspar. It also examines dose response and the thermal- and optical-bleaching behavior of these two principal traps to verify their different trap depths.

Chapter 6: Site-selective mapping of metastable states using electron-beam induced luminescence microscopy

This chapter presents the results on the mapping of the electron-trapping states in K-feldspar (potassium-rich) using spectrally-resolved cathodoluminescence (CL) microscopy at the spatial resolution of 6 to 22 µm. It demonstrates that the two NIR emission bands are spatially variable and, therefore, originate from different sites. It further explores the link between the individual NIR emission peaks with the chemical composition (K, Na, and Fe), and proposes a cluster model to explain the quenching of the near-infrared (NIR) emission by Fe^{4+}.

Chapter 7: A coupled PL-OSL system to probe dynamics of the metastable states

This chapter investigates the relationship between optically stimulated luminescence (OSL) and photoluminescence (PL) in order to understand the behavior of the metastable states participating in the luminescence production in feldspar. It shows a unique coupled OSL-PL physical system that can provide an unambiguous understanding of the thermal dependence, thermo-optical bleaching, and radiation-induced growth of electron and holes.

Chapter 8: Sediment dating using Infrared photoluminescence (IRPL)

This chapter presents the results on the development of a SAR protocol based on IRPL and tests its potential for sediment dating using known-age samples.

Chapter 9: Summary and conclusion

This chapter provides a summary of the major results from all the chapters and discusses the new understanding of luminescence mechanisms in feldspar.

References

Aitken, M. J. (1985). Thermoluminescence dating. London: Academic Press, 153.

Aitken, M. J. (1998). Introduction to optical dating: the dating of Quaternary sediments by the use of photon-stimulated luminescence. Clarendon Press.

Aitken, M. J. (1994). Optical dating: a non-specialist review. Quaternary Science Reviews, 13(5-7), 503-508.

Andersen, M. T., Jain, M., & Tidemand-Lichtenberg, P. (2012). Red-IR stimulated luminescence in K-feldspar: Single or multiple trap origin? Journal of Applied Physics, 112(4), 043507.

Bailiff, I. K., & Barnett, S. M. (1994). Characteristics of infrared-stimulated luminescence from a feldspar at low temperatures. Radiation Measurements, 23(2-3), 541-545.

Barnett, S. M., & Bailiff, I. K. (1997). Infrared stimulation spectra of sediments containing feldspars. Radiation Measurements, 27(2), 237-242.

Baril, M. R., & Huntley, D. J. (2003). Infrared stimulated luminescence and phosphorescence spectra of irradiated feldspars. Journal of Physics: Condensed Matter, 15(46), 8029.

Baele, JM., Decrée, S., and Brian, R. (2019). Section II New Methods for Mineral Exploration. John Wiley & Sons, Inc.

Bos, A. J. J. (2006). Theory of thermoluminescence. Radiation Measurements, 41, S45-S56.

Bos, A. J. (2017). Thermoluminescence as a research tool to investigate luminescence mechanisms. Materials, 10(12), 1357.

Bøtter-Jensen, L., McKeever, S. W., & Wintle, A. G. (2003). Optically stimulated luminescence dosimetry. Elsevier.

Buylaert, J. P., Jain, M., Murray, A. S., Thomsen, K. J., & Lapp, T. (2012a). IR-RF dating of sand-sized K-feldspar extracts: a test of accuracy. Radiation Measurements, 47(9), 759-765.

Buylaert, J. P., Murray, A. S., Vandenberghe, D., Vriend, M., & De Corte, F. (2008). Optical dating of Chinese loess using sand-sized quartz: establishing a time frame for Late Pleistocene climate changes in the western part of the Chinese Loess Plateau. Quaternary Geochronology, 3(1), 99-113.

Buylaert, J. P., Jain, M., Murray, A. S., Thomsen, K. J., Thiel, C., & Sohbati, R. (2012b). A robust feldspar luminescence dating method for Middle and Late Pleistocene sediments. Boreas, 41(3), 435-451.

Clark, R. J., & Bailiff, I. K. (1998). Fast time-resolved luminescence emission spectroscopy in some feldspars. Radiation Measurements, 29(5), 553-560.

Clark, R. J., & Sanderson, D. C. W. (1994). Photostimulated luminescence excitation spectroscopy of feldspars and micas. Radiation Measurements, 23(2-3), 641-646.

De St. Jorre, L., & Smith, D. G. (1988). Cathodoluminescent gallium-enriched feldspars from the Thore Lake rare metal deposits, Northwest Territories. The Canadian Mineralogist, 26(2), 301-308.

Degering, D., & Krbetschek, M. R. (2007). 11. Dating of interglacial sediments by luminescence methods. The Climate of Past Interglacials, Developments in Quaternary Sciences 157-171. Elsevier.

Duller, G. A. T., & Bøtter-Jensen, L. (1993). Luminescence from potas-

sium feldspars stimulated by infrared and green light. Radiation Protection Dosimetry, 47(1-4), 683-688.

Duller, G. A. T. (1991). Equivalent dose determination using single aliquots. International Journal of Radiation Applications and Instrumentation. Part D. Nuclear Tracks and Radiation Measurements, 18(4), 371-378.

Duller, G. A. T., Bøtter-Jensen, L., Kohsiek, P., & Murray, A. S. (1999). A high-sensitivity optically stimulated luminescence scanning system for measurement of single sand-sized grains. Radiation Protection Dosimetry, 84(1-4), 325-330.

Duller, G. A. T. (1995). Luminescence dating using single aliquots: methods and applications. Radiation Measurements, 24(3), 217-226.

Duller, G. A. T. (1997). Behavioural studies of stimulated luminescence from feldspars. Radiation Measurements, 27(5), 663-694.

Erfurt, G. (2003). Infrared luminescence of Pb+ centres in potassium rich feldspars. Physica status solidi (a), 200(2), 429-438.

Erfurt, G., & Krbetschek, M. R. (2003a). Studies on the physics of the infrared radioluminescence of potassium feldspar and on the methodology of its application to sediment dating. Radiation Measurements, 37(4-5), 505-510.

Erfurt, G., & Krbetschek, M. R. (2003b). IRSAR-a single-aliquot regenerative dose dating protocol applied to the infrared radiofluorescence (IR-RF) of coarse-grain K-feldspar. Ancient TL, 21(1), 35.

Finch, A. A., & Klein, J. (1999). The causes and petrological significance of cathodoluminescence emissions from alkali feldspars. Contributions to Mineralogy and Petrology, 135(2-3), 234-243.

Fox, M. (2002). Optical properties of solids. Oxford University Press.

Frouin, M., Huot, S., Kreutzer, S., Lahaye, C., Lamothe, M., Philippe,

A., & Mercier, N. (2017). An improved radiofluorescence single-aliquot regenerative dose protocol for K-feldspars. Quaternary Geochronology, 38, 13-24.

Geake, J. E., Walker, G., Telfer, D. J., & Mills, A. A. (1977). The Cause and Significance of Luminescence in Lunar Plagioclase. Philosophical Transactions of the Royal Society A: Mathematical, Physical and Engineering Sciences, 285, 403-405.

Garcia-Guinea, J., Townsend, P. D., Sanchez-Munoz, L., & Rojo, J. M. (1999). Ultraviolet-blue ionic luminescence of alkali feldspars from bulk and interfaces. Physics and chemistry of minerals, 26(8), 658-667.

Gorobets, B. S., Portnov, A. M., & Rogozhin, A. A. (1995). Luminescence spectroscopy of the earth. Radiation Measurements, 24(4), 485-491.

Götze, J. (2012). Application of cathodoluminescence microscopy and spectroscopy in geosciences. Microscopy and Microanalysis, 18(6), 1270–1284.

Guralnik, B., Jain, M., Herman, F., Ankjærgaard, C., Murray, A.S., Valla, P.G., Preusser, F., King, G.E., Chen, R., Lowick, S.E., & Kook, M. (2015). OSL-thermochronometry of feldspar from the KTB borehole, Germany. Earth and Planetary Science Letters, 423, pp.232-243.

Huntley, D. J., & Lamothe, M. (2001). Ubiquity of anomalous fading in K-feldspars and the measurement and correction for it in optical dating. Canadian Journal of Earth Sciences, 38(7), 1093-1106.

Huntley, D. J., & Lian, O. B. (2006). Some observations on tunnelling of trapped electrons in feldspars and their implications for optical dating. Quaternary Science Reviews, 25(19), 2503-2512.

Huntley, D. J., Godfrey-Smith, D. I., & Thewalt, M. L. (1985). Optical dating of sediments. Nature, 313(5998), 105-107.

Hütt, G., Jaek, I., & Tchonka, J. (1988). Optical dating: K-feldspars optical response stimulation spectra. Quaternary Science Reviews, 7(3-4),

381-385.

Jain, M., & Singhvi, A. K. (2001). Limits to depletion of blue-green light stimulated luminescence in feldspars: implications for quartz dating. Radiation Measurements, 33(6), 883-892.

Jain, M., & Ankjærgaard, C. (2011). Towards a non-fading signal in feldspar: insight into charge transport and tunnelling from time-resolved optically stimulated luminescence. Radiation Measurements, 46(3), 292-309.

Jain, M., Buylaert, J. P., Thomsen, K. J., & Murray, A. S. (2015b). Further investigations on 'non-fading'in K-Feldspar. Quaternary International, 362, 3-7.

King, G. E., Guralnik, B., Valla, P. G., & Herman, F. (2016). Trapped-charge thermochronometry and thermometry: A status review. Chemical Geology, 446, 3-17.

Kars, R. H., Poolton, N. R., Jain, M., Ankjærgaard, C., Dorenbos, P., & Wallinga, J. (2013). On the trap depth of the IR-sensitive trap in Na-and K-feldspar. Radiation Measurements, 59, 103-113.

Kars, R. H., Reimann, T., Ankjærgaard, C., & Wallinga, J. (2014). Bleaching of the post-IR IRSL signal: new insights for feldspar luminescence dating. Boreas, 43(4), 780-791.

Krbetschek, M. R., Rieser, U., & Stolz, W. (1996). Optical dating: some luminescence properties of natural feldspars. Radiation Protection Dosimetry, 66(1-4), 407-412.

Krbetschek, M. R., Trautmann, T., Dietrich, A., & Stolz, W. (2000). Radioluminescence dating of sediments: methodological aspects. Radiation Measurements, 32(5-6), 493-498.

Liritzis, I., Singhvi, A. K., Feathers, J. K., Wagner, G. A., Kadereit, A., Zacharias, N., & Li, S. H. (2013). Luminescence dating in archaeology, anthropology, and geoarchaeology: an overview (p. 70). Heidelberg:

Springer.

Li, B., & Li, S. H. (2011a). Luminescence dating of K-feldspar from sediments: a protocol without anomalous fading correction. Quaternary Geochronology, 6(5), 468-479.

Li, B., & Li, S. H. (2011b). Thermal stability of infrared stimulated luminescence of sedimentary K-feldspar. Radiation Measurements, 46(1), 29-36.

Mariano, A. N., & King, P. J. (1975). Europium-activated cathodoluminescence in minerals. Geochimica et Cosmochimica Acta, 39(5), 649-660.

Malins, A. E. R., Poolton, N. R. J., Quinn, F. M., Johnsen, O., & Denby, P. M. (2004). Luminescence excitation characteristics of Ca, Na and K-aluminosilicates (feldspars) in the stimulation range 5–40 eV: determination of the band-gap energies. Journal of Physics D: Applied Physics, 37(10), 1439.

Murray, A. S., & Wintle, A. G. (2000). Luminescence dating of quartz using an improved single-aliquot regenerative-dose protocol. Radiation measurements, 32(1), 57-73.

Murray, A. S., & Wintle, A. G. (2003). The single aliquot regenerative dose protocol: potential for improvements in reliability. Radiation measurements, 37(4-5), 377-381.

Morthekai, P., Jain, M., Murray, A. S., Thomsen, K. J., & Bøtter-Jensen, L. (2008). Fading characteristics of martian analogue materials and the applicability of a correction procedure. Radiation Measurements, 43(2-6), 672-678.

Pagel, M., Barbin, V., Blanc, P., & Ohnenstetter, D. (2000). Cathodoluminescence in geosciences: an introduction. In Cathodoluminescence in Geosciences (pp. 1-21). Springer, Berlin, Heidelberg.

Prasad, A. K., Poolton, N. R., Kook, M., & Jain, M. (2017). Optical dating in a new light: A direct, non-destructive probe of trapped elec-

trons. Scientific reports, 7(1), 1-15.

Prasad, A. K. (2017). Understanding defect related luminescence processes in wide bandgap materials using low temperature multi-spectroscopic techniques (Ph.D. thesis, Technical University of Denmark)

Prasad, A. K., & Jain, M. (2018). Breakdown of Kasha's Rule in a Ubiquitous, Naturally Occurring, Wide Bandgap Aluminosilicate (Feldspar). Scientific reports, 8(1), 810.

Poolton, N. R. J., Bøtter-Jensen, L., & Johnsen, O. (1996). On the relationship between luminescence excitation spectra and feldspar mineralogy. Radiation Measurements, 26(1), 93-101.

Poolton, N. R. J., Botter-Jensen, L., & Johnsen, O. (1995). Influence on donor electron energies of the chemical composition of K, Na and Ca aluminosilicates. Journal of Physics: Condensed Matter, 7(24), 4751–4762.

Poolton, N. R. J., Mauz, B., Lang, A., Jain, M., & Malins, A. E. R. (2006). Optical excitation processes in the near band-edge region of KAlSi3O8 and NaAlSi3O8 feldspar. Radiation Measurements, 41(5), 542-548.

Poolton, N. R. J., Kars, R. H., Wallinga, J., & Bos, A. J. J. (2009). Direct evidence for the participation of band-tails and excited-state tunnelling in the luminescence of irradiated feldspars. Journal of Physics: Condensed Matter, 21(48), 485505.

Poolton, N. R. J., Wallinga, J., Murray, A. S., Bulur, E., & Bøtter-Jensen, L. (2002). Electrons in feldspar I: on the wavefunction of electrons trapped at simple lattice defects. Physics and Chemistry of Minerals, 29(3), 210-216

Rhodes, E. J. (2011). Optically stimulated luminescence dating of sediments over the past 200,000 years. Annual Review of Earth and Planetary Sciences, 39, 461-488.

Rieser, U., Hütt, G., Krbetschek, M. R., & Stolz, W. (1997). Feldspar

IRSL emission spectra at high and low temperatures. Radiation Measurements, 27(2), 273-278.

Riedesel, S., King, G. E., Prasad, A. K., Kumar, R., Finch, A. A., & Jain, M. (2019). Optical determination of the width of the band-tail states, and the excited and ground state energies of the principal dosimetric trap in feldspar. Radiation Measurements, 125, 40–51.

Roberts, H. M. (2012). Testing Post-IR IRSL protocols for minimising fading in feldspars, using Alaskan loess with independent chronological control. Radiation Measurements, 47(9), 716-724.

Roberts, R. G., & Lian, O. B. (2015). Dating techniques: Illuminating the past. Nature, 520(7548), 438-439.

Schulman, J. H., Ginther, R. J., Klick, C. C., Alger, R. S., & Levy, R. A. (1951). Dosimetry of x-rays and gamma rays by radiophotoluminescence. Journal of Applied Physics, 22(12), 1479-1487.

Singhvi, A. K., & Porat, N. (2008). Impact of luminescence dating on geomorphological and palaeoclimate research in drylands. Boreas, 37(4), 536-558.

Spooner, N. A. (1994). The anomalous fading of infrared-stimulated luminescence from feldspars. Radiation Measurements, 23(2-3), 625-632.

Sohbati, R., Murray, A. S., Chapot, M. S., Jain, M., & Pederson, J. (2012). Optically stimulated luminescence (OSL) as a chronometer for surface exposure dating. Journal of Geophysical Research: Solid Earth, 117(B9).

Sohbati, R. (2015). Luminescence, rock surfaces. In Encyclopedia of Scientific Dating Methods (pp. 485-488). Springer Netherlands.

Short, M. A. (2003). An investigation into the physics of the infrared excited luminescence of irradiated feldspars (PhD thesis, Simon Fraser University, Canada).

Telfer, D. J., & Walker, G. (1975). Optical detection of Fe3+ in lunar plagioclase. Nature, 258(5537), 694-695.

Telfer, D. J., & Walker, G. (1978). Ligand field bands of Mn2+ and Fe3+ luminescence centres and their site occupancy in plagioclase feldspars. Modern Geology, 6, 199-210.

Thomsen, K. J., Murray, A. S., Jain, M., & Bøtter-Jensen, L. (2008). Laboratory fading rates of various luminescence signals from feldspar-rich sediment extracts. Radiation Measurements, 43(9), 1474-1486.

Trautmann, T., Krbetschek, M. R., Dietrich, A., & Stolz, W. (1998). Investigations of feldspar radioluminescence: Potential for a new dating technique. Radiation Measurements, 29(3–4), 421–425.

Trautmann, T., Dietrich, A., Stolz, W., & Krbetschek, M. R. (1999a). Radioluminescence dating: a new tool for Quaternary geology and archaeology. Naturwissenschaften, 86(9), 441-444.

Trautmann, T., Krbetschek, M. R., Dietrich, A., & Stolz, W. (1999b). Feldspar radioluminescence: a new dating method and its physical background. Journal of Luminescence, 85(1-3), 45-58.

Trautmann, T., Krbetschek, M. R., Dietrich, A., & Stolz, W. (2000). The basic principle of radioluminescence dating and a localized transition model. Radiation Measurements, 32(5-6), 487-492.

Tsukamoto, S., Denby, P. M., Murray, A. S., & Bøtter-Jensen, L. (2006). Time-resolved luminescence from feldspars: new insight into fading. Radiation Measurements, 41(7), 790-795.

Tsukamoto, S., Kondo, R., Lauer, T., & Jain, M. (2017). Pulsed IRSL: A stable and fast bleaching luminescence signal from feldspar for dating Quaternary sediments. Quaternary Geochronology, 41, 26-36.

Visocekas, R. (1985). Tunnelling radiative recombination in labradorite: its association with anomalous fading of thermoluminescence. Nuclear Tracks and Radiation Measurements (1982), 10(4-6), 521-529.

Visocekas, R. (2002). Tunnelling in afterglow: Its coexistence and interweaving with thermally stimulated luminescence. Radiation Protection Dosimetry, 100(1-4), 45-53

Wallinga, J. (2002). Optically stimulated luminescence dating of fluvial deposits: a review. Boreas, 31(4), 303-322.

Wintle, A. G., & Murray, A. S. (2006). A review of quartz optically stimulated luminescence characteristics and their relevance in single-aliquot regeneration dating protocols. Radiation Measurements, 41(4), 369-391.

Wintle, A. G. (2008). Fifty years of luminescence dating. Archaeometry, 50(2), 276-312.

Wintle, A. G. (1973). Anomalous fading of thermo-luminescence in mineral samples. Nature, 245(5421), 143-144.

Yi, S., Buylaert, J. P., Murray, A. S., Lu, H., Thiel, C., & Zeng, L. (2016). A detailed post-IR IRSL dating study of the Niuyangzigou loess site in northeastern China. Boreas, 45(4), 644-657.

CHAPTER 2

INSTRUMENTATION AND SAMPLES

Optical spectroscopy comprises a number of techniques to study the interaction of light with matter. It is a versatile tool for the characterization of various soft and condensed materials. Based on the response of the materials when the light strikes, a range of different spectroscopic techniques, for example absorption spectroscopy, scattering spectroscopy and emission spectroscopy are available. The success in experiments demands high-performance (sensitive, low noise, high-resolution etc.) measurement systems and attention to the experimental details.

The experimental work during my Ph.D. research was carried out using three measurement facilities: two of them (Risø station for CryOgenic LUminescence (COLUR) and Cathodoluminescence microscopy and spectroscopy) were used to study basic physical processes and material characteristics, while one (Risø TL/OSL reader modified to include infrared photoluminescence measurements) was used for the application in optically stimulated luminescence (OSL) dating. The details about the systems are explained below.

2.1 Risø station for CryOgenic LUminescence Research (COLUR)

CryOgenic LUminescence Research (COLUR) facility consists of a Horiba spectrofluorometer (Flurolog-3) modified to include additional excitation

and emission ports, He-cryostat for sample cooling, and an x-ray irradiator (Figure 2.1). The major elements and their properties are described in the following sections.

2.1.1 Flurolog-3

The Horiba Flurolog-3 spectrofluorometer incorporates two broadband excitation sources (a continuous wave Xenon lamp and a pulsed Xenon lamp), excitation and emission monochromators to select the emission and excitation wavelengths, photomultiplier tube (PMT), nitrogen-cooled charge coupled device (CCD) detector and Indium Gallium Arsenide (InGaAs) detector. Individual components of Fluorolog-3 are described below.

Light sources

Flurolog-3 consists of two Xenon (Xe) arc lamps (450 W), one is operated in continuous wave (CW) mode and the other one in pulsed mode. The lamp provides relatively continuous light output in the range 250-700 nm; the light output above 800 nm contains a number of sharp lines. The system is also modified to use external light sources such as lasers, and light emitting diodes (LEDs). I have mainly used near infrared (NIR) lasers at 830 nm (maximum power 150 mW) and 885 nm (maximum power 500 mW) in this study.

Monochromators

In contrast to lasers, Xe-lamp emits broadband radiation. Therefore, a monochromator is required to select the desired wavelength. The excitation and emission monochromators of Flurolog-3 contain Czerny-Turner double (330 nm Blaze, 1200 lines/mm) and single (500 nm Blaze, 1200 lines/mm towards PMT) gratings, respectively. The iHR320 spectrograph (coupled to CCD) contains 3 gratings (1) 500 nm Blaze, 300 lines/mm (2) 500 nm Blaze, 1200 lines/mm (3) 750 nm Blaze, 1200 lines/mm.

Filters

Optical filters are desirable in order to increase the sensitivity by sup-

pressing any stray and/or second-order light. I have used two long pass (LP) interference filters with cut-off wavelengths ∼850 nm (optical density 4) and ∼925 nm (optical density 4).

Detectors

Fluorolog-3 comprises of 3 detection systems 1) Hamamatsu R-928P PMT with detection window 200-1000nm (spectral correction is only available in the range of 290-850 nm), 2) a liquid-nitrogen-cooled charge-coupled device (CCD) with detection window 200-1050 nm (spectral correction is only available in the range of 290-1050 nm), 3) a liquid-nitrogen-cooled InGaAs detector with detection window 850-1600 nm. The CCD and InGaAs detectors (coupled to the iHR320 spectrograph) are placed at the axial and lateral positions, respectively, and can be accessed through the control software. Additionally, an external PMT can also be used through a port on the sample chamber unit. In this study, the CCD and external PMT detectors were mostly used. However, InGaAs detector was also used to check reproducibility.

Time-correlated Single Photon Counting (TCSPC) system

Time-correlated single-photon counting (TCSPC) is a technique to measure fluorescence decay lifetimes on the pico- and nanosecond timescale. It is based on the detection of single photons and measures their arrival times at the detector (mostly PMTs) with respect to a reference signal. Fluorolog-3's TCSPC attachment uses a Fluorohub to control or register the photon counting, a data acquisition system (DataStation hub), and many pulsed excitation sources.

Softwares

Fluorolog-3 uses a software package FluorEssence v3.5 to control the hardware and data-acquisition; the data is exported in Origin file format. The TCSPC system uses DataStation and DAS6 Softwares for data-acquisition.

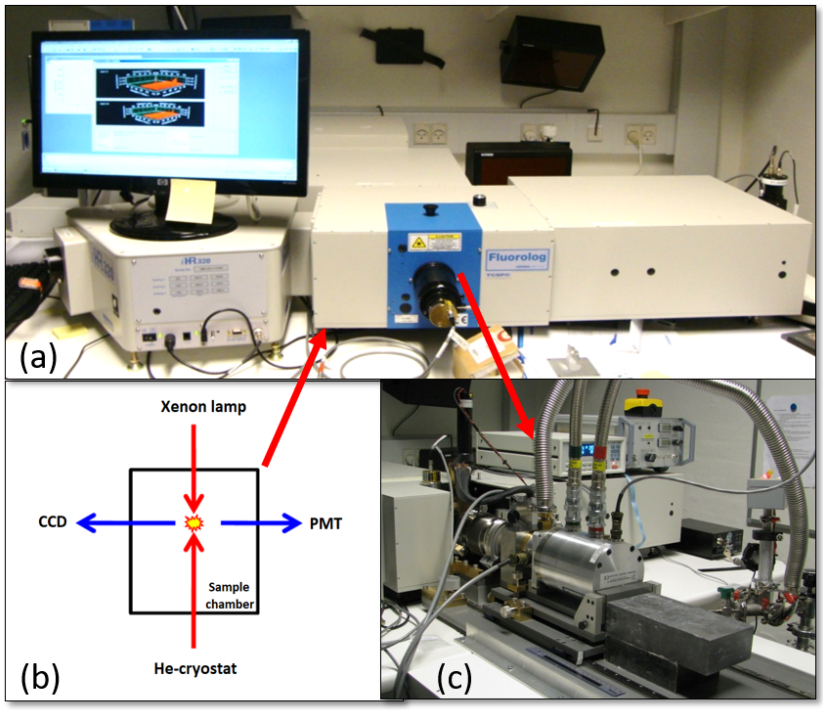

Figure 2.1: CryOgenic LUminescence Research (COLUR) facility. (a) Horiba spectrofluroromter (Flurolog-3). (b) Excitation and emission ports for Xenon lamp, charge coupled device (CCD), and photomultiplier tube (PMT). (c) Modified sample chamber to include a temperature controlled closed-loop He-cryostat.

2.1.2 Temperature control

Fluorolog-3 has been modified to include a temperature-controlled closed-loop He-cryostat to perform the measurements at cryogenic temperatures down to 7 K from room temperature (Figure 2.1c). The cryostat consists of a metallic chamber through which Helium gas is pumped. To perform temperature-dependent measurements, a Proportional-Integral-Derivative (PID) controller from Lakeshore (model 335) is used to control the temperature between 7 K to 300 K.

2.1.3 X-ray irradiator

Fluorolog-3 has been modified to include also an x-ray irradiator, placed on the top of the sample chamber. It is a filament-based x-ray tube with copper anode, operated at 40 kV anode voltage and 100 µA anode current. The x-ray tube can only be operated under low pressure ($\sim 10^{-4}$ mbar) due to security interlocking. This attachment allows x-ray excited luminescence (XEOL) measurements and sample irradiation to perform dose dependent optically stimulated luminescence (OSL) and photoluminescence (PL) measurements.

2.2 Scanning electron microscope based cathodoluminescence (SEM-CL) setup

The scanning electron microscope-cathodoluminescence (SEM-CL) setup with an energy-dispersive x-ray spectrometer (EDX) attachment allows simultaneous measurement of CL emission as well as chemical composition (Figure 2.2). This facility is available at the LumiLab, University of Ghent, Belgium. Different components of this set up are described below.

2.2.1 Scanning Electron Microscope (SEM)

Scanning electron microscope (SEM) uses a focused electron-beam over a solid surface to generate a number of signals, for example, Back-scattered electrons, secondary electrons, Auger electrons, characteristic x-rays, white

x-rays, light, etc (see Figure 2.2a). These signals are used to study several physical properties of a sample such as crystalline structure and orientation, morphology, chemical composition, etc. Emitted light during the interaction of the electron-beam and the sample can be collected and used to study spectral characteristics. In this thesis, a SEM system (Model no. S3400-N), provided by Hitachi Science Systems, Ltd., was used; this system utilizes an electron beam accelerated at 1000 V to 30 kV, and uses two detectors, secondary electron detector (need operation at high vacuum) and backscattered electron detector (need operation at low vacuum), to capture SEM images (Figure 2.2c).

2.2.2 Energy Dispersive X-ray Spectroscopy (EDX) system

Energy dispersive x-ray spectroscopy (EDX) is a chemical microanalysis technique that enables us to analyze the elemental composition of the sample. Interaction of electron beam with sample results in bremsstrahlung and characteristic x-rays. The energies of characteristic x-rays allow identification of the elements by determining the correlation between released photon energy and the atomic number of the atom. A ThermoScientific Noran System 7 attached to the SEM microscope was used for elemental mapping and quantification by probing the characteristic x-ray lines. This system incorporates spectral imaging capability and the ability to collect 1,000,000 x-ray counts per second in each digital pulse processor.

2.2.3 Spectrophotometer

Cathodoluminescence (CL) spectrum was captured using an optical fiber connected to an Acton SP monochromator (grating: 300 lines/mm) and ProEM 1600 EMCCD, both from Princeton Instruments. The system allows spectral detection in the wavelength range of 300-1050 nm. CL maps are created by recording the CL emission from each spot during an electron-beam scan (Figure 2.2c).

2.3 Risø TL/OSL reader with IRPL attachment

The Risø TL/OSL reader is a widely used measurement system to determine radiation doses in natural and artificial materials. It enables automated measurements of thermoluminescence (TL) and optically stim-

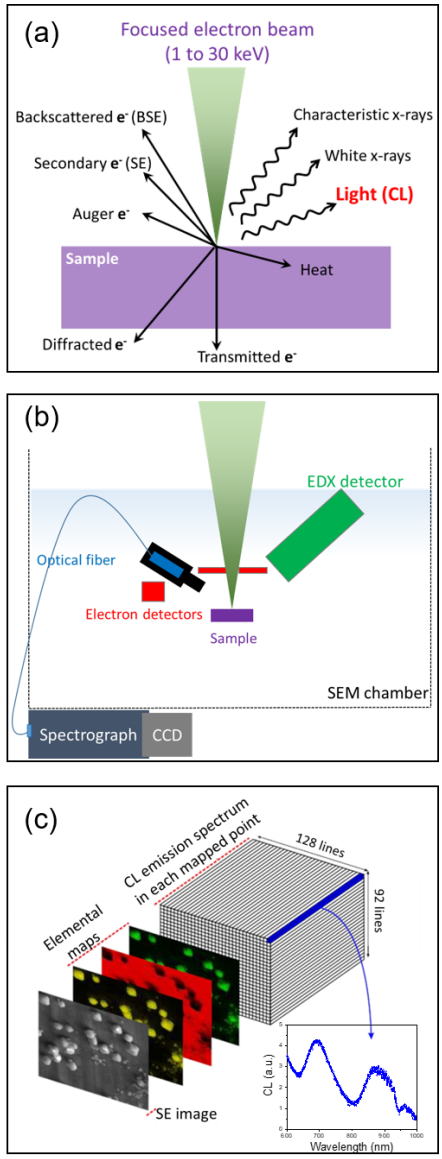

Figure 2.2: Experimental aspects of cathodoluminescence (CL) microscopy. (a) Interaction of electron beam with the sample and the resulting radiations. (b) Sketch of the main components of the scanning electron microscope (SEM) used for the CL mapping. (c) Examples of the secondary electrons (SE) image, elemental maps, CL maps, and spectrum.

ulated luminescence (OSL) signals and is equipped with a carousel with 48 positions and a reference radiation source. Apart from the existing components, it is also possible to attach external components such as photomultiplier tubes (PMTs), spectrometer, single-grain measurement system, optical camera, x-ray source, radio-luminescence facility, etc.

One of the objectives of my Ph.D. research has been to develop an automated measurement system for the infrared photoluminescence (IRPL) signal. This has been accomplished by upgrading the Risø TL/OSL reader using new attachments- external NIR laser, appropriate detection filters, and NIR PMTs (Figure 2.3). My main task was to help in the development of this system by obtaining an uniform laser intensity profile at the sample position using optical diffusers, tuning laser power at the sample position, optimizing signal-to-noise ratio, and testing different detection filters. The detailed description of the IRPL system is incorporated as a chapter (Chapter 4) in this thesis.

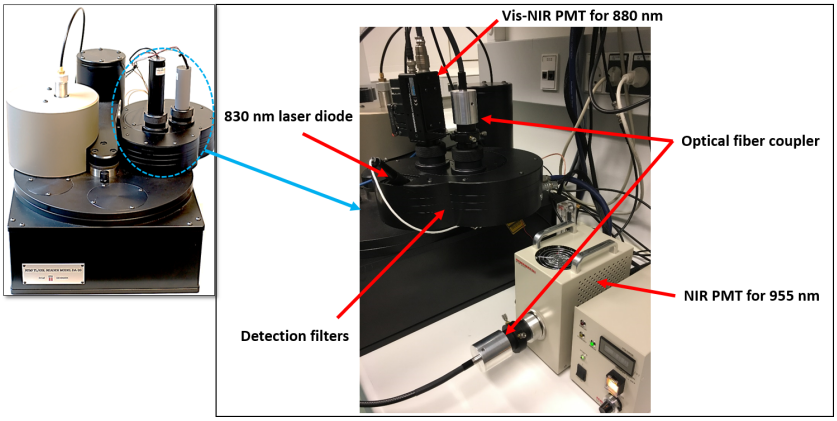

Figure 2.3: IRPL attachment to Risø TL/OSL reader (right figure). Dash head of a conventional reader (left figure) is modified to include 830 nm laser, and two photomultiplier tubes (Vis-NIR PMT and NIR PMT).

2.4 Samples

A number of feldspar samples, sedimentary, museum and rock extracts, were used in this study. Details can be obtained in Table 2.1 and Table 2.2. These samples are well characterized and studied previously by Baril (2002) and Prasad (2017).

Table 2.1: List of samples used in this study. For sample no. 1 to 6, the chemical composition was obtained using x-ray fluorescence (XRF) (taken from Prasad, 2017). For sample no. 7 to 10, the chemical composition was obtained using inductively coupled plasma emission spectroscopy (ICP-ES) (taken from Baril, 2002; Baril and Huntley, 2003; Meisl and Huntley, 2005). S = sedimentary origin, M = museum single crystal, and R=rock extracts. Samples K7, K8, K9, and K13 were obtained from Prof. D.J. Huntley.

No.	Sample Code	Nominal composition	Type of Feldspar	Provenance	K	Na	Ca	Chapter covered
1	R43	KF	S	China	0.91	0.08	0.01	6
2	R45	Amazonite	M	Norway	0.87	0.12	0.01	5
3	R47	KF	S	China	0.85	0.12	0.03	3,4,5,6
4	R48	Amazonite	M	Russia	0.83	0.16	0.02	5
5	R28	KF	M	Switzerland	0.95	0.05	0.00	3 and 5
6	R50	Microcline	M	Unknown	0.80	0.18	0.01	6
7	K7	Microcline	R	USA	0.70	0.30	0.00	6
8	K8	Microcline	R	Canada	0.84	0.15	0.01	5
9	K9	Microcline	R	Russia	0.84	0.15	0.01	5
10	K13	Microcline	R	Canada	0.85	0.15	0.00	6
11	MK	unknown	R	Denmark	-	-	-	4

Table 2.2: List of natural samples used in this study. Expected equivalent doses (D_es) are listed from the independent methods (Murray and Funder, 2003;Murray et al., 2007; Buylaert et al., 2012; Aubry et al.,2012. These samples were obtained from Dr. Jan-Pieter Buylaert, Prof. Andrew Murray, and Nordic Luminescence Laboratory (NLL), and have previously been used by Buylaert et al. (2012).

No.	Sample Code	Sediment type	Provenance	Grain size (μm)	Expected D_e (Gy $\pm$ se)	Chapter covered
1	901009	Coastal marine sands	Gammelmark (Denmark)	150-250	279 $\pm$ 11	7, 8
2	981010	Coastal marine sands	Gammelmark (Denmark)	150-250	298 $\pm$ 12	7, 8
3	981013	Coastal marine sands	Gammelmark (Denmark)	90-150	274 $\pm$ 12	7, 8
4	H22553	Coastal marine sands	Sula (Russia)	180-250	209 $\pm$ 11	7, 8
5	952503	Coastal marine sands	Sula (Russia)	150-210	262 $\pm$ 12	8
6	072255	Aeolian sand	Carregueira (Portugal)	180-250	97 $\pm$ 7	7, 8
7	092202	Slope desposit	Indre-et-Loire (France)	180-250	158 $\pm$ 10	7, 8
8	075407	Dune sands	Sinai peninsula (Egypt)	180-250	103 $\pm$ 7	8
9	075602	Aeolian sand	North Jutland (Denmark)	90-180	18 $\pm$ 1	8
10	082105	Aeolian sand	Zwolle (TheNetherlands)	90-180	Unknown	8
11	B12	Unknown	Unknown	90-250	Unknown	8
12	092204	Alluvial sands	Indre-et-Loire (France)	180-250	97 $\pm$ 3	7

References

Aubry, T., Dimuccio, L.A., Almeida, M., Buylaert, J.P., Fontana, L., Higham, T., Liard, M., Murray, A.S., Neves, M.J., Peyrouse, J.B., & Walter, B. (2012). Stratigraphic and technological evidence from the middle palaeolithic-Châtelperronian-Aurignacian record at the Bordes-Fitte rockshelter (Roches d'Abilly site, Central France). Journal of human evolution, 62(1), pp.116-137.

Baril, M. R. (2002). Spectral investigations of luminescence in feldspars (PhD thesis, Simon Fraser University, Canada).

Baril, M. R., & Huntley, D. J. (2003). Optical excitation spectra of trapped electrons in irradiated feldspars. Journal of Physics: Condensed Matter, 15(46), 8011.

Buylaert, J. P., Jain, M., Murray, A. S., Thomsen, K. J., Thiel, C., & Sohbati, R. (2012). A robust feldspar luminescence dating method for Middle and Late P leistocene sediments. Boreas, 41(3), 435-451.

Meisl, N. K., & Huntley, D. J. (2005). Anomalous fading parameters and activation energies of feldspars. Ancient TL, 23(1), 1.

Murray, A. S., & Funder, S. (2003). Optically stimulated luminescence dating of a Danish Eemian coastal marine deposit: a test of accuracy. Quaternary Science Reviews, 22(10-13), 1177-1183.

Murray, A. S., Svendsen, J. I., Mangerud, J., & Astakhov, V. I. (2007). Testing the accuracy of quartz OSL dating using a known-age Eemian site on the river Sula, northern Russia. Quaternary Geochronology, 2(1-4), 102-109.

Prasad, A. K. (2017). Understanding defect related luminescence processes in wide bandgap materials using low temperature multi-spectroscopic techniques (PhD thesis, Technical University of Denmark, Denmark).

CHAPTER 3

TOWARDS DIRECT MEASUREMENT OF ELECTRONS IN METASTABLE STATES IN K-FELDSPAR: DO INFRARED-PHOTOLUMINESCENCE AND RADIOLUMINESCENCE PROBE THE SAME TRAP?

Raju Kumar, Myungho Kook, Andrew Sean Murray & Mayank Jain

Abstract: Prasad et al. (2017) recently developed a new method of measuring the dosimetric signal in feldspar, based on a Stokes-shifted photoluminescence emission (excitation energy at 1.40 eV (885 nm), emission energy ∼1.30 eV (955 nm)). The new signal, termed as infrared photoluminescence (IRPL), was shown to arise from radiative relaxation of the excited state of the principal trap (dosimetric trap), and allows non-destructive probing of the dosimetric information. Thus, IRPL provides a unique tool to study physical characteristics of these metastable states in feldspar, e.g., number density and spatial distribution, trap depth, photoionization and capture cross-section, excited state lifetime, and tunneling probabilities. The IRPL emission is apparently related to the infrared radioluminescence (IRRL) in K-feldspar; in the latter, however,

the electrons relax after being trapped as a result of exposure to ionizing radiation, rather than as a result of excitation within the trap.

In this study, we report the discovery of a second IRPL emission centered at 1.41 eV (880 nm) in a K-feldspar which arises in response to excitation with 1.49 eV photons. Based on the temperature- and dose-dependent behavior of IRPL and IRRL, we conclude that the same defect(s) participates in these two emissions. However, IRPL emission is governed by the characteristics of the principal trap (defect) alone, whereas IRRL depends additionally on thermally-assisted transport within the band-tail states. Since IRPL is a site-selective technique, it does not, unlike IRRL, suffer from contamination from higher energy emissions (e.g. from Fe^{3+}). This lack of contamination, and the possibility for thermal/optical pre-treatments and repeated measurements of the same trapped electrons, suggest that IRPL is a robust alternative to IRRL.

3.1 Introduction

Commonly, feldspar is measured using near-infrared (NIR) photons in the range 850-880 nm; the resulting anti-Stokes emission (in UV to red) is called infrared stimulated luminescence (IRSL; Hütt et al., 1988). In IRSL, the dosimetric trap used in IRSL dating (henceforth, the principal trap) is photoionized by a two-step process; (i) IR photons interact with the trapped electrons to convert the occupied trap to its excited state, (ii) electrons in the excited state diffuse out into the band-tail states or the conduction band (depending on the ambient temperature) (Jain and Ankjærgaard, 2011). Eventually, a fraction of these detrapped electrons combines with trapped holes to produce IRSL. The IRSL signal has been subject to rigorous investigation in the last three decades, and promising results have been demonstrated from elevated temperature post IR- IRSL (Thomsen et al., 2008; Buylaert et al., 2012b; Li and Li, 2011) and pulsed IRSL signals (Tsukamoto et al., 2006, 2017; Jain and Ankjærgaard, 2011; Jain et al., 2015). However, the stability of the signal and possible artifacts e.g. due to thermally induced transfer are not fully understood (e.g., Jain et al., 2015; Tsukamoto et al., 2017). Based on excitation spectroscopy, Andersen et al. (2012) demonstrated that the different IRSL and post IR-IRSL signals result from the same trap (henceforth, the principal trap).

Trautmann et al. (1998, 1999a, 1999b) proposed an alternative mea-

surement method that seems to use the principal trap but does not rely on optical stimulation. This method, infrared radioluminescence (IRRL) or sometimes referred as infrared radiofluorescence (IRRF), is based on the observation that if one exposes the sample to ionizing radiation, a dose dependent prompt emission occurs in the near-infrared (NIR). These authors suggested that the IRRL originates from free electrons produced in the conduction band by ionizing radiation; trapping and radiative relaxation of these electrons in the principal trap gives rise to the dose dependent IRRL. Although the IRRL signal has not yet been explored as rigorously as the IRSL signals, limited tests suggest that the accuracy of equivalent dose (D_e) estimates may be sample dependent because of possible sensitivity change during measurement (e.g., Buylaert et al., 2012a). When used to determine dose, the IRRL measurement technique may be somewhat inflexible since it is not obvious how one can preferentially select signal components of different stabilities, as is, for instance, possible using thermal treatments and prior stimulation in optical probing methods (e.g. post IR-IRSL; Thomsen et al., 2008).

Recently, Prasad et al. (2017) developed a novel technique for the non-destructive measurement of trapped electrons in the principal trap. The signal they discovered is termed Infrared Photoluminescence (IRPL), where IR refers to the excitation energy and PL refers to the Stokes-shifted photoluminescence arising from radiative relaxation within the principal trap. For dosimetric investigations, these authors used a 1.40 eV (885 nm) laser to excite the trap and recorded emission at 1.30 eV (955 nm). Since IRPL is generated without involving recombination centers, it offers the potential for (i) isolating a non-fading signal using the same techniques that are used with IRSL, and (ii) making precise luminescence measurements at very small trapped electron populations or even very small scales (e.g., sub-micron) because of the ability to repeatedly (i.e. non-destructively) measure the same trapped electrons. In the OSL/IRSL method, one trapped electron can at the most produce one photon in a particular emission, since the measurement is destructive. In contrast, in IRPL, a single trapped electron can produce a large number of photons, because it can be re-excited many times; this aspect of IRPL allows very high precision measurements, potentially allowing mapping of even single trapping states. Equally importantly, because IRPL directly probes the principal trap, it can be used to improve our physical understanding of feldspar as a dosimetric system, such as e.g., number

density and spatial distribution, trap depth, photoionization and capture cross-section, excited-state lifetime and tunneling probabilities relevant to the electron-trapping states.

In this study, we explore the relationship between IRRL and IRPL because it is likely that they both use the same radiative relaxation mechanism within the principal trap. We use low temperature (7 K-300 K) measurements to provide a clearer resolution of the emission peak(s) due to subdued electron-phonon interactions, compared with the room temperature measurements. The purpose of this study is to advance our understanding of the principal trap in feldspar by providing a holistic model combining IRPL, IRSL and IRRL, so as to improve the dating technologies that make use of these signals.

3.2 Infrared radioluminescence: Previous Studies

Radioluminescence results from transitions of free electrons from the conduction band during trapping or recombination, during interaction of material with ionizing radiations such as x-rays, β-particles, etc. (e.g., Schulman et al., 1951). Radioluminescence emissions in feldspar are generally observed in the UV-Red region (e.g., Krbetschek et al., 1997; Prasad et al., 2016). However, in K-feldspar, radioluminescence is also observed in the near-infrared region, called Infrared Radio Luminescence (IRRL). IRRL in K-feldspar is thought to arise from the capture of free electrons in the conduction band by the same traps that give rise to IRSL (or trap, according to Andersen et al., 2012), resulting in a broad emission peaking around 865 nm at room temperature (Trautmann et al., 1999a, b; Krbetschek et al., 2000; Trautmann et al., 2000; Varma et al., 2013). Since the number of occupied trapping sites increases with ionizing radiation dose, the IRRL intensity decreases as irradiation progresses, as fewer and fewer sites are available for trapping. On the other hand, UV-Red intensities, presumably resulting from electron-hole recombination, increase with dose; this is possibly due to an increasing concentration of holes and decreasing competition from the principal trap (Trautmann et al., 1999b; Erfurt and Krbetschek, 2003a).

Trautmann et al. (1999a, b) demonstrated that IRRL emission at 865 nm can be used for dating. Based on the comparison of the IRSL excitation spectrum (peak emission ~1.44 eV) and IRRL emission spec-

trum (peak emission ∼1.43 eV) at room temperature, they concluded that these two signals originate from the same trap. Erfurt and Krbetschek (2003b) inferred two peaks in the near IR region at 910 nm and 865 nm, based on fitting the IRRL spectrum with a Gaussian distribution function. These authors suggested that the two emissions originate from Pb^+ centers in K-feldspar, by drawing analogy with the spectral response of synthetically grown KCl:Pb sample. Erfurt (2003) reported that IR emission in KCl:Pb crystal at 930 nm and 975 nm correspond to electronic transitions $7^2P_{1/2} \rightarrow 6^2S_{1/2}$ and $7^2S_{1/2} \rightarrow 6^2S_{1/2}$ respectively, and concluded that the same transitions are responsible for the 865 nm and 910 nm IRRL emissions in K-feldspar during exposure to ionizing radiation. Erfurt (2003) also monitored photoluminescence in the same IR region as the IRRL, while exciting the sample with UV photons (henceforth, UV-IRPL). This UV-IRPL presumably arises from photoionization of trapped electrons, and subsequent re-trapping of a fraction of the resulting free electron population from the conduction band. Thus, the mechanism generating UV-IRPL is similar to IRRL, but the emission intensity of UV-IRPL must depend both on a) the concentration of detrapped electrons in the conduction band due to photoionization of the principal trap as well as from other defects in the crystal that can be stimulated by UV, and b) the concentration of empty sites of the principal trap available for retrapping and hence able to generate UV-IRPL emission. Erfurt (2003) normalized IRRL using the UV-IRPL in different geological samples, and demonstrated that the ratio of these two signals (IRRL/UV-IRPL) decreases monotonically with dose; thus, he concluded that the two phenomena must be interlinked by reduction of the Pb^{2+} to Pb^+ during RL, and vice versa during UV photoionization. However, he did not attempt a quantitative correlation between the dose dependence of UV-IRPL and IRRL. Furthermore, there appears to be a discrepancy between the relative rate of change of IRRL and UV-IRPL signals in his bleaching experiments, and the inferred two peaks (∼910 nm and ∼865 nm) were never confirmed independently, e.g. by low temperature measurements. It is also important to clarify that the UV-IRPL reported by Erfurt (2003) is not generated by the same mechanism as the IRPL reported by Prasad et al. (2017). Considering a population of trapped electrons; in IRPL, excitation is done with IR photons and the electrons oscillate between the excited and ground state of the principal trap; because the electrons never leave the trap (at cryogenic temperatures), the

trapped electron population remains unchanged. This is a site-selective, non-destructive measurement technique resulting in a steady state signal. In contrast, in UV-IRPL, trapped electrons are photoionized by UV light; once in the conduction band these electrons (in addition to returning to the principal trap and so generating UV-IRPL) also have the possibility of recombination with the holes and being retrapped by the defects other than the principal trap. Thus, UV-IRPL changes the trapped electron population during readout; it is a destructive method. Furthermore, unlike IRPL which selectively targets the excited state of the principal trap, UV stimulation not only excites the principal trap but any electrons in other traps able to be photoionized by UV light.

While the proposed mechanism of IRRL (Erfurt, 2003) is convincing, it has not yet been investigated in detail. There are several unsolved issues, e.g. the absence of a dose-dependent IRRL signal in Na–feldspar, despite the existence of an IR resonance, the high non-dose dependent background (up to 60% of the signal), sensitivity change, etc., all of which require explanation. The IRRL model is mainly based on two indirect correlations: (i) the similarity of peak energy of IRRL emission ($\sim$1.43 eV) and IRSL resonance ($\sim$1.44 eV), and (ii) the decrease in IRRL intensity with ionizing radiation dose. In contrast, the IRPL is a site-selective technique, where the signal has been unambiguously tied to radiative relaxation within the principal trap (Prasad et al., 2017). Thus, a detailed comparison of the spectroscopy and dose-dependence of IRRL and IRPL should provide further insights into the IRRL mechanism and its link to the principal trap. This comparison is attempted in the following sections.

3.3 Experimental details

3.3.1 Samples

We have used well-characterized potassium-rich feldspars for our measurements. Major element analysis was carried out by x-ray fluorescence (XRF) on the Risø TL/OSL reader. Our first sample R47 (85% K-F, 12% Na-F, and 3% Ca-F by weight; here K-F: Potassium-Feldspar, Na-F: Sodium-Feldspar and Ca-F: Calcium-Feldspar) is a feldspar extract from sediment. The second sample R28 (95% K-F, 5% Na-F, and 0% Ca-F) is a museum feldspar specimen. Detailed investigations on these samples are presented in Prasad et al. (2017). The samples were bleached

for 48 hours in a solar simulator (Hönle SOL 2) before undertaking any measurements.

3.3.2 Instrumentation

All measurements were carried out using the Risø station for CryOgenic Luminescence Research (COLUR) at DTU Nutech, Denmark. It is based on a Horiba Fluorolog-3 spectrofluorometer expanded to include multi-excitation and -detection ports, an x-ray irradiator (40 kV anode voltage, 100 µA anode current, and 0.06 Gy s^{-1} dose rate to quartz), and a temperature-controlled closed-loop He cryostat (7-300 K) (refer instrumentation section).

A liquid nitrogen cooled charge coupled device (CCD) was used to record emission spectra following excitation using 1.40 eV (885 nm) and 1.49 eV (830 nm) laser sources. Two long pass interference filters (925 nm, optical density=4) were used to detect emission at 1.30 eV (955 nm), and two 850 nm long pass interference filters (optical density=4) were used to record emissions at 1.41 eV (880 nm) and ∼1.30 eV (955 nm). IRRL spectra were recorded with CCD detector during x-ray irradiation.

All the radio-luminescence measurements reported in this paper were obtained using x-rays. We used a filament-based x-ray tube with a Tungsten (W) anode, operated at 40 kV and 100 µA. The broad Bremsstrahlung x-ray spectrum was hardened through a 70 µm aluminium foil and RL measurements were made under low pressure (∼ 10^{-4} mbar) because of security inter-locking issues. The x-rays penetrate the bulk sample (mean energy ∼13 keV), thus the RL investigations presented here should be comparable to those using a beta source.

3.4 Results and discussion

3.4.1 IRPL emission spectra using 1.49 eV (830 nm) laser at 7 K

Prasad et al. 2017 used a 1.40 eV (885 nm) laser to excite the principal trap. The resulting Stokes-shifted emission peak at 1.30 eV (955 nm) at 7 K must represent the lowest principal-trap's excited state detectable with the CCD system. We measured the IRPL following Prasad et al. (2017) in R47 at 7 K (after giving ∼216 Gy dose using x-rays) by stimulating with a 1.40 eV (885 nm) laser and recording the emission spectrum

from 910 nm to 1000 nm through 925 nm long pass (LP) interference detection filters. As expected, the resultant emission (Figure 3.1, red curve) at 1.30 eV (955 nm) is similar to that reported by Prasad et al. (2017). In order to explore possible higher energy levels in the principal trap, we repeated the measurement using a 1.49 eV (830 nm) laser and 850 nm LP detection filters. Two emission peaks centered at 1.30 eV (955 nm) and 1.41 eV (880 nm) were observed (Figure 3.1, black curve; fluctuations possibly due to etalon effect); the peak at 1.30 eV (955 nm) is similar to that reported by Prasad et al. (2017) using 1.40 eV excitation whereas the IRPL peak at 1.41 eV (880 nm) has not been reported before. Given our lack of knowledge of the nature of the principal trap, one may question whether the two emissions using 1.49 eV (830 nm) excitation arise from: (i) the two excited levels of the same defect (two different excited electronic levels, or splitting of the excited level), or (ii) only one excited energy level of the defect but the defect resides in two different sites where the energy is modified by about 0.1 eV because of the difference in the environment (i.e., site dependence). The latter cannot, in principle, be distinguished from the case where the difference in excited energy is linked to two different defect types but this is unlikely given that energy difference is only 0.1 eV.

Interestingly, Erfurt (2003) also reported two IR emissions (∼1.36 eV (910 nm) and ∼1.43 eV (865 nm)) in feldspars by fitting Gaussian to the IRRL spectra recorded at room temperature (RT). If one accepts that the IRPL results from the same trap as IRRL, the difference in IRRL peak positions compared to those observed in the IRPL above (∼1.30 eV and ∼1.41 eV) may be related to the measurement temperature (our measurement at 7 K) or sample dependence. In the next section, we make a detailed comparison of the IRRL and IRPL emissions to further explore these possibilities.

3.4.2 IRRL and IRPL spectra at 7 K and 295 K

We first measured the IRRL emission spectrum at 7 K on sample R47 after bleaching for 48 hours. Two emission peaks centered at 1.30 eV (955 nm) and 1.41 eV (880 nm) were observed (Figure 3.2a); these are similar to the two IRPL peaks observed using the 1.49 eV (830 nm) laser (Figure 3.2b). However, the relative amplitude of the two peaks is different in IRPL and IRRL (Figure 3.2a and b). These IRRL and IRPL measurements were then repeated at room temperature (295 K); the emissions

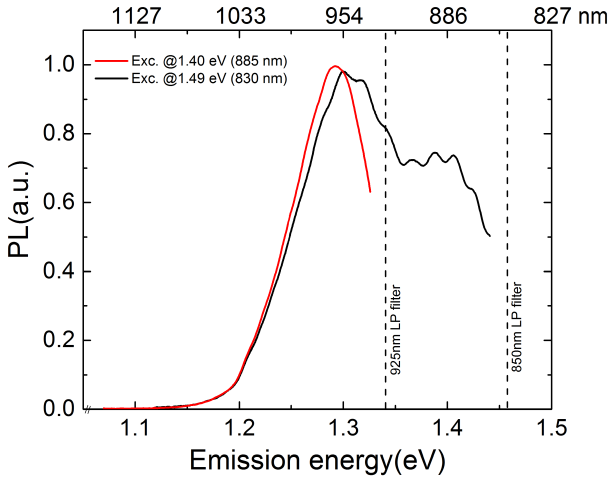

Figure 3.1: Infrared Photoluminescence (IRPL) emission spectra measured using two different excitation energies: 1.40 eV (red curve) and 1.49 eV (black curve). The data are measured at low temperature (7 K) on sample R47 (also dosed at 7 K). The spectral regions affected due to filters have been removed.

were found to merge into a single peak (Figure 3.2a and b). Interestingly, when compared to the measurements at 7 K, the peak amplitude was reduced in case of IRPL but increased in IRRL. Moreover, it appears that thermal quenching is larger for the 1.30 eV IRPL peak than for the 1.41 eV IRPL peak.

We repeated the same experiments using the R28 sample. In this sample only a single broad peak at 1.41 eV (880 nm) is present, in both IRRL and IRPL (Figure 3.2c and d). Again, when the temperature was increased from 7 K to 295 K, the IRRL peak intensity increased but the IRPL intensity decreased.

Several broad inferences follow from the data presented in Figure 3.2:

1. IRPL and IRRL show the same emission peaks at 1.30 eV and 1.41 eV at 7 K; however, the exact shape and relative amplitude (e.g. in R47) of these peaks differ in IRRL and IRPL.

2. While IRRL shows an apparent thermal assistance, the IRPL shows thermal quenching. Thermal quenching appears to differ between the 1.30 eV and 1.41 eV peaks.

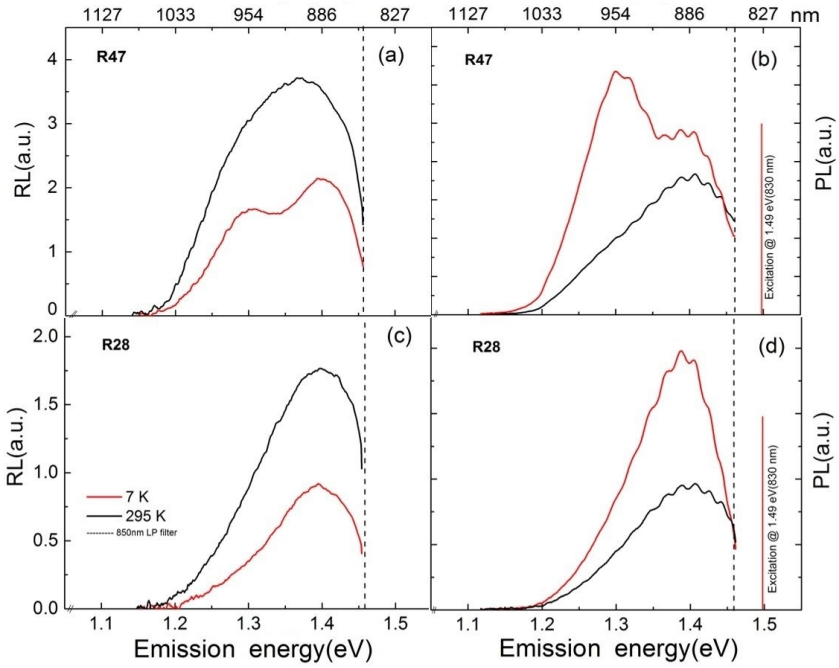

Figure 3.2: Left column: Infrared Radioluminescence (IRRL) spectra at 7 K and 295 K recorded during x-ray irradiation for samples (a) R47 and (c) R28. Right column: Infrared Photoluminescence (IRPL) spectra at 7 K and 295 K recorded using 830 nm (1.49 eV) laser excitation for samples (b) R47 and (d) R28. The red curve shows the data measured at 7 K, whereas, the black curves are the data measured at 295 K.

3. Whether there are one or two apparent IRPL emission peaks depends on the sample. Sample R47 (85% K-F) shows two clear peaks, whereas R28 (95% K-F) shows only one clear peak. However, two peaks, although not clearly visible, are almost certainly present in R28 spectrum since measurements using 1.40 eV (885 nm) laser excitation demonstrate an emission peak at 1.30 eV (see Prasad et al., 2017, Figure SI-2c)

Our 7 K data provides direct evidence confirming the interpretation of the two RL peaks by Erfurt (2003). However, their peak energies inferred by fitting data measured at room temperature are significantly different to those observed directly in our 7 K data. To examine the role of temperature on peak position, we fitted our IRRL data at 295 K (Supplementary Figure SI 3.1a) with a Gaussian function; this gave peak positions at 1.41 eV and 1.30 eV at 295 K, indistinguishable from the peak positions observed at 7 K. To test whether our room temperature data are nevertheless compatible with those of Erfurt (2003), we refitted our 295 K IRRL data with the two peak positions fixed at 1.43 eV and 1.36 eV, as reported by him, but this resulted in a significantly poorer fit (Figure SI 3.1b). Thus, we conclude that the difference between our result and that of Erfurt is not related to the measurement temperature. It may be because he used a different sample. Since the results of fitting at room temperature are consistent with the 7 K data, where the two peaks are resolved experimentally, we can only suggest that further work is necessary to test possible sample dependence of the two RL peak positions.

The difference in the emission characteristics of R28 and R47 suggests that two different defect sites (or defects) might be responsible for the two different emission peaks. Otherwise, the relative amplitude of the two IRPL or IRRL peaks should have remained constant in different samples.

3.4.3 Temperature dependent IRRL and IRPL

In order to further investigate the temperature dependence of the width of the IRRL and IRPL peaks observed above, we measured these signals in R47 at temperatures ranging from 7 K to 295 K at intervals of 20 K. The IRRL spectra were recorded for a sample after 48 hrs of SOL-2 bleaching, while the IRPL spectra were recorded after 1 hour x-ray

irradiation (∼216 Gy) of the bleached sample. Figure 3.3a shows the temperature-dependent IRRL spectra observed as the temperature was increased from 7 to 295 K; the x-ray was switched on (for 10 s) only during the RL measurement. Two IRRL emission peaks (∼880 nm and ∼955 nm) are observed, well resolved at 7 K. With an increase in the temperature (7 K to 295 K) the two peaks increasingly overlap, presumably due to phonon-induced broadening; this results in a single broad peak by ∼220 K. The peak amplitude systematically increases with temperature by about a factor of two; the increase becomes detectable at about 100 K, and it appears that there is no further increase above 250 K. To confirm that our results do not depend upon the exact temperature sequence, we repeated the IRRL measurements while the temperature was decreased from 295 K to 7 K; the results were indistinguishable from those obtained from the increasing temperature sequence (Figure SI 3.3).

In contrast to IRRL, the IRPL emission intensity decreases with an increase in temperature. The two peaks are well resolved at 7 K, as with IRRL, but merge into a single peak by ∼220 K (Figure 3.3c). Interestingly, the rate of decrease of the 1.41 eV peak intensity with temperature is different from that of the 1.30 eV peak.

In order to evaluate the temperature dependence of the broadening and amplitude of the two emissions, we attempted to deconvolute the data using 2 Gaussian peaks. However, due to temperature-dependent broadening of the spectra, it was difficult to obtain satisfactory fits. Instead, a semi-quantitative analysis was undertaken using two integration windows to separate the two emissions (shown as shaded regions in Figure 3.3a and 3.3c). The two peaks in the IRRL signal (∼1.41 eV (880 nm) and ∼1.30 eV (955 nm)) show similar behavior and increase in intensity relatively rapidly between 100 and 250 K. In case of IRPL the signal at 1.30 eV and 1.41 eV appear to be stable up to 200 K. At higher temperatures, emission at 1.30 eV quenches much faster than the emission at 1.41 eV.

Peak broadening is expected due to lattice vibrations at higher temperatures. At low temperature, lattice vibrations are weaker and thus peaks in both PL and RL spectra are better resolved. The increase in IRRL intensity with temperature suggests that efficient transport of electrons in the band-tail states (Poolton et al., 2002, 2009; Jain and Ankjærgaard, 2011) is important for trapping; this results from phonon-assisted diffusion (PAD) at higher temperatures (band-tail transport ceases at

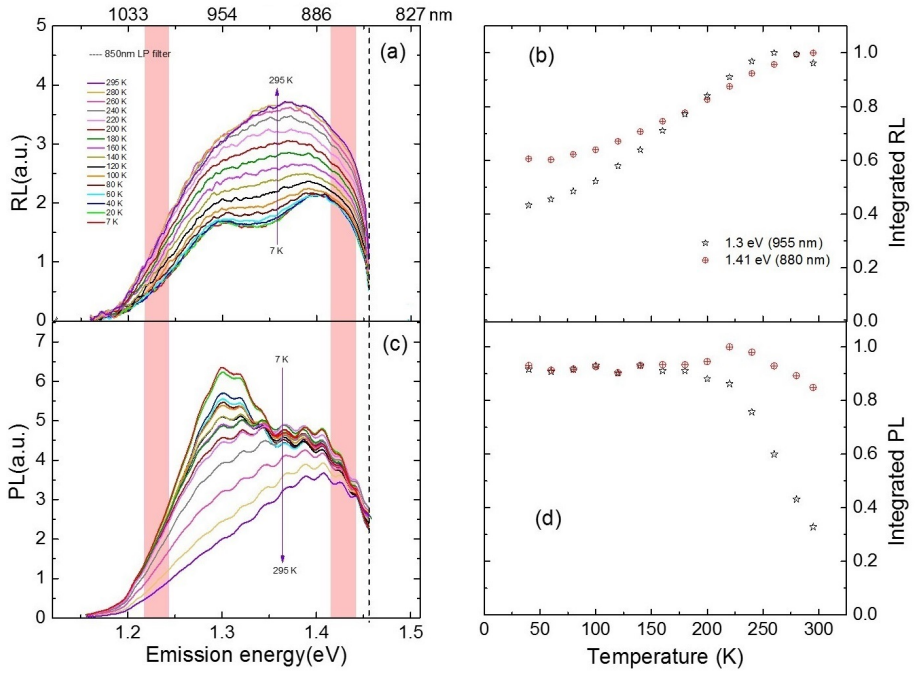

Figure 3.3: (a) Temperature dependent IRRL spectra, measured from 7 K to 295 K. (b) IRRL integrals (shaded area in (a)) plotted as a function of temperature. (c) Temperature dependent IRPL spectra measured using 1.49 eV laser excitation, measured from 7 K to 295 K. (d) Integrals (shaded area in (c)) plotted as a function of temperature. Shaded areas represent integration windows for two emissions ∼1.3 eV and ∼1.41 eV. All the measurements were made on sample R47.

low temperatures because of the lack of PAD). These results suggest that electron trapping during irradiation involves two steps; (i) thermalization of free electrons from the conduction band, and (ii) subsequent phonon-assisted transport within the band-tail states until trapping into the excited state in the principal trap.

IRPL on the other hand does not involve any band-tail transport at low temperatures; it is produced mainly by intra-defect excitation and emission (Prasad et al., 2017). The decrease in IRPL intensity with temperature is presumably dominated by an increase in non-radiative relaxation, with some leakage to the band-tail states at higher temperatures (e.g., Chithambo, 2007; Prasad et al., 2017). Our data suggest that the defects (or energy levels) giving rise to the 1.30 eV (955 nm) and 1.41 eV (880 nm) emissions have different thermal quenching behavior. Based on the inter-comparison of the responses of RL and PL to temperature, one may further conclude that IRRL involves a competition between thermal assistance due to more efficient diffusion of electrons within the band-tail states, and thermal quenching within the defect after trapping. On balance, it appears that PAD is the dominant effect in IRRL, which results in a similar increase in both the RL peaks. In contrast, quenching dominates in IRPL.

3.4.4 X-ray dose dependence of IRPL and IRRL

The IRPL and IRRL dose response at 7 K of sample R47 is examined next. To allow a direct comparison between the two techniques, IRPL measurements were carried out without preheating the sample. IRPL spectra were recorded using 850 nm long-pass filters and IRRL spectra were recorded using a 610 nm long-pass filter. As expected, the IRRL intensity for both the emission peaks is highest when no prior dose has been given (bleached feldspar) and decreases with x-ray irradiation duration. IRPL shows the opposite behavior due to an increase in the trapped electron concentration with dose (Figures 3.4a and b).

As with the temperature-dependence data, we integrated IRPL intensity in the energy range from 1.21-1.24 eV for the 1.30 eV emission and 1.41-1.44 eV for the 1.41 eV emission and plot the integrated signal as a function of dose. The increase with dose of both the two peaks, and the total IRPL area, is indistinguishable (Figure 3.4d). Fitting of an exponential function to the dose response curve (global fit to all the 3 data sets) gave a characteristic dose (D_0) of 641±12 Gy.

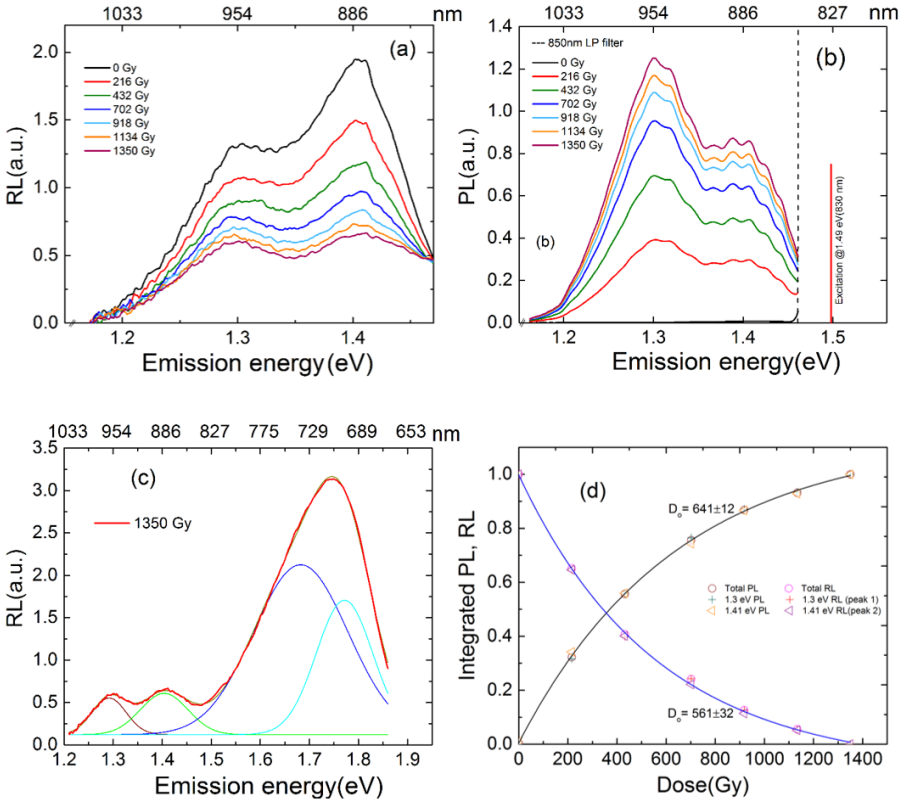

Figure 3.4: (a) X-ray dose response of IRRL signal at 7 K. The RL data were recorded from 1.2-1.85 eV using a 610 nm long pass filter, but they are only plotted here for the IRRL signal for clarity. Full data can be seen in Figure SI 3.2a. (b) X-ray dose response of IRPL signal at 7 K. (c) IRRL spectrum corresponding to 1350 Gy in the spectral range 1.2-1.85 eV; the data are best fitted to a sum of 4 Gaussian peaks. (d) Dose response curves for IRPL and IRRL. In case of IRPL, two integrated regions (1.21-1-24 eV for 1.30 eV emission and 1.41-1.44 eV for 1.41 eV emission) and total counts under the IRPL spectra were used to create the corresponding DRC. In case of IRRL peaks were deconvoluted (after subtracting the 'background' spectrum at 1350 Gy). The plot shows normalized areas of peak 1, peak 2, and the net counts under 'the background subtracted' IRRL spectra. The solid curves are global exponential fits to the data. All the measurements were made on sample R47.

The analysis of IRRL was, however, less straightforward because of the well known large background in the IRRL signal (Erfurt, 2003); up to 40% of the maximum in our sample) and the possible interference from the ∼1.72 eV (Fe^{3+} emission) which shows an increase in intensity with dose (Figure 3.4c; Figure SI 3.2a, b). Interestingly, it was observed that the width of the 'background' IRRL for the 1.41 eV emission (approximated as IRRL for our highest dose of 1350 Gy) is wider than that of the IRRL spectra corresponding to lower doses. This effect gave rise to an anomalous decrease in peak width with an increase in the peak area (Figure SI 3.2c). However, once the background spectrum was subtracted from the spectrum obtained at each dose, the spectral shapes were approximately similar for different doses (Figure SI 3.2d). For dose-response analysis, the subtracted spectra in the energy range of 1.21-1.46 eV were fitted to a sum of 2 Gaussian peaks (peak 1 at 1.30 eV and peak 2 at 1.41 eV). The responses, as a function of dose, of the normalized areas of peaks 1 and 2, and the net background-subtracted IRRL signal, are indistinguishable (Figure 3.4d). Fitting of an exponential decay function to the dose-response curve (global fit to all the 3 data sets) gave a characteristic dose of 561±32 Gy. This value is slightly lower than that obtained using IRPL; however, the considerable background in the IRRL affects the exact determination of D_0, and the difference is probably not significant. Certainly, to first order, the similar characteristic D_0 of the IRRL and IRPL suggests that the IRRL signal also arises from the principal trap, and that possible dose-dependent competition effects in IRRL generation (e.g. trapping or recombination in sites other than the principal trap) are not significant.

It is worth discussing the effect of interference from the ∼1.72 eV peak (likely Fe^{3+} emission) in IRRL dating. It can be seen from the data measured at 7 K and the corresponding peak fits (Figure SI 3.2a, b) that the Fe^{3+} peak increases rapidly with dose and interferes directly with both the IRRL signals. While not very significant in our sample, this interference can be important at high doses where the Fe^{3+} emission is relatively much greater than the IRRL emission. In routine IRRL dating measurements, one uses a photomultiplier tube with a detection filter and this combination is not able to discriminate against this contamination. One way to resolve this problem may be to preferentially detect the 1.30 eV emission; this is less affected by contamination. In contrast to IRRL, IRPL is a site-selective technique and thus not affected by such

contamination; other centres such as Fe^{3+} are not excited in IRPL.

In summary, our data demonstrate that the same defect very likely participates in both IRRL and IRPL; the proposed mechanisms are schematically represented in Figure 3.5. Interestingly, it appears that 1.72 eV RL peak shows a systematic increase with dose, which may have potential for RL dating (Figure SI 3.2a).

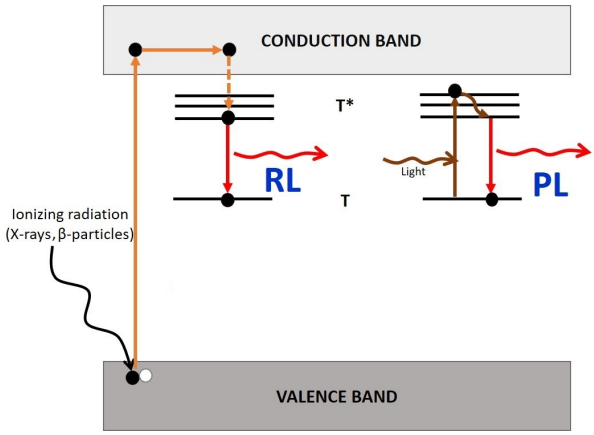

Figure 3.5: Band diagram to show the mechanism of IRRL and IRPL. Both signals arise from the same electron trapping center and their production does not involve recombination centers.

3.5 Conclusions

We report the discovery of an IRPL emission at 1.41 eV (880 nm), and demonstrate that the 1.30 eV (955 nm) IRPL emission reported by Prasad et al. (2017) can also be measured using a higher energy 1.49 eV (830 nm) excitation. Both these IRPL emissions show different thermal quenching behavior but grow similarly with dose. We demonstrate that the IRRL shows the same two emissions as the IRPL, and that these emissions have the similar dose dependence as IRPL. However, IRRL can be contaminated from higher energy emissions (e.g. ~1.72 eV) and contains a large background of unknown origin; these factors affect the shape of the dose response curve. This effect poses real challenges for the IRRL dating of old samples, especially using a standard photomultiplier and detection filter combination, and may contribute to the sensitivity changes in IRRL

reported earlier. Based on a comparison of the temperature dependence of IRRL and IRPL we conclude that IRRL arises from the thermalizaton of electrons from the conduction band into the band-tail states and subsequent trapping in the principal trap. A final radiative relaxation gives rise to the IRRL photons. In contrast, IRPL arises from intra-defect excitation and relaxation (Prasad et al., 2017). Thus, IRRL and IRPL are two complimentary signals from the same defect, the principal trap. Finally, the variation in the relative amplitudes of the IRPL and IRRL in our two feldspar samples leads to the suggestion that two different sites of the same defect are likely giving rise to the 1.41 eV (880 nm) and 1.30 eV (955 nm) emissions. This interpretation is different from Erfurt (2003) suggestion of two electronic levels in the same defect giving rise to the two IRRL emissions, and requires further investigations.

Supplementary Material

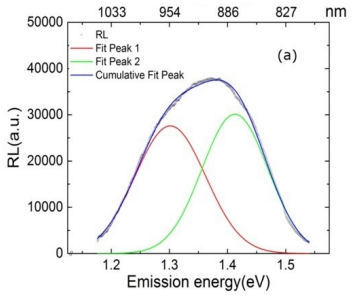

Model	Gaussian	
Equation	y = y0 + A/(w*sqrt(PI/(4*ln(2)))) * exp(-4*ln(2)*(x-xc)^2/w^2)	
Plot	Peak1(RL)	Peak2(RL)
y0	0.01 ± 0	0.01 ± 0
xc	1.30161 ± 9.95727E-4	1.41274 ± 8.0325E-4
A	4203.14029 ± 74.05796	4290.10973 ± 73.97947
w	0.1431 ± 0.00108	0.13378 ± 8.51914E-4
Reduced Chi-Sqr	244481.75454	
R-Square(COD)	0.99832	
Adj. R-Square	0.99831	

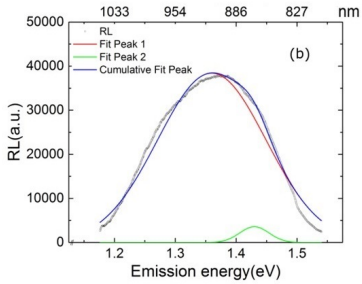

Model	Gaussian	
Equation	y = y0 + A/(w*sqrt(PI/(4*ln(2)))) * exp(-4*ln(2)*(x-xc)^2/w^2)	
Plot	Peak1(RL)	Peak2(RL)
y0	0.1 ± 0	0.1 ± 0
xc	1.36 ± 0	1.43 ± 0
A	8568.56838 ± 25.49468	215.59428 ± 14.28052
w	0.20952 ± 6.25679E-4	0.05656 ± 0.00371
Reduced Chi-Sqr	2.30507E6	
R-Square(COD)	0.98416	
Adj. R-Square	0.98411	

Figure SI 3.1: (a) IRRL spectrum at 295 K for sample R47. The data are fitted using Gaussian function with all free parameters. The best fit is shown in blue; the two component peaks plotted in red and green (∼1.3 eV and ∼1.41 eV) have an identical peak position as the directly observed peaks in the 7 K data (see Figure 3.2a). (b) The same IRRL data as (a) fitted while fixing the peak values to 1.36 and 1.43 eV, reported by Erfurt (2003). The fitting results are shown in the table on the right. The symbol 'w' signifies FWHM value. A much poorer fit is obtained suggesting that the inferred peak values of Erfurt (2003) do not explain our data.

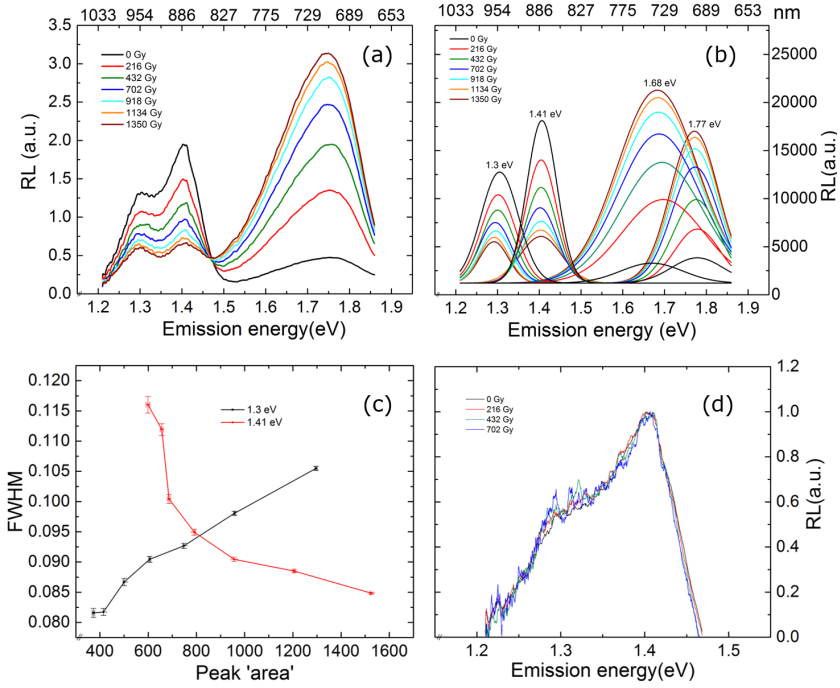

Figure SI 3.2: (a) Dose dependent RL spectra (in spectral range 1.2 eV to 1.85 eV) measured at 7 K in sample R47. A 610 nm long pass filter was used to obtain these results. RL spectra were measured intermittently while exposing the prior bleached sample (R47) to x-rays continuously. (b) Fitted RL spectra in (a) with four Gaussian peaks. (c) A plot showing the FWHMs of the individual IRRL peaks versus the area under these peaks. Peak at 1.41 shows an anomalous behavior, i.e. the FWHM becomes apparently smaller as the area increases. This is due to the effect of the large background (with a wide spectrum) inherent in IRRL. (d) Normalized IRRL spectra after subtracting the spectrum at 1350 Gy; the data suggest that the RL spectral shape does not change with dose if the background spectrum has been subtracted.

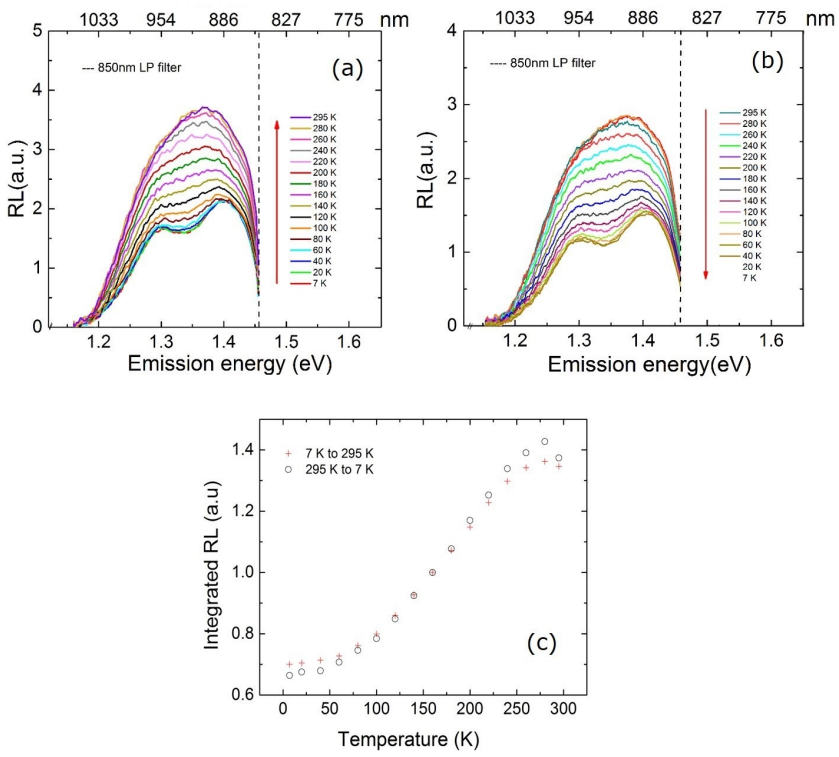

Figure SI 3.3: (a) Temperature dependent RL spectra measured from 7 K to 295 K. This data is the same data as that plotted in Figure 3.3a but is shown here again to enable comparison. (b) Temperature dependent RL spectra measured from 295 K to 7 K. (c) Normalized full IRRL integral (total counts under each spectrum) in sequences (a) and (b) potted against measurement temperature.

References

Andersen, T. M., Jain, M., & Tidemand-Lichtenberg, P. (2012). Red-IR stimulated luminescence in K-feldspar: Single or multiple trap origin?. Journal of Applied Physics, 112(4), 043507.

Buylaert, J. P., Jain, M., Murray, A. S., Thomsen, K. J., & Lapp, T. (2012a). IR-RF dating of sand-sized K-feldspar extracts: a test of accuracy. Radiation Measurements, 47(9), 759-765.

Buylaert, J. P., Jain, M., Murray, A. S., Thomsen, K. J., Thiel, C., & Sohbati, R. (2012b). A robust feldspar luminescence dating method for Middle and Late P leistocene sediments. Boreas, 41(3), 435-451.

Chithambo, M. L. (2007). The analysis of time-resolved optically stimulated luminescence: II. Computer simulations and experimental results. Journal of Physics D: Applied Physics, 40(7), 1880

Erfurt, G. (2003). Infrared Luminescence of Pb+ Centres in Potassium-Rich Feldspars. Physica Status Solidi (A) Applied Research 200 (2):429–38.

Erfurt, G., & Krbetschek, M. R. (2003a). Studies on the physics of the infrared radioluminescence of potassium feldspar and on the methodology of its application to sediment dating. Radiation Measurements, 37(4-5), 505-510.

Erfurt, G., & Krbetschek, M. R. (2003b). IRSAR-a single-aliquot regenerative dose dating protocol applied to the infrared radiofluorescence (IR-RF) of coarse-grain K-feldspar. Ancient TL, 21(1), 35.

Godfrey-Smith, D. I., Huntley, D. J., & Chen, W. H. (1988). Optical dating studies of quartz and feldspar sediment extracts. Quaternary Science Reviews, 7(3-4), 373-380.

Huntley, D. J., Godfrey-Smith, D. I., & Thewalt, M. L. (1985). Optical dating of sediments. Nature, 313(5998), 105-107.

Hütt, G., Jaek, I., & Tchonka, J. (1988). Optical dating: K-feldspars optical response stimulation spectra. Quaternary Science Reviews, 7(3-4),

381-385.

Jain, M., & Ankjærgaard, C. (2011). Towards a non-fading signal in feldspar: insight into charge transport and tunnelling from time-resolved optically stimulated luminescence. Radiation Measurements, 46(3), 292-309.

Jain, M., Sohbati, R., Guralnik, B., Murray, A.S., Kook, M., Lapp, T., Prasad, A.K., Thomsen, K.J. & Buylaert, J.P. (2015). Kinetics of infrared stimulated luminescence from feldspars. Radiation Measurements, 81, pp.242-250.

Krbetschek, M. R., Götze, J., Dietrich, A., & Trautmann, T. (1997). Spectral information from minerals relevant for luminescence dating. Radiation Measurements, 27(5-6), 695-748.

Krbetschek, M. R., Trautmann, T., Dietrich, A., & Stolz, W. (2000). Radioluminescence dating of sediments: methodological aspects. Radiation Measurements, 32(5-6), 493-498.

Li, B., & Li, S. H. (2011) Luminescence dating of K-feldspar from sediments: a protocol without anomalous fading correction. Quaternary Geochronology, 6(5), 468-479.

Poolton, N. R. J., Ozanyan, K. B., Wallinga, J., Murray, A. S., & Bøtter-Jensen, L. (2002). Electrons in feldspar II: a consideration of the influence of conduction band-tail states on luminescence processes. Physics and Chemistry of Minerals, 29(3), 217-225.

Poolton, N. R. J., Kars, R. H., Wallinga, J., & Bos, A. J. J. (2009). Direct evidence for the participation of band-tails and excited-state tunnelling in the luminescence of irradiated feldspars. Journal of Physics: Condensed Matter, 21(48), 485505.

Prasad, A. K., Lapp, T., Kook, M., & Jain, M. (2016). Probing luminescence centers in Na rich feldspar. Radiation Measurements, 90, 292-297.

Prasad, A. K., Poolton, N. R., Kook, M., & Jain, M. (2017). Optical

dating in a new light: A direct, non-destructive probe of trapped electrons. Scientific reports, 7(1), 1-15.

Schulman, J. H., Ginther, R. J., Klick, C. C., Alger, R. S., & Levy, R. A. (1951). Dosimetry of x-rays and gamma-rays by radiophotoluminescence. Journal of Applied Physics, 22(12), 1479-1487.

Thomsen, K. J., Murray, A. S., Jain, M., & Bøtter-Jensen, L. (2008). Laboratory fading rates of various luminescence signals from feldspar-rich sediment extracts. Radiation measurements, 43(9-10), 1474-1486..

Trautmann, T., Krbetschek, M. R., Dietrich, A., & Stolz, W. (1998). Investigations of feldspar radioluminescence: potential for a new dating technique. Radiation Measurements, 29(3), 421-425.

Trautmann, T., Dietrich, A., Stolz, W., & Krbetschek, M. R. (1999a). Radioluminescence dating: a new tool for Quaternary geology and archaeology. Naturwissenschaften, 86(9), 441-444.

Trautmann, T., Krbetschek, M. R., Dietrich, A., & Stolz, W. (1999b). Feldspar radioluminescence: a new dating method and its physical background. Journal of Luminescence, 85(1-3), 45-58.

Trautmann, T., Krbetschek, M. R., Dietrich, A., & Stolz, W. (2000). The basic principle of radioluminescence dating and a localized transition model. Radiation Measurements, 32(5-6), 487-492.

Tsukamoto, S., Denby, P. M., Murray, A. S., & Bøtter-Jensen, L. (2006). Time-resolved luminescence from feldspars: new insight into fading. Radiation Measurements, 41(7-8), 790-795.

Tsukamoto, S., Kondo, R., Lauer, T., & Jain, M. (2017). Pulsed IRSL: A stable and fast bleaching luminescence signal from feldspar for dating Quaternary sediments. Quaternary Geochronology, 41, 26-36.

Varma, V., Biswas, R., & Singhvi, A. (2013). Aspects of Infrared Radioluminescence dosimetry in K-feldspar. Geochronometria, 40(4), 266-273.

Wintle, A. G. (1973). Anomalous Fading of Thermo-Luminescence in Mineral Samples. Nature 245 (5421):143–44.

CHAPTER 4

INSTRUMENTATION FOR THE NON-DESTRUCTIVE OPTICAL MEASUREMENT OF TRAPPED ELECTRONS IN FELDSPAR

Myungho Kook, Raju Kumar & Mayank Jain

Abstract: A facility for the measurement of infrared photoluminescence (IRPL) has been developed for the Risø TL/OSL reader. The new IRPL measurement system uses an external laser light source at 1.49 eV (830 nm) and two photomultiplier tubes (PMT) for detecting emissions at 1.41 eV (880 nm) and 1.30 eV (955 nm) and an electron multiplying charge coupled device (EMCCD). Pulsed IRPL measurement ensures a low background count rate by allowing the rejection of breakthrough from excitation light. We present the results of integrated IRPL measurements on both multiple- and single-grain aliquots, and finally demonstrate the potential of imaging natural K-feldspar samples and a granite rock slice.

4.1 Introduction

Optically stimulated luminescence (OSL) emission arises from recombination of trapped electrons and holes in a crystal due to stimulation by

light of appropriate energy; this signal is dose dependent and typically measured in the anti-Stokes mode to avoid contamination from prompt fluorescence and phosphorescence emissions (Bøtter-Jensen et al., 2003). OSL decays during stimulation because luminescence emission is the result of progressive release of charge from traps followed by electron-hole recombination. In contrast, infrared photoluminescence (IRPL), detected for the first time in feldspar at 955 nm during IR excitation at 885 nm by Prasad et al. (2017), is a Stokes-shifted emission resulting from internal excitation-relaxation within the dosimetric trap (i.e. principal trap). Kumar et al. (2018; Chapter 3 in this thesis) have since discovered a second IRPL emission at 880 nm using a shorter wavelength excitation at 830 nm in a potassium-rich feldspar. IRPL does not involve release of charge from traps, nor does it require hole-centers to produce luminescence; the signal can thus be accumulated over long periods by repeated excitation of the same trapped electron, without significant signal loss. This is especially true for electron traps with a large distance to the nearest recombination site (i.e. non-fading traps) or when measurements done at cryogenic temperatures (Prasad et al., 2017).

The first identification of IRPL and the subsequent basic investigations into its origin were made on the Risø station for CryOgenic LUminescence Research (COLUR); this system is not convenient for routine dosimetric measurements because it is manually operated, does not include a beta source, and must be evacuated before cooling. Prasad et al. (2017) also explored the use of the spectrometer attachment to the Risø TL/OSL reader to measure IRPL for dosimetric investigations; this system is based on a spectrograph and an EMCCD camera but is relatively insensitive due to the fiber-optic coupling. Initial measurements suggested that IRPL spectra are similar across samples; hence it may be possible to modify the system to use a broad bandpass detection. This would both increase the sensitivity and cut costs.

In this article, we describe new measurement systems based on IRPL detection through a wavelength bandpass, both using photomultiplier tubes (PMTs) and imaging cameras on the new automated detection and stimulation head (DASH) for the Risø TL/OSL reader (Lapp et al., 2015). DASH provides a port for an external light source and an automated filter and detector changer; this configuration gives the flexibility to allow the measurement of both IRPL and infrared stimulated luminescence (IRSL) from the same sample. For multiple-grain IRPL

measurements, we use integrated measurement using PMTs. For IRPL measurements from individual grains we either use spatially resolved measurements using an EMCCD (Kook et al., 2015), or the single grain X-Y laser scanning system (Duller et al., 1999, 2003), modified to reduce the IR laser power. Because the detection bandpass is close in wavelength to the light source, we must specifically address the challenge of avoiding excitation-light breakthrough into the detector. Finally we demonstrate the potential of these new measurement systems using results from a typical natural feldspar (multiple grains and single grains) samples and rock slices.

4.2 Instrumentation

For the development of the IRPL measurement system, we use an existing platform consisting of a standard Risø TL-DA-20 reader and DASH (Lapp et al., 2015). The DASH includes 3 software-selectable detector positions in a detector changer module and two layers of selectable filters (up to 4 in each layer). We used two PMTs and one EMCCD camera as detectors, together with appropriate filters to allow measurement of both IRSL and IRPL in integrated or spatially-resolved mode. The different configurations are discussed below.

4.3 Detection configurations for IRPL at 880 nm or 955 nm

Kumar et al. (2018; see Chapter 3, Figure 3.1) show that laser excitation at 1.49 eV (830 nm) gives rise to two IRPL emission peaks at 1.41 eV (880 nm) and 1.30 eV (955 nm); the first emission is the same as that reported by Prasad et al. (2017) using the 1.40 eV (885 nm) laser excitation. These authors further demonstrate that IR radioluminescence (IRRL; Trautmann et al., 1999) and IRPL have the same emissions. The two IRPL emission peaks are resolved at low temperature (7 K), but at room temperature they merged together as a single peak. The standard PMTs (ET9245QB or PDM9107-CP-TTL) used for OSL or IRSL measurement (Bøtter-Jensen et al., 2010; Lapp et al., 2015) are not sufficiently sensitive to measure these near-infrared (NIR) emissions. Charged couple devices (CCD) are sensitive in this wavelength range but it is usually difficult to operate a CCD or an EMCCD in pulsed mode; this is more likely to be

needed when, as here, the excitation and emission wavelengths are close to each other. A PMT detector is preferred for spatially integrated luminescence measurements as it offers the possibility of reducing background by fast gating in the presence of pulsed stimulation.

Since the IRRL and IRPL emissions are similar, we use the PMT (Hamamatsu H7421-50) used in the IRRL system (Buylaert et al., 2012; Lapp et al., 2012) for detecting the 1.41 eV (880 nm) IRPL emission. This PMT has a GaAs photocathode with maximum quantum efficiency (QE) around 830 nm gradually dropping to almost zero by 890 nm (Figure 4.1a). The head is thermoelectrically cooled to 0 °C to reduce the dark count rate. When the PMT is combined with two 875 nm long pass (LP) filters (Edmund optics, high performance interference filter, optical density 4), the peak of the IRPL detection window lies at 873 nm (FWHM 15 nm; Figure 4.1a). Furthermore, the QE of the PMT extends down to 380 nm (∼1.2% at 400 nm); it is thus possible to measure IRSL using the same detector by using the automated filter changer in DASH to provide a blue band-pass filter combination (BG3 and BG39).

The 1.30 eV (955 nm) emission from feldspar has to our knowledge never been measured using a PMT detector before. Here we use a Hamamatsu H10330C-25 with a spectral response from 950 nm to 1200 nm with a QE of ∼5% (Figure 4.1b). This PMT is contained in a thermally-insulated high vacuum housing and the internal thermoelectric cooler can reduce the temperature to -60°C. Because of this cooling, it is possible to detect in the NIR region with <100 counts/s background count rate (for an applied voltage of 800 V). A combination of two 925 nm long pass (LP) filters (Edmund optics, high performance interference filter, optical density 4) and one 950 nm band pass (BP) filter (Edmund optics, high performance interference filter, optical density 4) are used in combination with this PMT to reject the excitation light and define a IRPL detection window at 950 nm (FWHM 50 nm) (Figure 4.1b).

For IRPL imaging one may use a CCD detector because of their high QE to >1000 nm. Kook et al. (2015) developed a TL/OSL imaging system using a UV-enhanced EMCCD; the QE of their detector is ∼40% at 880 nm and ∼20% at 950 nm (Figure 4.1c). However, a broad spectral response with a high QE extending to UV poses disadvantage when measuring IRPL; unlike the PMT detector, the EMCCD is very sensitive to the excitation wavelength at 830 nm. Also, unlike the PMT, it is not possible to use pulsed laser excitation and detection only during the

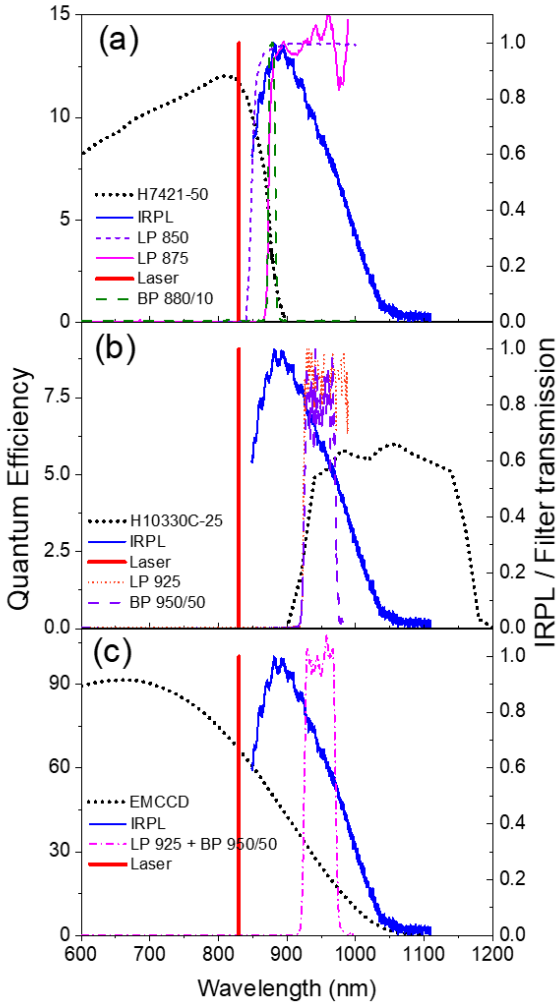

Figure 4.1: (a) Quantum efficiency of H7421-50 PMT (black dot), 830 nm excitation laser (red line). (b) Quantum efficiency of H10330C-25 PMT (black dot). (c) Quantum efficiency of EMCCD (black dot). All three figures also present transmission characteristics of the relevant long pass and band pass interference filters (see legend) and the IRPL emission spectrum (blue curve) at room temperature. Filter transmittance was recorded with Shimadzu spectrophotometer (UV-2600/2700). Note: In the following chapters, two 880 nm (FWHM 10 nm) BP filters has been used for detecting the 1.41 eV (880 nm) IRPL emission instead of 875 nm LP filters. The use of 880 nm BP filters results in better signal-to-noise ratio.

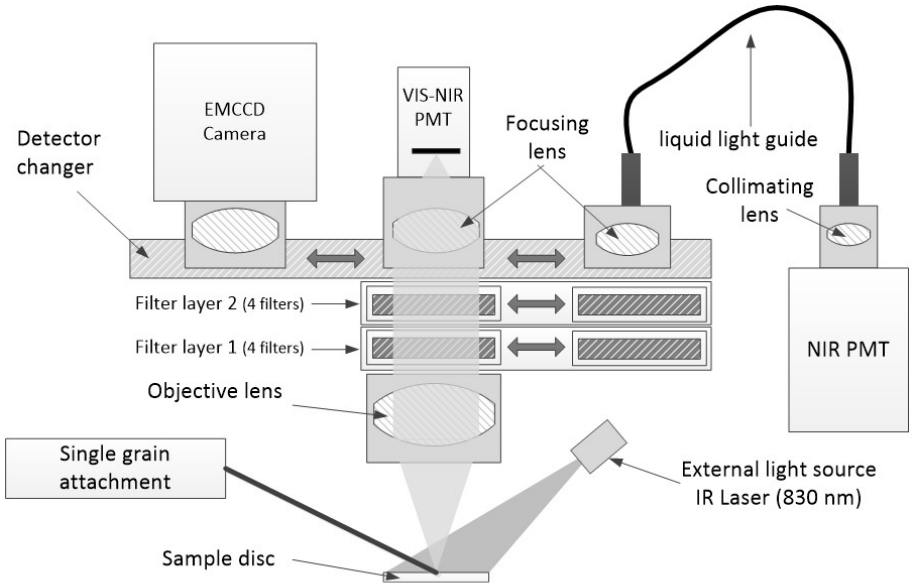

Figure 4.2: Schematic diagram showing the components of the IRPL measurement system mounted on the Risø TL/OSL reader.

off-time because of the slow read-out speed of EMCCD. Thus, efficient blocking of the excitation laser becomes critical for an EMCCD-based imaging system. Here we use the EMCCD system of Kook et al. (2015) in combination with two 925 nm long pass (LP) filters and one 950 band pass (BP) filter; this configuration gives IRPL detection from 925 nm to 975 nm (1.30 eV band). It was not possible to measure the 1.41 eV IRPL band with the EMCCD because of high breakthrough from the laser.

4.4 The IRPL attachment

A diagram of the integration of the components into the reader head is shown in Figure 4.2. The automated DASH has a port for an external light source (in addition to the built-in light emitting diodes), and provides a control signal for external continuous or pulsed excitation (minimum 5 µs with 0.1 µs resolution). In this study we attached an IR diode laser (Power Technology incorporated, 150 mW, 830 nm) to the external port. The laser beam passes through a ground-glass diffuser to provide

uniform illumination at the sample position; this reduces the power density to $\sim$3 mWcm^{-2}. Since IRPL measurement is a non-destructive, even the low excitation powers can give robust counting statistics; as a result, the optical power after diffusing the laser is sufficient for high sensitivity IRPL measurements. The objective lens (biconvex fused silica lens with anti-reflection coating) collimates the IRPL light to detectors throughthe detection filters (LP 875 nm, LP 925 nm and BP 950/50 nm).

The Hamamatsu H7421-50 PMT module is mounted directly on top of the DASH; a lens focuses the collimated IRPL beam from the sample to an effective measurement area of 5 mm diameter in the PMT module. In contrast, the module of Hamamatsu H10330C-25 (NIR-PMT) is more bulky as it consists of a NIR-PMT main unit and its controller; the PMT cannot be placed directly on the DASH because of space restrictions. Therefore the module is placed beside the reader and a 3 mm diameter liquid light guide (Lumatec Liquid Light Guide series 2000; transmission range of 350-2000 nm) couples the DASH to the NIR-PMT. The IRPL at the end of the liquid light guide is divergent (uncollimated) and a lens is placed between the light guide and the detector to direct the IRPL photons onto the PMT photocathode (18 mm effective diameter).

Using the Sequence Editor control software, the detector changer locates either the PMT (H7421-50), or the liquid light guide (for H10330C-25), or the EMCCD at the measurement position. The automated filter changer then moves the appropriate filters under the chosen detector.

4.5 Rejecting the excitation light in IRPL detection

Despite using the detection filters, there is a large breakthrough from the excitation light into the PMT detectors. In order to avoid this problem we used pulsed OSL (POSL), where the excitation light is turned on and off at a fixed time interval, and the luminescence is only measured when the excitation light is off (e.g. McKeever et al., 1996; Sanderson and Clark, 1994). This technique has earlier been used to measure a quartz signal in the presence of feldspar contamination, by exploiting the different lifetimes of quartz and feldspar OSL (Thomsen et al., 2008; Ankjærgaard et al., 2010). POSL can be used to reject the breakthrough in IRPL measurement, because the switch-off time of the laser excitation pulse (<0.1 µs) is much shorter than the IRPL lifetime of 28 µs (Prasad

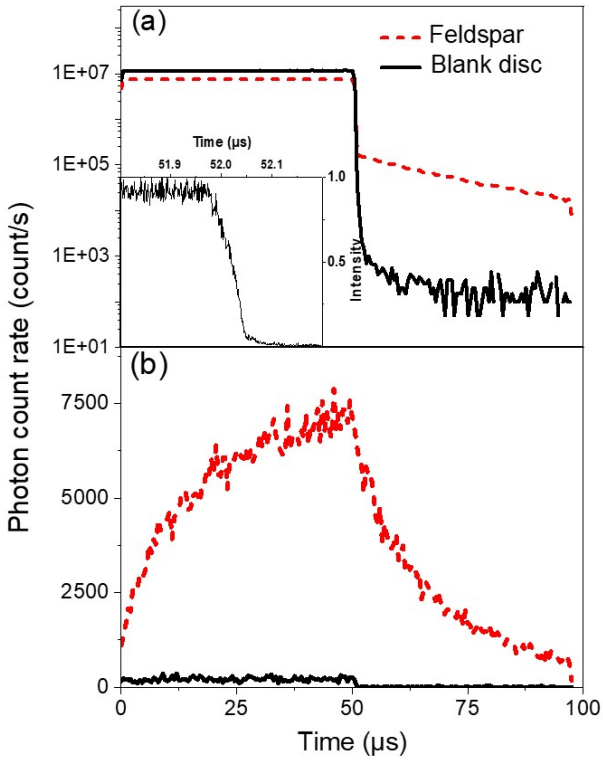

Figure 4.3: (a) Time-resolved IRPL signals using the H7421-50 PMT from feldspar (red dash) and a blank disc (solid black line). These curves were produced by summing signals from all the pulses produced in 4 s, using an on-time of 50 µs and an off-time 50 µs at room temperature. Note that the log y-axis. (b) Time-resolved IRPL signal with the H10330C-25 PMT from feldspar (red dash) and blank disc (black line) using the same configuration as in (a).

et al., 2017).

To optimize the PMT counting window within the off period, a time-resolved IRPL measurement was carried out using the Risø Time-Correlated Single Photon Counting (TCSPC) attachment (Lapp et al.,2009). The laser was operated using 50 µs on (pulse width) and 50 µs off time, for total of 4 s. Figure 4.3a shows the measurement using a blank disc and a K-feldspar (R47) disc with the H7421-50 detector (for 880 nm peak detection). A large breakthrough was observed during the on time ($\sim$1.1 $\times$ 10^4 s^{-1}) using a 3 $mWcm^{-2}$ optical power density on the sample position (contrast this with 140 $mWcm^{-2}$ for a classic DASH and 300 $mWcm^{-2}$ for an automated DASH for standard IRSL measurements). At least an order of magnitude higher excitation power may be used, if necessary, without risking the saturation of the PMT. The switch off time of the laser was measured to be < 0.1 µs (Figure 4.3a inset), but there appears to be an afterglow lasting $\sim$2 µs. Based on these data, we set the PMT counting period to begin 3 µs after the laser switch off.

Figure 4.3b shows TCSPC data with the NIR PMT used for measuring the 955 nm IRPL peak. In contrast to the result for the H7421-50 PMT, here the measurement of the empty disc shows that the NIR PMT is almost insensitive to the excitation laser; this is because of the very low QE at 830 nm and the sufficiently large wavelength difference between detection and excitation wavelength. The measurement of the disk containing feldspar grains shows a clear build up and decay of the 1.30 eV IRPL emission, giving a single exponential lifetime of $\sim$40 µs. Thus, the 1.30 eV IRPL may be measured either using continuous wave- or pulsed stimulation, whereas the 1.41 eV IRPL requires pulsed stimulation.

4.6 IRPL measurements on feldspar extracts and rock slices

4.6.1 Multiple grain IRPL measurement

To illustrate the application of the IRPL measurement system, we used a SAR protocol (Murray and Wintle, 2000) on a feldspar sample (R47; detailed investigations on the sample are presented in Prasad et al., 2017). A disc of R47 was initially bleached for 48 h under Hönle solar simulator (SOL2) before measurements began. A preheat of 250 °C for 60 s was used after both the regeneration and test doses, followed by a pulsed

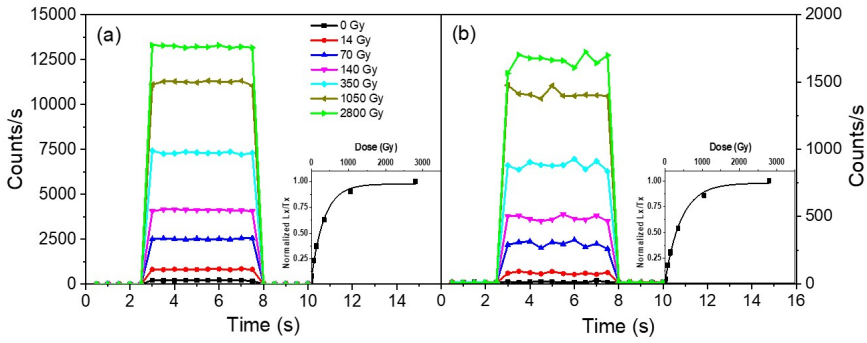

Figure 4.4: (a) IRPL (1.41 eV; 880 nm emission) signals in response to increasing regeneration dose. The inset shows the corresponding SAR dose response curve. (b) IRPL (1.30 eV; 955 nm emission) signals in response to increasing regeneration dose. The inset shows the corresponding dose SAR response curve.

IRPL measurement at room temperature for 5 s (on-time: 50 µs; off-time: 50 µs; detection in the off-time after 3 µs delay). A 395 nm UV LED (1 W optical power) mounted on the reader was used for bleaching the IRPL signal before giving a test dose or a regeneration dose. A dose response curve was measured using 6 regeneration doses including a recuperation point (0 Gy) and a repeat dose (recycling point). Figures 4.4a and b shows the IRPL signals after different regenerations doses (L_x) for the 880 nm and 955 nm emissions, respectively. The respective dose response curves are shown inset. The L_x signals increases systematically with beta dose and the sensitivity-corrected dose response curve can be satisfactorily fitted using a single exponential function, with D_0=346 ± 24 Gy (880 nm) and 436 ± 30 Gy (955 nm).

4.6.2 Single grain IRPL measurement

For the single grain IRPL measurements the existing single grain system in the Risø reader (Duller et al., 2003) was adapted for use with the new detectors (H7421-50 or H10330C-25). This system already contains an IR laser (830 nm, 150 mW) for excitation, but this laser is normally operated at power density of ∼500 Wcm^{-2} at the grain to maximize the signal to noise ratio. The same power density is not necessary for IRPL; this nearly time invariant signal is orders of magnitude more intense than IRSL and

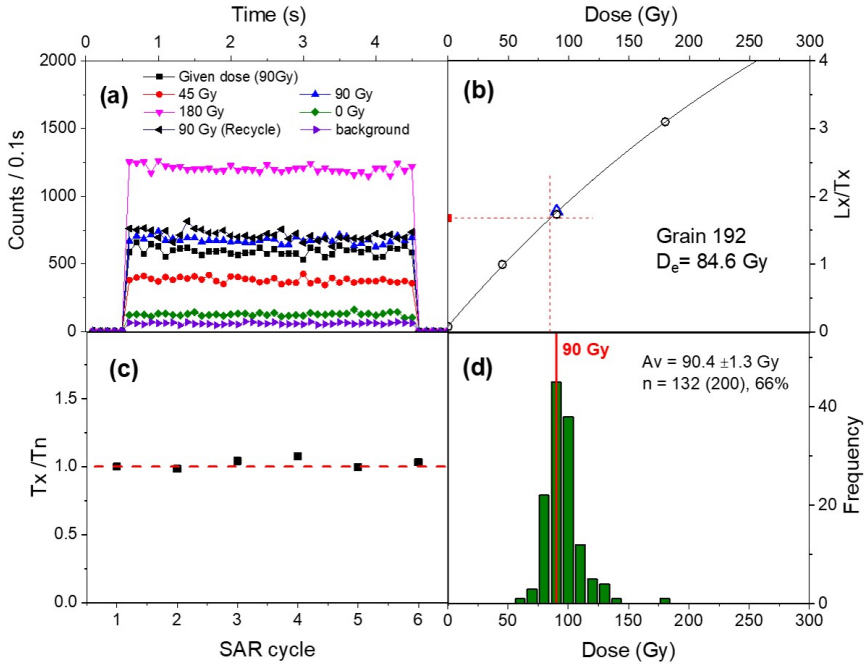

Figure 4.5: Dose recovery for IRPL (1.30 eV; 955 nm) using the single grain attachment. a) IRPL curves from the 90 Gy given dose, a 45, 90, 180, 0 and 90 Gy regeneration dose, and the background IRPL at the end of the first SAR cycle. b) Dose response curve for the same grain as shown in (a). (c) Normalized sensitivity of the test dose signal during the different SAR cycles from the same grain as in (a). (d) A histogram of the recovered doses based on 132 accepted grains.

can also be measured over a prolonged period to increase the signal-to-noise ratio. In addition, a very intense IR laser stimulation power may also heat the grain during measurement. To minimize these effects, we reduced the laser power by a factor of ∼100 using a neutral density filter (OD:2). To reduce the breakthrough of excitation light, we also modified the existing stimulation control in the single grain system to allow pulsed IR stimulation. For single grain measurement, the laser was pulsed with a 5 µs on-time and 95 µs off-time, and signal was accumulated by the PMT for 92 µs during the off time, after a delay of 3 µs.

Figure 4.5 shows the results of the IRPL-SAR dose recovery measurements using two single grain discs of a calibration feldspar sample (Hansen et al., 2018) given an in-situ beta dose of 90 Gy in the Risø reader. A preheat 280 °C for 60 s was used prior to the measurement of the IRPL signals (for both regeneration and test dose). Optical bleaching at 260 °C using the blue LEDs was used to reset the IRPL before the next measurement both within and at the end of a SAR cycle. Figure 4.5a shows the IRPL signals from a typical grain (with above average brightness) after a given dose of 90 Gy, a regeneration dose of 45, 90, 180, 0 and 90 Gy, and the background IRPL (after bleaching) at the end of the first SAR cycle. The IRPL curves were flat (non decaying) for most grains; a few grains showed up to 10% decay in the 3 s stimulation period. Figure 4.5b, shows the SAR dose response curve from the same grain, and Figure 4.5c the normalised test-dose as a function of SAR cycle. This particular grain shows negligible sensitivity change (a common but not universal observation). Figure 4.5d shows a histogram of the recovered doses; the measured to given dose recovery ratio based on 132 accepted grains was 1.004 ± 0.014.

4.6.3 IRPL imaging system

Figure 4.6 shows the results obtained using the IRPL imaging system. Figures 4.6a and b shows the optical and IRPL image, respectively, following 105 Gy dose to a feldspar single grain disc (sample R47). The IRPL signal was integrated for 5 s; the IRPL signal was constant with time, whereas the IRSL decayed during the 5 s stimulation. Because of this, the IRPL sensitivity can be increased arbitrarily by increasing the integration time. In this particular data set (Figure 4.6a), grain 43 gave an IRPL count rate of 1.3×10^5 s^{-1} and grain 45 gave 5.4×10^5 s^{-1}. These high count rates also allow the use of a smaller optical aperture to

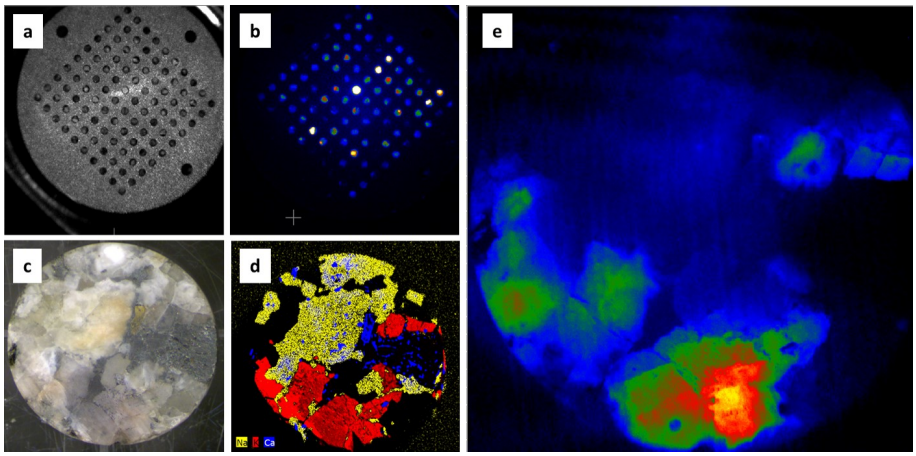

Figure 4.6: (a) The optical image of a feldspar (R47) single-grain disc under low power IR illumination (b) IRPL image of the same disc following a beta dose of 105 Gy; the integration time for IRPL was 5 s (c) optical image of a granite rock slice. (d) Compositional image of the same rock slice showing K-F, Na-F and Ca-F rich areas; the image was measured using μXRF. (e) IRPL image of the same rock slice following a beta dose of 100 Gy. The integration time for IRPL was 10 s.

improve image resolution and so reduce cross talk.

Figure 4.6c shows the optical image of a granite rock slice (from an archaeological stone pier near Fyn, Denmark). A corresponding data set for the mineralogical composition (K-F, Ca-F and Na-F) was obtained using x-ray fluorescence µXRF; Bruker, Tornado M4) (Figure 4.6d); the red areas in this figure are rich in potassium, presumably in potassium feldspar. Figure 4.6e shows the IRPL image of the same slice; it appears that the IRPL is strongly correlated with the potassium-rich areas.

4.7 Conclusions

We have demonstrated a new measurement system for detecting infrared photoluminescence (IRPL) emissions at 1.41 eV (880 nm) and 1.30 eV (955 nm). The system uses an external light source at 1.49 eV (830 nm) and three detectors based on PMTs or and EMCCD (coupled to appropriate filters), all mounted on the automated DASH unit in the Risø TL/OSL reader. Pulsed stimulation using the PMT detectors proves to

be useful to reject excitation light breakthrough, especially in case of the 1.41 eV emission. We demonstrate the potential of the PMT based system for dosimetric investigations using pulsed IRPL on both multiple-grain and single-grain measurement systems. Using the latter, we gave a calibration feldspar a known dose of 90 Gy, and measured 90.4 ± 1.3 Gy.

We have also demonstrated the potential of IRPL (1.30 eV) for imaging using a single grain disc and a rock slice; these measurements used CW-IR stimulation and EMCCD detector. A strong correlation between the IRPL and K-feldspar concentration is inferred based on the µXRF measurements on the same granite slice.

In order to further develop IRPL imaging future effort will concentrate on either rejecting the excitation light more efficiently by the use of filters or using pulsed stimulation, or alternatively reducing the image area using, for example, microscopic techniques. Furthermore, since very low excitation light power is required, high resolution imaging of large samples is straightforward. This is particularly relevant for rock surface dating (Sohbati et al., 2015; Freiesleben et al., 2015).

References

Ankjærgaard, C., Jain, M., Thomsen, K. J., & Murray, A. S. (2010). Optimising the separation of quartz and feldspar optically stimulated luminescence using pulsed excitation. Radiation measurements, 45(7), 778-785.

Bøtter-Jensen, L., McKeever, S.W.S., & Wintle, A.G. (2003). Optically Stimulated Luminescence Dosimetry. Elsevier.

Bøtter-Jensen, L., Thomsen, K. J., & Jain, M. (2010). Review of optically stimulated luminescence (OSL) instrumental developments for retrospective dosimetry. Radiation Measurements, 45(3-6), 253-257.

Buylaert, J. P., Jain, M., Murray, A. S., Thomsen, K. J., & Lapp, T. (2012). IR-RF dating of sand-sized K-feldspar extracts: a test of accuracy. Radiation Measurements, 47(9), 759-765.

Duller, G. A., Bøtter-Jensen, L., Murray, A. S., & Truscott, A. J. (1999). Single grain laser luminescence (SGLL) measurements using a novel au-

tomated reader. Nuclear instruments and methods in physics research Section B: beam interactions with materials and atoms, 155(4), 506-514.

Duller, G. A. T., Bøtter-Jensen, L., & Murray, A. S. (2003). Combining infrared-and green-laser stimulation sources in single-grain luminescence measurements of feldspar and quartz. Radiation Measurements, 37(4-5), 543-550.

Freiesleben, T., Sohbati, R., Murray, A., Jain, M., Al Khasawneh, S., Hvidt, S., & Jakobsen, B. (2015). Mathematical model quantifies multiple daylight exposure and burial events for rock surfaces using luminescence dating. Radiation Measurements, 81, 16-22.

Kook, M., Lapp, T., Murray, A. S., Thomsen, K. J., & Jain, M. (2015). A luminescence imaging system for the routine measurement of single-grain OSL dose distributions. Radiation Measurements, 81, 171-177.

Kumar, R., Kook, M., Murray, A. S., & Jain, M. (2018). Towards direct measurement of electrons in metastable states in K-feldspar: Do infrared-photoluminescence and radioluminescence probe the same trap?. Radiation Measurements, 120, 7-13.

Lapp, T., Jain, M., Ankjærgaard, C., & Pirtzel, L. (2009). Development of pulsed stimulation and Photon Timer attachments to the Risø TL/OSL reader. Radiation Measurements, 44(5-6), 571-575.

Lapp, T., Jain, M., Thomsen, K. J., Murray, A. S., & Buylaert, J. P. (2012). New luminescence measurement facilities in retrospective dosimetry. Radiation Measurements, 47(9), 803-808.

Lapp, T., Kook, M., Murray, A. S., Thomsen, K. J., Buylaert, J. P., & Jain, M. (2015). A new luminescence detection and stimulation head for the Risø TL/OSL reader. Radiation Measurements, 81, 178-184.

McKeever, S. W. S., Akselrod, M. S., & Markey, B. G. (1996). Pulsed optically stimulated luminescence dosimetry using alpha-Al2O3: C. Radiation Protection Dosimetry, 65(1-4), 267-272.

Murray, A. S., & Wintle, A. G. (2000). Luminescence dating of quartz using an improved single-aliquot regenerative-dose protocol. Radiation measurements, 32(1), 57-73.

Prasad, A. K., Poolton, N. R., Kook, M., & Jain, M. (2017). Optical dating in a new light: A direct, non-destructive probe of trapped electrons. Scientific reports, 7(1), 1-15.

Sanderson, D. C. W., & Clark, R. J. (1994). Pulsed photostimulated luminescence of alkali feldspars. Radiation Measurements, 23(2-3), 633-639.

Sohbati, R., Murray, A. S., Porat, N., Jain, M., & Avner, U. (2015). Age of a prehistoric "Rodedian" cult site constrained by sediment and rock surface luminescence dating techniques. Quaternary Geochronology, 30, 90-99.

Thomsen, K. J., Jain, M., Murray, A. S., Denby, P. M., Roy, N., & Bøtter-Jensen, L. (2008). Minimizing feldspar OSL contamination in quartz UV-OSL using pulsed blue stimulation. Radiation Measurements, 43(2-6), 752-757.

Trautmann, T., Krbetschek, M. R., Dietrich, A., & Stolz, W. (1999). Feldspar radioluminescence: a new dating method and its physical background. Journal of Luminescence, 85(1-3), 45-58.

CHAPTER 5

CHARACTERIZATION OF ELECTRON-TRAPPING CENTERS IN FELDSPAR BY LOW-TEMPERATURE PHOTOLUMINESCENCE EXCITATION-EMISSION SPECTROSCOPY

Raju Kumar, Myungho Kook & Mayank Jain

Abstract: Feldspar, a ubiquitous naturally occurring aluminosilicate, is widely used in optically stimulated luminescence (OSL) geochronometry. Despite many decades of research, it has been challenging to establish the physical characteristics of the main electron-trapping center (the principal trap) in feldspar because of the inherent complexity of the OSL process. Recently, a site-selective technique based on the Infrared photoluminescence (IRPL) has been developed to directly probe the principal dosimetric trap. Unlike OSL, which results from electron-hole recombination, IRPL results from radiative relaxation of the excited state of the principal trap.

Here, using novel site-selective techniques, we show that there exist two distinct electron-trapping centers in feldspar (i.e. two principal traps). We determine the trap depth, excited-state energies, and the

excited-state relaxation lifetime of these defect centers, and further examine their dose response, and the thermal- and optical-bleaching behavior. The two centers share the same dose response (electron capture cross-section) and relaxation lifetimes but have different ground and excited state energies leading to different bleaching characteristics. Based on these data we suggest that the principal trap consists of the same defect residing at two different sites.

5.1 Introduction

Feldspars make up more than half of the Earth's crust and are widely used to date (up to 0.5 million years) geological and archaeological events for understanding climate change, human evolution, etc. Feldspars are aluminosilicate minerals with a wide bandgap of ∼7.7 eV (Malins et al., 2004), which crystallize in monoclinic or triclinic structures. Feldspars are usually designated in terms of their end-member composition as $KAlSi_3O_8$, $NaAlSi_3O_8$, and $CaAl_2Si_2O_8$. Deep-lying defects in their bandgap can capture free electrons or holes created due to interaction with ionizing radiation and thus form metastable states. These states decay by thermal or optical excitation often producing luminescence (Huntely, 1985; Wintle, 2008). In nature, these states can exist for thousands to millions of years at ambient temperatures allowing widespread use of feldspar in luminescence geochronology.

Despite many decades of research, the luminescence mechanisms in feldspar are still not fully understood. Similarly, the defects forming the metastable states are not fully characterized or identified. This lack of knowledge is due to the inherent complexities and uncertainties involved in dealing with luminescence production in natural minerals. Routine sediment dating relies mainly on accurate calibration of the luminescence-dose response, without necessarily a detailed knowledge of the underlying physics. However, many model-based applications, e.g., thermochronometry (Guralnik et al., 2015; King et al., 2016), rock surface dating (Sohbati et al., 2012), anomalous fading correction (Visocekas, 1985; Visocekas, 2002; Huntley and Lamothe, 2001), etc., make it imperative that we obtain a better understanding of charge trapping, detrapping, and transport in a feldspar crystal. Equally, the variation in the signal sensitivity in different types of feldspar (K-, Na-, and Ca-feldspar) entail the detailed investigation of the luminescent defects and their linkages

with geochemistry.

The defect responsible for electron capture in feldspar, also called as the principal trap, is not known (Short, 2003). The dosimetric signal from this defect is measured using optically stimulated luminescence (OSL; blue or green light stimulation) or IR stimulated luminescence (IRSL). Despite a wide range in composition and geological origins of feldspar, there are several similarities in their luminescence characteristics, e.g. in the OSL excitation and emission spectra (Baril and Huntley, 2003a, b). The OSL process involves several steps: 1) trapped electrons are excited to the conduction band (CB), and 2) electrons in the CB migrate to combine with the trapped holes in the crystal to produce luminescence (Bøtter-Jensen et al., 2003). The IRSL (Hütt et al., 1988) emission process is slightly different as low energy photons (IR light) are used to excite electrons in the trap. In this process, electrons in the excited state diffuse out into the band-tail states (localized states below the CB edge) and finally recombine with the trapped holes (Poolton et al., 2009). OSL or IRSL is not ideal for characterizing the principal trap (e.g. optical trap depth, excited energy levels, number of defects and their concentration) since they involve both electron and hole sites as well as the transport dynamics (Jain and Ankjærgaard, 2011), making any interpretation ambiguous.

A particularly challenging aspect for understanding the luminescence processes in feldspar has been the determination of the trap depth of the principal trap. A variety of values (1.9-2.5 eV) have been reported depending on the method of investigation (Huntley et al., 1985; Hutt et al., 1988; Poolton et al., 1995, 2002, 2009; Li & Li, 2013; Kars et al., 2013). The presence of the band-tail states below the conduction band edge provides alternative routes of charge transport to the conduction band route; this makes the conventional OSL methods ambiguous, as they cannot discriminate between the routes responsible for detrapping and eventual electron-hole recombination. The efficiency of charge transport (i.e. diffusion vs. retrapping) in the band-tail states is energy-dependent (Jain and Ankjærgaard, 2011); this adds further complexity to the detrapping process. Finally, OSL or IRSL technique is not site-specific; it is possible that traps other than the principal trap may also get photo-ionized during optical stimulation and contribute to the OSL signal, adding extra uncertainty. Ideally, the characterization of the principal trap requires a site-specific probing method that does not involve

holes for the emission process.

Recent developments in feldspar luminescence physics have led to such a site-selective method. Prasad et al. (2017) demonstrated that electrons in the principal trap could also be measured using the photoluminescence (PL) technique. Unlike OSL, which involves electron-hole recombination, PL is produced from the intra-defect electronic transitions (excitation-relaxation) within the principal trap. Prasad et al. (2017) used a 1.40 eV (885 nm) laser to excite the principal trap and observed a Stokes-shifted emission at 1.30 eV (955 nm), which they termed as infrared photoluminescence (IRPL). Since IRPL does not involve recombination centers and is emitted due to internal transitions within the trap, it offers a non-destructive and site-selective technique at low temperature. Recently, Kumar et al. (2018; Chapter 3 in this thesis) found that there exist two IRPL emission bands centered at 1.41 eV (880 nm) and 1.30 eV (955 nm) using a higher energy excitation source (830 nm laser). These authors showed that the two IRPL emission peaks are clearly resolved when measured at low temperature (7 K) but merge into a broad single peak at room temperature (∼300 K).

The purpose of this study is to advance our understanding of luminescence mechanisms and the associated defect system using infrared photoluminescence (IRPL) as a site-selective tool. This study focuses on a) determining whether there are single or multiple defect types giving rise to IRPL and IRSL, b) measuring the optical trap depth, and c) mapping the excited state energies of the principal trap.

5.2 Previous studies investigating the principal trap

In this section, we aim to bring together some of the previous studies to obtain an overview of the principal trap in feldspar. We focus on the excited states, the number of participating defects and the optical trap depth.

5.2.1 Excited states of the principal trap

In the earlier work, the excited states of the principal trap have been identified using OSL excitation spectroscopy. In general, the OSL excitation spectrum of a deep-lying defect, e.g. quartz, shows an exponential

rise in OSL intensity with excitation energy (Ditlefsen et al., 1994). Such a form is expected when there are no excited states of the defect below the conduction band edge. In contrast to quartz, feldspar OSL excitation spectrum shows a peak around 1.44 eV superimposed upon an exponential rise at higher excitation energies; this was first reported by Hütt et al. (1988). These authors also observed other peaks at 1.29, 1.33, and 2.25 eV, which they inferred to arise from the resonant excitation from the ground state to the different excited states of the trap. The dominant broad peak around 1.44 eV is universally found in most feldspar samples (Baril and Huntley, 2003; Poolton et al., 2009; Andersen et al., 2012; Riedesel et al., 2018). The other peaks identified by Hütt et al. (1988) have over the course of time been suggested to be experimental artifacts (Bailiff and Barnett, 1994; Barnett and Bailiff, 1997). More recently, Poolton et al. (2009) reported a peak at 1.24 eV in the OSL excitation spectrum of a K-feldspar sample.

The 1.44 eV peak is considered to consist of two or three overlapping peaks (Baril and Huntley, 2003; Poolton et al., 2009). Based on an extensive study on feldspar of different compositions, Baril and Huntley (2003a) have reported two resonance peaks at 1.57 and 2.0 eV in addition to the main resonance around 1.44 eV. Andersen et al. (2012) identified three overlapping resonances around 1.36, 1.45, and 1.55 eV in the IRSL excitation spectra measured in the range 1.20-1.70 eV. Recently, Prasad et al. (2017) reported two overlapping resonances around 1.45 and 1.56 eV in the OSL excitation spectrum at room temperature. Prasad et al. (2017) also deduced overlapping peaks around 1.39, 1.45, and 1.53 eV in the IRPL excitation spectra at 7 K.

In brief, previous work indicates that there should occur one or multiple excited states around 1.44 eV and possibly another one around 2.0 eV. However, since the OSL process is affected by the transport in the band-tail states and the conduction band, the OSL excitation spectrum is the convolution of excitation in the principal trap and the transport/recombination process. Furthermore, the existence of the excited states above the conduction band, if any, cannot be probed by OSL, since electrons become delocalized as soon as an occupied trap is photo-ionized with energy equal to or greater than the trap depth.

5.2.2 Single vs. multiple principal traps

It has been widely debated whether OSL in feldspar results from a single trap or multiple traps. Based on the bleaching behavior of the luminescence signal, it has been proposed that IRSL and OSL signals originate from two different types of traps (e.g., Duller and Bøtter-Jensen, 1993; Jain and Singhvi, 2001). However, consideration of the OSL decay rate over the excitation energy range 1.24-2.4 eV suggests that a single trap participates in the IRSL and OSL emissions (Baril and Huntley, 2003a; Andersen et al., 2012).

Interestingly, IRSL signals generate even after reducing the signal to the background level during IR exposure (e.g., at T °C), if the sample temperature is elevated to above T °C. These signals known as the post IR-IRSL (pIRIR) signals are much more stable (both thermally and athermally) than the IRSL signals (Thomsen et al., 2008). The fact that IRSL signal intensity increases with an increase in the measurement temperature, and that these pIRIR signals show less fading can be explained both in terms of a single trap (Thomsen et al., 2008; Jain and Ankjærgaard, 2011) or a multiple trap model (Li and Li, 2011). The experimental data such as the pulse anneal curves, bleaching, or the dose response curves may also be interpreted in terms of single or multiple trap models. Although the single trap model (Jain and Ankjærgaard, 2011) is both scientifically and aesthetically elegant in that it combines many apparently unrelated aspects of feldspar luminescence, there remains a need for unambiguous experimental data to close the debate.

Some new insights have been obtained recently from the comparison of the Infrared radioluminescence (IRRL) and IRPL (Kumar et al., 2018; Chapter 3 in this thesis). Erfurt (2003) and Erfurt & Krbetschek (2003) reported two overlapping IRRL emission bands centered at 865 nm (1.43 eV) and 910 nm (1.36 eV) based on curve fitting analysis. Recently, Kumar et al. (2018; Chapter 3 in this thesis) observed that the two overlapping peaks are resolved at low temperatures; two distinct NIR emission bands (peaking at 880 nm (1.41 eV) and 955 nm (1.30 eV)) exist in both IRPL and IRRL at 7 K. These authors concluded that IRRL and IRPL arise from the same principal trap(s), the former reflecting the trapping process, while the latter the resonant excitation after trapping. The two emissions may arise from different excited states of the same trap suggested to be Pb^{+} (Erfurt & Krbetschek, 2003). Equally, they may represent two traps (or defects). Kumar et al. (2018; Chapter 3 in

this thesis) found that the two emission peaks in IRPL and IRRL show markedly different temperature dependence but a similar response to x-ray dose. They, therefore, suggested that the principal trap probably consists of the same defect residing in two different sites; the crystal field variation because of the site dependence gives rise to a slight shift in the emission wavelength.

5.2.3 Optical trap depth

The optical trap depth corresponds to the photon energy required to excite a trapped electron from the ground state into the conduction band. Using OSL, the trap depth for the principal trap has been assigned a number of values ranging from ∼1.9 to 2.5 eV. Hutt et al. (1988) derived an optical trap depth of around 2.5 eV based on the relationship between optical and thermal activation energies used for alkali halides. Clark and Sanderson (1994) suggested the optical trap depth to be smaller than 2.5 eV using the OSL excitation spectra. Using a hydrogenic model, Poolton et al. (1995, 2002) derived a value of around 2.0 eV. Baril and Huntley (2003a) suggested trap depth to be greater than 2.5 eV using OSL excitation spectroscopy. Poolton et al. (2009) applied photo-transferred OSL and TL measurements at 10 K and suggested that trap depth to be somewhere between 2.0 and 2.5 eV. Based on the time-resolved optically stimulated luminescence technique, Jain and Ankjægaard (2011) suggested that trap depth is likely to be greater than 2.4 eV. Kars et al. (2013) fitted their excitation spectra (10 K) using an equation for the photoionization cross-section of a deep defect (Bøtter-Jensen et al., 2003) and derived a value of around 2.5 eV (or greater) for K-feldspar and around 2.1 eV for Na-feldspar. Using the same method, Riedesel et al. (2019) obtained trap depths of around 2.04 eV on many feldspar samples irrespective of their chemical composition.

This large range of values of the optical trap depth suggests that there must be local effects, which likely influence the measurement. The width and the density of the band tail states (Poolton et al., 2009) are important parameters that can vary from sample to sample. Thus given the same trap depth, a larger band-tail width in one sample will initialize OSL recombination much earlier than in the other (Kars et al., 2013). The presence of several recombination pathways influences the luminescence response (Jain and Ankægard, 2011). Finally, it is likely that other traps (apart from the principal trap) also get photoionized and contribute to

signal during the measurement of the OSL excitation spectrum.

In this paper, we use novel site-selective excitation-emission spectroscopy in combination with x-ray irradiation, to solve these long-standing issues related to the characterization of the principal trap. We expect that IRPL, being a site-selective process and independent of the recombination process, can overcome many of the challenges involved in the measurement of the trap depth, excited state and, answer the question of single vs. multiple traps. We also study the thermal and optical behavior of the two IRPL emission bands at room temperature.

5.3 Materials and methods

Six different potassium feldspar ($KAlSi_3O_8$) mineral samples, both sedimentary and museum, were used in this study. They are listed in Table 5.1 with their geographical location and chemical composition. Detailed investigations of the IRPL characteristics were made on a bright sample R47, whereas in the other samples only IRPL excitation spectra were measured. The excitation and emission spectra were recorded using COLUR (Risø Station for Cryogenic Luminescence Research) at DTU Nutech, Denmark. This facility consists of a Horiba spectrofluorometer (Fluorolog-3), modified to include multiple excitation and detection ports, a temperature-controlled (7–300 K) closed-loop He cryostat, and an in-situ x-ray irradiator (40 kV, 100 µA copper anode) (See Chapter 2). Samples grains were attached to stainless steel cups using silicone spray. The cups were then placed onto the cryostat cold finger using carbon tape. The IRPL emission spectra, excitation using 830 nm (1.49 eV) laser (power density of $\sim$3 mW cm^{-2} at the sample position), were measured using a Jobin-Yvon HR-320 spectrometer (300 lines/mm grating) coupled to a liquid nitrogen-cooled charge-coupled device (CCD) detector with an 850 nm LP filter (optical density 4) at 7 K or 300 K. Dose was delivered to the samples using x-ray irradiation at low temperature (7 K).

The IRPL excitation spectra were measured using a xenon lamp (450 W) lamp, and the CCD detector. The data were measured in the three dimensional (3D) mode: two axes were reserved for the emission wavelengths and the intensity, and a third one for the excitation wavelengths. To obtain the excitation spectra, for the emission at 1.41 eV (880 nm), the excitation wavelengths were varied from 300-820 nm, and the emis-

Table 5.1: K-feldspar samples used in this study and their chemical compositions. Chemical compositions of samples R47, R45, R48, and R28 were determined by x-ray fluorescence (XRF), while the compositions of samples K8 and K9 were determined by inductive coupled plasma mass spectroscopy (ICP-MS). Samples R47, R45, R48, and R28 have previously been used by Prasad (2017), and samples K8 and K9 by Baril and Huntley (2003b). Here, K-F: K-Feldspar, Na-F: Na-Feldspar and Ca-F: Ca-Feldspar.

Sample code	Sample location	Type	Size	% composition		
				K-F	Na-F	Ca-F
R47	China	Sediment grains	90-250 μm	85	12	3
R45	Norway	Sediment grains	90-250 μm	87	12	1
R48	Russia	Sediment grains	90-250 μm	82	16	2
K8	Canada	single crystal	3x3x1 mm	84	15	1
R28	Switzerland	single crystal	2x2x2 mm	95	5	0
K9	Russia	rock grains	90-150 μm	86	14	1

sion spectrum in the range 850-1000 nm was recorded corresponding to each excitation wavelength with an 850 nm long pass (LP) interference filter. While this also provides an excitation spectrum for the 1.30 eV (955 nm) emission, we wanted to get as close an excitation wavelength to the emission peak as possible without a light breakthrough. Therefore, to obtain the excitation spectra, for the emission at 1.30 eV (955 nm), the excitation wavelengths were varied from 300 to 920 nm, and the emission spectrum (925-1000 nm) was recorded for each excitation wavelength while using a 925 nm long pass (LP) interference filter (OD:4). The typical integration time per excitation wavelength was kept between 2 s to 4 s based on the signal sensitivity in different samples. To derive an excitation spectrum, two bandwidths 878-882 nm and 953-957 nm (corresponding to the two IRPL peaks) from each emission spectrum were plotted as a function of the excitation wavelength.

Measurement of dose-dependent excitation spectra was carried out by giving different doses to the sample using the x-ray source and then recording the excitation spectrum. Each dose-dependent excitation spectrum consists of two separate dose-measurement cycles: one for the high wavelength (low energy) range and the other for the low wavelength (high energy) range. The signal was reset between different dose-measurement cycles using a solar simulator (Hönle SOL2) for 48 hours. Measurements in two cycles are done to avoid artifacts due to the loss of trapped electrons in an otherwise long, single excitation scan, especially at higher excitation energies.

The OSL/IRSL excitation spectrum was measured using a tungsten halogen lamp (20 W) and an external PMT detecting the UV emission with a 7.5 mm Hoya U-340 filter. All the emission spectra reported in this study have been corrected for the instrumental response, and the excitation spectra have been corrected for the number of incident photons. All the spectra were corrected for conversion from wavelength to energy by multiplying with $\lambda^2 \cdot hc^{-1}$ (Jacobian correction; Mooney and Kambhampati, 2013).

Thermal and optical bleaching experiments were carried out using Risø TL/OSL DA-20 reader, upgraded to include an external laser light source at 830 nm (1.49 eV) and two different photomultiplier tubes (Hamamatsu H7421-50 and Hamamatsu H10330C-25). The IRPL emissions at 1.41 eV (880 nm) and 1.30 eV (955 nm) were discriminated using two emission bandpass interference filters transmitting 880 nm (FWHM=10

nm) or 950 nm (FWHM=50 nm), respectively (see Chapter 4). The laser power was tuned to provide ∼3 mW cm^{-2} power density at the sample position. Irradiation was made using a ^{90}Sr/^{90}Y beta source inside the reader that provides a dose rate of about 0.22 Gy s^{-1}. The IRPL signals were measured in a pulsed excitation and detection mode (pulse width: 50 µs, and off-time: 50 µs). The signals were detected during the off-time (PMT gate: 51-100), and measured for 5 seconds. Time-resolved IRPL curves were measured using a time-correlated single-photon counting (TCSPC) attachment to the Risø reader (photon timer; Lapp et al. 2015); the data obtained between light pulses (off-time) were fitted to a single exponential to get an IRPL lifetime.

Bleaching experiments in the Risø reader used IR (850 nm), blue (470 nm) or UV (405 nm) light-emitting diodes (LEDs) delivering power densities ∼250, ∼80, and ∼140 mW cm^{-2}, respectively, at the sample position. A Hönle SOL2 solar simulator was used for the daylight bleaching experiments.

5.4 Emission and excitation spectra at 7 K

In this section, we present the results on the characterization of the principal trap using photoluminescence excitation-emission spectroscopy. PL emission spectra provide information about the excited-to-ground state transitions of a trap(s). Site-selective PL excitation spectra provide information about the ground-to-excited state transitions of the trapped electrons. Such excitation spectra are obtained by selectively examining the emission from only one particular defect. Figure 5.1a shows the IRPL emission spectrum measured at 7 K after 2 hours of x-ray irradiation (approximate dose 432 Gy) on an aliquot of sample R47. We observe two distinct emission bands centered at 1.30 eV and 1.41 eV. Hereafter, we refer to the 1.30 eV (955 nm) emission band as IRPL$_{1.30}$ and the 1.41 eV (880 nm) emission band as IRPL$_{1.41}$.

In order to determine whether the two emissions, IRPL$_{1.30}$ and IRPL$_{1.41}$, represent different excited states of the same defect (Erfurt, 2003) or of two different defect sites (Kumar et al., 2018; Chapter 3 in this thesis), we measured the excitation spectrum individually for each emission peak. The excitation spectra should be identical if both the emissions arise from the same trap (same defect in an identical environment). Figure 5.1b shows the individual excitation spectrum measured at 7 K for

the two IRPL emission bands centered at 1.30 ± 0.01 and 1.41 ± 0.01 eV after the sample was given an x-ray dose of ∼432 Gy. Measurement at 7 K was chosen in order to avoid any leakage of charge through the band-tail states; as demonstrated in earlier work (Poolton et al., 2009; Prasad et al., 2017) the band tail transport is frozen at this temperature.

The shape of the excitation spectra for $IRPL_{1.30}$ and $IRPL_{1.41}$ are similar but the peak positions are slightly shifted in energy. The excitation peak in the UV region is superimposed on a continuum for both the emissions.

The excitation spectrum for $IRPL_{1.30}$ shows three broad peaks centered at 1.45, 2.05 and 3.35 eV. The 1.45 eV peak matches with the well-known resonance peak identified from the OSL excitation spectra (Hütt et al., 1988; Poolton et al., 2009; Prasad et al., 2017).

The excitation spectrum for $IRPL_{1.41}$ shows two broad peaks at 2.15 eV and 3.55 eV (Figure 5.1b). With the existing COLUR setup comprising a CW Xenon source, we need to maintain about 20-30 nm difference between the excitation and the emission light to avoid any breakthrough. This limits the excitation spectra to start from ∼1.50 eV for $IRPL_{1.41}$; therefore, we only see one side of the resonance excitation peak in the near-infrared (NIR) region (1.5-1.9 eV). Given that we are measuring a Stokes shifted emission, the peak must lie between 1.41 and 1.50 eV.

The emission and excitation spectra from three other K-rich feldspar samples (K8, R45, and R48) are plotted in Figure 5.2. All the emission spectra (Figures 5.2a, c and e) show two peaks ($IRPL_{1.41}$ and $IRPL_{1.30}$) similar to sample R47 (Figure 5.1a) but the relative intensity of these peaks differs from sample to sample. In sample K8, the two emission peaks are of relatively similar magnitude, whereas, in R48 and R45, the $IRPL_{1.30}$ peak is much smaller than the $IRPL_{1.41}$ peak.

The exact position of the excitation peaks differs from sample to sample. Similarly, the excitation spectra of each emission are different for every sample. The excitation spectra for $IRPL_{1.30}$ in all three samples consist of three main peaks similar to R47 (Figure 5.2b, d, and f). However, sample K8 shows an additional peak around 2.40 eV (not clearly resolved), and samples R45 and R48 around 2.75 eV. For the $IRPL_{1.41}$ emission, the samples R45 and R48 show a partial resonance excitation peak in the NIR region around 1.60 eV; again due to instrumental limitation discussed above, the full peak cannot be measured. The fact that the excitation peaks are shifted for the two IRPL emissions supports that

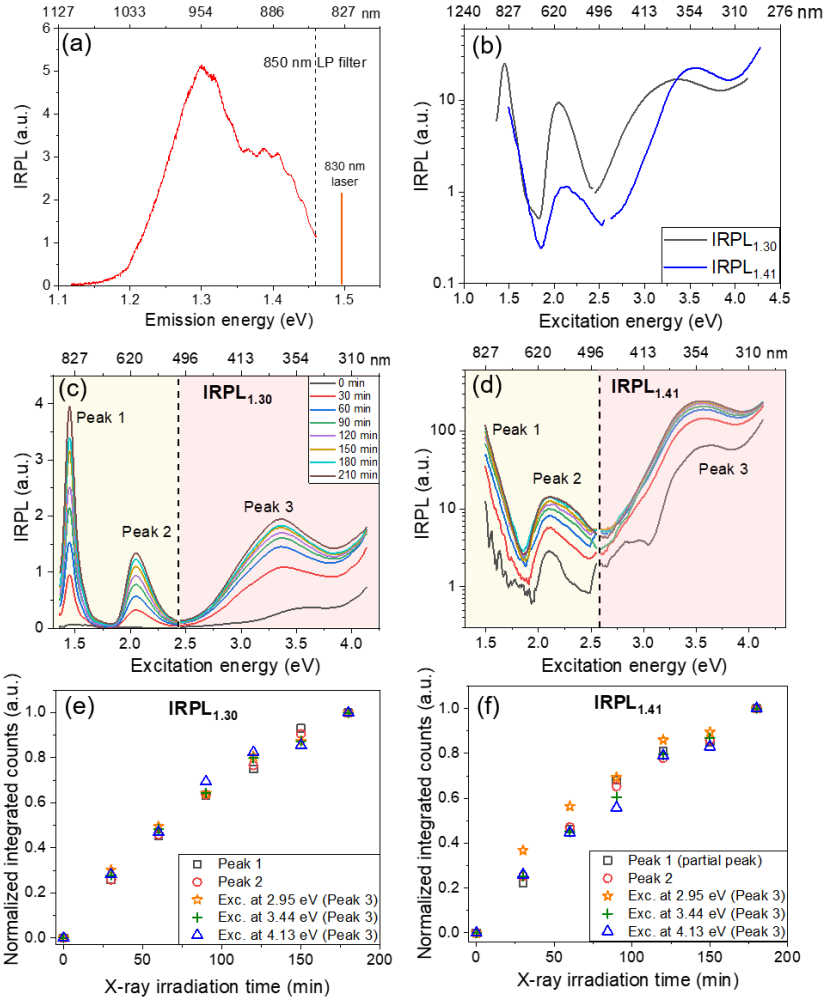

Figure 5.1: (a) Emission spectrum recorded using 830 nm laser excitation. (b) Excitation spectra corresponding to the two NIR emission bands centered at 955 nm (1.30 eV) and 880 nm (1.41 eV). (c) Dose dependent excitation spectra for the $IRPL_{1.30}$. A spectrum was measured after every 30 minutes of x-ray irradiation. (d) Dose dependent excitation spectra for the $IRPL_{1.41}$. A spectrum was measured after every 30 minutes of x-ray irradiation. (e) Dose response curves for peak 1 (the NIR peak at 1.45 eV), peak 2 (2.05 eV), and peak 3 (3.35 eV). DRC of peak 3 is constructed using selective excitation energies (2.95, 3.44 and 4.13 eV). (f) Dose response curves for peak 1 (the partial peak), peak 2 (2.15 eV), and peak 3 (3.55 eV). DRC of peak 3 is constructed using selective excitation energies (2.95, 3.44 and 4.13 eV). All measurements were done at 7 K on sample R47.

IRPL does not originate from a single site.

In the following sections, we investigate the origin of the dominant excitation peaks common to all the samples. Our detailed investigations are performed on sample R47. Henceforth, we name these excitation peaks in R47 as peak 1 (the NIR peak at 1.45 eV), peak 2 (2.05 eV), and peak 3 (3.35 eV) for the $IRPL_{1.30}$ emission. Similarly, peak 1 (partial peak in the 1.41-1.50 eV range), peak 2 (2.15 eV), and peak 3 (3.55 eV) for $IRPL_{1.41}$ emission (see Table 5.2).

5.4.1 Site-selective excitation spectra

In Figures 5.1 and 5.2, the excitation spectra were derived from detecting/choosing two narrow emission bands, 880±2 nm and 955±2 nm, from the emission spectra. However, as seen in the emission spectrum in Figure 5.1a and Figure 5.2 (a, c, e), the two IRPL emission peaks ($IRPL_{1.30}$ $IRPL_{1.41}$) are overlapping. To test whether this has an effect on the excitation spectrum, and thus on our interpretations in the previous section, we re-investigated the emission spectra for some selective excitation energies (between 1.50 eV and 4.13 eV) for sample R47. These emission spectra were recorded using an 850 nm longpass filter, as they capture both the IRPL bands. Figure 5.3a shows the IRPL emission spectra using excitation energies 2.03, 2.25, 2.48, 2.75, 2.95, 3.44 and 4.13 eV. It is observed that the relative amplitude of the two peaks changes with the change in the excitation energy; this suggests that the two centers giving rise to $IRPL_{1.30}$ and $IRPL_{1.41}$ have different photon interaction cross-sections. These data support those in Figures 5.1 and 5.2. For the high energy excitations (e.g. 4.13 eV) the $IRPL_{1.41}$ center interacts more efficiently, whereas, for lower energy excitations (e.g., 2.03 eV) the $IRPL_{1.30}$ center interacts more efficiently. The emission spectrum for each excitation energy was then fitted using a sum of two Gaussian functions centered at 1.30 eV and 1.41 eV. Peak areas from the fitted curves were then plotted against the excitation energies to obtain individual, site-selective, excitation spectra of each IRPL center. This technique avoids the problem of peak overlap in conventional spectroscopy (e.g. Figures 5.1 and 5.2). The site-selective excitation spectra for the $IRPL_{1.30}$ and $IRPL_{1.41}$ centers are plotted in Figure 5.3b. The overall shape and the shift of peak 2 (1.8-2.5 eV) between the two centers is similar to those observed in the direct (without deconvolution) excitation spectra reported in Figure 5.1.

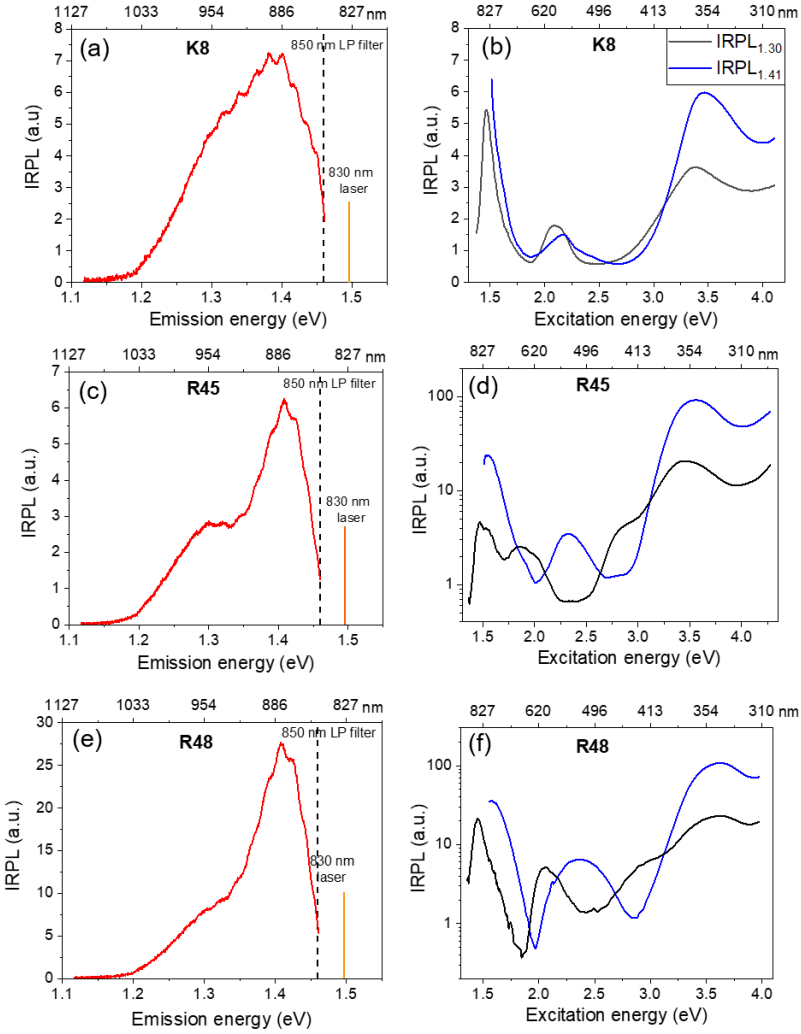

Figure 5.2: Emission and excitation spectra of samples K8 (a, b), R45 (c, d) and R48 (e, f). All measurements were done at 7 K.

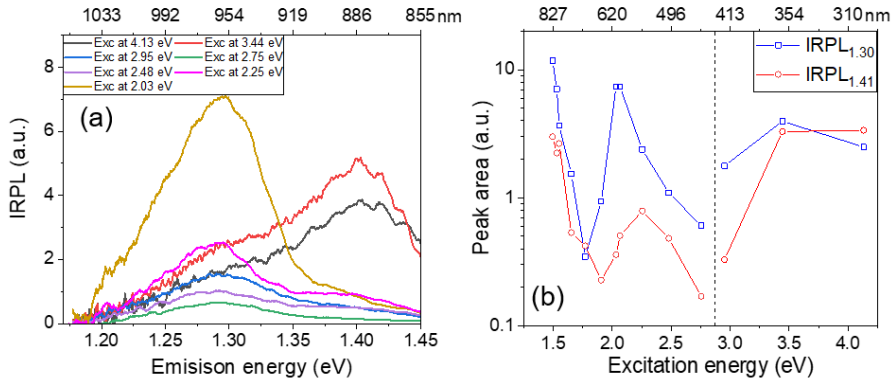

Figure 5.3: (a) IRPL emission spectra obtained using some specific excitation energies. The relative peak heights of the $IRPL_{1.30}$ and $IRPL_{1.41}$ are a function of the excitation energy. (b) Peak areas under the emissions centered at 1.30 eV ($IRPL_{1.30}$) or 1.41 eV ($IRPL_{1.41}$) plotted as a function of the excitation energy used to obtain the emission spectrum. The areas were obtained based on the deconvolution of the emission spectrum using a sum of two Gaussian peaks. The relationship between peak area and excitation energy mimics the excitation spectra reported in Figure 5.1. All the measurements were done at low temperature (7 K) on sample R47.

These site-specific excitation spectra confirm that the two IRPL emissions, $IRPL_{1.30}$ and $IRPL_{1.41}$, arise from two different centers. Furthermore, these data suggest that it is possible to sample electrons from the two centers preferentially by choosing appropriate excitation energy. For example, 2.03 eV will preferentially excite the trap responsible for the $IRPL_{1.30}$, while 4.13 eV will preferentially excite the trap responsible for the $IRPL_{1.41}$. This technique has important implications for studying the linkages between geochemistry and defect emission to identify the principal trap(s). Moreover, since both IRPL and IRRL originate from the same defect, these data imply that Erfurt's (Erfurt, 2003) interpretation that the two IRRL emissions arise from two excited states of the Pb^{+}-center is incorrect.

5.4.2 Origin of the three excitation peaks

In this section, we investigate the origin of peaks 1, 2 and 3 in the excitation spectra of $IRPL_{1.41}$ and $IRPL_{1.30}$ in R47. These peaks may represent either some or a combination of the following phenomena:

1. A resonance phenomenon, i.e. a transition to the excited state of the defect followed by relaxation and PL emission.

2. A delocalized energy level. The rising limb of a peak may reflect an increase in the ionization cross-section as excitation energy approaches a delocalized band edge. The falling limb may then represent the loss of electrons via delocalized recombination, implying less and less retrapping in the principal trap to produce IRPL.

3. Photo-transfer from other traps. It is possible, especially at higher excitation energies in the UV, that some deep traps are photo-ionized and the resulting free electrons are trapped in unoccupied principal traps.

In this section, we discuss which of these three phenomena apply to the three excitation peaks in R47. Based on the results from the previous sections, we use the directly measured excitation spectrum. Deconvolution of peak 1, 2 or 3, as reported in the previous section, was not found to be necessary for the experiments reported below.

In ordinary PL, these scenarios may be difficult to distinguish. However, since we are dealing with the metastable states, one simple yet

powerful method to distinguish between these phenomena is to deliberately increase the population of the metastable states (e.g., by x-ray irradiation) and compare the rate of growth of each peak. If the dose response curve (DRC) of each peak has the same curvature (i.e. same exponential constant or the characteristic dose) then it may imply that phenomena 1) or 2) are active since signal growth in both the cases is linked to the growth of the occupied principal trap. If the DRCs are different then phenomenon 3) may be active, where one of the DRCs may represent the growth of a donor center that transfers electrons into the principal trap.

We measured dose-dependent excitation spectra on the same sample (R47) for both the IRPL emissions. The principal traps were first emptied using a solar simulator and the excitation spectrum recorded for $IRPL_{1.30}$ (labeled as 0 min in Figure 5.1c). The sample was then irradiated with x-rays for a total of 180 minutes (dose ∼650 Gy) and an excitation spectrum was measured after every 30 minutes of irradiation (dose ∼108 Gy). The same procedure was repeated for $IRPL_{1.41}$ after resetting the signal on the same aliquot. The measurement method was the same as that used in Figure 5.1b. The UV and NIR-visible spectra were measured individually in two separate bleaching-irradiation cycles: a) The NIR-visible spectrum (1.35-2.42 eV for $IRPL_{1.30}$, 1.49-2.56 eV for $IRPL_{1.41}$) and the Vis-UV spectrum (2.45-4.13 eV for $IRPL_{1.30}$, 2.59-4.13 eV for $IRPL_{1.41}$). Figures 5.1c and d show the dose-dependent excitation spectra measured for $IRPL_{1.30}$ and $IRPL_{1.41}$, respectively. As expected the peaks 1, 2 and 3 all increase with dose confirming that they arise from metastable states created by the ionizing radiation.

For the construction of dose response curves for the individual peaks, it is important to consider potential signal loss during the measurement; this can be especially important for the spectral measurements in the UV excitation range. We measured this by giving 2 hours of x-ray dose to the bleached sample and doing repeated measurements of the excitation spectrum. The signal loss in the case of the excitation spectra for $IRPL_{1.41}$ was calculated by considering the bands 2.04-2.21 eV for peak 2 and 3.44-3.73 eV for peak 3. Whereas the signal loss in the case of the excitation spectra for $IRPL_{1.30}$ was calculated by considering the bands 1.98-2.14 eV for peak 2 and 3.16-3.60 eV for peak 3. In the three repeated measurements of the UV excitation spectrum (2.45-4.13 eV), a loss of ∼25% and ∼60% was observed for $IRPL_{1.41}$ and $IRPL_{1.30}$, re-

spectively (Figure SI 5.1a and c). Whereas the same number of repeated measurements of the NIR-visible (1.35-2.70 eV) show that the spectra are indistinguishable within our experimental precision (Figure SI 5.1b and d). These data suggest that we can rely on the DRCs of peak 1 and peak 2 derived from Figure 5.1c and d, but not peak 3.

Dose response curves of the excitation peaks 1 and 2 were derived by integrating signals in the small energy range around the individual peaks of the $IRPL_{1.40}$ and $IRPL_{1.30}$ excitation spectra. For $IRPL_{1.30}$, counts in the energy range 1.37-1.58 eV under peak 1, and 1.86-2.40 eV under peak 2 were integrated. Whereas for $IRPL_{1.41}$, counts in the energy range 1.52-1.67 eV under the limb of the peak 1, and 1.93-2.49 eV under peak 2 were integrated. The integrated counts in the same energy range in the excitation spectra after solar bleaching were treated as the background and subtracted from all the signal integrals. The DRC for peak 1 and peak 2 are shown in Figure 5.1e for $IRPL_{1.30}$ and in Figure 5.1f for $IRPL_{1.41}$. The two peaks have an indistinguishable dose response curvature (or characteristic dose) for each emission.

In order to avoid the signal depletion problem for the dose-dependent measurement of peak 3, we repeated the measurements but instead of doing a full excitation scan, we only used some selective excitation energies (at 2.95, 3.44 and 4.13 eV) covering the entire peak. The resulting emission spectra were then used to derive the dose response curves. This reduces the total exposure time from 200 s in a full excitation scan to 0.2-0.5 s for the measurements using these three selected excitation energies. The counts obtained in the two narrow bands (880 $\pm$ 2 nm or 955 $\pm$ 2 nm) from the IRPL emission spectra were integrated; the corresponding background counts were derived from the emission spectra obtained using the same excitation energies but measured after solar bleaching. The net depletion per measurement cycle was less than 5% for the excitations performed in order 2.95 $\rightarrow$ 3.44 $\rightarrow$ 4.13 eV.

The normalized DRCs from all the selective excitation energies are plotted together with the data from peak 1 and peak 2 in Figure 5.1e (for $IRPL_{1.30}$) and 1f (for $IRPL_{1.41}$). Based on the similar curvature of these signals, we conclude that the dose response curves for each peak (peak 1, 2 and 3) are indistinguishable for the $IRPL_{1.30}$ and $IRPL_{1.41}$ emissions. These data confirm to the first order that peaks 1, 2, and 3 are all arising from the principal trap, and thus reflect possible higher energy allowed states of the system.

Based on these data we conclude that:

1. The three main peaks in the excitation spectra (Table 5.2) define the higher energy transitions of the $IRPL_{1.30}$ and $IRPL_{1.41}$ center. The rising continuum in the visible-UV excitation range is perhaps due to charge transfer from a deeper trap (s).

2. Based on comparison with the IRSL excitation spectrum (Baril and Huntley, 2003b; Andersen et al., 2012), we conclude that the peak 1 at 1.45 eV defines the first excited state of $IRPL_{1.30}$ center. We do not fully measure the first excited state (peak 1) of the $IRPL_{1.41}$ center because of the instrumental limitations, but we expect that the peak position must lie between 1.41 eV and 1.50 eV. In samples R45 and R48, the peak appears to be at 1.60 eV for $IRPL_{1.41}$.

3. Peak 2 at 2.05 eV for $IRPL_{1.30}$ center and 2.15 eV for $IRPL_{1.41}$ center likely represents the transition from the principal trap to the conduction band. We base this conclusion on the published values of trap depth using IRSL to be of the order of $\sim$2.0 eV (Kars et al., 2013; Riedesel et al., 2019). The rising part of the peak represents an increase in the photoionization cross-section. The falling part of the peak represents a decrease in the probability of retrapping/relaxation (i.e. the IRPL production step). This decrease in IRPL production occurs because electrons enter into the conduction band where increased mobility leads to an increased probability of recombination with the holes (the OSL route). This aspect is investigated in detail in the next section.

4. Finally, because of similarity in the dose response of peaks 1, 2 and 3, peak 3 must represent a higher excited state of the trap, above the conduction band edge. Our data suggest that despite the fact that this excited state lies in the delocalized band there occurs preferential relaxation as opposed to diffusion and transport (loss) in the conduction band.

The results from all the samples on the peak positions are listed in Table 5.2.

Table 5.2: Summary of the excited states and the optical trap depth in different K-feldspar samples, obtained using excitation spectra at 7 K (Figures 5.1, 5.2, and SI 5.2). Samples R28 and K9 are only used to study the first excited state and the trap depth; their excitation spectra are reported in the supplementary information (Figure SI 5.2).

Sample	Excited state energies (eV)				Trap depth ± 0.02 (eV)	
	Peak 1 $IRPL_{1.30}$	Peak 3 $IRPL_{1.30}$	Peak 1 $IRPL_{1.41}$	Peak 3 $IRPL_{1.41}$	Peak 2 $IRPL_{1.30}$	Peak2 $IRPL_{1.41}$
R47	~1.45	~3.35	<1.50	~3.55	2.05	2.15
R45	~1.46	~3.47	~1.60	~3.57	1.90	2.32
R48	~1.45	~3.60	~1.60	~3.62	2.05	2.38
K8	~1.46	~3.37	<1.50	~3.45	2.09	2.18
R28	~1.46	-	<1.50	-	2.15	2.31
K9	~1.46	-	<1.50	-	2.21	2.25

5.4.3 Does excitation peak 2 reflect the trap depth?

In this section, we compare the OSL excitation spectrum with the IRPL excitation spectrum to obtain and visualize the two complementary processes that follow excitation of electrons in the principal trap: a) retrapping/relaxation back into the principal trap (the IRPL route), and b) loss of electrons and subsequent electron-hole recombination (the OSL route). These measurements were performed at 7 K to minimize any recombination through the band-tail states, although it is not completely avoidable.

The OSL method for the trap depth measurement follows that reported in Kars et al. (2013) and Riedesel et al. (2019). This method is not ideal since the increase in the OSL intensity with the excitation energy maps both the band tail-states (Urbach-tail) as well as the density of states in the conduction band; the distinction between the two is somewhat arbitrary. After removing the initial exponential rising part in the OSL excitation spectrum arising from the band-tail states, the remaining higher energy data may be fitted to the following expression for the spectral dependence of the cross-section (photoionization cross-section) on the trap depth. This expression assumes that an increase in the OSL intensity is due to an increase in the photoionization cross-section.

$$\sigma(E, E_t) \propto \frac{(E - E_t)^{3/2}}{E[E - E_t(1 - \frac{m_o}{m^*})]^2}, \tag{5.1}$$

where σ represents photoionization cross-section, E the excitation energy (eV), E_t the trap depth, m_o the electron rest mass, and $m*$ the effective electron mass (m^*= 0.79 m_o).

Figure 5.4 shows the excitation spectra of $IRPL_{1.30}$ and $IRPL_{1.41}$ emissions, black curve and blue curve, respectively, and the OSL excitation spectrum (red curve) at 7 K. The first excited state as discussed earlier is seen in both the OSL and IRPL excitation spectra. The fitting of equation 5.1 to the different sets of selected energy intervals (listed in Table 5.3) results in an optical trap depth values ranging between 2.08 and 2.25 eV; the minimum estimate is 2.08 ± 0.001 eV. The rising OSL signal above this energy represents an increase in the photoionization cross-section, as the energy is increased further above the conduction band edge.

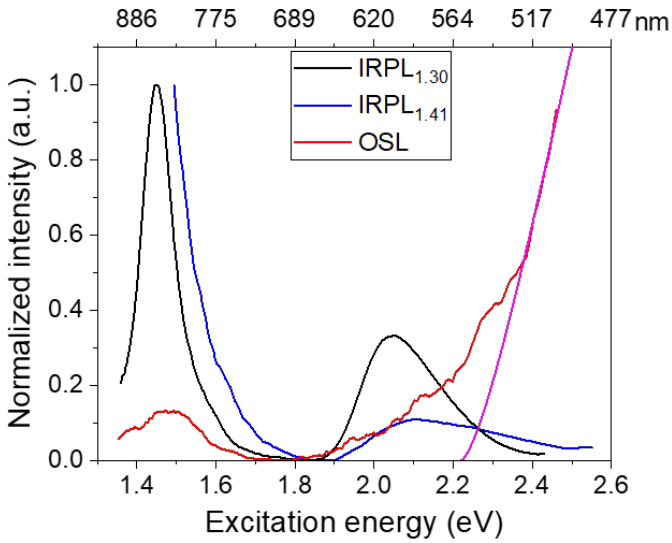

Figure 5.4: IRPL and OSL excitation spectra in the energy range 1.35-2.60 eV. All measurements were done at low temperature (7 K) on sample R47. OSL excitation spectrum is fitted with equation 5.1 to estimate the optical trap depth.

The excitation spectrum of $IRPL_{1.41}$ intensity begins to increase around

1.90 eV, reaches a maximum around 2.15 eV and then decreases to nearly zero intensity around 2.50 eV. The excitation spectrum of $IRPL_{1.30}$ shows a similar form but it reaches a peak at about 0.1 eV earlier than $IRPL_{1.41}$. Furthermore, the excitation spectra at 300 K of IRPL and OSL emissions (Figure 5.5a) suggest that both the defect centers ($IRPL_{1.30}$ and $IRPL_{1.41}$) participate in OSL/IRSL emission; the resonance peaks of OSL and IRPL (peak 1) around 1.45 eV have similar shapes and are at about the same position.

Interestingly, the range in the peak position of the IRPL signals (2.05 to 2.15 eV) is approximately of the same order as the beginning of the rise in the IRSL/OSL signal according to equation 5.1. Based on the OSL excitation spectrum, we inferred that electrons enter a delocalized state somewhere between 2.08 to 2.25 eV. Thus, it appears that peak 2 at 2.05 and 2.15 eV in the IRPL excitation spectra must represent the position of the conduction band edge with respect to the ground states of the $IRPL_{1.30}$ and the $IRPL_{1.41}$ centers, respectively. As the excitation energy is further increased above the peak energy; the IRPL signals begin to fall. This is because the electrons become delocalized within the conduction band and are therefore able to recombine with the hole, leading to a decreased return (retrapping) to the principal trap.

In summary, we interpret that peak 2 represents the optical trap depth (energy between the ground state and the conduction band edge). The trap depths for the $IRPL_{1.30}$ and the $IRPL_{1.41}$ centers for all six samples, based on the position of peak 2 are listed in Table 5.2. The excitation spectra of sample R28 and K9 can be seen in the supplementary information (Figure SI 5.2). The difference in the trap depths between the two IRPL centers is significant in all the samples and can vary by 0.04 eV to up to 0.42 eV in an individual sample. Based on the position of peak 2, we conclude that there is a real variation in trap depth across samples (Table 5.2); thus the intra-sample variation observed in the previous studies is not an artifact of the OSL technique. However, since both the centers participate in the IRSL/OSL process, the trap depth derived based on the OSL spectrum (Equation 5.1) must be a mix of the two individual trap depths derived from IRPL. Our data suggest that the trap depth measured using OSL must be significantly influenced by the relative contribution from the $IRPL_{1.30}$ and $IRPL_{1.41}$ centers to the OSL signal.

Table 5.3: Trap depth obtained from the OSL excitation spectrum at 7 K using different energy ranges fitted to equation 5.1.

Energy range (eV)	Trap depth, E_t (eV)
2.41-2.47	2.25 ± 0.007
2.37-2.47	2.23 ± 0.005
2.32-2.47	2.19 ± 0.010
2.32-2.39	2.08 ± 0.010

5.5 Similarities and differences in the behavior of the $IRPL_{1.30}$ and $IRPL_{1.41}$ centers

Based on the experimental data and our interpretations presented in the previous sections, it is clear that $IRPL_{1.30}$ and $IRPL_{1.41}$ emissions arise from two different principal traps. These traps have different excited state energies and trap depths. Earlier work has shown that two centers also show different thermal quenching behavior but a similar dose response curve (Kumar et al., 2018; Chapter 3 in this thesis). We have plotted the DRCs of $IRPL_{1.30}$ and $IRPL_{1.41}$ together for peak 1(Figure SI 5.3a), peak 2 (Figure SI 5.3b) and peak 3 (Figures SI 5.3c, d and e). These data are replotted from Figures 5.1e and f. We observe that DRCs of $IRPL_{1.30}$ and $IRPL_{1.41}$ emissions are very similar, irrespective of the excitation energy. A minor difference for the excitation energy 2.95 eV could potentially represent measurement error. This comparison supports the data of Kumar et al. (2018; Chapter 3 in this thesis) and suggests that both of the centers ($IRPL_{1.30}$ and $IRPL_{1.41}$) have similar capture cross-sections.

We further test the behavior of the two centers using thermal and optical bleaching, and their characteristic relaxation lifetime. We used the Risø TL-OSL reader with IRPL attachments (Kook et al., 2018) to do these measurements. All the experiments for this section have been performed at room temperature (∼300 K).

Figure 5.5b shows the IRPL emission spectrum after 2 hours of x-ray irradiation at room temperature on sample R47 using 830 nm laser. This peak consists of the two overlapping thermally broadened IRPL

emissions resolved into separate peaks at 7 K (Figure 5.1a). The two IRPL emissions at 1.41 eV (880 nm) and 1.30 eV (955 nm) (Kumar et al., 2018; Chapter 3 in this thesis) can be detected at room temperature through a combination of bandpass interference filters (880/10 nm or 950/50 nm) and appropriate NIR photomultiplier tubes, while exciting the sample with a pulsed laser at 830 nm (see Chapter 4). The results from thermal and optical bleaching, and lifetime measurements using these excitation and bandpass detection are reported below.

5.5.1 Thermal and optical bleaching of IRPL emissions

Trap emptying, i.e. IRPL depletion should be related to the trap depth. We performed bleaching experiments on sample R47 using IR (850 nm), blue (470 nm), UV (405 nm) light, and solar simulator, in separate experiments.

The sample aliquot was first bleached by keeping it in the solar simulator for 48 hours followed by irradiation with the β-particles for 2000 s ($\sim$400 Gy). Then, the IRPL signal reduction was measured as a function of the exposure time (0 s to 4000 s) using IR, Blue or UV light. The same experiment was repeated for solar simulator but exposure times were varied from 0 to 213000 s ($\sim$59 hrs).

From the bleaching curves (Figures 5.5c, d, e, and f), it is observed that, irrespective of the light source, the $IRPL_{1.41}$ bleaches at a slower rate and reaches a higher slowly-bleachable residual value than the $IRPL_{1.30}$. Using the IR light exposure, the $IRPL_{1.41}$ is reduced by $\sim$20% while the $IRPL_{1.30}$ is reduced by $\sim$60% in $\sim$4000 s. Using blue light, the $IRPL_{1.41}$ is reduced by $\sim$60% while the $IRPL_{1.30}$ is reduced by $\sim$90% in $\sim$4000 s. Using UV light, the $IRPL_{1.41}$ is reduced $\sim$90% while $IRPL_{1.30}$ is reduced by $\sim$95% in $\sim$4000 s. A residual level very close to zero is obtained by 60 hours bleaching for both the signals using the solar simulator; however, the $IRPL_{1.41}$ bleaches slightly slower than the $IRPL_{1.30}$.

We also measured the depletion in the IRPL signals by systematically raising the temperature of the samples. A solar bleached sample (R47) was irradiated for an hour with the β-source mounted on the Risø TL/OSL reader (dose $\sim$220 Gy). It was then preheated to different temperatures from 30 °C to 540 °C (with an interval of 30 °C) and IRPL measured for 100 s after each heating step. The intensity of the IRPL as a function of preheat temperature is plotted in Figure 5.5g. These data show that $IRPL_{1.41}$ is more thermally stable than $IRPL_{1.30}$. The

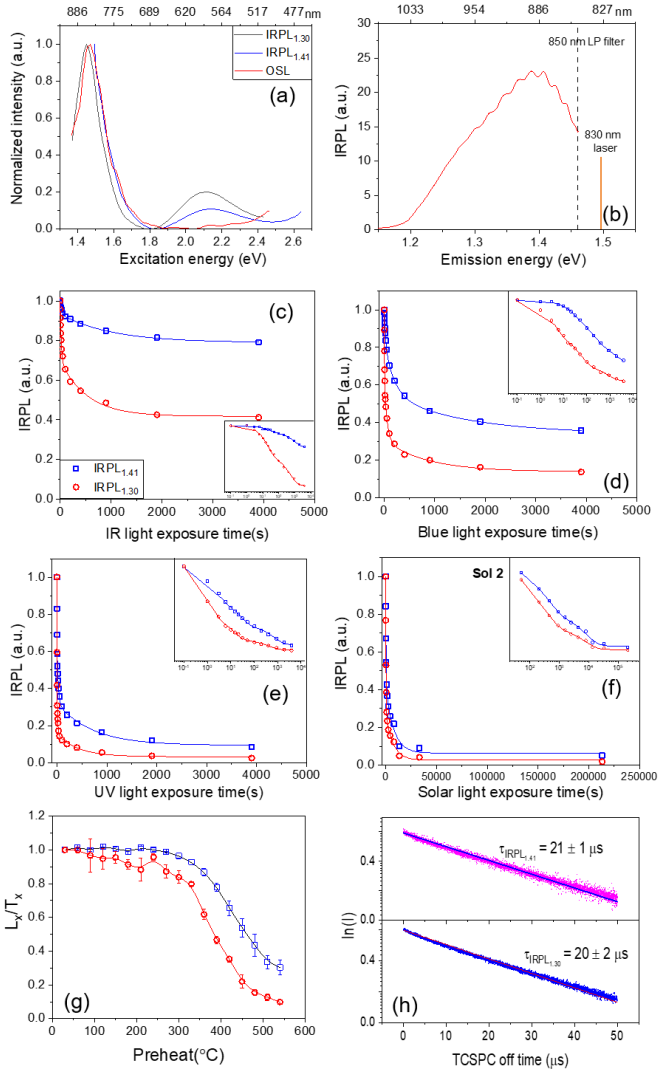

Figure 5.5: (a) IRPL and OSL excitation spectra measured at room temperature (∼300 K), (b) IRPL emission spectrum recorded at ∼300 K. A single broad peak is obtained, (c, d, e and f) depletion of IRPL signals as a function of exposure duration for IR, Blue, UV and solar simulator, respectively; inset figures show the same data on log scale. (g) Depletion of IRPL signals as a function of preheat temperature. L_x/T_x represents sensitivity corrected signal. L_x= IRPL intensity after irradiation and T_x= IRPL intensity after a test dose. (h) Semi-log plot of the time-resolved IRPL for the $IRPL_{1.41}$ and $IRPL_{1.30}$ at room temperature (∼300 K); 'I' stands for IRPL intensity. The data are fitted to a single exponential decay function. All measurements were done on sample R47.

$IRPL_{1.41}$ begins to deplete around 300 °C while the $IRPL_{1.30}$ starts to deplete at 250 °C.

These data demonstrate that even at room temperature the two centers can be distinguished from each other, despite a significant overlap in the emission peaks, and further confirm that the two emissions arise from the two different centers. Both the optical (blue and UV) and the thermal bleaching data are consistent with a greater trap depth of the $IRPL_{1.41}$ center compared to the $IRPL_{1.30}$ center, as discussed in the previous section.

5.5.2 Luminescence lifetime

The data above prove that the two IRPL emissions (∼1.30 eV and ∼1.41 eV) arise from two distinct centers (or sites), and not just the different excited states of the same trap. IRPL(s) decay lifetime can provide information on whether the same or different defects are present at these two different sites.

The decay of IRPL signals (Figure 5.5h) was measured at room temperature using time-correlated single-photon counting (TCSPC) attachment to the Risø TL-OSL reader. An 830 nm laser, operated at 10 kHz frequency (pulse width: 50 µs, and off-time: 50 µs; detection during off-time) was used. The obtained TCSPC data were fitted with a single exponential function (a linear function on the log intensity scale) that yield the lifetimes of 21 ± 1 µs and 20 ± 2 µs for the $IRPL_{1.41}$ and $IRPL_{1.30}$, respectively (Figure 5.5h).

5.6 Discussion

The luminescence lifetime data suggest that the same defect is involved in the $IRPL_{1.41}$ and $IRPL_{1.30}$ emissions. This similarity in the dose response curves (analogous to the electron capture cross-section) for the two emissions data confirms this interpretation (Figure SI 5.3). However, we also concluded based on the excitation spectra that $IRPL_{1.41}$ and $IRPL_{1.30}$ arise from two different centers with different trap depths and excited state energies. We find it intriguing that the ground and excited state energies of the two centers change without changing their capture cross-section or the relaxation lifetime. Lin et al. (2017) have reported a similar observation on the lifetime in silicate compounds. These

authors obtained deteriorated emission spectra from a Ce^{3+} center at two different sites in the host material but no change in the luminescence decay lifetimes.

A combination of all these observations suggests that the two IRPL emissions arise from the same defect at two different sites, experiencing different crystal fields that alter the energy levels. Since we are dealing with granular samples, one explanation could be that these centers vary from grain to grain because of the difference in composition. However, our samples are 82-95% K-feldspar (grains and single crystals) in composition. Therefore, the different centers must be present in feldspar grains of the same composition.

Interestingly, the appearance of distinct additional excitation peaks in samples K8, R45, and R48 suggests that the defect i.e. principal trap may have additional excited states. Full deconvolution of the excitation spectra for each sample is necessary to identify all these excited states.

5.7 Conclusions

Infrared photoluminescence (IRPL) has provided new insights on the principal trap in feldspar. Our investigations on K-rich feldspar samples show for the first time that:

1. There exist two distinct electron-trapping centers, emitting IRPL (excited $\rightarrow$ ground state) at 1.41 eV (880 nm) or 1.30 eV (955 nm). A comparison of OSL and IRPL excitation spectra indicates that both the centers participate in the OSL and IRSL processes.

2. There are at least three resonance peaks in the excitation spectra for each center. Peak 1 and 3 represent the excited states of the trap below and above the conduction band edge. Whereas, peak 2 represents the conduction band edge. The trap depths and the excited state energies vary across samples for both the $IRPL_{1.41}$ and $IRPL_{1.30}$ centers. Further work should focus on the precise deconvolution of the IRPL excitation spectra to obtain the exact number of excited states and their relative photon interaction cross-sections.

3. Based on the position of peak 2, the trap depth estimates range from 2.15-2.38 eV for the $IRPL_{1.41}$ center and 1.90-2.21 eV for the

$IRPL_{1.30}$ center, in our different K-feldspar samples. In any particular sample, the trap depth for the $IRPL_{1.41}$ center is always greater than that for the $IRPL_{1.30}$ center.

4. The $IRPL_{1.41}$ and $IRPL_{1.30}$ centers have different thermal stabilities, and they bleach at different rates when exposed to IR, blue, UV or solar spectrum. In agreement with the trap depth estimates, the $IRPL_{1.41}$ center shows greater thermal stability and bleaches more slowly than the $IRPL_{1.30}$ center.

5. Although the two centers have different ground and excited-state energies, they show identical dose response and relaxation lifetimes. We, therefore, infer that the two centers consist of the same defect in slightly different environments (crystal fields).

Acknowledgments

We thank Prof. D.J. Huntley, Simon Fraser University, Canada, for providing us samples K8 and K9.

Supplementary Material

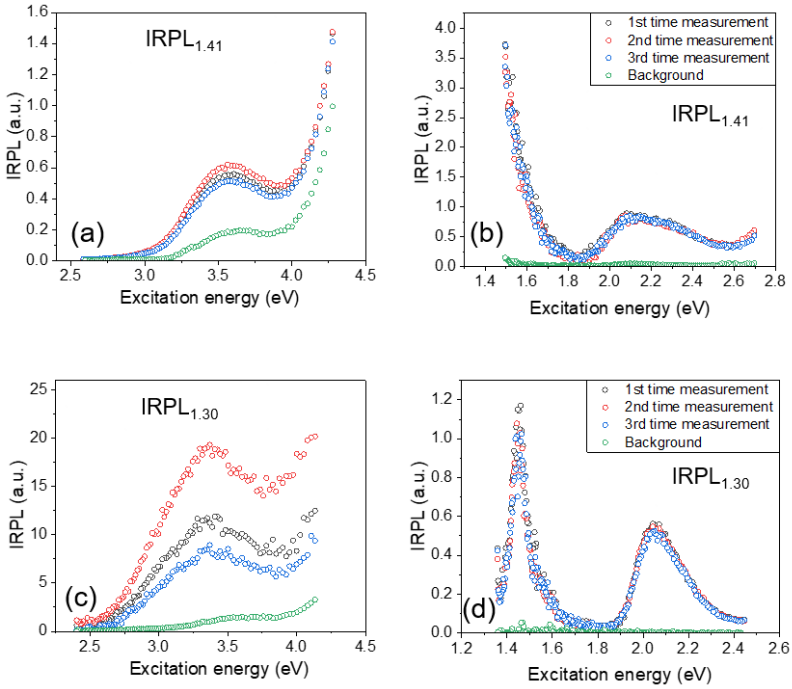

Figure SI 5.1: Repeated measurements of the excitation spectra in the UV energy range for the emissions (a) $IRPL_{1.41}$ and (c) $IRPL_{1.30}$. Repeated measurements of the excitation spectra in the NIR-Vis energy range for the emissions (b) $IRPL_{1.41}$ and (d) $IRPL_{1.30}$. These measurements were carried out at 7 K on the sample R47.

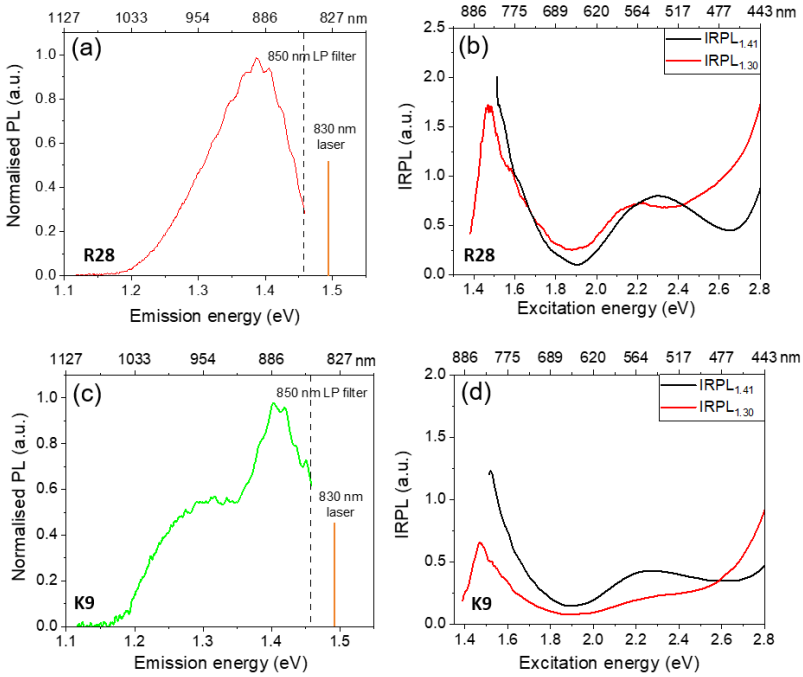

Figure SI 5.2: (a), (c) IRPL emission spectra of sample R28 and K9, respectively. (b), (d) IRPL excitation spectra of samples R28 and K9, respectively. All measurements were carried out at 7 K.

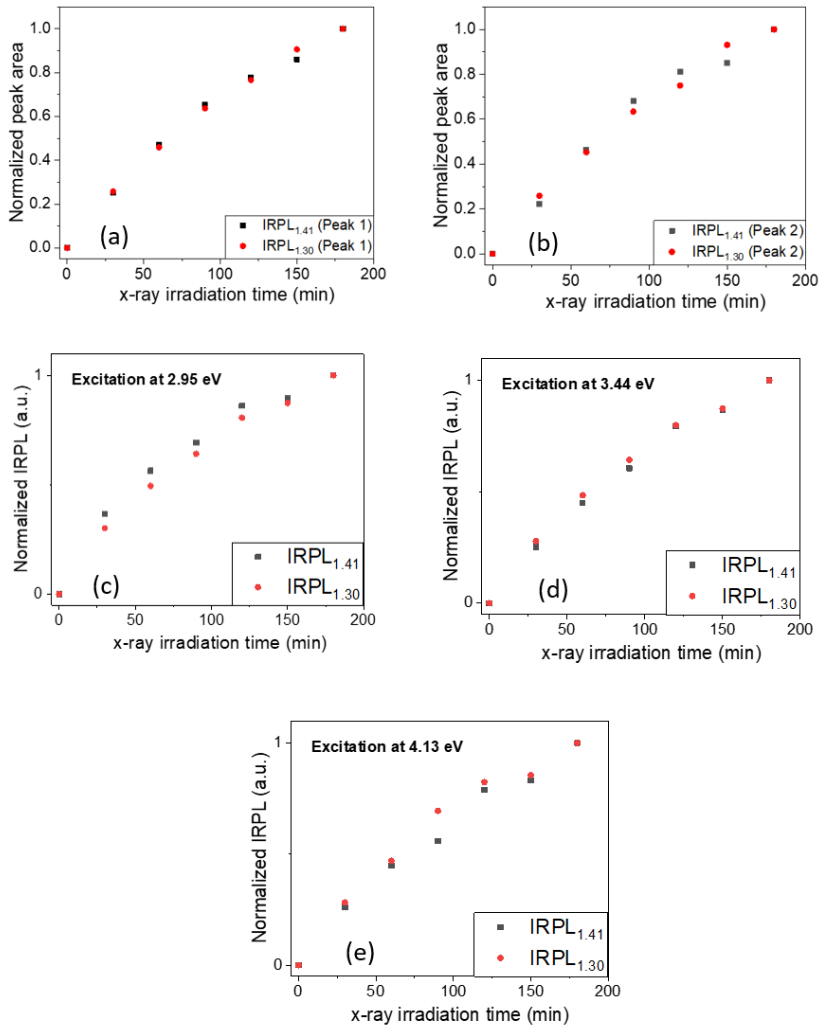

Figure SI 5.3: Dose response curves for $IRPL_{1.41}$ and $IRPL_{1.30}$ emissions potted together for (a) peak 1, (b) peak 2, and (c, d, e) peak 3. In case of peak 3, DRCs are constructed using selective excitation energies (2.95, 3.44 and 4.13 eV).

References

Andersen, M. T., Jain, M., Tidemand-Lichtenberg, P. (2012). Red-IR stimulated luminescence in K-feldspar: Single or multiple trap origin? Journal of Applied Physics, 112(4), 043507.

Bailiff, I. K., & Barnett, S. M. (1994). Characteristics of infrared-stimulated luminescence from a feldspar at low temperatures. Radiation Measurements, 23(2-3), 541-545.

Barnett, S. M., & Bailiff, I. K. (1997). Infrared stimulation spectra of sediments containing feldspars. Radiation Measurements, 27(2), 237-242.

Baril, M. R. (2002). Spectral investigations of luminescence in feldspars. Simon Fraser University, Canada.

Baril, M. R., & Huntley, D. J. (2003a). Optical excitation spectra of trapped electrons in irradiated feldspars. Journal of Physics: Condensed Matter, 15(46), 8011.

Baril, M. R., & Huntley, D. J. (2003b). Infrared stimulated luminescence and phosphorescence spectra of irradiated feldspars. Journal of Physics: Condensed Matter, 15(46), 8029.

Bøtter-Jensen, L., McKeever, S. W., & Wintle, A. G. (2003). Optically stimulated luminescence dosimetry. Elsevier.

Buylaert, J. P., Jain, M., Murray, A. S., Thomsen, K. J., Thiel, C., & Sohbati, R. (2012). A robust feldspar luminescence dating method for Middle and Late Pleistocene sediments. Boreas, 41(3), 435–451.

Clark, R. J., & Sanderson, D. C. W. (1994). Photostimulated luminescence excitation spectroscopy of feldspars and micas. Radiation Measurements, 23(2-3), 641-646.

Ditlefsen, C., & Huntley, D. J. (1994). Optical excitation of trapped charges in quartz, potassium feldspars and mixed silicates: the dependence on photon energy. Radiation Measurements, 23(4), 675-682.

Duller, G. A. T., & Bøtter-Jensen, L. (1993). Luminescence from potassium feldspars stimulated by infrared and green light. Radiation Protection Dosimetry, 47(1-4), 683-688.

Erfurt, G. (2003). Infrared luminescence of Pb+ centres in potassium-rich feldspars. Physica Status Solidi (A) Applied Research, 200(2), 429–438.

Erfurt, G., & Krbetschek, M. R. (2003). IRSAR-A single-aliquot regenerative-dose dating protocol applied to the infrared radiofluorescence (IR-RF) of coarse-grain K feldspar. Ancient TL, 21(1), 35-42.

Götze, J. (2012). Application of cathodoluminescence microscopy and spectroscopy in geosciences. Microscopy and Microanalysis, 18(6), 1270–1284.

Guralnik, B., Jain, M., Herman, F., Ankjærgaard, C., Murray, A.S., Valla, P.G., Preusser, F., King, G.E., Chen, R., Lowick, S.E. & Kook, M. (2015). OSL-thermochronometry of feldspar from the KTB borehole, Germany. Earth and Planetary Science Letters, 423, pp.232-243.

Huntley, D. J., Godfrey-Smith, D. I., & Thewalt, M. L. (1985). Optical dating of sediments. Nature, 313(5998), 105-107.

Hütt, G., Jaek, I., & Tchonka, J. (1988). Optical dating: K-feldspars optical response stimulation spectra. Quaternary Science Reviews, 7(3-4), 381-385.

Hütt, G., Jaek, I., Brodski, L., & Vasilchenko, V. (1999). Optically stimulated luminescence characteristics of natural and doped quartz and alkali feldspars. Applied radiation and isotopes, 50(5), 969-974.

Jain, M., & Ankjærgaard, C. (2011). Towards a non-fading signal in feldspar: insight into charge transport and tunnelling from time-resolved optically stimulated luminescence. Radiation Measurements, 46(3), 292-309.

Kars, R. H., Poolton, N. R., Jain, M., Ankjærgaard, C., Dorenbos, P., & Wallinga, J. (2013). On the trap depth of the IR-sensitive trap in Na-and K-feldspar. Radiation Measurements, 59, 103-113.

King, G. E., Herman, F., Lambert, R., Valla, P. G., & Guralnik, B. (2016). Multi-OSL-thermochronometry of feldspar. Quaternary Geochronology, 33, 76-87.

Kook, M., Kumar, R., Murray, A. S., Thomsen, K. J., & Jain, M. (2018). Instrumentation for the non-destructive optical measurement of trapped electrons in feldspar. Radiation Measurements, 120, 247–252.

Kumar, R., Kook, M., Murray, A. S., & Jain, M. (2018). Towards direct measurement of electrons in metastable states in K-feldspar: Do infrared-photoluminescence and radioluminescence probe the same trap? Radiation Measurements, 120, 7–13.

Li, B., & Li, S. H. (2011). Luminescence dating of K-feldspar from sediments: a protocol without anomalous fading correction. Quaternary Geochronology, 6(5), 468-479.

Li, B., & Li, S. H. (2013). The effect of band-tail states on the thermal stability of the infrared stimulated luminescence from K-feldspar. Journal of Luminescence, 136, 5–10.

Lin, L., Huang, X., Shi, R., Zhou, W., Huang, Y., Zhong, J., & Liang, H. (2017). Luminescence properties and site occupancy of Ce^{3+} in Ba_2SiO_4 : A combined experimental and Ab initio study. RSC Advances, 7(41), 25685-25693.

Malins, A. E. R., Poolton, N. R. J., Quinn, F. M., Johnseir, O., & Denby, P. M. (2004). Luminescence excitation characteristics of Ca, Na and K-aluminosilicates (feldspars) in the stimulation range 5-40 eV: Determination of the band-gap energies. Journal of Physics D: Applied Physics, 37(10), 1439–1450.

Mooney, J., & Kambhampati, P. (2013). Get the basics right: Jacobian conversion of wavelength and energy scales for quantitative analysis of emission spectra.

Poolton, N. R. J., Botter-Jensen, L., & Johnsen, O. (1995). Influence on

donor electron energies of the chemical composition of K, Na and Ca aluminosilicates. Journal of Physics: Condensed Matter, 7(24), 4751–4762.

Poolton, N. R. J., Kars, R. H., Wallinga, J., & Bos, A. J. J. (2009). Direct evidence for the participation of band-tails and excited-state tunnelling in the luminescence of irradiated feldspars. Journal of Physics Condensed Matter, 21(48).

Poolton, N. R. J., Ozanyan, K. B., Wallinga, J., Murray, A. S., & Bøtter-Jensen, L. (2002). Electrons in feldspar II: A consideration of the influence of conduction band-tail states on luminescence processes. Physics and Chemistry of Minerals, 29(3), 217–225.

Prasad, A. K., Poolton, N. R. J., Kook, M., & Jain, M. (2017). Optical dating in a new light: A direct, non-destructive probe of trapped electrons. Scientific Reports, 7(1), 1–15.

Prasad, A. K. (2017). Understanding defect related luminescence processes in wide bandgap materials using low temperature multi-spectroscopic techniques (PhD thesis, Technical University of Denmark, Denmark).

Riedesel, S., King, G. E., Prasad, A. K., Kumar, R., Finch, A. A., & Jain, M. (2019). Optical determination of the width of the band-tail states, and the excited and ground state energies of the principal dosimetric trap in feldspar. Radiation Measurements, 125, 40–51.

Sohbati, R., Murray, A. S., Chapot, M. S., Jain, M., & Pederson, J. (2012). Optically stimulated luminescence (OSL) as a chronometer for surface exposure dating. Journal of Geophysical Research: Solid Earth, 117(B9).

Thomsen, K. J., Murray, A. S., Jain, M., & Bøtter-Jensen, L. (2008). Laboratory fading rates of various luminescence signals from feldspar-rich sediment extracts. Radiation Measurements, 43(9–10), 1474–1486.

Visocekas, R. (1985). Tunnelling radiative recombination in labradorite: its association with anomalous fading of thermoluminescence. Nuclear Tracks and Radiation Measurements (1982), 10(4-6), 521-529.

Visocekas, R. (2002). Tunnelling in afterglow: Its coexistence and interweaving with thermally stimulated luminescence. Radiation Protection Dosimetry, 100(1-4), 45-53.

Wintle, A. G. (1973). Anomalous fading of thermo-luminescence in mineral samples. Nature, 245(5421), 143–144.

Wintle, Ann G. (2008). Luminescence dating: Where it has been and where it is going. Boreas, 37(4), 471–482.

CHAPTER 6

SITE-SELECTIVE MAPPING OF METASTABLE STATES USING ELECTRON-BEAM INDUCED LUMINESCENCE MICROSCOPY

Raju Kumar, Lisa Martin, Dirk Poelman, Dimitri Vandenberghe, Johan Grave, Myungho Kook & Mayank Jain

---

Abstract: Metastable states created by electron or hole capture in crystal defects are widely used in dosimetry and photonic applications. Feldspar, the most abundant mineral in the Earth's crust (>50%), generates metastable states with lifetimes of millions of years upon exposure to ionizing radiation. Although feldspar is widely used in dosimetry and geochronometry, the creation of metastable states and charge transfer across them is poorly understood in this material. Understanding such phenomena requires next-generation methods based on high-resolution, site-selective probing of the metastable states. Recent studies using site-selective techniques such as photoluminescence (PL), and radioluminescence (RL) at 7 K have revealed that feldspar exhibits two NIR emission bands peaking at 880 nm and 955 nm), which are believed to arise from the principal electron-trapping states.

Here we for the first time map the electron-trapping states in potassium-

rich alkali feldspar using spectrally-resolved cathodoluminescence microscopy at the spatial resolution of ∼6 to 22 µm. Each pixel probed by a scanning electron microscope provides us a cathodoluminescence spectrum (SEM-CL) in the range 600-1000 nm, and elemental data from energy-dispersive x-ray spectroscopy (EDX). We conclude that the two near-infrared (NIR) emissions are spatially variable and, therefore, originate from different sites. This conclusion contradicts the existing model that the two emissions arise from two different excited states of a principal trap. Moreover, we are able to link the individual NIR emission peaks with the geochemical variations (K, Na and Fe concentration), and propose a cluster model that explains quenching of the NIR emission by Fe^{4+}. This study has implications for developing sub-single grain dating techniques.

6.1 Introduction

Feldspar, a natural crystalline aluminosilicate, is the most abundant mineral in the Earth's crust (>50%). It crystallizes in monoclinic or triclinic systems depending on the temperature of formation. The crystal structure consists of AlO_4 and SiO_4 tetrahedron frameworks connected through shared oxygen atoms. In the framework, Si and Al sites are named as the T sites, while the interstices (normally occupied by cations K, Na, or Ca) are called the M sites. Based on whether M = K, Na or Ca, a feldspar crystal occurs as $KAlSi_3O_8$ (sanidine, orthoclase, and microcline), $NaAlSi_3O_8$ (albite), or $CaAl_2Si_2O_8$ (anorthite); these are end members of the K-Na (alkali feldspar) and Na-Ca (plagioclase) solid solution series. Furthermore, there exist T_1 and T_2 sites because of two distinct Si or Al sites lying in different environments (Götze, 2012).

Luminescence from feldspar arises mainly due to defects and impurities that occupy energy levels within the bandgap (bandgap, E_g ∼7.7 eV; Malins et al., 2004). For example, well-known emissions occur from the Fe^{3+} and Mn^{2+} ions occupying the T_1 and M sites, respectively (Short, 2003; Götze, 2012). Some defects form metastable states by capturing free electrons or holes created due to ionizing radiation. Annihilation of these states can be induced by thermal or optical stimulation; this leads to electron-hole recombination and subsequent luminescence emission in the ultra-violet (UV) to near-infrared (NIR) range. The fact that the resulting luminescence intensity is proportional to the prior concen-

tration of the metastable states is exploited in solid-state luminescence dosimetry. Here the change in the concentration of the metastable states due to absorbed dose (unit Gy=J kg^{-1}) from ionizing radiation is read out via luminescence. The most widespread dosimetric application of feldspars is in luminescence dating where a feldspar grain buried in sediment accumulates dose from the environmental ionizing radiation during burial (Huntley et al., 1985; Wintle, 2008). This accumulated dose is proportional to its burial age.

Dosimetry and geochronology applications using feldspar are based on the main electron-trapping defect called the principal trap. Electrons in the principal trap are excited using infrared light (850 ± 30 nm), and the luminescence arising from electron-hole recombination is measured in the violet-blue emission band (340-450 nm). This technique called infrared stimulated luminescence (IRSL; Hütt et al., 1988) is a variant of the optically stimulated luminescence (OSL) method. Despite rapid advances in this technique over the last two decades (see review by Wintle, 2008), the basic characterization and the exact identification of the metastable states giving rise to OSL or IRSL has not been possible. This lack of knowledge can be partly attributed to the fact that OSL (or IRSL) is not an ideal method to study the physical characteristics of the traps (e.g., excited state energies, trap depth, number of traps and distribution) since the luminescence signal is a convolution of electron excitation, transport, and recombination.

In contrast to OSL, infrared radioluminescence (IRRL; Trautmann et al., 1998, 2000) and infrared photoluminescence (IRPL; Prasad et al., 2017 and Chapter 3 in this thesis) arise directly from the electron traps without involving any electron-hole recombination. IRRL provides real-time measurement of luminescence emitted during the capture of electrons in the principal trap while feldspar is exposed to ionizing radiation. IRPL measures electrons trapped in the principal trap after exposure to ionizing radiation using the photoluminescence (PL) technique; electrons are excited with NIR and the resulting Stokes-shifted emission from the relaxation of the excited state is measured.

Previous studies show the existence of two overlapping emissions in both IRPL and IRRL emission spectra. In the case of IRRL, these emissions inferred to be centered at ∼865 and ∼910 nm based on spectral deconvolution, have been attributed to two excited states of a Pb electron trapping center (Erfurt and Krbetschek, 2003; Erfurt, 2003). Based

on low-temperature spectroscopy, Kumar et al. (2018; Chapter 3 in this thesis) have recently reported two distinct emission bands centered at 880 nm and 955 nm, both in IRRL and IRPL at 7 K. The authors confirmed experimentally that IRRL and IRPL are two complementary signals from the same trap. IRRL arises during capture of electrons into the principal trap, whereas IRPL arises from subsequent resonant excitation and radiative relaxation of these trapped electrons. Based on the temperature and sample dependent variations in the two IRPL bands (∼880 nm and ∼955 nm), Kumar et al. (2018; Chapter 3 in this thesis) suggested that these emissions arise from two different sites, and not the same defect site as inferred by Erfurt (2003). In order to better understand the characteristics of the electron trapping centers in feldspars, it is important to establish whether the two NIR emissions (∼880 nm and ∼955 nm) arise from the same defect or two different defects, how these defects are distributed in the crystal, and what is their link to the feldspar's mineralogical composition. This knowledge also has important implications for improving the accuracy and precision in luminescence dating, especially if the two emissions have different stabilities.

Since both IRPL and IRRL techniques examine the trapped electrons, selectively, they have the potential for site-specific probing of the principal trap. One way to examine the link between the emission band and the trapping state is to map the emissions spatially and understand their linkages to the chemical composition. Recently, Thomsen et al. (2018) investigated the spatial distribution of IRPL in feldspar and related this to the corresponding map of the chemical composition obtained using micro x-ray fluorescence (μ-XRF). These authors concluded that IRPL mainly arises from the K-rich regions. The available spatial resolution in this study (because of cross-talk) restricted interpretations at the sub-single-grain level, and furthermore, only one IRPL emission (955 nm emission) was examined. Similarly, Sellwood et al. (2019) have shown that IRPL (955 nm emission) is correlated with K concentration in feldspar in granitic rocks.

The purpose of this article is to use cathodoluminescence (CL; luminescence emitted during interaction of an electron beam with the sample) microscopy combined with visible-NIR spectroscopy (Yacobi and Holt, 1986; Martin et al., 2018) to map the two NIR emissions (880 nm and 955 nm), simultaneously with energy-dispersive x-ray spectrometry to determine elemental composition.

This is the first investigation studying the spectrally-resolved spatial distribution of the principal trap emissions (880 nm and 955 nm) and its link to feldspar geochemistry. This work has implications for understanding the behavior of metastable states in feldspar, the most widespread naturally occurring mineral, and for developing next-generation luminescence dating techniques at a sub-single-grain resolution.

6.2 Previous studies on cathodoluminescence in feldspar

Cathodoluminescence (CL) is emitted when a sample is exposed to an electron beam. The mechanism is similar to radioluminescence which is induced by x-rays, γ-rays, and α and β particles; the main difference is in the penetration depth of the different particles. The CL technique typically samples the near-surface volume of the material, of the order of 1 µm, depending on the acceleration voltage of the electron beam and the sample composition. There are several ways by which CL in semiconductors or insulators is produced: 1) band-to-band transitions, 2) band-to-defect transitions i.e. trapping of charge by a defect, 3) trap-assisted, band-to-band transitions, and 4) intra-defect transitions (Pagel et al., 2000; Baele et al., 2019). Cathodoluminescence of feldspars is regarded as an important tool to interpret genetic conditions of rock formation and alteration (Marshall, 1988; Götze, 2012). Forensic science makes use of CL to study the provenance of feldspar (Brokus et al., 2015). CL has also been used to study the luminescence behavior of feldspars, and identify activators or defects (Götze, 2012). These investigations have mainly focused on greenish-yellow (∼560 nm) and red (∼700 nm) emission bands that are suggested to arise from Mn^{2+} and Fe^{3+} defects, respectively (Sippel and Spencer, 1970; Krbetscheck et al., 2002; Visocekas et al., 2014). Other crystal defects such as Ce^{3+}, Eu^{2+}, Cu^{2+}, Al-O^{-}-Al, Ga^{3+}, Sm^{3+}, Dy^{3+}, Eu^{3+}, Tb^{3+}, Nd^{3+}, Pb^{+}, etc. have also been identified using the CL spectra of feldspars (Walker, 1985; Götze et al., 1999a,b; Götze, 2012); however, only a few investigations have been done on the spectral emission region beyond 800 nm in which the principal dosimetric trap emits (Krbetschek et al., 1997; Visocekas et al., 2014). The main source of information on the emission above 800 nm is through radioluminescence obtained from exposure to beta particles. The radioluminescence spectrum of feldspar consists of a broad emission

band centered at ∼865 nm at room temperature. Major research on this peak was carried out by Trautmann et al. (1998), Krbetschek et al. (2000), Trautmann et al. (2000), Erfurt and Krbetschek (2003), and Erfurt (2003). However, this band at ∼865 nm was initially reported in the CL spectrum by Krbetschek et al. (1997). Based on the comparison of the OSL/IRSL excitation spectrum (excitation peak ∼860 nm) and the IRRL emission spectrum (emission peak ∼865 nm) at room temperature, the origin of these two signals was suggested to be from the same trap, i.e. the principal trap (Trautmann et al., 1999 a, b; Krbetschek et al., 2000; Erfurt and Krbetschek, 2003).

6.3 Experimental and analytical details

We used four $KAlSi_3O_8$ (K-rich) as well as one mixed (K and Na) feldspars. All samples were bleached for 48 hours in a solar simulator (Hönle SOL 2) before any measurement. All other details (for e.g. grain size, sampling location, etc.) are listed in Table 6.1.

Photoluminescence (PL; excitation using 830 nm laser) and x-ray excited optical luminescence (XEOL; note that XEOL is a form of radioluminescence) were recorded at room temperature (RT; 300 K) using the Risø station for CryOgenic LUminescence Research (COLUR) at DTU Nutech, Denmark. This facility consists of a Horiba spectrofluorometer (Fluorolog-3) modified to include multi-excitation and -detection ports, an x-ray irradiator (filament-based x-ray tube with copper anode, operated at 40 kV anode voltage, 100 µA anode current), and a temperature-controlled closed-loop He cryostat (7-300 K).

CL mapping was carried out using a Hitachi S3400-N scanning electron microscope (SEM) operated at 20 kV. The SEM images were obtained using a back-scattered electron (BSE) detector. The secondary electron (SE) detector of this system is not suitable for SEM imaging at the pressure (20 Pa) used here. The cathodoluminescence (CL) spectrum (600-1000 nm) was captured for each pixel in a mapping grid of 128-by-92 pixels using an optical fiber connected to an Acton SP monochromator and ProEM 1600 EMCCD, both from Princeton Instruments. The map's pixel size reflects the spatial resolution that is decided by the chosen grid and the magnification. Magnification was decided based on the dominant grain size in a sample; it was set to be higher for samples with relatively smaller grains and, therefore, the resolution of the map is different (∼6-22

µm) for different samples (see Table 6.1).

The electron-beam scanned the area within a pixel for a fixed number of times, and the data from each pixel is a sum of all these scans. All the measurements were performed at room temperature (300 K). Chapter 2 (Section 2.2) can be referred to for an overview of the technique and the CL system. All the CL measurements were carried out at the LumiLab, Department of Solid state Sciences, University of Ghent, Belgium. For spectrum analysis, all the local spectra (i.e. CL spectrum measured for each pixel) were corrected for the detector sensitivity and processed in Matlab.

To examine shifts in the emission band or peak position across pixels, we calculate a barycenter of each local emission spectrum in the wavelength range of our interest. The barycenter is calculated as follows:

$$\lambda_{bary} = \frac{\int I(\lambda) \cdot \lambda \, d\lambda}{\int I(\lambda) \, d\lambda}, \tag{6.1}$$

where I(λ) is the CL intensity at a particular wavelength (λ).

The emission range from 800 to 1000 nm was used to evaluate barycenter of each local spectrum in the NIR spectral region; collected data below this energy range were ignored since we were only interested in investigating the principal trap here. We did not use absolute CL intensity to derive any conclusions, given the fact that the feldspar grains used in this study do not have a flat, homogeneous surface and absolute intensities thus cannot be compared.

Major element analysis was carried out using an energy-dispersive x-ray spectrometer at the same time when CL measurements were carried out. A ThermoScientific Noran System 7 enabled elemental mapping and quantification by probing the characteristic x-ray lines of the major elements, Na (K_α, 1.0 keV), K (K_α, 3.3 keV), Fe (K_α, 6.4 keV) Si (K_α, 1.7 keV), Al (K_α, 1.5 keV), Ca (K_α, 3.7 keV), Mg (K_α, 1.3 keV), C (K_α, 0.3 keV), O (K_α, 0.5 keV), and Ba (L_α, 4.5 keV) (see Table 6.1).

Table 6.1: Compositions for feldspar samples measured using energy-dispersive x-ray spectrometry (EDX); cumulative concentrations (from total mapping area) are given in atom %. Such a high concentration of carbon in feldspar is not possible; it is due to the carbon tape, which was used to hold the samples. Elemental mapping and quantification were done by probing the characteristic x-ray lines of Na (K_α, 1.0 keV), K (K_α, 3.3 keV), Fe (K_α, 6.4 keV) Si (K_α, 1.7 keV), Al (K_α, 1.5 keV), Ca (K_α, 3.7 keV), Mg (K_α, 1.3 keV), C (K_α, 0.3 keV), O (K_α, 0.5 keV), and Ba (L_α, 4.5 keV)

		Sample				
		R47	R43	K7	R50	K13
Location		China	China	U.S.A	Unkown	Canada
Type		Sediment	Sediment	Rock	Museum	Rock
Grain size (µm)		120-300	50-150	10- 300	50-250	100-250
CL map resolution (µm)		12.6	6.7	9.1	11.2	22.4
Magnification		80	180	110	90	45
Chemical composition (Atom %)	C	18.35 ± 0.12	26.28 ± 0.13	8.86 ± 0.1	39.46 ± 0.18	39.68 ± 0.18
	O	53.62 ± 0.26	50.17 ± 0.24	57.98 ± 0.3	42.31 ± 0.21	41.91 ± 0.2
	Na	0.36 ± 0.01	0.97 ± 0.01	3.29 ± 0.03	0.71 ± 0.01	0.53 ± 0.01
	Mg	0.06 ± 0.01	0.07 ± 0.01	0.08 ± 0.02	0.09 ± 0.01	0.07 ± 0.01
	Al	6.1 ± 0.03	4.54 ± 0.02	7.34 ± 0.04	4.45 ± 0.02	4.37 ± 0.02
	Si	17 ± 0.06	15.25 ± 0.05	19.17 ± 0.07	10.35 ± 0.03	10.61 ± 0.04
	K	4.43 ± 0.02	2.62 ± 0.01	3.17 ± 0.03	2.53 ± 0.01	2.77 ± 0.01
	Ca	0.04 ± 0.01	0.04 ± 0.01	0.02 ± 0.01	0.03 ± 0.01	0.02 ± 0.01
	Fe	0.02 ± 0.01	0.04 ± 0.01	0.08 ± 0.01	0.09 ± 0.01	0.04 ± 0.01
	Ba	0.03 ± 0.01	0.02 ± 0.01	0 ± 0.01	0 ± 0.01	0.01 ± 0.01
	Total	100	100	100	100	100

6.4 Cathodoluminescence (CL), x-ray excited optical luminescence (XEOL), and photoluminescence (PL) emission spectra at room temperature

Figures 6.1a, b and c show the CL, XEOL, and PL emission spectra, respectively, of sample R47, measured at room temperature. The CL and XEOL spectra were recorded in the wavelength range of 600-1000 nm. However, the PL emission spectrum was measured only from 850 to 1000 nm since an 830 nm laser was used to excite the sample, and an 850 nm long pass interference filter was used to detect the NIR emission bands. CL and XEOL emissions were recorded after 48 hours of bleaching in the solar simulator (Hönle SOL 2) in order to empty the principal trap; this maximizes the radioluminescence signal sensitivity by increasing the concentration of traps available for the electron capture.

In each excitation mode, the emission spectrum in the NIR range (850-1000 nm) consists of a broad band centered at 900 nm. For the XEOL and PL measurements on the same sample (R47), Kumar et al. (2018; Chapter 3 in this thesis) have previously shown that this broad peak splits into two peaks at 880 nm (1.41 eV) and 955 nm (1.30 eV) at low temperature (7 K). XEOL and CL mechanisms are similar in terms of ionization and trapping; the only difference is the interaction volume of the crystal. In the case of CL, we are biased by the near-surface traps as the penetration depth of 20 keV electrons is only about 4 µm in feldspar (Flude et al., 2013). Whereas, in the case of XEOL we have a relatively greater penetration depth of about 100 µm using x-rays of mean energy ∼13 keV (Brokus et al., 2015). The XEOL and the CL data look very similar in the NIR region supporting that there is no significant modification of the principal trap, closer to the crystal surface. The CL data can be fitted to a linear combination of two Gaussian peaks (inset Figure 6.1a); the peak maxima are the same as those observed for the XEOL and the PL. A peak ∼720 nm (1.72 eV) is also observed in the CL and XEOL emission spectra; this peak has been rigorously studied previously and has been attributed to the Fe-centers (Geake et al., 1973; Visocekas et al., 2014).

Based on the comparison of PL, XEOL, and CL spectra, we conclude that the CL emission in the NIR region arises from the principal trap as it is similar to the XEOL and PL from the bulk crystal vol-

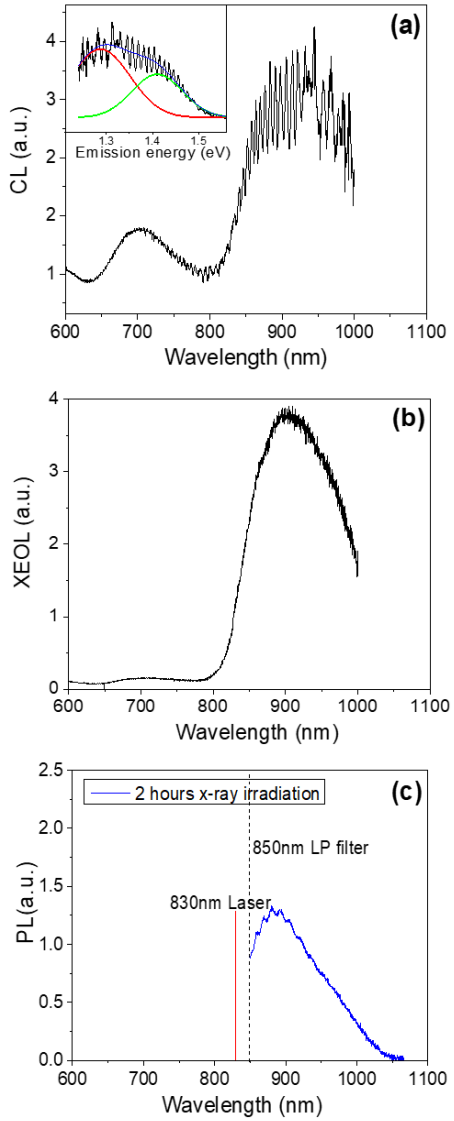

Figure 6.1: (a) Cathodoluminescence (CL), (b) x-ray excited optical luminescence (XEOL), and (c) photoluminescence (PL) emission spectra of a sample R47 at room temperature (∼300 K). The inset in (a) shows the deconvolution of the CL peak (∼900 nm) into two peaks at 880 nm (1.41 eV) and 955 nm (1.30 eV). CL and XEOL emission spectra were measured after bleaching the sample for 48 hours in a solar simulator. PL emission spectrum was measured after 2 hours of x-ray irradiation.

ume. This raises exciting possibilities to map the defects using scanning electron microscope-cathodoluminescence (SEM-CL) imaging. In the remaining paper, we investigate spectrally-resolved CL mapping on 5 different feldspar samples. We henceforth refer to CL in the NIR spectral region as infrared CL (IRCL).

6.5 Mapping of two IRCL emission bands

Figure 6.2 shows the CL mapping data from sample R47. Figure 6.2a shows the backscattered electron (BSE) image. Figure 6.2b shows the IRCL intensity map for the feldspar grains, measured at 300 K; intensity below a certain value ($I/I_{max} < 0.235$; I_{max}=maximum intensity) has been masked using a filter (black background). Figure 6.2c shows the barycenter map of IRCL in the spectral range 880-925 nm, calculated using equation 6.1. This region was selected to ensure minimum contamination effect from the adjacent Fe^{3+} peak. We observed certain pixels (very deep red spots), called hot spots, which are likely artifacts from spurious noise during photon detection; therefore the maximum cut-off of 925 nm was imposed on the barycenter value. This resulted in the rejection of only a few pixels per image. A barycenter map reflects a shift in the emission band across pixels. For example, a barycenter is expected to shift to longer wavelengths if peak position or emission band shifts to longer wavelengths. Most of the grains appear to be dominated by the barycenter at longer wavelengths (>915 nm; light and deep reddish regions), and a few grains by slightly shorter wavelengths (<915 nm; yellow-blue-greenish regions). Local CL emission spectra from low ($I \approx 0.3\ I_{max}$) and high intensity ($I \approx 0.9\ I_{max}$) regions are shown in Figure 6.2d. Figure 6.2e shows a map of the relative CL intensity between two bands: band 1 (890-910 nm) and band 2 (960-980 nm); the map was created by taking the ratio of areas under the two bands of the local CL emission spectra from each pixel. It can be seen in Figure 6.2e that the relative intensity between these two bands varies from grain to grain (the blueish region is dominated by band 2 while yellowish and reddish regions are dominated by band 1). It is interesting that the relative intensity between two bands varies even within the grain (Figures 6.2c and e, circled gains). The ratio map supports the barycenter map; a relative increase in the 955 nm emission band compared to the 880 nm band corresponds to a redshift in the barycenter (Figures 6.2c and e). Figure 6.2f

shows the elemental map (K/(K+Na)) from EDX for the same sample. Excluding a couple of grains and grain boundaries with high Na content, the composition generally varies from about 80 to near 100% potassium. It appears that the Na rich regions (bluish regions in Figure 6.2f) emit a relatively stronger 880 nm IRCL emission (Figures 6.2c and e), while the K rich regions emit a stronger 955 nm emission.

Figure 6.3 shows the same data as Figure 6.2 but for sample R43. The main differences between Figures 6.2 and 6.3 are: 1) the size of each pixel is 12.6 µm for sample R47 and 6.7 µm for sample R43, and 2) $I < 0.235\ I_{max}$ and $I < 0.135\ I_{max}$ have been treated as background in the case of Figure 6.2 (sample R47) and Figure 6.3 (sample R43), respectively.

By focusing the discussion around the two NIR emission bands (Figure 6.1a), we extract the following information from the data presented in Figures 6.2 and 6.3:

1. The barycenter varies from 880 nm to 925 nm in both samples R47 and R43.

2. From the barycenter map, it is clear that some grains emit at shorter wavelengths (the 880 nm emission band) and some at longer wavelengths (the 955 nm emission band). This suggests that the two IRCL emission bands, and therefore, the relative concentrations of the principal traps responsible for these emissions vary spatially.

3. The barycenter shifts are seen even within an individual K-rich feldspar grain (Figure 6.2c, circled grain) with a size of ∼250 µm. This indicates that the trapping states and thus the luminescence properties can vary within a single-grain at the scale smaller than 250 µm.

4. Na-rich feldspar grains seem to preferentially emit the 880 nm IRCL compared to the K-rich feldspar grains.

6.6 Elemental concentrations and the CL emission bands

Since EDX and CL spectra were collected simultaneously, each pixel in the map contains data for CL emission and information on the chemical composition. Correlation between IRCL emissions and chemical composition can be studied by using the EDX and the local CL spectrum from

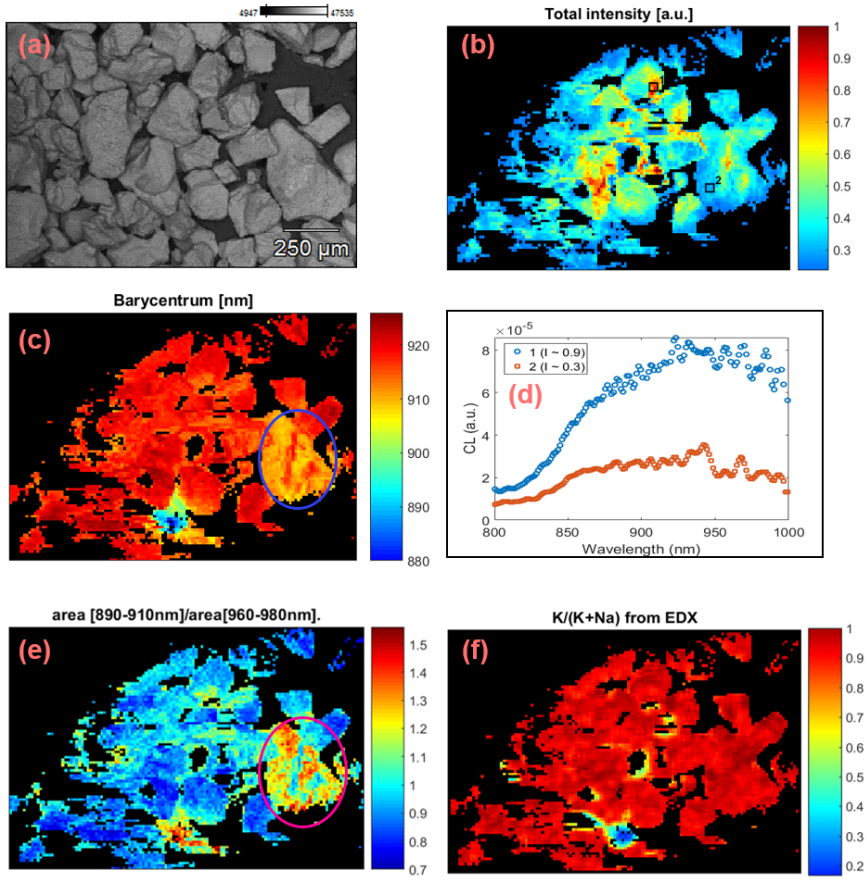

Figure 6.2: CL and elemental data of sample R47. (a) BSE image, (b) cathodoluminescence intensity map; intensity below a value of $0.235I_{max}$ has been filtered out using a mask, (c) barycenter map in the range 880-925 nm. The barycenter is calculated using equation 6.1, (d) local CL spectra of two regions at intensities, I $\approx$0.9 I_{max} and $\approx$0.3 I_{max} on the intensity map, (e) intensity ratio map between the two NIR bands, 890-910 nm and 960-980 nm, and (f) relative concentration map of the K-content (K/(K+Na)).

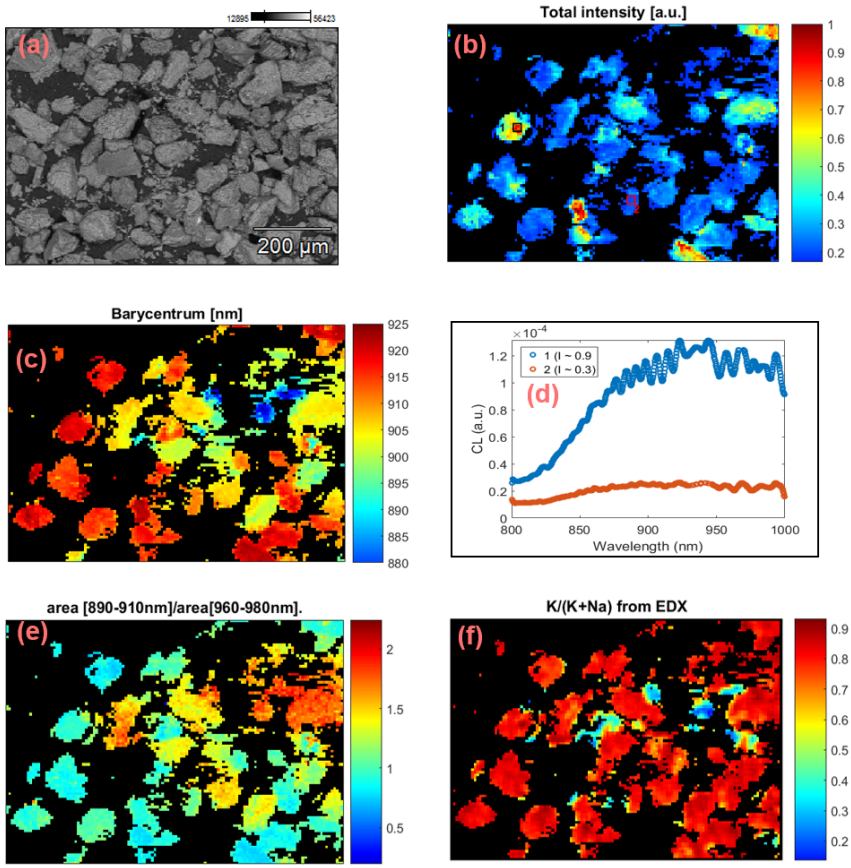

Figure 6.3: CL and elemental data of sample R43. (a) BSE image, (b) cathodoluminescence intensity map; intensity below a value of 0.135 I_{max} has been filtered out using a mask, (c) barycenter map in the range 880-925 nm. The barycenter is calculated using equation 6.1, (d) local CL spectra of two regions at intensities, I ≈0.9 I_{max} and ≈0.3 I_{max} on the intensity map, (e) intensity ratio map between the two NIR bands, 890-910 nm and 960-980 nm, and (f) relative concentration map of the K-content (K/(K+Na)).

each pixel. We did not observe any significant correlation between the measured elements and the CL emissions except K, Na, and Fe. Here, we focus on the main cationic constituents K, and Na, as well as Fe. As we are dealing with alkali feldspars only, the Ca concentration in our samples (see Table 6.1) is not high enough (0.02-0.04%) to attempt any correlations. Elemental ratio K/(K+Na) maps created from the EDX data are shown in Figure 6.2f for sample R47 and Figure 6.3f for sample R43. It is observed that more than 95% of the elemental map is dominated by the K-content in the case of sample R47 whereas more than 80% of the studied area has K/(K+Na) ratio >0.8 in the case of sample R43. In both samples, most of the grains are highly K-rich (80-100%), however, we occasionally observe significant intra-grain K variation (between 50 to 100%).

The relation between the barycenter in the range 880-925 nm and the K/(K+Na) of sample R47 ratio is plotted in Figure 6.4a. Each data point in Figure 6.4a is an average of two neighboring pixels. Figure 6.4b shows the same plot for sample R43. We observe a positive correlation between the IRCL emission and the K-content (Pearson's correlation coefficient, r = 0.57 for sample R47 and 0.53 for sample R43). The barycenter shifts towards longer wavelengths with increasing K-content. Furthermore, the barycenter is mostly observed at longer wavelengths (>905 nm) for higher K-content (80 to 100% in R47; 75 to 95% in R43). It is also evident that the sample R47 contains relatively less Na-rich pixels compared to the sample R43; the bulk composition of R47 lies between 80-100% K-feldspar.

These data suggest that the IRCL emission peak at 955 nm is more prominent in the K-feldspar end member regions. On the other hand, the emission at 880 nm is emitted from the moderately K-doped or Na-rich regions (Figures 6.4a and b). The interpretation that the longer IRCL band (∼955 nm) band is emitted preferentially from K feldspar end members is confirmed by our other K-rich samples (see Figures SI 6.1 and SI 6.2 for samples R50 and K13, respectively). Elemental maps of these samples are dominated by a K-ratio >0.8 (more than 95% of the data) and the corresponding barycenters are in the range 910-926 nm. Thomson et al. (2018) and Sellwood et al. (2018) also observed that the IRPL (∼955 nm emission) originates preferentially from K-feldspar grains; note that these studies did not detect the 880 nm emission. In the same article by Thomsen et al. (2018), the IRSL signals (above room

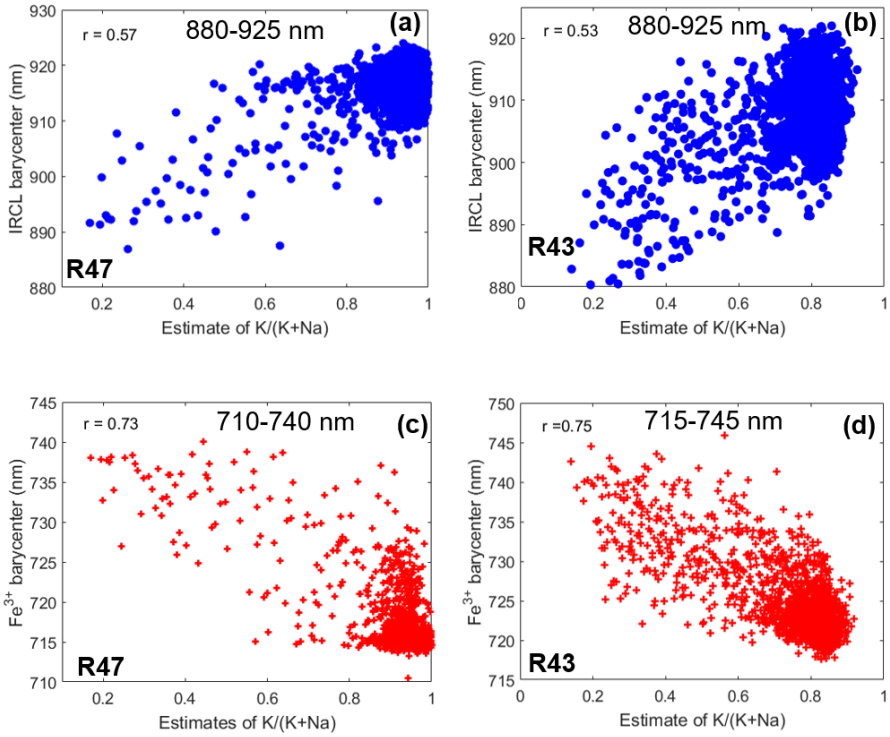

Figure 6.4: Correlation between the IRCL emission barycenter and relative K concentration in (a) sample R47, (b) sample R43. Correlation between the Fe^{3+} emission barycenter and relative K concentration in (c) sample R47, (d) sample R43. Each data point is obtained by the binning of two nearby pixels. 'r' represents Pearson's correlation coefficient.

temperature) were observed to emit from both Na- and K-rich regions in the spatially resolved luminescence images. Thus, one may conclude that both 880 nm and 955 nm centers contribute to the IRSL (OSL) signal.

The spatial variations in the relative intensities of the two IRCL emissions and their link to K- and Na-content suggest that two different sites are responsible for these emissions. If both the emissions arose from the same site, then one should not see a change in the ratio of the two peaks, irrespective of the spatial location. This conclusion is supported by our other investigations on site-selective PL excitation spectroscopy (see Chapter 5 in this thesis).

In addition to the IRCL emission bands, the CL spectrum shows a broad peak centered at ∼720 nm (Figure 6.1a). This emission band has been suggested to originate from the iron (Fe^{3+}) impurities in feldspar when it substitutes for Al^{3+} in the tetrahedral sites T_1 and/or T_2 (Telfer and Walker, 1975; Poolton et al., 2006; Prasad and Jain, 2018). The Fe^{3+} emission peak shifts towards shorter wavelengths (for e.g. 720 nm to 680 nm) when the composition varies from Na-rich to K-rich feldspar (Dütsch and Krbetscheck, 1997; Brooks et al., 2002; Visocekas et al., 2014). As reported in the literature, the origin of this shift is suggested to be the change in the Fe-O bond length due to potassium ions in K-rich feldspar and crystal field effect, which modify the energy levels (Brookes et al., 2002; Prasad, 2017). We created a barycenter map for the Fe^{3+} emission using equation 6.1 on CL data in the spectral range of 630-800 nm. The shift in Fe^{3+} emission is confirmed in our data, both in the local spectra (Figure 6.5a and b for samples R47 and R43, respectively) as well as in the correlation plot of barycenter (710 nm to 745 nm) versus the relative K-content (Figure 6.4c and d for samples R47 and R43, respectively).

6.7 Correlation between Fe^{3+} emission and IRCL

We observe that as the Fe^{3+} barycenter shifts towards shorter wavelengths due to change in composition from Na-rich to K-rich feldspar, while the barycenter in the NIR region shifts towards longer wavelengths (Figure 6.4). These wavelength shifts in the Fe^{3+} and IRCL emissions appear to mirror each other. For sample R47, a barycenter shift for Fe^{3+} emission is observed from 740 nm to 710 nm and a barycenter shift for IRCL emission is observed from 885 nm to 925 nm when the K-content varies from 20 to 100% (Figure 6.4a and c). For sample R43, the barycen-

ter shift for Fe^{3+} emission is observed from 745 nm to 715 nm and the barycenter shift for IRCL emission is observed from 880 nm to 925 nm when the K-content varies from 20 to 90% (Figure 6.4b and d).

The relationship between the peak shift of Fe^{3+} and IRCL emissions is confirmed by the local CL spectra. Figure 6.5a and b show the normalized spectra from regions with different K concentration (K ratio) for samples R47 and R43, respectively. Figure 6.5a shows local spectra of the regions with K-contents 30%, 90%, 96%, and 98%, for sample R47. Figure 6.5b shows local spectra of the regions with K-contents 30%, 75%, 80%, and 88%, for sample R43. A ∼70% change (30% to 98%) in K-content results in about ∼45 nm blueshift of the Fe^{3+} peak (∼745 nm to ∼690 nm) and a ∼70 nm redshift of the IRCL peak (∼890 nm to ∼960 nm) in the case of sample R47. On the other hand, a change of ∼60% (30% to 88%) in K-content results in a ∼40 nm blueshift of the Fe^{3+} peak (∼740 nm to ∼700 nm) and a ∼70 nm redshift of the IRCL peak (∼885 nm to ∼955 nm) in the case of sample R43. There is a systematic shift of both the IRCL and the Fe^{3+} peaks with K-content in sample R43 (Figure 6.5b). There seems to be a tendency that the relative intensity of the IRCL emission decreases (compared to the Fe^{3+} peak) as the Fe^{3+} emission moves to longer wavelengths with a decrease in the K-content. At the same time, there is a peak shift to shorter wavelengths in the IRCL emission. Thus the two peaks tend to come closer, with a simultaneous decrease in the relative IRCL intensity with a decrease in the K-content. A compilation of data from all the local spectra within a sample (Figures 6.4 and 6.5) confirms this picture. There exists a negative correlation between barycenters for the IRCL band and for the Fe^{3+} emission; this negative correlation is linked to the K- and Na- content in the measured regions.

We investigate here if this apparent correlation between Fe^{3+} and IRCL emissions is just a coincidence or if there exists a common physical mechanism that creates this relationship. To further investigate the relationship between Fe^{3+} and IRCL emissions, we chose a different sample (K7) with approximately equal K and Na contents. The measurements were carried out in the same manner as discussed for the other samples in the previous sections, however, the size of each pixel in the map is 9.1 µm for this sample K7. The data are presented in Figure 6.6. Figure 6.6a shows the backscattered electron image (BSE). Figure 6.6b shows the barycenter map in the spectral range 755-812 nm; no values were ob-

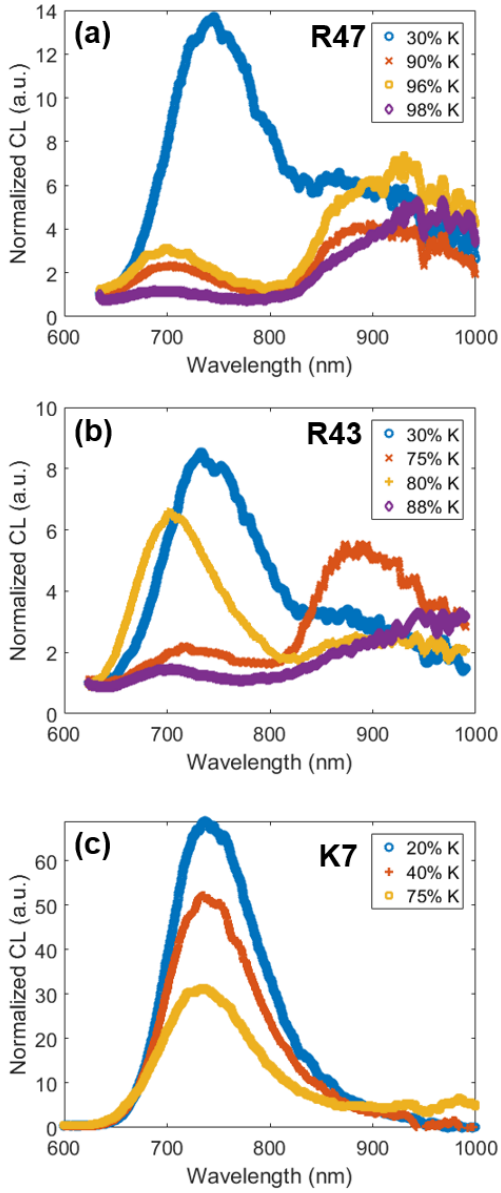

Figure 6.5: Local CL spectra of samples (a) R47 (b) R43, and (c) K7, obtained from low (20-30%), moderate and high K-rich regions (40%-98%).

tained above 810 nm because of undetectable emission in the NIR region. Figure 6.6c shows the elemental map (K/(K+Na)) from EDX. Local CL emission spectra (800-1000 nm) from low (I ≈0.3 I_{max}) and high intensity (I ≈0.9 I_{max}) regions are shown in Figure 6.6d, while spectra in a complete range (600-1000 nm) are shown in Figure 6.5c.

We see that, in K7, the K-content is generally less than 75% (Figure 6.6c). Here the Fe^{3+} peak does not shift significantly with a change in K-content; it shifts only from about 735 nm to 730 nm for a change of 20% to 75% K-content in different pixels. This behavior is reflected in a fairly uniform barycenter across the sample (Figure 6.6b). This relatively flat response in the 20–75% K regions is consistent with the earlier CL studies (Krbetscheck et al., 2002). Interestingly, the IRCL emission bands are generally absent in this sample (Figure 6.6d). If we compare the K-concentrations, then we should have expected to see the IRCL bands in K7, since medium to low-K regions showed IRCL in R47 and R43. If we compare the absolute concentration of Fe, K7 has about two times the concentration compared to R47 and four times that of R43. It is plausible that a relatively high concentration of Fe^{3+} quenches the IRCL emission when it exists in a moderately K-rich (20-75%) feldspar lattice. In a K-rich lattice such as in sample R50 (K>80%), we observe that IRCL is not quenched (Figure SI 6.1) even though this sample has a similar absolute concentration of Fe as K7 (Table 6.1).

We propose here that the wavelength shifts of IRCL predominantly occur if a Fe defect exists in the vicinity of the principal trap in a K-deficient lattice. This leads to a competition in electron capture (e.g. $Fe^{4+} + e^- \rightarrow Fe^{3+}$; see Jain et al., 2015) between the Fe and the principal trap, resulting in an apparent quenching of the IRCL emission. Since the defect responsible for IRCL is unknown, it is difficult to understand the reason for the shift in the IRCL peak wavelength, and why this shift is in the opposite direction as the Fe^{3+} emission peak. It is conceivable that the change in the electrostatic field because of the presence of Fe results in a shift of the IRCL to shorter wavelengths. Further investigations are necessary to test this cluster model proposed here.

6.8 Summary and discussion

A combined study of spatially and spectrally resolved cathodoluminescence data in the spectral range 800-1000 nm suggests that the relative

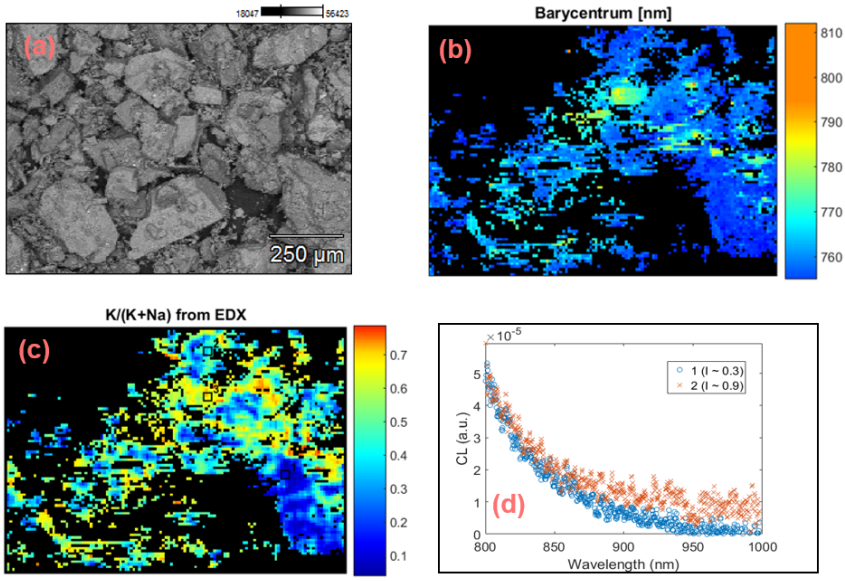

Figure 6.6: CL and elemental data of sample K7. (a) BSE image, (b) barycenter map in the range 755-810 nm, (c) relative concentration map of the K-content (K/K+Na), and (d) local CL spectra of two regions at the intensities, I ≈0.9 I_{max} and ≈0.3 I_{max} on the intensity map (not shown).

intensity of the two NIR emission bands reported by Kumar et al. (2018; Chapter 3 in this thesis) vary spatially within a sample and even within a grain. We see a clear correlation between the relative intensities of the IRCL emission at 880 nm and the emission at 955 nm with the K-content in our investigated samples. The IRCL emission at 955 nm appears from the samples with high K-concentration. On the other hand, the emission at 880 nm is emitted from the moderately K- or Na-rich samples. This relationship suggests that the principal trap giving rise to the NIR emissions (PL and CL) occurs at two different sites or in two different environments within K- or Na- rich regions. This suggests that OSL or IRSL is a mixture of signals from principal traps in two different sites; thus, parameters like athermal and thermal stability of the OSL or IRSL are influenced by 'mixed' kinetics of these individual sites.

The presence of two sites of the principal traps has implications for further development of luminescence geochronology. Firstly, it has the potential to give information on the defect locations that give rise to OSL/IRSL at the sub-single grain level; this is otherwise not possible by directly measuring the OSL because of its poor efficiency. Secondly, this opens up the potential to develop site-specific dating techniques. Since radioluminescence is a highly sensitive process, we should be able to detect light from very small volumes of the order of 1-10^3 µm^3; this is less than 10^3-10^6 of the total volume of a 100 µm diameter feldspar grain.

We also observe the well-known peak shift of the Fe^{3+} emission with the K-content. However, the Fe^{3+} shows a redshift whereas the IRCL shows a blueshift in the barycenter with a decrease in the K-content. We propose that Fe^{4+} ions act as a quencher by competing with the principal trap for free electrons. This interpretation suggests that the principal trap and Fe^{3+} occur within a defect cluster and the local crystal field altered by the presence of Fe^{4+} results in preferential blueshifted IRCL emission. This model needs to be tested on well-characterized (structurally and mineralogically) single crystal samples.

For IRRL or infrared radiofluorescence (IRRF) dating (Erfurt & Krbetschek, 2003) our data imply that the bulk signal is coming from different sites, with different K and Fe contents. Interference from Fe^{3+} is expected to be more important for the emission band at 880 nm than the emission at 955 nm. Therefore, both these bands may show different stability and apparent sensitivity change. Our measurements directly

demonstrate the potential of spatially resolved IRRL dating at the sub-grain level, using, for example, a beta source, and a CCD detector with appropriate detection filters for the two IRCL bands. Equally it may be worthwhile to perform a quality control on the single grain measurements by a subsequent compositional analysis such as by µ-XRF; it will be worthwhile to explore how the dose estimates change by selectively including more and more K-rich grains in the analysis (to reduce the signal contamination from Fe^{3+} as the IRCL and the Fe^{3+} peaks are most separated at the highest K-concentration).

This study raises the exciting possibility for mapping metastable states in feldspar using optical site-selective techniques such as IRPL and study charge transfer dynamics on spatial scales. The advantage of the PL mapping techniques is that one can avoid contamination from Fe^{3+}. On the other hand, one will be restricted by the diffraction limit. Nonetheless, a significant advance is possible using confocal microscopes and techniques such as Stimulated Emission Depletion (STED) microscopy (Vicidomini et al., 2018).

6.9 Conclusions and outlook

For the first time the spatial distribution of the metastable states (principal trap) in feldspar at a micron-scale (6-22 µm) was studied. We demonstrated that the two NIR cathodoluminescence emission bands (∼880 nm and ∼955 nm) vary spatially, even within a single-grain of feldspar. We suggested that these emissions arise from two different sites of the principal trap in the feldspar lattice.

We observed a correlation between K-content and the peak positions of the IRCL (principal trap) and Fe^{3+} emissions. We proposed a defect cluster model in which Fe competes with the principal trap to capture free electrons, and hence is responsible for IRCL quenching.

In terms of defect mapping of feldspar, a better spatial resolution in the future may be achieved by reducing the grid size and/or energy of the incident electrons (thereby electron range). Similarly, IRPL microscopy, based on laser scanning, may be explored; this has the potential to yield a spatial resolution of ∼0.5 µm. Further resolution is obtainable using a new technique such as Stimulated Emission Depletion (STED) microscopy which will be ideal to pursue this research further. Measurement of trapping of charge at such a high-resolution has implications for

microdosimetry and for developing next-generation luminescence dating techniques based on the sub-single-grain level.

Acknowledgments

We thank Prof. D.J. Huntley, Simon Fraser University, Canada, for samples K7 and K13.

Supplementary Material

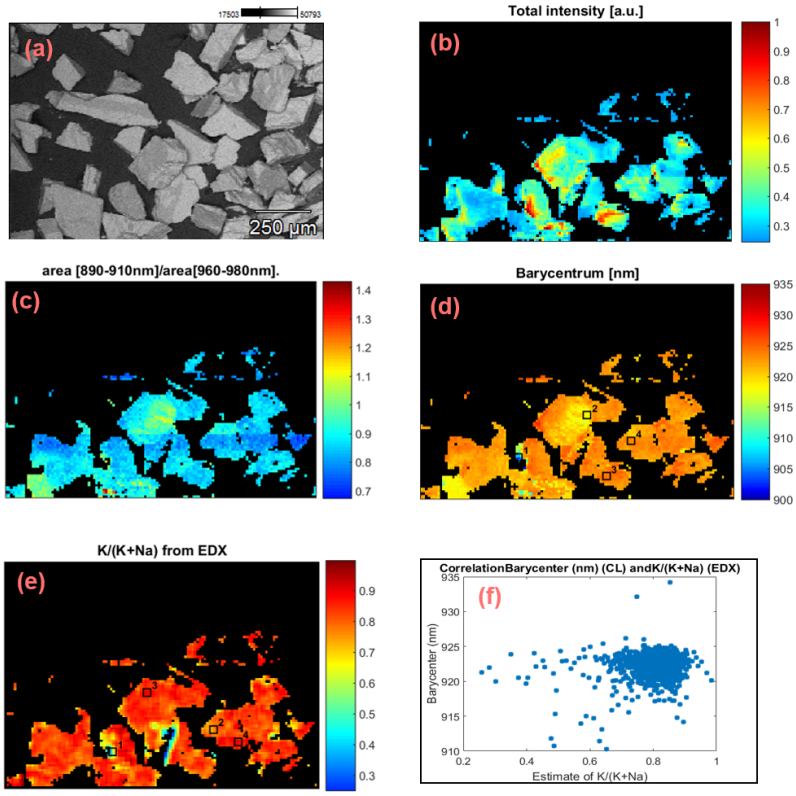

Figure SI 6.1: CL and elemental data of sample R50. (a) BSE image, (b) cathodoluminescence intensity map; intensity below a value 0.235 I_{max} has been filtered out using a mask, (c) intensity ratio map between the two NIR bands, 890-910 nm, and 960-980 nm. (d) barycenter map in the range 910-935 nm, (e) relative concentration map of the K content (K/K+Na), and (f) correlation between the IRCL emission barycenter and relative K concentration.

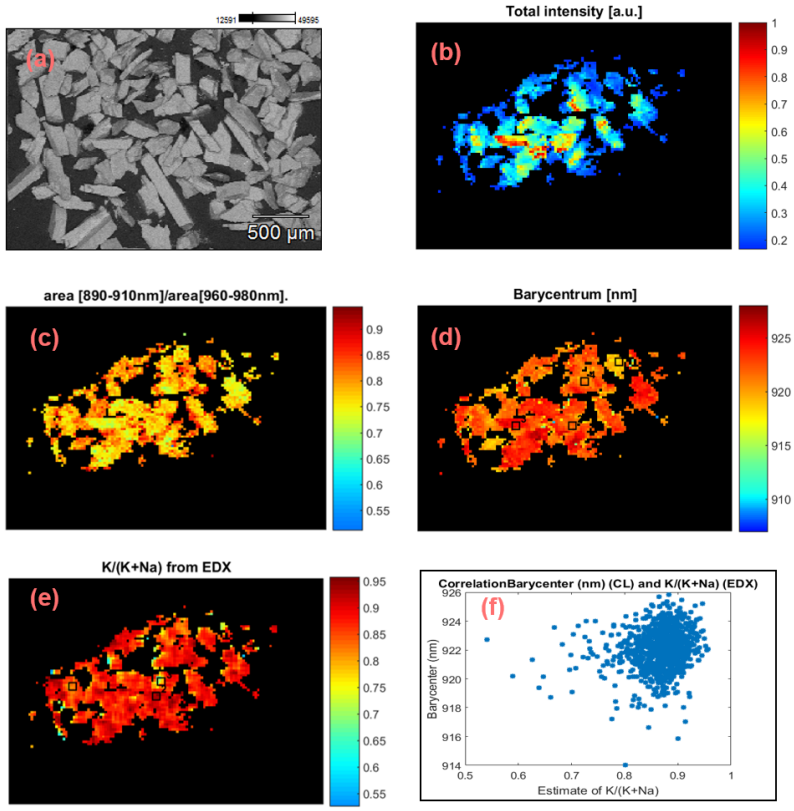

Figure SI 6.2: CL and elemental data of sample K13. (a) BSE image, (b) cathodoluminescence intensity map; intensity below a value 0.235 I_{max} has been filtered out using a mask, (c) intensity ratio map between the two NIR bands, 890-910 nm, and 960-980 nm. (d) barycenter map in the range 910-935 nm, (e) relative concentration map of the K content (K/K+Na), and (f) correlation between the IRCL emission barycenter and relative K concentration.

References

Baele, JM, Decrée, S., & Rusk, B. (2019). Section II New Methods for Mineral Exploration. John Wiley & Sons, Inc.

Brooks, R. J., Finch, A. A., Hole, D. E., Townsend, P. D., & Wu, Z. L. (2002). The red to near-infrared luminescence in alkali feldspar. Contributions to Mineralogy and Petrology, 143(4), 484-494.

Brokus, S. A., Silletti, D. K., Lunderberg, J. M., DeYoung, P. A., Peaslee, G. F., Carpenter, D. E., & Buscaglia, J. (2015). Cathodoluminescence dependence on feldspar mineral structure and implications for forensic geology. American Mineralogist, 100(2-3), 451-458.

Dütsch, C., & Krbetschek, M. R. (1997). New methods for a better internal 40K dose rate determination. Radiation Measurements, 27(2), 377-381.

Erfurt, G. (2003). Infrared luminescence of Pb+ centres in potassium-rich feldspars. Physica Status Solidi (A) Applied Research, 200(2), 429–438.

Erfurt, G., & Krbetschek, M. R. (2003). IRSAR–A single-aliquot regenerative dose dating protocol applied to the infrared radiofluorescence (IR-RF) of coarse-grain K feldspar. Ancient TL, 21(1), 35–42.

Flude, S., Sherlock, S. C., Lee, M. R., & Kelley, S. P. (2013). Disturbance to the 40Ar/39Ar system in feldspars by electron and ion beam irradiation. Chemical Geology, 355, 1-12.

Geake, J.E., Walker, G., Telfer, D.J., Mills, A.A., & Garlick, G. F. J. (1973). Luminescence of lunar, terrestrial, and synthesized plagioclase, caused by Mn2+ and Fe3+. Proc. Fourth Lunar Sci. Conf. Geochim. Cosmochim. Acta 3 (Suppl. 4), 3181–3189.

Goetze, J., Habermann, D., Kempe, U., Neuser, R. D., & Richter, D. K. (1999). Cathodoluminescence microscopy and spectroscopy of plagioclases from lunar soil. American Mineralogist, 84(7-8), 1027-1032.

Götze, J., Habermann, D., Neuser, R.D., and Richter, D.K. (1999a) High-

resolution spectrometric analysis of REE-activated cathodoluminescence (CL) in feldspar minerals. Chemical Geology, 153, 81–91

Götze, J., Krbetschek, M.R., Habermann, D., Wolf D. (1999b) High-resolution cathodoluminescence studies of feldspar minerals. In M. Pagel, V. Barbin, Ph. Blanc, and D. Ohnenstetter, Eds., Cathodoluminescence in geosciences, in press. Springer Verlag, Berlin.

Götze, J. (2012). Application of cathodoluminescence microscopy and spectroscopy in geosciences. Microscopy and Microanalysis, 18(6), 1270–1284.

Huntley, D. J., Godfrey-Smith, D. I., & Thewalt, M. L. (1985). Optical dating of sediments. Nature, 313(5998), 105-107.

Hütt, G., Jaek, I., & Tchonka, J. (1988). Optical dating: K-feldspars optical response stimulation spectra. Quaternary Science Reviews, 7(3-4), 381-385.

Jain, M., Sohbati, R., Guralnik, B., Murray, A. S., Kook, M., Lapp, T., & Buylaert, J. P. (2015). Kinetics of infrared stimulated luminescence from feldspars. Radiation Measurements 81, 242-250.

Krbetschek, M. R., Götze, J., Dietrich, A., & Trautmann, T. (1997). Spectral information from minerals relevant for luminescence dating. Radiation Measurements, 27(5-6), 695-748.

Krbetschek, M. R., Trautmann, T., Dietrich, A., & Stolz, W. (2000). Radioluminescence dating of sediments: methodological aspects. Radiation Measurements, 32(5-6), 493-498.

Krbetschek, M. R., Götze, J., Irmer, G., Rieser, U., & Trautmann, T. (2002). The red luminescence emission of feldspar and its wavelength dependence on K, Na, Ca–composition. Mineralogy and Petrology, 76(3-4), 167-177.

Kumar, R., Kook, M., Murray, A. S., & Jain, M. (2018). Towards direct measurement of electrons in metastable states in K-feldspar: Do infrared-photoluminescence and radioluminescence probe the same trap?

Radiation Measurements, 120(December 2017), 7–13.

Marshall, D. J., & Mariano, A. N. (1988). Cathodoluminescence of geological materials. Taylor & Francis.

Malins, A. E. R., Poolton, N. R. J., Quinn, F. M., Johnseir, O., & Denby, P. M. (2004). Luminescence excitation characteristics of Ca, Na and K-aluminosilicates (feldspars) in the stimulation range 5-40 eV: Determination of the band-gap energies. Journal of Physics D: Applied Physics, 37(10), 1439–1450.

Martin, L. I. D. J., Poelman, D., Smet, P. F., & Joos, J. J. (2018). Microscopic study of dopant distribution in europium doped SrGa2S4: Impact on thermal quenching and phosphor performance. ECS Journal of Solid State Science and Technology, 7(1), R3052-E3056.

Pagel, M., Barbin, V., Blanc, P., & Ohnenstetter, D. (2000). Cathodoluminescence in geosciences: an introduction. In Cathodoluminescence in Geosciences (pp. 1-21). Springer, Berlin, Heidelberg.

Poolton, N. R. J., Mauz, B., Lang, A., Jain, M., & Malins, A. E. R. (2006). Optical excitation processes in the near band-edge region of KAlSi3O8 and NaAlSi3O8 feldspar. Radiation measurements, 41(5), 542-548.

Prasad, A. K., Poolton, N. R. J., Kook, M., & Jain, M. (2017). Optical dating in a new light: A direct, non-destructive probe of trapped electrons. Scientific Reports, 7(1), 1–15.

Prasad, A. K., & Jain, M. (2018). Dynamics of the deep red Fe3+ photoluminescence emission in feldspar. Journal of Luminescence, 196, 462-469.

Rendell, H. M., & Clarke, M. L. (1997). Thermoluminescence, radioluminescence and cathodoluminescence spectra of alkali feldspars. Radiation Measurements, 27(2), 263–272.

Sellwood, E.L., Guralnik, B., Kook, M., Prasad, A.K., Sohbati, R.,

Hippe, K., Wallinga, J. & Jain, M. (2019). optical bleaching front in bedrock revealed by spatially-resolved infrared photoluminescence. Scientific reports, 9(1), pp.1-12.

Short, M. A. (2003). An investigation into the physics of the infrared excited luminescence of irradiated feldspars (PhD thesis, Simon Fraser University, Canada).

Sippel, R. F., & Spencer, A. B. (1970). Cathodoluminescence properties of lunar rocks. Science, 167(3918), 677-679.

Telfer, D. J., & Walker, G. (1975). Optical detection of Fe3+ in lunar plagioclase. Nature, 258(5537), 694-695.

Trautmann, T., Krbetschek, M. R., Dietrich, A., & Stolz, W. (1998). Investigations of feldspar radioluminescence: Potential for a new dating technique. Radiation Measurements, 29(3–4), 421–425.

Trautmann, T., Krbetschek, M. R., Dietrich, A., & Stolz, W. (2000). Basic principle of radioluminescence dating and a localized transition model. Radiation Measurements, 32(5), 487–492.

Thomsen, K. J., Kook, M., Murray, A. S., & Jain, M. (2018). Resolving luminescence in spatial and compositional domains. Radiation Measurements, 120, 260-266.

Vicidomini, G., Bianchini, P., & Diaspro, A. (2018). STED super-resolved microscopy. Nature methods, 15(3), 173.

Visocekas, R., Barthou, C., & Blanc, P. (2014). Thermal quenching of far-red Fe3+ thermoluminescence of volcanic K-feldspars. Radiation Measurements, 61, 52–73.

Walker, G. (1985). Mineralogical applications of luminescence techniques. In F.J.Berry and D.J. Vaughan, Eds., Chemical bonding and spectroscopy in mineral chemistry, p. 103–140. Chapman and Hall, London.

Wintle, A. G. (2008). Luminescence dating: Where it has been and where it is going. Boreas, 37(4), 471–482.

Yacobi, B. G., & Holt, D. B. (1986). Cathodoluminescence scanning electron microscopy of semiconductors. Journal of Applied Physics, 59(4), R1-R24.

CHAPTER 7

A COUPLED PL-OSL SYSTEM TO PROBE DYNAMICS OF THE METASTABLE STATES

Mayank Jain, Raju Kumar & Myungho Kook

Abstract: Metastable states form by charge (electron and hole) capture in defects in a solid. These play an important role in dosimetry, information storage, and many medical and industrial applications of photonics. Despite many decades of research, charge transfer across metastable states and its role in luminescence production is poorly understood. This is mainly because the measurement of luminescence from metastable states involves several processes such as detrapping, transport, competition, and electron-hole (henceforth e-h) recombination.

Here we present a novel, coupled OSL-PL (optically stimulated luminescence–photoluminescence) system in a natural alumina-silicate feldspar which comprises >50% of the Earth's crust, to understand the dynamics of the metastable states. Infrared PL (IRPL) in feldspar is capable of directly probing the trapped electrons. Whereas, OSL measures e-h recombination. Combining these two pieces of information, we develop here new analytical methods, and based on these elucidate for the first time the thermal dependence, diffusion, thermo-optical bleaching, and radiation-induced growth of electron and holes in feldspar. These results support a strong presence of localized recombination mechanisms

in feldspar. These new methods and insights provide unique information for developing robust mathematical models that are crucial to the next generation applications of luminescence dosimetry in Earth and environmental sciences. We expect that this work will inspire a search of similar coupled OSL-PL systems in other solid-state dosimeters and enrich our understanding of luminescence phenomena involving the metastable states.

7.1 Introduction

Metastable states in solids play an important role in dosimetry (Bøtter-Jensen et al., 2003) and have exciting potential applications in bio-imaging, radiobiology and information storage (Chakrabarti et al., 1989; Meijerink et al., 1991). These metastable states are created by the capture of free charge (electrons and holes) in a solid by exposure to ionizing radiation, followed by charge capture within distinct defects or defect clusters. This process is commonly referred to as trapping. The thermal lifetime of a metastable state (i.e. trapped electron or hole) may range from microseconds to millions of years depending on the depth of the potential wells formed by electron or hole capture and the ambient temperature. Eventual detrapping by photon/phonon interactions with the traps may lead to radiative recombination of the opposite charge carriers. The resultant luminescence, for example, can be used to estimate prior absorbed dose ($\mathrm{J\,kg^{-1}}$) from ionizing radiation (dosimetry), measure the burial age of sediment or rock (geochronology), map location of the emitting particles (imaging), etc. Depending on whether light or heat is used for detrapping (readout), the process is called optically stimulated luminescence (OSL), thermoluminescence (TL) or prompt phosphorescence, if it results in luminescence emission. Similarly, prompt e-h recombination at a luminescence center, during exposure to ionizing radiation can be measured as radio-luminescence (RL) (Trautmann et al., 1999; Erfurt et al., 2000).

Different metastable states are used in different applications. In SiO_2, for example, trapped electrons at about 2.8 eV below the conduction band edge are commonly used in OSL dating applications (Huntley et al., 1996). In persistent phosphors, on the other hand, traps with intermediate depths ($\sim$0.7 eV) are required to obtain detrapping at room temperature (Van den et al., 2013).

Despite many decades of research aimed at understanding luminescence generation from the metastable states, there remain significant gaps in our knowledge. There exist a plenitude of phenomenological and mathematical models to describe the same signal, even within the same material. Largely, this ambiguity arises from the fact that measurement of luminescence signal (OSL or TL) typically involves a convolution of three processes: charge release (detrapping), charge transport (localized or delocalized), and e-h recombination. Therefore, it becomes challenging to ascribe luminescence kinetics to any particular process; often there are multiple solutions impeeding an exact understanding of the physical process. This challenge can be overcome if one were able to observe independently the dynamics of the trapped electron (or hole) population and thus by comparison with OSL or TL decouple these different processes.

Independent measurement of trapped electrons can be made through electron paramagnetic resonance (EPR), but this technique applies only to unpaired electrons, and it is often ambiguous to relate ESR signals to the traps that participate in OSL or TL. One can also probe metastable states by optically induced intra-defect transitions (excitation $\rightarrow$ radiative relaxation) using radio-photoluminescence (RPL); the prefix radio is used to indicate that the probed states are created by ionizing radiation, to distinguish it from the ordinary photoluminescence (PL). Until recently, the RPL method has only been available in hole-trapping states, in materials such as Mg or Ag doped glasses, and C, Mg doped Al_2O_3. In these materials, there is no direct link between OSL and RPL making the technique inappropriate for providing a holistic picture of detrapping and charge transport.

For investigating the physics of charge transport across the metastable states, it is desirable to be able to observe RPL from trapped electrons using their excited state below the conduction band edge, and then detrap the same electrons by higher energy excitation to produce OSL. Such a coupled OSL-RPL system can offer a better understanding of the OSL kinetics, by providing an opportunity to directly examine the changes in trapped electron population (through RPL). Furthermore, in terms of applications, such a physical system can be measured non-destructively by resonant excitation PL, providing a high sensitivity dosimetry system, and can be easily reset with light (similar to OSL and unlike the hole based RPL systems). Thus, a combined OSL-RPL system based on the excitation of trapped electrons offers great advantages both for improving

our understanding as well as for practical applications. One example of such a system is the Sm^{2+} defect in YPO_4: Sm, Ce. This shows both RPL and OSL behavior (Dorenbos et al., 2003, 2011; Poolton et al., 2010, 2012; Prasad et al., 2017a). Prasad et al. (2017) used this system to obtain insights into excited state tunneling induced recombination ($Sm^{2+} \rightarrow Ce^{4+}$) in YPO_4. The PL from Sm^{2+}, unfortunately, quenches at around 180 K, severely restricting the physical investigations and applications.

More recently our group has shown the RPL mechanism in the electron trap in feldspar (Prasad et al., 2017 and Chapter 3 in this thesis), an aluminosilicate that comprises >50% of the Earth's crust. Metastable states in feldspar are widely used in luminescence dating and retrospective dosimetry (Huntley et al., 1985; Hütt et al., 1988; Thomsen et al., 2008; Buylaert et al., 2012). The RPL signal in feldspar, termed as infrared photoluminescence (IRPL), derives from radiative relaxation of the excited state of the main dosimetric trap (principal trap) with a lifetime of about 30 µs at room temperature (Prasad et al., 2017). Based on low temperature spectroscopic measurements, Prasad et al. (2017) concluded that both the IRPL and the OSL obtained using near-infrared (NIR) excitation (i.e. infrared stimulated luminescence, IRSL) arise from the principal trap. A simplified IRPL-IRSL mechanism in feldspar is shown in Figures 7.1; here electron detrapping followed by e-h recombination via the band-tail states leads to IRSL (7.1a) (Poolton et al., 2002, 2009; Jain and Ankjærgaard, 2011), whereas, electron retraping/relaxation leads to IRPL (7.1a and b). The excitation spectrum and the Stokes shifted IRPL emission spectrum are shown in Figure 7.1c. Each defect emits IRPL at the rate of thousands of photons per second (depending on the excitation rate). This provides an unprecedented sensitivity for 2D and 3D mapping (Sellwood et al., 2019) of defect distribution and examining charge transfer.

IRPL has the potential for providing a direct assessment of thermal and optical stabilities, as well as the behavior of trapped electrons during different laboratory protocols. In this study we explore the potential of the coupled OSL-IRPL from the principal trap, to obtain a better understanding of charge transfer and recombination processes. While the results here apply specifically to feldspar like systems (with both localized and delocalized charge transport), they give general insights into the behaviour of metastable states under an external stimulus.

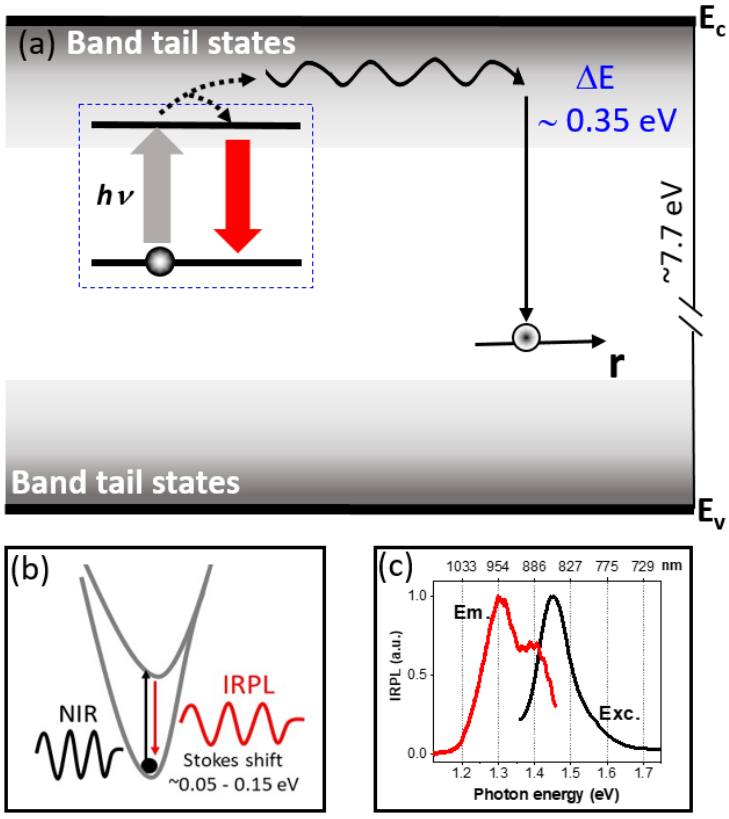

Figure 7.1: (a) Band diagram showing the OSL (infrared excitation) and the IRPL process from the principal trap. (b) Configurational coordinate diagram showing PL generation in the defect responsible for the principal trap. The corresponding excitation and Stokes-shifted emission spectra are shown in (c).

7.2 Materials and methods

Samples used in this study consist of K-feldspar (7) and Na-Feldspar (1) extracts from sediment samples (see Table 7.1). These samples, 072255(K), 981009(K), 981010(K), 981013(K), 092202(K), 092204(N) and H22553(K) have been reported in Buylaert et al. (2012). Note that we have added (K) or (N) to indicate the composition, potassium or sodium, respectively. We have deliberately chosen sediment samples, because in our experience these samples generally consist of mature minerals that have survived the physical and chemical weathering process, and because the results of our investigations here are relevant for sediment dating. X-ray fluorescence (XRF) measurements show that our samples are K or Na rich feldspar samples.

All measurements were performed using the photomultiplier (PMT) based IRPL attachment to the Risø TL/OSL reader. This attachment consists of an external laser light source at 1.49 eV (830 nm). We measure both the dose-dependent Stokes-shifted emissions in feldspar at 880 and 955 nm in all the measurements (Kumar et al., 2018; Chapter 3 in this thesis). Two different photomultiplier tubes in combination with the emission bandpass interference filters transmitting 880/10 nm or 950/50 nm were used for detecting the IRPL emissions at 1.41 eV (880 nm) and 1.30 eV (955 nm), respectively (see Chapter 4). The power density of the laser at the sample position was measured to be $\sim$3 mW cm^{-2}. The IRPL signals were measured in pulsed excitation mode (laser on-time 50 µs, and off-time 50 µs; detection during off-time 51-100 µs). Throughout the text, the IRPL (955 nm) and IRPL (880nm) emissions are denoted as IRPL_{955} and IRPL_{880}, respectively. Kumar et al. (2018; Chapter 3 in this thesis) demonstrated that these signals do not represent the two excited states of the same defect site. Here, the respective (unknown) principal traps that give rise to these signals are referred to as the 880 or 955 nm (emission) centers/traps. Room temperature refers to the controlled laboratory temperature of 25 °C.

The OSL signals obtained using a NIR excitation (i.e. 850 nm), known as infrared stimulated luminescence (IRSL) were detected using the same PMT as the IRPL_{880} but using BG39 and BG3 filters. IR light-emitting diodes (LEDs; power density $\sim$250 mW cm^{-2} at the sample position) were used as the excitation light source. The switch over between different filters and detectors was achieved using the automated detection and stimulation head (DASH) (Lapp et al., 2015).

Table 7.1: Feldspar samples investigated in this study. These samples are extracted from sediments from different geographical regions. (K) denotes K-feldspar and (N) denotes Na-feldspar.

Sample code (K- or Na- Feldspar)	Site and Location	Grain size (μm)	Known D_e (Gy)	Reference
981009 (K)	Gammelmark (Denmark)	150-250	279±11	Murray and Funder (2003); Buylaert et al. (2012)
981010 (K)		150-250	298±12	
981013 (K)		90-250	274±12	
H22553 (K)	Sula (Russia)	180-250	209±11	Murray et al. (2007); Buylaert et al. (2012)
072255 (K)	Carregueira (Portugal)	180-250	97±7	Buylaert et al. (2012)
092202 (K)	Indre-et-Loire (France)	180-250	158±10	Aubry et al. (2012); Buylaert et al. (2012)
092204 (Na)	Sinai peninsula (Egypt)	180-250	97±3	Buylaert et al. (2012)

Both IRPL and IRSL data were analyzed using the Matlab and Microsoft Excel software. OriginPro 2018b is used for model fitting and for plotting the figures.

7.3 Current understanding of stimulated luminescence generation in feldspar

Infrared stimulated luminescence (IRSL) is widely used in luminescence dating (Balescu and Lamothe, 1994; Buylaert et al., 2009; Li and Li, 2011; Thiel et al., 2011; Tsukamoto et al., 2017). This method, however, suffers from an athermal loss of signal (anomalous fading), a problem that has been addressed in the last decade using preferential sampling of a more stable signal. Discrimination between more and less stable signals can, for example, be achieved using a sequential measurement of IRSL at increasing sample temperatures; it is observed that the subsequent elevated temperature IRSL is more stable than the preceding low temperature measurement (Thomsen et al., 2008). Buylaert et al. (2012) tested an approach using post-IR_{50} $IRSL_{290}$ ($pIR_{50}IRSL_{290}$, subscripts refer to IR stimulation temperature at °C; Thiel et al., 2011) using known age samples, to determine if it is possible to eliminate the fading component. These authors found that $pIR_{50}IRSL_{290}$ gives an age that is consistent with the expected age, on an average, supporting that such

an approach can be successful in isolating stable trapped electron population. Such data indicate the existence of localized recombination in feldspar (Jain and Ankjærgaard, 2011, Jain et al., 2012, 2015), explained as follows. Around room temperature, the recombination primarily occurs between close e-h neighbors either by excited-state tunneling or by limited diffusion within the band-tail states. Such close neighbors are likely to recombine in nature due to tunneling, and therefore prone to fading (Huntley et al., 2007). There remains however a finite population of distant e-h neighbors that are not accessed by the first IRSL (IR_{50}) measurement since the probability of recombination is much lower than the probability of retrapping or relaxation (i.e., mean diffusion length « the distance to the nearest hole). However, when the temperature is increased in the subsequent IRSL measurement it becomes possible for detrapped electrons to access distant holes and thereby recombine, thus giving rise to the regeneration of IRSL (i.e. pIR_TIRSL_T) signal; since this signal is based on distant pairs it is by definition less prone to athermal fading in nature.

Numerical models of feldspar suggest that intra-defect transition (excitation and relaxation) within the principal trap is the most dominant process during the resonant light excitation (Jain et al., 2012, 2015); however, this transition is overlooked in the typical anti-Stokes measurements performed in OSL. IRPL measures this transition. IRPL shows a dose response similar to that of OSL, but since it does not involve e-h recombination, the signal can be read out non-destructively (especially at cryogenic temperatures). Since IRPL can be measured even from traps remote from recombination centers (Prasad et al., 2017b), it must include a stable, steady-state component (i.e. one that does not suffer from anomalous fading).

While this model successfully explains our experimental observations, we do not have any information on how electrons-hole distances are actually distributed in the crystal. Furthermore, there is no direct proof that only a fraction of trapped electrons are measured during IRSL at a given temperature and the remaining electrons that do not participate in the IRSL are more stable. Within this model framework, the specific questions that we ask of a coupled PL-OSL system are:

1. What fraction of the occupied principal trap participates in the IRSL process?

2. How do trapped electrons and/or trapped holes deplete by thermal vibrations, and which of the two processes (electron or hole depletion) is responsible for the thermal stability of the IRSL signal?

3. What is the nature of the increase of trapped electron and hole concentrations due to exposure to ionizing radiation?

4. Does electron trapping cross-section vary as a function of the e-h distance?

5. How does thermal partitioning of detrapped electrons occur within the band-tail states?

6. How does the probability of finding a recombination center change with thermal diffusion of electrons in the band-tail states?

These aspects are investigated in the following sections.

7.4 Trapped electron population participating in IRSL

Here we try to experimentally determine how different sub-populations in the nearest-neighbor e-h distribution recombine in response to thermal or thermo-optical excitation. We do this by monitoring IRPL (trapped electron population) before and after IRSL (e-h recombination) at different temperatures. The experimental protocol is outlined in Table 7.2. Seven different samples with palaeodose ranging from about 100 to 300 Gy were measured. First three large aliquots of each sample were measured using their 'natural' signals (i.e., signal due to dose received in nature). Subsequently, the protocol in Table 7.2 was repeated on these aliquots, after delivering the same beta dose as the palaeodose to avoid any dose dependence. A high temperature IR bleach (step 7) was carried out at the end of the cycle to reset the signal.

Before we discuss the effect of IRSL on IRPL, it is interesting to examine the change in trapped electron population due to a preheat (step 2) and high temperature cleanout (step 7) for the laboratory dose cycle. For the 955 emission, the residual IRPL after a high temperature IR bleach ($(\text{IRPL}_i - \text{IRPL}_{bkg})$ / IRPL_i) ranged from about 3% to 14% in different samples, with a mean (%) $\pm 1\sigma$ (absolute standard deviation) of 9 ± 4 of the IRPL_i. This residual level is similar to that obtained after

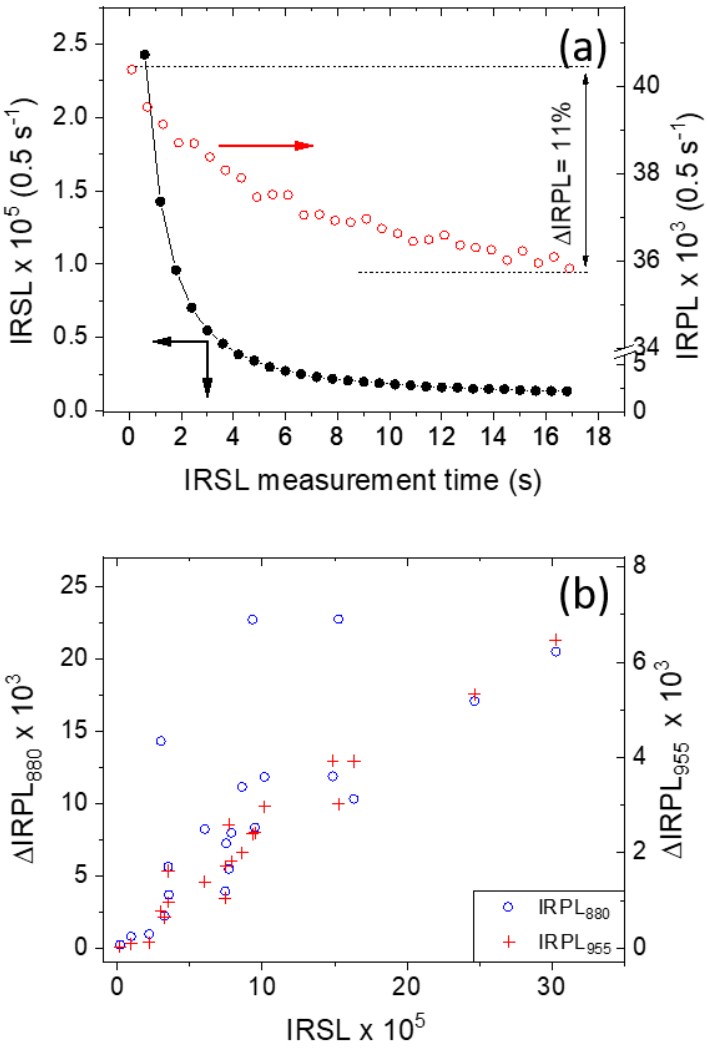

Figure 7.2: (a) An IRSL (bottom and left axis) signal and the corresponding change in the intensity of the IRPL signal (right axis) after different time intervals of the IRSL measurement (bottom axis). The net change in the IRPL at the beginning and the end of the IRSL measurement is used to calculate the ΔIRPL. b) Correlation between $\Delta IRPL_{880}$ (left) or $\Delta IRPL_{955}$ (right) and the IRSL photons emitted during the depletion of the IRPL. Three aliquots were measured from each sample. Individual data points represent one aliquot.

several hours of exposure under solar simulator (data not shown) and therefore considered to represent the difficult-to-bleach trapped electron population. The residual signal was found to be reproducible from cycle to cycle (data not shown). The change in the IRPL signal due to preheat ($IRPL_0 - IRPL_i/IRPL_0$) ranged from -14 to +5% with a mean of -2 ± 8%. This change arises from a combination of a) thermal depletion of the electrons in the principal trap, and b) recuperation due to electron capture in the principal trap during the decay of other shallow states. The minus sign indicates that there is a net increase in IRPL after preheat, i.e., recuperation is more dominant. For the 880 emission, the $IRPL_{bkg}$ ranged from about 4% to 25% in different samples, with a mean of 16±8% of the $IRPL_i$. The change in $IRPL_{880}$ due to preheat (($IRPL_0 - IRPL_i$) / $IRPL_0$) ranged from -20 to +1% with a mean reduction of -7 ± 9%.

Table 7.2: Measurement of depletion in IRPL due to preheat and due to IRSL at different temperatures. 'β' denotes the heating rate. 'p' denotes the holding time (pause) after reaching the desired end-temperature before switching on the light.

Step no	Measurement	Signal
0	Prepare naturally irradiated aliquots	
1a	IRPL (880 nm) for 5 s	$IRPL_0$ *(880)*
1b	IRPL (955 nm) for 5 s	$IRPL_0$ (955)
2	Preheat (200° C) for 60s (β = 5° $C.s^{-1}$)	
3a	IRPL (880 nm) for 5 s	**$IRPL_i$ (880)**
3b	IRPL (955 nm) for 5 s	**$IRPL_i$ (955)**
4	**IRSL at T° C for 95 s (β = 5 °$C.s^{-1}$; p = 5s)**	Bleaching using IR
5a	IRPL (880 nm) for 5 s	**pIR_T IRPL (880)**
5b	IRPL (955 nm) for 5 s	**pIR_T IRPL (955)**
6	Repeat steps 3-5 for T=50, 100, 150, 200, 250	
7	IRSL at 290° C for 95 s (β = 5° $C.s^{-1}$; p = 5s)	Cleanout
8a	IRPL (880 nm) for 5 s	$IRPL_{bkg}$ (880)
8b	IRPL (955 nm) for 5 s	$IRPL_{bkg}$ (955)
9	Laboratory irradiation	
	Repeat steps 1-8	

The comparison of these $IRPL_{880}$ and $IRPL_{955}$ data shows that there

is a greater net capture of electrons in the 880 nm traps during preheat than in the 955 nm traps. Similarly, there is a greater proportion of difficult-to-empty electrons in the 880 nm traps compared to the 955 nm traps.
The depletion in the trapped electron population due to IR stimulation was calculated as follows:

$$\Delta IRPL(T)\% = \frac{IRPL_i - pIR_T IRPL}{IRPL_i - IRPL_{bkg}} \times 100 \quad (7.1)$$

ΔIRPL was measured both for the $IRPL_{880}$ and $IRPL_{955}$ signals. Figure 7.2a shows ΔIRPL graphically for the IRSL measurement at 50 °C for the laboratory irradiated aliquots. The IRSL signal reaches a near-constant level towards the end of the 17 s measurement. This level represents a stage where e-h recombination becomes inefficient at 50 °C due to reduced access to the nearby holes; the dominant mechanism is, therefore, excitation-relaxation (or retrapping) within the principal trap (Figure 7.1a). The difference in the IRPL signals before and after the IRSL (i.e., ΔIRPL) should reflect the population of the principal traps that participated in the IRSL (e-h recombination) process. This reasoning is tested in Figure 7.2b, which plots the relationship between ΔIRPL and net IRSL counts from the 3 aliquots each of all seven samples. We see a positive correlation between the two, however, there is a slightly greater scatter in $IRPL_{880}$ compared with the $IRPL_{955}$ signal. Interestingly, the three outliers in the $IRPL_{880}$ are all from the same sample 092202. There seems to be a tendency for a slight sub-linear ΔIRPL vs. IRSL behavior with an increase in the luminescence sensitivity; this indicates that the depletion ratios may vary from aliquot to aliquot depending on IRSL sensitivity. In general the majority of these data, despite very different geographical origins of the feldspar samples, support to a first-order approximation that ΔIRPL is proportional to IRSL.

ΔIRPL for the IR bleach at different temperatures are plotted in Figure 7.3 (note that the data for pIR_{250} ΔIRPL are not plotted since IR stimulation temperature is significantly higher than the preheat temperature). The trends between laboratory and natural dose are similar; however, there is a tendency for slightly greater ΔIRPL for the laboratory irradiated samples compared with the naturally irradiated samples. For $IRPL_{955}$ one can conclude that about 40-50% trapped electron population participates in IRSL (step 5) at 50°C. There is a significantly larger spread in ΔIRPL from sample to sample for IR depletion at 50°C than

at the higher temperatures; this partly explains the scatter observed in Figure 7.2b. Further, sequentially raising the IRSL temperature (step 5) to 100, 150 or 200°C results in a depletion of trapped electrons of about 70, 85 and 95% of the initial signal, respectively.

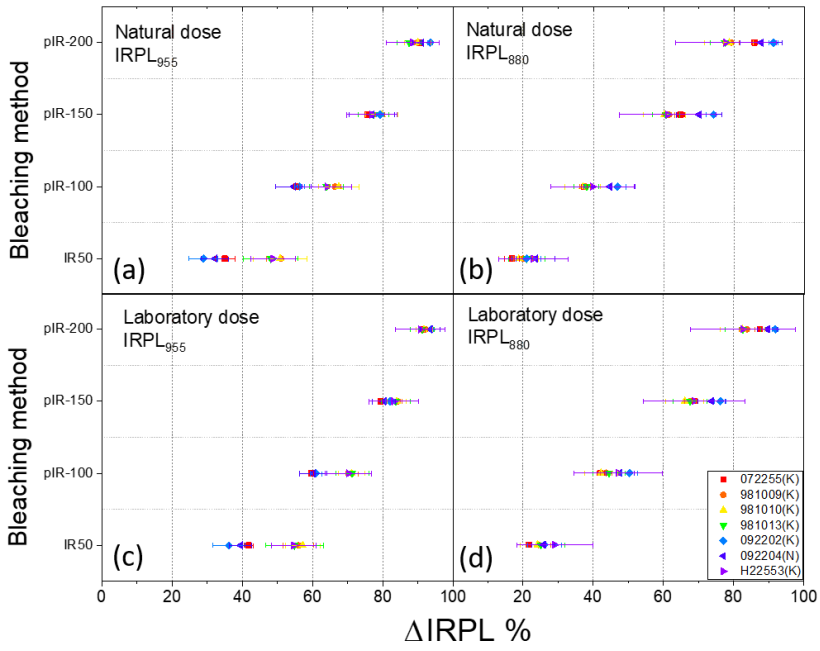

Figure 7.3: ΔIRPL measured after IR exposures at different temperatures (denoted on the y-axis). IRPL after preheat (200 °C for 60 s) but before the IR_{50} has been used as the baseline for the calculation. (a) and (b) show data for the natural dose for $\Delta IRPL_{955}$ and $\Delta IRPL_{880}$, respectively. (c) and (d) show data for the laboratory dose for $\Delta IRPL_{955}$ and $\Delta IRPL_{880}$, respectively. The size of the laboratory dose was kept to be the same as the natural dose for each sample. See Table 7.2 for details. Each data represents the average and standard deviation of 3 aliquots per sample.

In contrast, for $IRPL_{880}$ only about 20% of the trapped electron population participates in IRSL (step 5) at 50°C. Further sequential raising the IRSL temperature (step 6) to 100, 150 or 200 °C results in depletion of trapped electrons to about 40, 65 and 80%, respectively. A higher $\Delta IRPL_{955}$ (50%) than $\Delta IRPL_{880}$ (20%) is perhaps the reason for a higher correlation between IRSL and $\Delta IRPL_{955}$ than $\Delta IRPL_{880}$; these observa-

tions show that there is preferentially higher contribution of luminescence from the 955 traps over the 880 traps during the IRSL measurement.

We also measured ΔIRPL following Table 7.2 but with a preheat of 320 °C for 60 s, commonly used in feldspar $pIR_{50}IRSL_{290}$ dating. The results are shown in Figure 7.4. The $IRPL_{880}$ behaves in a similar way as in Figure 7.3. However, in case of $IRPL_{955}$, some samples show only 20 and 40% depletion at IR_{50} and $pIR_{100}IRPL$, respectively. This change probably represents a significant depletion of the unstable electron population in the 955 emission center in some samples due to a higher preheat for the data in Figure 7.4 than in Figure 7.3.

With regards to dating, this implies that the stable electron population in the pIR-IRSL methods samples from 50-80% (depending on the preheat) of the total population remaining after the preheat.

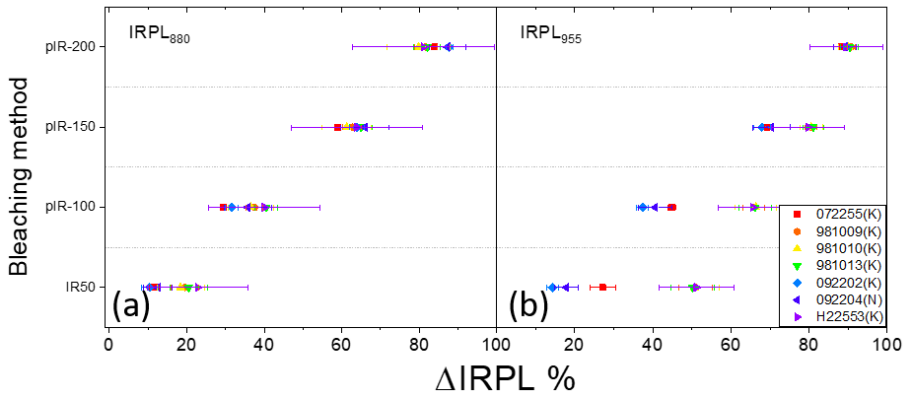

Figure 7.4: ΔIRPL measured after IR exposures at different temperatures (denoted on the y-axis). IRPL after preheat (320 °C for 60 s) but before the IR_{50} exposure has been used as the baseline for the calculation. (a) and (b) show data for the laboratory dose for $\Delta IRPL_{955}$ and $\Delta IRPL_{880}$, respectively. The size of the laboratory dose was kept to be the same as the natural dose. The difference between Figure 7.3 (c, d) and Figure 7.4 is in the preheat temperature after the regeneration dose. Each data represents the average and standard deviation of 3 aliquots per sample.

7.5 Thermally-induced depletion of trapped electron and hole populations

The response of OSL to heating is commonly investigated through so called 'pulse annealing curves', where the sample is heated to different temperatures between beta or gamma irradiation and the OSL measurement (Duller, 1991). Since OSL measurements involve both electrons and holes, the OSL pulse anneal curve cannot distinguish between which of the general processes below (a-d) are responsible for the decrease in the signal. Here, E_e is the trap depth of the principal trap, and E_h is the trap depth of the recombination center involved in OSL or IRSL.

a) $E_e > E_h$ in a delocalized model (i.e. eviction of electrons into the conduction band or holes into the valence band). The pulse anneal curve will reflect the thermal depletion of the trapped holes.

b) $E_e < E_h$ in a delocalized model. The pulse anneal curve will reflect the thermal depletion of the trapped electrons. This is the common conventional interpretation of the OSL or IRSL thermal depletion data.

c) Simultaneous depletion of holes and electrons in a localized model (Jain et al., 2012). Here both E_e and E_h are significantly larger than the activation energy required to induce local e-h recombination. The pulse anneal curve will reflect the thermal activation energy for excited state tunneling or localized recombination.

d) Localized or delocalized model with competition from shallow traps. Here holes (or electrons) are used up due to thermal depletion of electrons (or holes) in a shallow trap, i.e. both E_e and E_h are greater than $E_{\text{shallow trap}}$. The pulse anneal curve will reflect the thermal depletion of charge in the shallow trap.

In a coupled PL-OSL system one can make some predictions of the behavior of the pulse anneal curves under these different scenarios. In a) and d), the IRPL curves will be more stable than the IRSL. In both b) and c) the IRPL and IRSL pulse anneal curve will overlap.

A combination of IRPL and IRSL can for the first time directly provide tracking of both electrons and holes in the system as follows:

$$IRPL(T) \propto n_e(T) \tag{7.2}$$

$$IRSL(T) \propto n_e(T).m_h(T) \tag{7.3}$$

So,

$$m_h \propto \frac{IRSL(T)}{IRPL(T)} \tag{7.4}$$

Here n represents the population of the occupied principal traps, and m represents the trapped hole population in the crystal, that is available for IRSL or OSL.

However, one needs to be cautious, as in the context of the feldspar model (Jain and Ankjærgaard, 2011; Jain et al., 2015) we know that pure delocalized transitions do not exist at near room temperature IR stimulations. As discussed in the previous Sections 7.3 and 7.4, the IRSL process has a strong recombination bottleneck; so only fraction of the electron population (20-50%) takes part in the IRSL production, e.g. at 50 °C. Thus, Equation 7.4 is not fully justified since IRPL originates from the entire crystal, whereas IRSL only originates from a small sub-population that satisfy nearest neighbor condition for IRSL production. To tackle this problem, we also derive the thermal dependence of the IRPL lost due to the IRSL measurement, i.e. ΔIRPL(T) following equation 7.1. As discussed in the previous section (Figure 7.2b), this signal should correspond to the population that participates in the IRSL process. Thus, we define two new parameters n'_e and m'_h; these are more relevant estimates of the behavior of trapped electrons and holes that are active in the IRSL process:

$$n'_e \propto \Delta IRPL(T) \tag{7.5}$$

$$m'_h(T) \propto \frac{IRSL(T)}{\Delta IRPL(T)} \tag{7.6}$$

The pulse anneal data were measured using the protocol outlined in Table 7.3 using three aliquots of sample 981010. The protocol followed here is based on a single aliquot regenerative (SAR) dose method where any possible sensitivity change during repeated measurements is

corrected for by using the response to a test dose. We derived the following data as a function of anneal temperature using the protocol outlined in Table 7.3:

#1. IRSL(T) / IRSL (test dose): sensitivity corrected IRSL signal.

#2. IRPL(T) / IRPL (test dose): sensitivity corrected IRPL signal. This signal measures the changes in trapped electrons in the principal trap in the entire crystal (n_e) as a function of preheat temperature (Equation 7.2).

#3. $pIR_{50}IRPL(T)$ / $pIR_{50}IRPL$(test dose): sensitivity corrected $pIR_{50}IRPL$, i.e. IRPL signal measured after an IRSL measurement at 50 °C. This signal should measure the relatively stable principal trap population, i.e. distant e-h neighbors.

#4. ΔIRPL(T) / ΔIRPL (test dose): this represents the thermal dependence of electrons in the principal trap (n'_e; equation 7.5), which participate in the IRSL process.

#5. IRSL(T) / IRPL(T): this represents thermal dependence of trapped holes (m_h; equation 7.4) for a delocalised model [models a), b) or d)].

#6. IRSL(T) / ΔIRPL(T): this represents thermal dependence of trapped holes (m'_h; equation 7.6) for the localized model [models c) or d)] .
For #1, #2 and #3, the test dose response was almost invariable as a function of the SAR cycle; nonetheless using sensitivity correction improved the reproducibility. Therefore, we decided to use the sensitivity corrected ratio.

These ratios (#1 to #6) are plotted in Figures 7.5a and c for $IRPL_{880}$ and in Figures 7.5b and d for $IRPL_{955}$. The data were measured on 3 aliquots of the sample 981010. The thermal stability of the different signals is similar for both the IRPL (880 and 955 nm) emissions. The IRSL data (#1) show a steep decrease from 50 to 100°C where it reaches a plateau between 100 and 220°C, followed by a monotonic decrease up to 450°C where it reaches a near-zero value. IRPL (#2) on the other hand is relatively stable from 50 to 400°C, followed by a monotonic decrease from 400 to 600°C. Even at 600°C, ∼10% of the IRPL still remains. The

$pIR_{50}IRPL$, i.e. the IRPL signal remaining after IR bleach (#3), is only slightly more stable than the IRPL (#1) for the 880 nm emission, while it is significantly more stable than the IRPL (#1) for the 955nm emission. This difference is not surprising since as discussed in the previous section, the change (depletion) in IRPL by IR stimulation at 50 °C is much smaller for the 880 nm emission than the 955 nm emission. An increase in the stability is supported by the feldspar model, which suggests that IRSL uses the nearest e-h neighbors, which are easy to recombine through the excited state of the electron trap (Jain et al., 2012, 2015).

Table 7.3: Measurement of pulse-anneal curves. IRPLs(λ) refer to IRPL (880 nm) followed by IRPL (955nm). 'β' denotes the heating rate, 'p' denotes the holding time (pause) after reaching the desired end-temperature before switching on the light.

Step no	Measurement	Signal
1	Beta irradiation 110 Gy	
2	IRPLs *(λ)* at 20℃ for 10 s	
3	TL to T° C *(β = 10°C.s^{-1})*	
4	IRPLs *(λ)* at 20℃ for 10 s	***$IRPL_{\lambda}$***
5	IRSL at 30° C for 100 s *(β = 5°C.s^{-1}; p = 5s)*	**$IRSL_{T}$**
6	IRPLs *(λ)* at 20℃ for 10 s	***$pIR\text{-}IRPL_{\lambda}$***
7	IRSL at 290° C for 100 s *(β = 5°C.s^{-1}; p = 5s)*	Cleanout
8	IRPLs *(λ)* at 20℃ for 10 s	*$IRPL_{bkg}$*
9	Test dose (td) of 110 Gy	
10	IRPLs *(λ)* at 20℃ for 10 s	
11	TL to 250° C *(β = 10°C.s^{-1})*	
12-16	repeat steps 4-8	***$IRPL_{td}$*; $IRSL_{td}$; *$pIR\text{-}IRPL_{td}$***
	Repeat the entire cycle (steps 1-16) for T= 50, 80, 100, 120, 140, 160, 180, 200, 220, 240, 260, 280, 300, 320, 340, 360, 380, 400, 420, 440, 460, 480, 500, 520, 540, 560, 580, 600, 100, 200, 300, or 100 *℃*	

The IRSL signal has already decreased by 75% (compared to its plateau value at 100 °C) at 400 °C when the IRPL signal only begins to deplete. The ratio IRSL(T) and IRPL(T) gives m_h (#5). These data very closely follow the IRSL(T) depletion pattern for both the $IRPL_{880}$ and $IRPL_{955}$ emissions, suggesting that to a first-order approximation, the main cause of the decrease in IRSL is hole depletion.

However, a slight shift in the $pIR_{50}IRPL$ compared to IRPL suggests that electrons participating in the IRSL measurement (ΔIRPL) are only

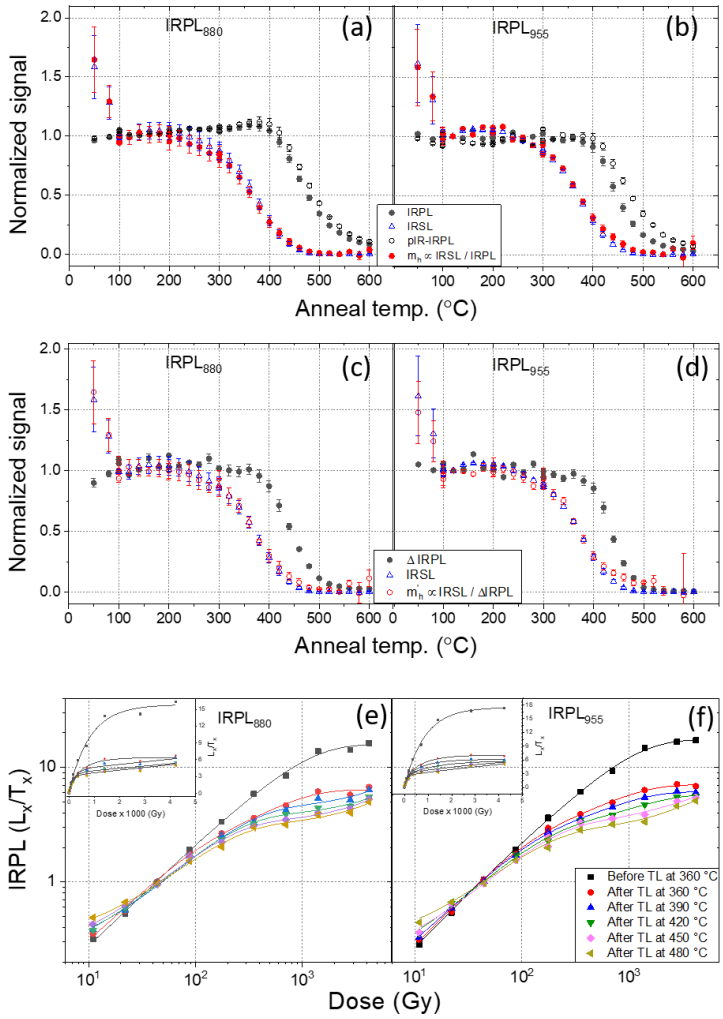

Figure 7.5: Pulse-anneal curves (signal vs. preheat temperature) and the dose-response curves (signal vs. beta dose) measured for different signals using three aliquots of sample 981010. See Table 7.3 for details. (a) Preheat dependence of the IRSL, IRPL, $pIR_{50}IRPL$ signals for $IRPL_{880}$. The behavior of holes is calculated using equation 7.4. (b) The same data as '(a)' but for $IRPL_{955}$. (c) Preheat dependence of the IRSL (same data as in (a) and (b)), ΔIRPL, and behavior of holes calculated using Equation 7.6 for $IRPL_{880}$. (d) The same data as '(c)' but for $IRPL_{955}$.(e) Dose response curve of the IRPL signals remaining after different preheats for $IRPL_{880}$. (f) Dose response curve of the IRPL signals remaining after different preheats for $IRPL_{955}$.

a part of the total electron population. Thus, $m'_h(T)$ (#6) is the more relevant representation of the hole population participating in the IRSL process. Interestingly, both m_h (Figures 7.5a, b) and m'_h (Figures 7.5c, d) show strong overlap with the temperature dependence of IRSL. These data (m'_h) indicate that (i) the IRSL pulse anneal curve is governed by the depletion of trapped holes and not the trapped electrons, and (ii) the thermal dependence of trapped electrons is very similar whether or not they are close to the holes i.e. IRPL(T) $\approx$ ΔIRPL(T). Thus, of the 4 possible processes (a-d) discussed at the beginning of this section, we can rule out that either b) or c) is responsible for the thermal depletion behavior of the IRSL; this is because the electron population is more stable than the IRSL curve. To distinguish between a) and d) as the relevant process, we examined the relationship between the TL emitted in the region 280-600 °C and the subsequent IRSL counts (Figure 7.6). These data show a negative correlation between IRSL and TL between 300 to 400 °C, i.e. the region in which the IRSL signal depletes rapidly. It is to be noted that both the IRSL and TL are measured in the same emission window (blue emission). Since we already know that the principal trap (both IRPL and ΔIRPL) is quite stable up to a temperature of 400 °C, the reduction in the IRSL must be arising from depletion of holes consumed during the TL production. These data suggest that the high temperature TL peak must be arising from an electron trap different from the principal trap and the electrons from this trap compete with the holes that are used by the principal trap.

In conclusion, based on the novel PL-OSL system, we are able to infer for the first time that the thermal dependence of the IRSL curve can be attributed to process d), i.e., depletion of holes because of competitive recombination. This is a markedly different interpretation of pulse anneal curves which are commonly believed to arise from the thermal erosion of the electrons in the principal trap (e.g., Murray et al., 2009; Li and Li, 2011), or from localized e-h recombination (Jain and Ankjærgaard, 2011). Furthermore, we establish unequivocally that TL and IRSL may not arise from the same electron trap but both the processes use the same hole traps. Thus a commonly observed decrease in the area of the high temperature TL peak due to IR exposure (Murray et al., 2009) must be due to a reduction in the hole population during IR light exposure.

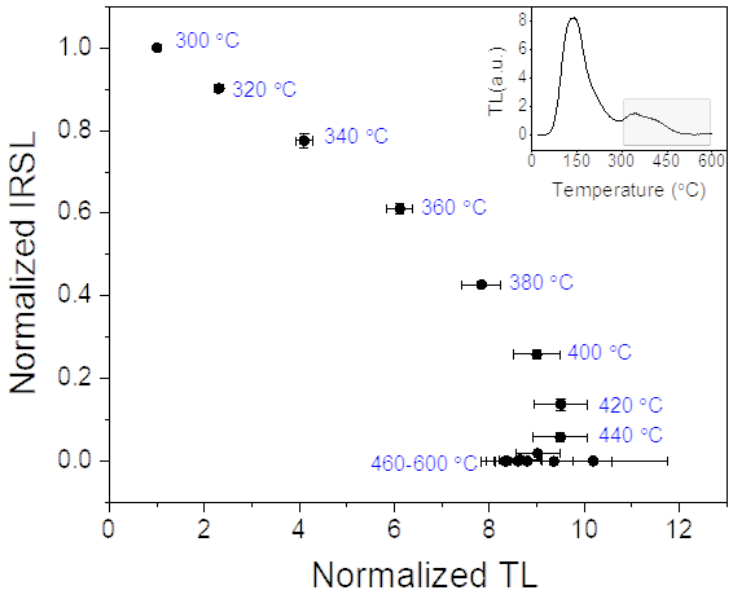

Figure 7.6: Correlation between integral TL intensity in the region 280 °C to T °C, and the subsequent IRSL signal based on the pulse-anneal data (Table 7.3). The net TL signal corresponding to the IRSL was calculated from the TL curves (step 3) measured before each IRSL (step 5); this is the difference in TL counts (I) in the two integral regions ($I_{20-T°C}$) minus $I_{20-280°C}$). T is marked as the temperature against each data point. Inset shows the TL curve measured up to 600 °C; the shaded area is the TL the peak used for TL-IRSL comparison

7.6 Competition in electron transport pathways

During resonant excitation, such as during IRSL, electrons can undertake several different pathways from the excited state: a) tunneling recombination, b) relaxation to the ground state, and/or c) diffusion through the band-tail states (temperature-dependent) followed by eventual recombination or retrapping (Jain and Ankjærgaard, 2011; Jain et al., 2012). Furthermore, during relaxation there may exist a combination between radiative and non-radiative processes leading to the well-known thermal quenching of luminescence in defects by the Mott-Seitz mechanism (Pagonis et al., 2010). A coupled IRPL-OSL system can for the first time allows discrimination between these competitions involved in these different transport/transition pathways.

We examine the dependence of IRPL and IRSL on the measurement (stimulation) temperature from room temperature to 260 °C. The measurement protocol is outlined in Table 7.4. Three aliquots of sample 981010 were first emptied of their natural signal by a high temperature IRSL cleanout. They were then given a laboratory dose of 220 Gy followed by preheating and measurement of IRPL signals at different temperatures. There is no detectable depletion of the signal due to the measurement itself, which makes it possible to do consecutive IRPL measurements at different temperatures without repeated beta irradiation. Several recycling points were introduced in the sequence in order to check that temperature trends are not affected by possible signal depletion during the repeated measurements. In a twin experiment, the same protocol was followed, however, an additional IRSL bleaching at 50°C for 100 s was inserted just before the IRPL measurements. The idea behind this modification was to selectively examine only those electrons (n_e-n'_e) that are distant from hole centers and thus do not participate in the IRSL at 50°C (see Section 7.4); by doing this we deliberately reduce the loss to the recombination centers.

In a similar manner, the stimulation temperature dependence of the IRSL signal was measured (Table 7.4). The measurement time of IRSL was restricted to 0.02 s per measurement in order to minimize any depletion during the measurement.

The data are plotted in Figure 7.7 as an Arrhenius plot (Log intensity vs. $1/k_B$T, where k_B is the Boltzmann's constant). The IRSL signal shows the well-known increase with measurement temperature, commonly referred to as thermal assistance. This increase observed mainly

Table 7.4: Dependence of IRPL and IRSL signals on the measurement temperature. IRPLs (λ) refer to IRPL (880 nm) followed by IRPL (955 nm). 'β' denotes the heating rate. 'p' denotes the holding time (pause) after reaching the desired end-temperature before switching on the light.

For IRPL		
Step no.	**Measurement**	**Signal**
1	IRSL at 290° C for 95 s (β = 5°C.s^{-1}; p = 5s)	Cleanout
2	Beta irradiation 220 Gy	
3	Preheat (300° C) for 60s (β = 5°C.s^{-1})	
4	No bleaching or IRSL bleaching at 50° C for 100 s	
5	IRPLs (λ) at T° C for 10 s; (β = 5°C.s^{-1}; pause =15s)	**IRPL$_T$** or **pIR-IRPL$_T$**
	Repeat steps 5 and 6 for T = 20, 40, 60, 80, 20, 100, 120, 140, 160, 80, 180, 200, 220, 240, 260, 80	
6	IRSL at 290° C for 95 s (β = 5°C.s^{-1}; p = 5 s)	Cleanout
7	IRPLs (λ) at 20° C for 5 s	IRPL$_{bkg}$
For IRSL		
1	IRSL at 290° C for 95 s (β = 5°C.s^{-1}; p = 5s)	Cleanout
2	Beta irradiation 220 Gy	
3	Preheat (300° C) for 60 s (β = 5°C.s^{-1})	
4	IRSL at T °C for 0.02 s; (β = 5°C.s^{-1}; pause =15 s)	
	Repeat steps 4 for T = 20, 40, 60, 80, 20, 100, 120, 140, 160, 80,180, 200, 220, 240, 80, 260, 280, 300, 80	

above 60°C, is understood to arise from the increased efficiency of transport in the band-tail states at higher and higher temperatures (Poolton et al. 2009) leading to more efficient recombination (Jain and Ankjærgaard, 2011). In a simple model, we expect that the IRPL(T) data should mirror the IRSL(T) data since electrons lost to the recombination pathway through the band-tail states must lead to a corresponding decrease in the IRPL signal. Such a trend in IRPL is, however, not observed (Figure 7.7a). Instead, the following observations can be made regarding the IRPL signal:

1. The decrease in $IRPL_{955}$ with temperature is faster than $IRPL_{880}$. This possibly indicates the fact that the 955 nm center loses electrons more easily than the 880 nm center, and is the main contributor to the IRSL; this inference is consistent with the data and interpretations based on Figure 7.2 and 7.3, where ΔIRPL is larger for the 955 emission.

2. The $pIR_{50}IRPL$ data (empty circles; Figure 7.7a), i.e. IRPL measured after the $IRSL_{50}$ measurement, decrease much slower than the IRPL; this is consistent with the model that the decrease in IRPL is due to loss of electrons to the recombination route. Since a significant proportion of charge has already been removed by the $IRSL_{50}$, the remaining charge has less likelihood to find recombination centers and therefore likely ends up being re-trapped in the principal trap.

3. IRPL is not a mirror image of IRSL. The increase in IRSL with stimulation temperature is much more rapid than the decrease in IRPL (Figure 7.7 inset).

It is likely that the decrease in IRPL is a combination of charge loss to the recombination route and intra-defect quenching within the principal trap (Prasad et al., 2017). Intra-defect thermal quenching can be examined using time-resolved IRPL measurements. We repeated the measurements in Table 7.4 and collected IRPL data for both the $IRPL_{880}$ and $IRPL_{955}$ in the time-resolved mode using time-correlated single-photon counting. Figure 7.8a shows these data for the same temperatures; unlike Prasad et al. (2017) our data is best fitted by a linear sum of two exponential decay functions. The two lifetimes are plotted as a function of measurement temperature in Figure 7.8b. The dominant lifetime of 20 µs is constant

up to about 80 °C and then decreases almost linearly to ∼12.5 µs until 260 °C. The lifetime of the less dominant component remains at ∼4 µs up to 100 °C and then decreases linearly to ∼2.5 µs until 260 °C. The net decrease in the lifetime is about 38% for both components. The tenfold drop in the IRPL intensity above 100 °C is not consistent with the change in lifetime, which only decrease by 38%. Instead, the lifetimes data indicate that we are, if at all, only at the beginning of an intra-defect thermal quenching process. This relatively weak dependence of lifetime on temperature probably suggests that the decrease in lifetime at higher temperatures is not due to intra-defect quenching but due to loss of electrons from the excited state to the band-tail states (this is equivalent to a non-radiative competition process). This is possible if electrons are not excited to the excited state but near it; thus, only a fraction of electrons are in fact retrapped, and this changes with temperature.

A question then arises why the decrease is IRPL is not mirrored by an increase in the IRSL signal. We interpret that the difference in the rate of change of IRPL and IRSL is due to a net increase in the number of holes available for recombination. As electrons become more mobile at higher and higher temperatures, there should be an increase in the probability of finding a trapped hole (because of the larger distance traversed by a detrapped electron). Thus, the probability of recombination per detrapped electron increases volumetrically with temperature (greater crystal volumes accessed at higher temperatures). If we divide the IRSL (product of electrons lost and the probability of finding a trapped hole) by the IRPL signal (probability of electron loss), the resultant ratio shows the availability of holes as a function of mean diffusion volume of a detrapped electron, which in turn is a function of the stimulation temperature. These data are plotted in Figure 7.7b; there is a non-exponential increase per unit energy; the mathematical form of this curve needs to be investigated but it is likely to be a convolution of the temperature-dependent loss of electrons from the excited state and the volume traversed by these detrapped electrons via the band-tail states.

7.7 Electron and hole trapping by ionizing radiation

Finally, we examine how the population of electrons in the principal trap and the holes at the IRSL recombination centers grow by exposure to

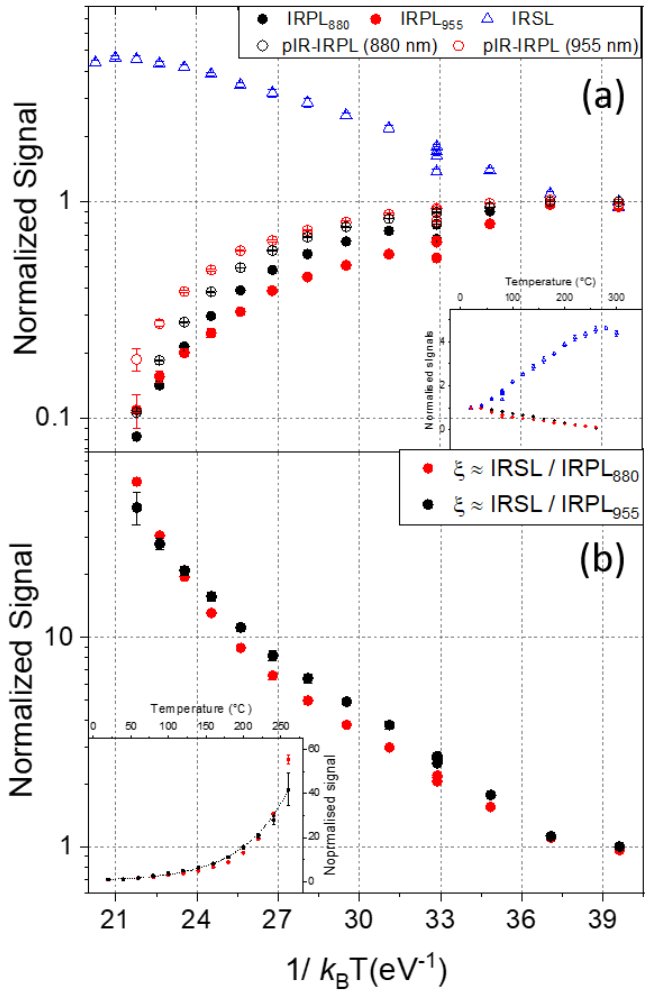

Figure 7.7: (a) Arrhenius plot of the IRPL (for both $IRPL_{880}$ and $IRPL_{955}$), IRSL and $pIR_{50}IRPL$ (in case of both $IRPL_{880}$ and $IRPL_{955}$) signals for the different measurement temperatures. See Table 7.4 for the details. Each signal intensity has been normalized with its intensity at room temperature. The inset shows the same data vs. the measurement temperature. (b) Arrhenius plot of efficiency of finding a hole. The inset shows the same data on a linear temperature scale. Sample 981010 was used for these measurements. Each data point represents the mean and standard deviation from three aliquots of sample 981010.

beta radiation. The measurement sequence for the dose response curves (DRC) for IRPL and IRSL is outlined in Table 7.5.

The DRCs were measured on three aliquots of sample 981010 whose average values are presented in Figure 7.9. Figure 7.9a shows the response of the sensitivity corrected IRPL signals and the IRSL signal. The dose response of the $IRPL_{880}$ is indistinguishable from that of the $IRPL_{955}$ signal. Both IRPL signals reach saturation in dose response slightly faster than the IRSL.

Table 7.5: Measurement of dose response curves. IRPLs (λ) refer to IRPL (880 nm) followed by IRPL (955nm). 'β' denotes the heating rate. 'p' denotes the holding time (pause) after reaching the desired end-temperature before switching on the light.

Step no.	Measurement	Signal
1	IRSL at 290° C for 95 s (β = 5°C.s^{-1}; p = 5s)	Cleanout
2	Beta irradiation (regeneration dose)	
3	Preheat (320° C) for 60 s (β = 5°C.s^{-1})	
4	IRPLs (λ) at 20°C for 10 s	L_x IRPL
5	IRSL bleaching at 50° C for 100s	L_x IRSL
6	IRPLs (λ) at 20°C for 10 s	L_x pIR-IRPL
7	IRSL at 290° C for 95 s (β = 5°C.s^{-1}; p = 5s)	Cleanout
8	IRPLs (λ) at 20°C for 10 s	$IRPL_{bkg}$
9	Test dose 220 Gy	
	Repeat steps 3-8 to monitor possible sensitivity changes	T_x IRPL (880); T_x IRSL; T_x pIR-IRPL ; $IRPL_{bkg}$ (880)

Figure 7.9b shows the dose response of the ΔIRPL signals, which is also very similar to the response of the IRPL signal; note that IRPL data from Figure 7.9a is also plotted for comparison. Based on the reasoning in the previous section the dose response of the holes is derived by dividing the IRSL signal by the ΔIRPL signals. These data indicate that there is about a 40% increase in the hole population from the smallest to the highest dose. The holes reach a saturation value much earlier ($\sim$0.5 kGy) than the electron trap (IRPL or ΔIRPL). Thus 'hole trap dating' as suggested in previous work (Li et al., 2013) is not feasible, probably because holes do not seem to be fully reset during a SAR cycle.

One question that arises is whether the dose response is similar for every principal trap, or if there is a systematic variation in the DRC as we approach more and more thermally stable components of the principal trap. To investigate this we examined the DRC of the $IRPL_{880}$ and

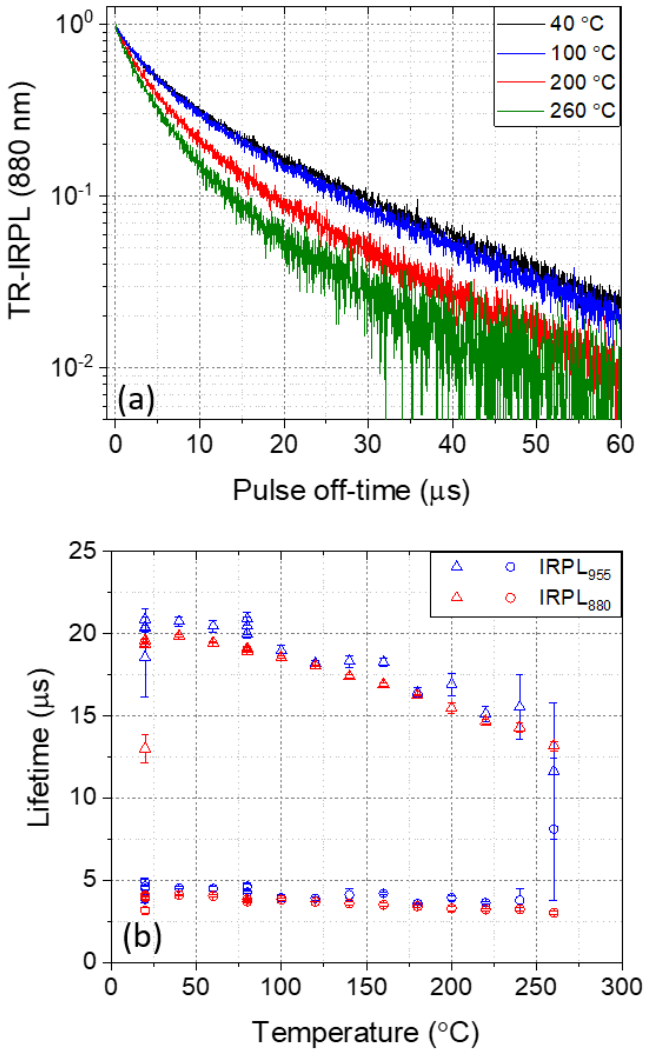

Figure 7.8: (a) Time-resolved $IRPL_{880}$ curves for some selected measurement temperatures. Each curve is best fitted to a sum of two exponential decays. Sample 981010 was used for these measurements. (b) IRPL lifetime as a function of measurement temperature. Each data point represents the mean and standard deviation from three aliquots of sample 981010.

$IRPL_{955}$ after different preheats ranging from 360° to 480°C. The same protocol was followed as outlined in Table 7.5, except for the change in thermal treatment after beta irradiation (TL to T°C; T = 360, 390, 420, 450 or 480). These data are plotted in Figures 7.5e and f for the $IRPL_{880}$ and $IRPL_{955}$, respectively. A linear sum of two exponential is fitted to these data. Figures 7.5a and b show the remaining electron population after each of these TL treatments. It is observed that there is a tendency for the DRCs to saturate earlier with dose as we access more and more thermally stable sub-populations within the principal trap. The biggest change occurs from no preheat to the preheat scenario (Figures 7.5e and f). This behavior is consistent with the response of pIR-IRSL signals, which show earlier saturation as a more stable signal is accessed (e.g., Andersen et al., 2012). In the framework of the feldspar nearest neighbor distribution model, these data suggest that it is more difficult to trap pairs with short distances (thermally unstable) than those with large distances. This is expected since trapping an e-h pair in a small volume is probabilistically a rarer event than trapping an electron and hole in a large volume.

7.8 Summary and discussion

In order to develop the future applications of the OSL/IRSL technique to understand environmental processes such as erosion and transport (Gray et al., 2019), it is imperative that the luminescence kinetics under thermal or optical exposure is fully understood. Based on the coupled PL-OSL system in feldspar, we elucidate here the long-standing unknowns in the luminescence model of feldspar.

We propose a new quantity called ΔIRPL, which reflects the principal traps that participate in the IRSL or OSL process. The very existence of ΔIRPL and change in it after different pre-treatments support the feldspar luminescence model proposed by Jain and Ankjærgaard (2011). Our data indicate that IRSL may be preferentially derived from the principal trap emitting PL at 955 nm (955 nm center) as against that emitting at 880 nm (880 nm center). As demonstrated above ΔIRPL is a powerful tool to individually examine the behavior of the electron and hole populations due to heating, laboratory irradiation, etc.

The measurements here give a new physical interpretation of the thermal stability of the IRSL signals. Conventional wisdom suggests that

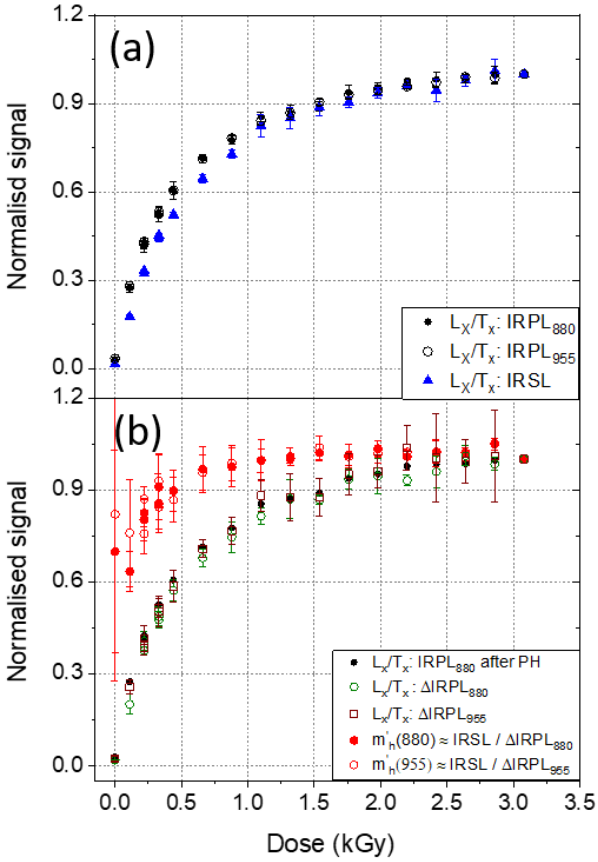

Figure 7.9: (a) Dose response curves of the sensitivity corrected $IRPL_{880}$, $IRPL_{955}$, and IRSL signals. See Table 7.5 for details. (b) Dose response curves of the sensitivity corrected $\Delta IRPL_{880}$, $\Delta IRPL_{955}$ and $IRPL_{880}$ (repeated from (a) for comparison) signals. The dose dependence of holes using Equation 7.6 is also plotted for $IRPL_{880}$ and $IRPL_{955}$. Each data point represents the mean and standard deviation from three aliquots of sample 981010

the decrease in the IRSL signal due to prior thermal treatment (preheat or thermal bleaching) results due to a decrease in the trapped electron population in the principal trap. We show instead that the electron population is stable up to 400 °C (in this sample), a temperature by which about 60-75% of the IRSL is depleted. We show for the first time thermal response of the electrons (n_e, n'_e) and the holes participating in the IRSL process (m_h, m'_h) individually. Based on the relationship between different signals, we conclude that the thermally–induced decay of the IRSL signal occurs mainly because the IRSL active holes are used up by electrons derived from a different trap (i.e. not the principal trap) that produces the TL peak in the region 300-400°C. In other words, the main part of the IRSL decay curve represents the kinetics of this different electron trap. These unique first insights imply that the fundamental of the kinetic models (Li and Li, 2013; Jain et al., 2015; Guralnik et al. 2015b) need to be revisited in the light of these new data. To arrive at a universal picture, such data need to be measured on many different types of samples. This is especially important for producing robust models for thermochronometry (Guralnik et al., 2015; King et al., 2016; Brown et al., 2017).

The dose response data presented here show, for the first time, the growth of the electrons and holes separately. These data preclude the use of holes for dating as suggested by Li et al. (2013), since it is apparent that holes are not reset during a SAR protocol, and probably not in nature either. We propose a novel mechanism to explain the change in DRC of the trapped electrons a function of preheat temperature, which are reflected in both the IRPL and post IR IRSL data. According to this mechanism based on the nearest neighbor model (Jain and Ankjærgaard, 2011), it becomes increasingly difficult to capture electrons in the principal trap, below a certain threshold, as the e-h distance becomes smaller and smaller. In other words, the capture probability is a product of both the electron capture cross-section of a trap and the distance between that electron trap and its nearest hole. This is reflected as a higher D_0 for the less stable (i.e. nearer e-h) population. The difficulty in trapping in a small volume may arise from a combination of the following:

1. The probability of randomly trapping both an electron and a hole in a given volume element is a function of the pre-existing hole density. Based on Huntley et al. (2007), this probability becomes smaller and smaller with a decrease in the nearest neighbor distance

(see Figures 1a, 2a of Jain et al, 2012). The relative probability of creating a shorter-distance nearest-neighbor can be defined as:

$$P(r) = \frac{\int_0^r exp(-\frac{4}{3}\pi\rho r^3) \cdot 4\pi\rho r^2 dr}{\int_0^{r_{max}} exp-(\frac{4}{3}\pi\rho r^3) \cdot 4\pi\rho r^2 dr} \tag{7.7}$$

where r is the distance between the nearest e-h neighbor and ρ is the number density of holes.

2. As a free-electron approaches a principal trap at a few nm distance to a trapped hole, there is a finite probability that this electron instead of filling the electron trap may collide with the hole trap and recombine with a hole. The electron and hole trapping has to then start again from scratch to create a nearby e-h pair.

The elegance of this model is that it does not invoke different principal traps to explain the variation in the dose response curves across different trapped electron populations. Instead, such a dependence comes naturally from our existing understanding of the existence of localized processes in feldspar. From the IRPL data, we have no suggestion that different sub-populations of the principal trap should have different physical characteristics, such as trap depth or electron capture cross-section. The apparent change in the electron capture probability for different sub-populations of the principal trap arises due to their proximity to the hole centers. This new understanding has important implications for developing a mathematical model of electron trapping which for example is relevant for thermochronometry.

The coupled PL-OSL system also throws light on the fate of the electrons in the band-tail states after their release from the principal trap. We discuss that IRSL arises both from a) increased partitioning of electrons to the recombination route (vs the retrapping route) with an increase in measurement temperature above 80 °C, and b) greater availability of holes because of an increase in the diffusion volume. This model assumes that electrons that do not recombine are trapped again into the principal trap, which needs to be tested in future studies.

Finally, a comparison between the $IRPL_{880}$ and $IRPL_{955}$ emissions confirms that there are two different centers (sites) comprising the principal trap. These centers show a very similar radiation-induced growth behavior, as also observed by Kumar et al. (2018; Chapter 3 in this

thesis), and have indistinguishable relaxation lifetimes. However, they differ in their thermal stability, stimulation temperature dependence and ability to be bleached by IR photons (at different temperatures). These data suggest that it is likely that the principal trap consists of the same defect; however, the mean distance of this trap to the recombination sites is different for the 880 nm and 955 nm centers. Future studies involving high-resolution mapping of IRPL emitting volumes can throw light on possible dependence between micro-structure or compositional variations and their effect on the principal trap.

These physical insights obtained from direct observation of trapped electrons have significantly enriched the feldspar model. The next step is to obtain a universal picture by applying the new techniques developed here to different feldspar samples and develop robust mathematical models for developing areas such as thermochronometry and sediment transport, which currently work on 'black box' assumptions.

7.9 Conclusions

We develop here a coupled PL-OSL system and demonstrate its unique importance for understanding luminescence recombination pathways involving the metastable states in feldspar. We suggest for the first time new quantities which measure changes in trapped electron and hole populations individually. The new insights obtained are:

1. Only a fraction of trapped electrons participate in IRSL.

2. The thermal stability of the IRSL is governed by hole depletion and not by electron depletion.

3. Electron trapping probability in the principal trap is both a function of electron capture cross-section (Coulomb attraction) and its distance to the nearest hole.

4. The volume-dependent probability of finding a hole is a major factor in the IRSL production.

These new insights are critical for the development of exact mathematical models of luminescence phenomena involving metastable states.

Acknowledgments

We thank Dr. Jan-Pieter Buylaert, Prof. Andrew Murray, and National Luminescence Laboratory (NLL) for sediment samples.

References

Andersen, M. T., Jain, M., Tidemand-Lichtenberg, P. (2012). Red-IR stimulated luminescence in K-feldspar: Single or multiple trap origin? Journal of Applied Physics, 112(4), 043507.

Bailiff, I. K., & Barnett, S. M. (1994). Characteristics of infrared-stimulated luminescence from a feldspar at low temperatures. Radiation Measurements, 23(2-3), 541-545.

Balescu, S., & Lamothe, M. (1994). Comparison of TL and IRSL age estimates of feldspar coarse grains from waterlain sediments. Quaternary Science Reviews, 13(5-7), 437-444.

Baril, M. R. (2002). Spectral investigations of luminescence in feldspars (PhD thesis, Simon Fraser University, Canada).

Barnett, S. M., & Bailiff, I. K. (1997). Infrared stimulation spectra of sediments containing feldspars. Radiation Measurements, 27(2), 237-242.

Bøtter-Jensen, L., McKeever, S. W., & Wintle, A. G. (2003). Optically stimulated luminescence dosimetry. Elsevier.

Brown, N. D., Rhodes, E. J., & Harrison, T. M. (2017). Using thermoluminescence signals from feldspars for low-temperature thermochronology. Quaternary Geochronology, 42, 31-41.

Buylaert, J. P., Jain, M., Murray, A. S., Thomsen, K. J., Thiel, C., & Sohbati, R. (2012). A robust feldspar luminescence dating method for Middle and Late Pleistocene sediments. Boreas, 41(3), 435–451.

Buylaert, J.P., Murray, A.S., Thomsen, K.J. & Jain, M. (2009). Testing the potential of an elevated temperature IRSL signal from K-feldspar.

Radiation Measurements, 44(5-6), pp.560-565.

Chakrabarti, K., Mathur, V. K., Thomas, L. A., & Abbundi, R. J. (1989). Charge trapping and mechanism of stimulated luminescence in CaS: Ce, Sm. Journal of applied physics, 65(5), 2021-2023.

Clark, R. J., & Sanderson, D. C. W. (1994). Photostimulated luminescence excitation spectroscopy of feldspars and micas. Radiation Measurements, 23(2-3), 641-646.

Dorenbos, P. (2003). Systematic behaviour in trivalent lanthanide charge transfer energies. Journal of Physics: Condensed Matter, 15(49), 8417.

Dorenbos, P., Bos, A. J. J., & Poolton, N. R. J. (2011). Electron transfer processes in double lanthanide activated YPO4. Optical Materials, 33(7), 1019-1023.

Duller, G. A. T. (1991). Equivalent dose determination using single aliquots. International Journal of Radiation Applications and Instrumentation. Part D. Nuclear Tracks and Radiation Measurements, 18(4), 371-378.

Duller, G. A. T., & Bøtter-Jensen, L. (1993). Luminescence from potassium feldspars stimulated by infrared and green light. Radiation Protection Dosimetry, 47(1-4), 683-688.

Erfurt, G., Krbetschek, M. R., Trautmann, T., & Stolz, W. (2000). Radioluminescence (RL) behaviour of Al2O3: C-potential for dosimetric applications. Radiation Measurements, 32(5-6), 735-739.

Gray, H. J., Jain, M., Sawakuchi, A. O., Mahan, S. A., & Tucker, G. E. (2019). Luminescence as a sediment tracer and provenance tool. Reviews of Geophysics.

Guralnik, B., Jain, M., Herman, F., Ankjærgaard, C., Murray, A.S., Valla, P.G., Preusser, F., King, G.E., Chen, R., Lowick, S.E. & Kook, M. (2015a). OSL-thermochronometry of feldspar from the KTB borehole, Germany. Earth and Planetary Science Letters, 423, pp.232-243.

Guralnik, B., Li, B., Jain, M., Chen, R., Paris, R.B., Murray, A.S., Li, S.H., Pagonis, V., Valla, P.G. & Herman, F. (2015). Radiation-induced growth and isothermal decay of infrared-stimulated luminescence from feldspar. Radiation Measurements, 81, pp.224-231.

Huntley, D. J., Godfrey-Smith, D. I., & Thewalt, M. L. (1985). Optical dating of sediments. Nature, 313(5998), 105-107.

Huntley D. J., Short M. A. & Dunphy K. (1996) Deep traps in quartz and their use for optical dating. Canadian Journal of Physics 74, 81-91.

Huntley, D. J., Baril, M. R., & Haidar, S. (2007). Tunnelling in plagioclase feldspars. Journal of Physics D: Applied Physics, 40(3), 900.

Hütt, G., Jaek, I., & Tchonka, J. (1988). Optical dating: K-feldspars optical response stimulation spectra. Quaternary Science Reviews, 7(3-4), 381-385.

Jain, M., & Ankjærgaard, C. (2011). Towards a non-fading signal in feldspar: insight into charge transport and tunnelling from time-resolved optically stimulated luminescence. Radiation Measurements, 46(3), 292-309.

Jain, M., Guralnik, B., & Andersen, M. T. (2012). Stimulated luminescence emission from localized recombination in randomly distributed defects. Journal of physics: Condensed Matter, 24(38), 385402.

Jain, M., Sohbati, R., Guralnik, B., Murray, A. S., Kook, M., Lapp, T., & Buylaert, J. P. (2015). Kinetics of infrared stimulated luminescence from feldspars. Radiation Measurements 81, 242-250.

King, G. E., Herman, F., Lambert, R., Valla, P. G., & Guralnik, B. (2016). Multi-OSL-thermochronometry of feldspar. Quaternary Geochronology, 33, 76-87.

Kook, M., Kumar, R., Murray, A. S., Thomsen, K. J., & Jain, M. (2018). Instrumentation for the non-destructive optical measurement of trapped

electrons in feldspar. Radiation Measurements, 120, 247–252.

Kumar, R., Kook, M., Murray, A. S., & Jain, M. (2018). Towards direct measurement of electrons in metastable states in K-feldspar: Do infrared-photoluminescence and radioluminescence probe the same trap? Radiation Measurements, 120, 7–13.

Li, B., & Li, S. H. (2011). Thermal stability of infrared stimulated luminescence of sedimentary K-feldspar. Radiation Measurements, 46(1), 29-36.

Li, B., & Li, S. H. (2013). The effect of band-tail states on the thermal stability of the infrared stimulated luminescence from K-feldspar. Journal of Luminescence, 136, 5–10.

Li, B., Jacobs, Z., Roberts, R. G., & Li, S. H. (2013). Extending the age limit of luminescence dating using the dose-dependent sensitivity of MET-pIRIR signals from K-feldspar. Quaternary Geochronology, 17, 55-67.

Malins, A. E. R., Poolton, N. R. J., Quinn, F. M., Johnseir, O., & Denby, P. M. (2004). Luminescence excitation characteristics of Ca, Na and K-aluminosilicates (feldspars) in the stimulation range 5-40 eV: Determination of the band-gap energies. Journal of Physics D: Applied Physics, 37(10), 1439–1450.

Meijerink, A., Schipper, W. J., & Blasse, G. (1991). Photostimulated luminescence and thermally stimulated luminescence of Y2SiO5-Ce, Sm. Journal of Physics D: Applied Physics, 24(6), 997.

Murray, A. S., Buylaert, J. P., Thomsen, K. J., & Jain, M. (2009). The effect of preheating on the IRSL signal from feldspar. Radiation Measurements, 44(5-6), 554-559.

Pagonis, V., Ankjærgaard, C., Murray, A. S., Jain, M., Chen, R., Lawless, J., & Greilich, S. (2010). Modelling the thermal quenching mechanism in quartz based on time-resolved optically stimulated luminescence. Journal of luminescence, 130(5), 902-909.

Poolton, N. R. J., Bos, A. J. J., & Dorenbos, P. (2012). Luminescence emission from metastable Sm2+ defects in Y PO4: Ce, Sm. Journal of Physics: Condensed Matter, 24(22), 225502.

Poolton, N. R. J., Bos, A. J. J., Jones, G. O., & Dorenbos, P. (2010). Probing electron transfer processes in Y PO4: Ce, Sm by combined synchrotron–laser excitation spectroscopy. Journal of Physics: Condensed Matter, 22(18), 185403.

Poolton, N. R. J., Kars, R. H., Wallinga, J., & Bos, A. J. J. (2009). Direct evidence for the participation of band-tails and excited-state tunnelling in the luminescence of irradiated feldspars. Journal of Physics Condensed Matter, 21(48).

Poolton, N. R. J., Ozanyan, K. B., Wallinga, J., Murray, A. S., & Bøtter-Jensen, L. (2002). Electrons in feldspar II: A consideration of the influence of conduction band-tail states on luminescence processes. Physics and Chemistry of Minerals, 29(3), 217–225.

Prasad, A. K. (2017c). Understanding defect related luminescence processes in wide bandgap materials using low temperature multi-spectroscopic techniques (PhD thesis, Technical University of Denmark, Denmark).

Prasad, A. K., Kook, M., & Jain, M. (2017a). Probing metastable Sm2+ and optically stimulated tunnelling emission in YPO4: Ce, Sm. Radiation Measurements, 106, 61-66.

Prasad, A. K., Poolton, N. R. J., Kook, M., & Jain, M. (2017b). Optical dating in a new light: A direct, non-destructive probe of trapped electrons. Scientific Reports, 7(1), 1–15.

Sellwood, E.L., Guralnik, B., Kook, M., Prasad, A.K., Sohbati, R., Hippe, K., Wallinga, J. & Jain, M. (2019). optical bleaching front in bedrock revealed by spatially-resolved infrared photoluminescence. Scientific reports, 9(1), pp.1-12.

Thiel, C., Buylaert, J. P., Murray, A. S., & Tsukamoto, S. (2011). On the

applicability of post-IR IRSL dating to Japanese loess. Geochronometria, 38(4), 369.

Thomsen, K. J., Murray, A. S., Jain, M., & Bøtter-Jensen, L. (2008). Laboratory fading rates of various luminescence signals from feldspar-rich sediment extracts. Radiation Measurements, 43(9–10), 1474–1486.

Trautmann, T., Krbetschek, M. R., Dietrich, A., & Stolz, W. (1999). Feldspar radioluminescence: a new dating method and its physical background. Journal of Luminescence, 85(1-3), 45-58.

Tsukamoto, S., Kondo, R., Lauer, T., & Jain, M. (2017). Pulsed IRSL: A stable and fast bleaching luminescence signal from feldspar for dating Quaternary sediments. Quaternary Geochronology, 41, 26-36.

Van den Eeckhout, K., Bos, A. J., Poelman, D., & Smet, P. F. (2013). Revealing trap depth distributions in persistent phosphors. Physical Review B, 87(4), 045126.

CHAPTER 8

SEDIMENT DATING USING INFRARED PHOTOLUMINESCENCE (IRPL)

Raju Kumar, Myungho Kook & Mayank Jain

Abstract: Infrared photoluminescence (IRPL) is a Stokes-shifted emission arising from internal radiative relaxation of the excited state of the principal dosimetric tap in feldspar (Prasad et al., 2017). Recent investigations have revealed that there exist two IRPL emissions at 880 nm and 955 nm (excitation at 830 nm). Since IRPL does not depend on the recombination centers, the signal can be read out nondestructively; this allows us to insert its measurement in a conventional IRSL (infrared stimulated luminescence) or post IR-IRSL single-aliquot regenerative dose (SAR) protocol.

In this study, we focus on the development of a SAR protocol using the two different IRPL emission bands (centered at 880 nm and 955 nm) and test their potential for sediment dating with known-age samples. Our results show that accurate equivalent doses from 100 to 300 Gy (age range 20-128 ka) can be obtained using an IRPL-based SAR protocol without a fading correction.

8.1 Introduction

Optically stimulated luminescence (OSL) is widely used in geochronology for measuring absorbed dose ($J\,kg^{-1}$) from exposure to ionizing radiation in natural minerals such as quartz and feldspars (Huntley et al., 1985; Wintle, 2008). In the case of feldspar, near-infrared photons (850-880 nm) are used for excitation and the resulting anti-Stokes emission is typically detected in the violet-blue spectral window (340-450 nm). This signal, referred to as infrared stimulated luminescence (IRSL; Hütt et al., 1988) arises from the interaction of the IR photons with the metastable state of the main dosimetric trap (the principal trap) formed by the capture of electrons during prior exposure to ionizing radiation. Interaction between the trapped electrons and the IR photons may lead to de-trapping (i.e. eviction of electrons from the principal trap), transport and eventual radiative recombination with the trapped holes to emit the IRSL signal. Sediment dating using IRSL suffers from an unwanted, time-dependent loss of signal by a process known as anomalous fading (Wintle, 1973). This fading problem can be addressed to a satisfactory extent by either correcting for the fading loss in nature (Huntley and Lamothe, 2001), or utilising novel methods such as the elevated temperature post IR-IRSL (pIR_TIRSL_T, where T is the temperature of IR stimulation) and pulsed IRSL (pIRSL) which rely upon selective sampling of non-fading signals (Thomsen et al., 2008; Buylaert et al., 2012b; Li and Li, 2011; Tsukamoto et al., 2006, 2017; Jain and Ankjærgaard, 2011; Jain et al. 2015b). While these methods present a great advance in our ability to date old samples, there are some inherent problems that restrict their universal application. For example, fading correction is only applicable to natural signals in the linear range of the dose response curve (Huntley and Lamothe, 2001; Morthekai et al., 2008). The pIR_TIRSL_T methods may suffer from problems like poor bleaching, thermal transfer and poor dose recovery, especially for the high temperature signals (T>230 °C) (Yi et al., 2016; Roberts et al., 2012; Lowick et al., 2012; Kars et al., 2014). The pIRSL method is not fully free from fading and has low sensitivity since the signal during the on-time of the pulse is rejected in the data analysis (Jain and Ankjærgaard, 2011; Jain et al., 2015b; Tsukamoto et al., 2017).

Infrared radiofluoroscence (IRRF) or infrared radioluminescence (IRRL) provides an alternative to the optical stimulation methods to date feldspar (Trautmann et al., 1998, 1999; Frouin et al., 2017). The IRRL signal

(peaking at ∼865 nm) originates during exposure to ionizing radiation (e.g., beta particles) from trapping of free electrons into the principal trap (Trautmann et al., 2000; Erfurt and Krbetschek 2002). It has been suggested that IRRL is not affected by anomalous fading (Erfurt and Krbetschek, 2003a, b; Degering and Krbetschek, 2007). However, equivalent dose (D_e) determination on a variety of samples with this method suggests that IRRL suffers from sensitivity changes that could potentially lead to under- or overestimation of the palaeodose (Buylaert et al., 2012a).

Prasad et al. (2017) developed a new method to measure dose in feldspar using a steady-state (non-decaying) signal termed Infrared photoluminescence (IRPL). IRPL is generated by intra-defect transitions in an occupied electron trap; exposure to near infrared light leads to the ground → excited state transition, which is followed by radiative relaxation producing IR photoluminescence (PL). The concentration of occupied traps, and hence the IRPL intensity increases with dose (Prasad et al., 2017). Prasad et al. (2017) used a 1.40 eV (885 nm) laser to excite electrons in the principal trap and measured the Stokes-shifted emission at 1.30 eV (955 nm). In subsequent work, Kumar et al. (2018; Chapter 3 in this thesis) showed that excitation of the principal trap with a lower excitation wavelength (830 nm) results in an additional IRPL emission peak at 1.41 eV (880 nm). Kumar et al. (2018; Chapter 3 in this thesis) also showed that IRPL and IRRL have a similar dosimetric response to x-ray irradiation suggesting that the two signals probe the same trap. Since IRPL is generated without involving recombination centers and can be measured at room temperature, it offers the potential for (i) isolating a non-fading dosimetric signal by selectively sampling electrons from the distant electron-hole pair population using appropriate optical or thermal pretreatment, (ii) enhanced sensitivity (signal-to-noise ratio) because of the repeated excitation of the same trapped electron i.e. single trapped electron gives rise to multiple photons, (iii) non-destructive readout of the dosimetric information (Prasad et al., 2017; Chapter 3 in this thesis), and iv) high-resolution imaging (Sellwood et al., 2019).

The dating potential of IRPL has not been tested thoroughly since its initial demonstration on one sample by Prasad et al. (2017). These authors used an EMCCD (electron multiplying charged couple device) based spectrograph to make these measurements, where breakthrough from the excitation light was an issue. With the integration of the pulsed-

stimulation based IRPL system into the Risø reader for both the 880 nm and the 955 nm emissions (see Chapter 4), it now becomes possible to measure data with high precision (signal-to-noise ratio), and perform routine, automated measurements on a large number of samples and test the potential of IRPL for accurately measuring a palaeodose. In this study, we present the development of a single-aliquot regenerative dose (SAR) protocol for IRPL dating. We then apply this protocol to determine the palaeodose in eight known-age samples. We also examine residual doses in three modern/young samples.

8.2 Samples and instrumentation

Eleven natural sedimentary samples (grain sizes between 90-250 µm) consisting of 8 old (20-128 ka) and 3 young/modern samples (0-10 ka), were used for developing and testing an IRPL SAR protocol (see Table 8.1). These samples have an independent age control from quartz OSL dating, C-14 dating, and have been investigated earlier for testing the performance of the IRRL and pIR_TIRSL_T dating protocols by Buylaert et al. (2012a, b). Expected dose, for each sample, has been calculated from the known age and the dose rate. IRRL ages of these samples were found to be overestimated for younger samples (20-45 ka) and underestimated for older samples (∼130 ka).

All the measurements were performed using a photomultiplier tube (PMT) based IRPL attachment to the Risø TL/OSL reader (Kook et al., 2018; see Chapter 4). This attachment consists of an external laser light source emitting at 1.49 eV (830 nm) and two different photomultiplier tubes (Hamamatsu H7421-50 and Hamamatsu H10330C-25) in combination with the emission bandpass interference filters transmitting 880 nm (FWHM=10 nm) and 950 nm (FWHM=50 nm) for detecting the IRPL emissions at 1.41 eV (880 nm) and 1.30 eV (955 nm), respectively. The power density of the laser at the sample position was measured to be ∼3 mW cm^{-2}. Irradiation of samples was done using a ^{90}Sr/^{90}Y beta source that provides a dose rate of about 0.22 Gy s^{-1}.

The IRPL signals were measured in a pulsed excitation mode (laser on-time 50 µs, and off-time 50 µs; see Chapter 4). The signal was detected after rejecting the first 1 µs in the off-time (PMT gate 51-100 µs) to avoid any contamination from the excitation light during the laser switch-off. The total IRPL measurement time was 5 seconds.

The IRSL signals were detected using BG39 and BG3 filters in front of the same PMT (Hamamatsu H7421-50) that is used to detect the IRPL emission at 1.41 eV (880 nm). IR LEDs emitting at 850 nm (power density ∼250 mW cm^{-2} at the sample position) were used as the excitation source. The switch between different filters and detectors was accomplished using the automated detection and stimulation head (DASH) (Lapp et al., 2015).

Bleaching experiments were performed using IR (850 nm), blue (470 nm) or UV (405 nm) LEDs with power densities of ∼250, ∼80, and ∼140 mW cm^{-2} at the sample position, respectively. A solar simulator (Hönle, SOL2) was also used to mimic signal resetting in daylight.

Room temperature (RT) mentioned throughout the text refers to ∼25 °C. Both IRPL and IRSL data were analyzed using the Matlab software. Analysis of the IRSL data was confirmed using the Analyst software.

Table 8.1: List of samples used in this study. Sample 075602, superscripted with *, is considered to have an unknown dose in this study.

Site and Location	Sample code	Sediment type	Expected D_e (Gy±se)	Reference
Gammelmark (Denmark)	981009	Sand	279±11	Murray and Funder, 2003; Buylaert et al., 2012b
	981010	Sand	298±12	
	981013	Sand	274±12	
Sula (Russia)	H22553	Sand	209±11	Murray et al., 2007; Buylaert et al., 2012b
	952503	Coastal marine	262±12	
Carregueira (Portugal)	072255	Aeolian sand	97±7	Buylaert et al., 2012b
Indre-et-Loire (France)	092202	Colluvium	158±10	Aubry et al.,2012; Buylaert et al., 2012b
Sinai peninsula (Egypt)	075407	Reworked dune sands	103±7	Buylaert et al., 2012b
North Jutland (Denmark)	075602	Aeolian sand	18±1*	Buylaert et al., 2012b
Zwolle (TheNetherlands)	082105	Aeolian sand	Unknown	Buylaert et al., 2012b
Unknown	B12	Unknown	Unknown	this study

8.3 Development of the IRPL dose measurement protocol

Current luminescence dating techniques are based on estimating equivalent dose (D_e) or palaeodose from dose distributions measured using multi-grain single-aliquots or single grains (Duller 1991, 1995, 1999). Two main approaches used for measuring D_e are 'additive dose' and 'regenerative dose'. In the additive dose approach, laboratory doses are added onto the natural signal to build a dose-response curve (DRC). This curve is then extrapolated to the dose axis to estimate the D_e. In the regenerative approach, the luminescence signal is zeroed each time after measuring the luminescence response to the natural or the laboratory dose. The natural signal is then interpolated onto the laboratory DRC to obtain an equivalent dose (Duller 1995). In the regenerative dose methods, the luminescence sensitivity may change during laboratory treatments such as preheating and optical bleaching leading to an under- or overestimate of the palaeodose. Such a sensitivity change can be monitored and corrected by using luminescence response to a test dose delivered after the measurement of the natural or the regenerated signals (Murray and Wintle, 2000; Murray et al., 2002; Murray et al., 2003; Wintle and Murray, 2006); this method is known as the single-aliquot regenerative (SAR) dose technique. The main advantage of the SAR compared to the additive dose technique is that dose estimation relies on interpolation rather than extrapolation of the natural signal making it less sensitive to the DRC fitting model. Furthermore, the interpolation method is more precise and accurate than extrapolation when dealing with older samples whose natural signal lies at >40% of the saturation level (corresponding to about half of the characteristic dose, D_0, of the DRC).

Prasad et al. (2017) demonstrated that IRPL is amenable to both the additive and the regenerative dose methods. It is possible to apply all the tests of internal consistency such as recuperation, recycling, preheat plateau and dose recovery tests commonly used in the SAR method to the IRPL signal. Since one of the main applications of feldspar is extending the age range compared to that of quartz, in this article we have chosen to focus on the regenerative dose method rather than the additive dose method since it allows estimation by interpolation. Because of its high sensitivity, IRPL can be measured using very low power laser excitation leading to a non-destructive measurement even at room temperature

(Kook et al., 2018; Chapter 4 in this thesis). Thus, IRPL can be easily integrated into the existing SAR protocols used for IRSL and pIR_TIRSL_T to monitor the population of trapped electrons after each step such as preheating, optical stimulation and high temperature clean-out.

In order to develop the SAR protocol, it is first necessary to find out how to reset the signal; this is investigated in the next section.

8.3.1 Thermo-optical resetting of IRPL

Signal resetting is a pre-requisite for designing a SAR protocol. The resetting behavior of IRPL was investigated using sample 981010 (3 aliquots; see Table 8.1) and measuring its response to IR (∼850 nm), blue (∼470 nm) or UV (∼405 nm) light exposure in the Risø reader. Signal resetting was also evaluated using the solar simulator.

Table 8.2 shows the steps involved in the measurement of the IRPL bleaching curves. The aliquots were first bleached with IR light at 290 °C for 100 s to reset the signal; this bleaches the IRPL signals at 880 nm and 955 nm to ∼85% and ∼95%, respectively, of the initial value; note that, although this treatment empties the IRPL signal to a residual, the purpose of these investigations is to optimize the bleaching procedure for the SAR protocol. The bleached aliquots were given a dose (∼440 Gy) followed by a preheat at 320 °C for 60 s. Subsequently, the 'initial' IRPL signals were recorded for 5 s (steps 3 and 4). The aliquots were then exposed to IR or blue light at different temperatures (50-290 °C) for 100 s in different cycles followed by the measurement of the IRPL signals. Since IRPL does not decay during the 5 s readout, no correction is required for possible loss of signal due to the measurement itself. The ratio of the remaining IRPL divided by the initial IRPL for different bleaching conditions is shown in Figures 8.1a and b. As expected, for both IR and blue light, the bleaching efficiency increases with the bleaching temperature. Maximum bleaching was observed at 290 °C resulting in a signal loss of ∼47% and ∼70% for the blue light, and ∼85% and ∼95% for the IR light, for the 880 nm and 955 nm emission bands, respectively.

We then measured the bleaching as a function of exposure time using IR or blue light (at 290 °C or room temperature) for exposure times varying from 0 s to 900 s. The bleaching curve was also measured for UV light at room temperature (UV_{RT}, where RT refers to room temperature; our experimental setup did not allow changing temperature during the UV exposure). The results are summarised in Figures 8.1c and d, where de-

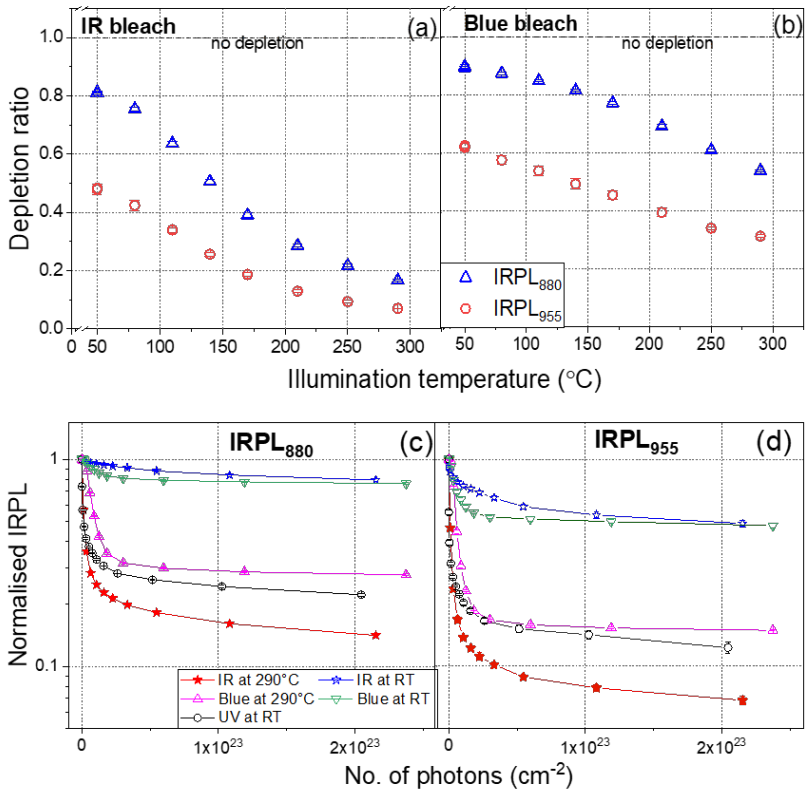

Figure 8.1: IRPL bleaching experiments on sample 981010. Three aliquots were used for each data point. (a) Depletion ratio of the IRPL signals plotted against the IR illumination temperature. (b) Depletion ratio of the IRPL signals plotted against blue illumination temperature. (c, d) IRPL signals plotted as a function of the number of photons (cm^{-2}) from different light sources (IR, blue and UV) hitting the sample. The data are presented for measurements at 25 °C (RT) and at 290 °C.

pletion in IRPL is plotted against the number of photons (cm^{-2}) hitting the sample. Resetting of the IRPL signals in daylight was studied over 40 hours using a solar simulator (Hönle SOL2) (Figure SI 8.1). These results lead to the following conclusions:

1. From the different wavelength-temperature (λ-T) configurations used here (Figure 8.1), IR light is more effective in bleaching than blue light.

2. For signal resetting, IR exposure at 290 °C (IR_{290}) is the most efficient; this results in a residual level of ∼15% for the 880 nm emission, and ∼5% for the 955 nm emission compared to the unexposed sample. UV_{RT} exposure is the second most efficient followed by Blue exposure at 290 °C ($Blue_{290}$) for the approximately same number of photons hitting the sample. Both in the case of UV_{RT} and IR_{290}, the bleaching curve has not reached a constant value but seems to decrease very slowly, as it approaches the maximum exposure durations in our experiments.

3. Both IR and Blue light are rather inefficient in zeroing the IRPL signal at room temperature. The net signal depletion in the plateau region is ∼20% in the case of the 880 nm emission and ∼45% in the case of the 955 nm emission (Figure 8.1c and d). These results imply that during IRSL or OSL measurement at room temperature in feldspar we only sample about 20-45% of the total electron population in the principal trap. The remaining population does not participate in room temperature OSL likely because of a recombination bottleneck, i.e. the lack of trapped holes in the vicinity of the electron trap (Jain and Ankjærgaard, 2011).

4. The 880 and 955 nm emissions show similar trends for different bleaching ($\lambda - T$) configurations. However, for any given configuration the 955 nm emission ($IRPL_{955}$) bleaches significantly faster and reaches the lowest value at the end of 100 s of bleaching than the 880 nm emission ($IRPL_{880}$) (Figure 8.1).

5. A 1000 s of daylight (solar simulator) exposure bleaches $IRPL_{880}$ by ∼75% and $IRPL_{955}$ by ∼85%. Further exposure (up to 20 hours) bleaches the IRPL signals at 880 nm and 955 nm slowly to a residual level of ∼90% and ∼95%, respectively. The signals decay very

slowly afterwards and are bleached by only ∼1% during additional 20 hours of exposure (Figure SI 8.1).

Table 8.2: Outline of the protocol used to investigate laboratory resetting of the IRPL signals. All the IRPL measurements are made at room temperature for 5 s. Aliquots were exposed to IR at 290 °C before starting step 1.

Step	Measurement
1	Beta irradiation for 2000 s (440 Gy)
2	Preheat at 320 °C for 60 s
3	**$IRPL_{880}$**
4	**$IRPL_{955}$**
5	IR or Blue bleaching at T °C for 100 s (T= 50, 100,....., or 290)
6	**$IRPL_{880}$**
7	**$IRPL_{955}$**
8	IR Bleaching at 290 °C for 100 s
9	Return to step 1

Given its lower photon energy, it is somewhat surprising that IR_{290} is more efficient in emptying the principal trap than $Blue_{290}$, and it results in a plateau value that is significantly lower than that for $Blue_{290}$ bleaching (∼20% for $IRPL_{880}$ and ∼15% for $IRPL_{955}$). Similarly, UV, which must release almost all the electrons into the conduction band, is not as efficient as IR_{290}. We interpret these data to suggest that there must be significant charge transfer from the deeper traps into the principal trap when using higher energy light (blue and UV). In the case of IRSL, even at high temperature, we are probably mainly looking at the emptying of the principal trap without significant retrapping from the shallow traps accessible by the IR light. From the point of view of signal emptying during SAR, we therefore, choose IR_{290} or IR_{220} (Figure 8.1a) for 100 s depending on the preheat (discussed in the next section).

8.4 A coupled IRPL-IRSL SAR protocol

Table 8.3 shows the steps involved in the IRPL-IRSL SAR protocol. This protocol consists of the insertion of the two IRPL measurements, 880 and 955 nm, at the different stages of a multiple elevated temperature IRSL

protocol (MET-pIRIR; Li and Li, 2011). The IRPL signals were always measured at 25 °C (RT) at the following stages of the SAR cycle: i) before and after the preheat, ii) after each IRSL measurement (pIR_T-IRPL), and iii) after the high temperature optical clean-out for determining the 'unbleachable' IRPL for background subtraction ($IRPL_{bkg}$). The reason we chose a multiple-step protocol instead of a single step protocol is because we are not limited by the signal sensitivity as compared to the IRSL signals in the MET-pIRIR, and because it allows us to directly track the trapped electron population after different levels of detrapping by high temperature IR exposure. However, our initial results demonstrated that the IRPL signals measured after $pIRIR_{>90°C}$ suffered from poor bleaching; therefore, we restricted the MET-pIRIR protocol to only 50 °C and 90 °C temperatures as shown in Table 8.3.

We investigated two different measurement protocols, A and B. The main difference between these protocols lies in the choice of the preheat temperature, 320 °C/60 s (protocol A) corresponding to the $pIR_{50}IRSL_{290}$ protocol (Thomsen et al., 2008; Buylaert et al., 2009), and 260 °C/60 s (protocol B) corresponding to the $pIR_{50}IRSL_{225}$ protocol (Thomsen et al., 2008, 2011). The clean-out temperatures before administering a regenerative or test dose are adjusted accordingly to be at 290 °C and 220 °C, respectively. These clean-out temperatures were kept to be significantly below the preheat temperature to avoid any charge transfer or sensitivity change induced due to high temperature bleaching.

The two IRPL signals were measured before (BPh-IRPL; steps 1 and 2) and after (APh-IRPL; steps 4, and 5) preheat (step 3). This was followed by IRSL measurement at 50 ∘C ($IRSL_{50}$; step 6), and again the measurement of the IRPL signals ($pIR_{50}IRPL$; steps 7, and 8) to observe the depletion in trapped electrons due to IRSL. The IRSL-IRPL procedure was then repeated for IRSL at 90 °C ($IRSL_{90}$, $pIR_{50,90}IRPL$; steps 9, 10 and 11). Finally, a high-temperature IR exposure (at 290 °C or 220 °C) was performed to reduce the IRPL signal to a background or residual level (steps 12, 13, and 14). This residual IRPL likely represents traps that are hard to empty because of the lack of association with a nearby recombination center (Jain et al., 2012, 2015a). This set of measurements was repeated after a test dose for monitoring any possible sensitivity change (steps 15 to 29), to complete a full SAR cycle.

Table 8.3: Outline of the coupled IRPL-IRSL SAR protocol. Two protocols were tested that differ in the combination of preheat and high temperature IR bleaching used to clean out the signals. The protocol that uses a preheat temperature of 320 °C and IR bleaching at 290 °C is referred to as 'protocol A'. The protocol that uses a preheat temperature of 260 °C and IR bleaching at 220 °C is referred to as 'protocol B'. All the IRPL measurements are made at room temperature for 5 s. BPh=before preheat, APh= after preheat. * refers to the same indices as used in the preceding steps (1 - 14) for the measurement of the natural or the regeneration dose signals (L_x).

Step	Measurement	Signal
0	Natural or Regeneration dose	
1	$IRPL_{880}$	L_x BPh-IRPL
2	$IRPL_{955}$	
3	**Preheat at T°C for 60 s (T_1=320 or T_2=260)**	
4	$IRPL_{880}$	L_x APh-IRPL
5	$IRPL_{955}$	
6	**IRSL at 50 °C for 100 s**	**L_x $IRSL_{50}$**
7	$IRPL_{880}$	L_x pIR_{50} IRPL
8	$IRPL_{955}$	
9	**IRSL at 90 °C for 100 s**	**L_x $pIR_{50}IRSL_{90}$**
10	$IRPL_{880}$	L_x $pIR_{50,90}$ IRPL
11	$IRPL_{955}$	
12	**IR bleaching T°C for 100 s (T_1=290 or T_2=220)**	
13	$IRPL_{880}$	L_{BG}
14	$IRPL_{955}$	
15	Test dose	
16-29	Repeat 1-14	T_x *

8.5 Performance of the IRPL-IRSL SAR protocol

The results from the coupled IRPL-IRSL protocol A and protocol B are described below.

8.5.1 Dose response curves

Figures 8.2a and b show the two $IRPL_{880}$ and $IRPL_{955}$ signals, respectively, measured after different doses given to sample 981010, following protocol A. As expected the signal intensity is constant (steady-state) over the 5 s measurement period for all doses. For a given dose, the relative intensity of the two IRPL signals differs by more than an order of magnitude because of the difference in the sensitivity of the two IRPL detectors (PMTs). Furthermore, from the spectroscopic data, we know that the two peaks have different intensities (880 nm peak is generally stronger) and the relative intensity of the two peaks varies between samples (Kumar et al., 2018; Chapter 3 in this thesis).

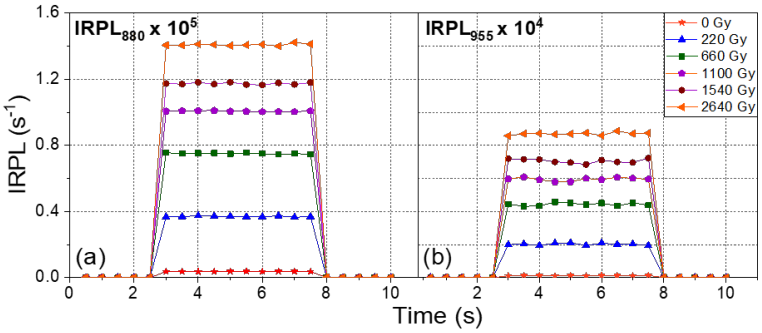

Figure 8.2: Representative IRPL signals at (a) 880 nm and (b) 955 nm for different regeneration doses delivered to an aliquot of sample 981010. These data are obtained using protocol A. Two different detectors were used to measure these two IRPL emissions (see Section 8.2). The signals are not background subtracted. The intensity of the zero (0) dose signal is close to the unbleachable residual remaining after IR bleaching at 290 °C for 100 s.

Figure 8.3 shows the dose response curves (DRCs) obtained using the IRPL signals at different stages and the $IRSL_{50}$ signal (Table 8.3). For a given dose, the signal is calculated as the average IRPL intensity (during

the 5 s measurement) minus the average IRPL intensity obtained after the clean-out steps (13 or 14 for the regeneration or natural dose, 28 or 29 for the test dose). Following the SAR procedure (Murray and Wintle, 2000), the test dose signals were used for sensitivity correction. Figures 8.3a and c show the results for the $IRPL_{880}$ signal obtained using protocol A and protocol B, respectively. Figures 8.3b and d show the results from these protocols for the $IRPL_{955}$ signal. Note that $IRSL_{50}$ DRC in the top and bottom figures are the same since there is only one IRSL corresponding to both the IRPL emissions (Table 8.3). All DRCs are best fitted to a double exponential function (characteristic dose values, D_{01} and D_{02} at different stages of the protocols are listed in Table 8.4). The IRPL signals at different stages of the protocols (BPh-IRPL, APh-IRPL, $pIR_{50}IRPL$, and $pIR_{50,90}IRPL$) have different saturation levels which are also different from the saturation level of the $IRSL_{50}$ signal.

For protocol A, the IRPL signals before preheating (BPh-IRPL) saturate at a significantly higher dose compared to all the other IRPL signals (APh-IRPL, $pIR_{50}IRPL$, $pIR_{50,90}IRPL$). The $IRSL_{50}$ signal saturates somewhere between these two sets of IRPL DRCs. For protocol B, we see a similar trend as protocol A, however, there exist slight differences in the dose responses between APh-IRPL, $pIR_{50}IRPL$, and $pIR_{50,90}IRPL$ signals. Furthermore, the DRCs in protocol A saturate slightly earlier than those in protocol B; this may be attributed to higher preheat and cleanout temperature in protocol A. In general, the IRPL DRCs saturate earlier when the IRPL signal intensity is depleted either by preheat or IRSL measurement; this trend is similar to that observed for the IRSL and pIR_TIRSL_T signals where the pIR_TIRSL_T DRCs saturate earlier as more stable (thermal and athermal) signals are accessed (Andersen et al., 2012; Li & Li, 2011). The highest characteristic dose (D_{02} ~1900 Gy) is obtained for the IRPL signal before preheat (BPh-IRPL) using protocol A or B.

8.5.2 Recycling and recuperation

The recycling ratio is the ratio between the L_x/T_x values obtained from two different SAR cycles performed using the same regeneration dose. Figure 8.4 summarises the recycling ratio for all the measured samples. Figures 8.4a and b show recycling of the $IRPL_{880}$ and $IRPL_{955}$ signals respectively at each stage of protocol A, whereas Figures 8.4c and d show recycling of the IRPL signals at each stage of the protocol B, for all the

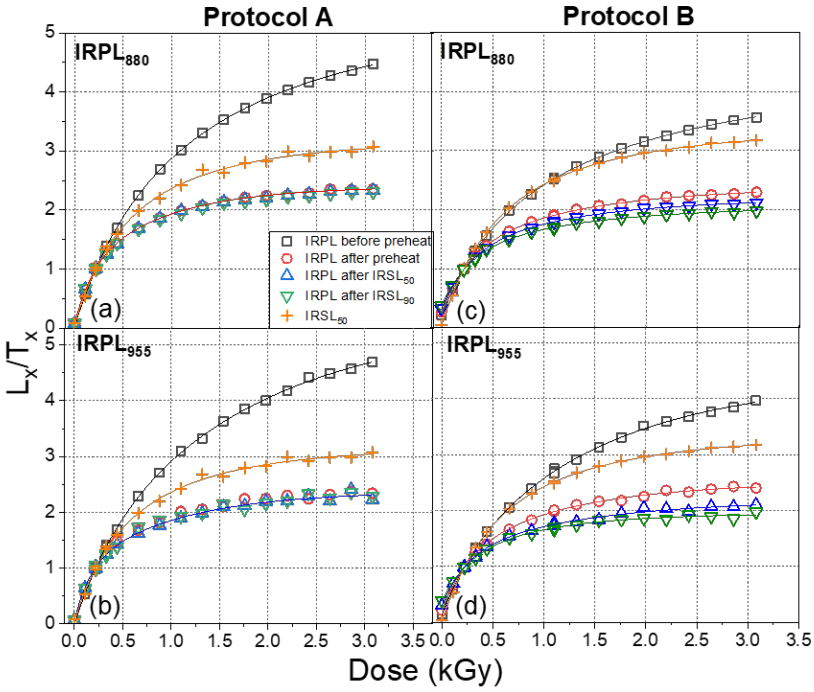

Figure 8.3: *Left column:* dose response curves (DRCs) of the IRPL signals (a) 880 nm and (b) 955 nm using protocol A. *Right column:* DRCs of the IRPL signals (c) 880 nm and (d) 955 nm using protocol B. See Table 8.3 for details. The signals have been sensitivity corrected (L_x/T_x). Protocol A results in similar DRC for IRPL signals after preheat (APh-IRPL), after $IRSL_{50}$ ($pIR_{50}IRPL$), and after $IRSL_{90}$ ($pIR_{50,90}IRPL$), which are together fitted to a sum of two exponential functions. The DRCs obtained using protocol B have different saturation characteristics. The characteristic doses obtained from each DRC are listed in Table 8.4.

Table 8.4: Summary of characteristic dose (D_0) values obtained using protocol A and protocol B. The measurements were made using one aliquot of the sample 981010. The D_0 values for the $IRSL_{50}$ signal are listed commonly. Errors here are obtained from fitting of the exponential function.

Signal	Protocol A				Protocol B			
	$IRPL_{880}$		$IRPL_{955}$		$IRPL_{880}$		$IRPL_{955}$	
	D_{01} (Gy)	D_{02} (Gy)	D_{01} (Gy)	D_{02} (Gy)	D_{01} (Gy)	D_{02} (Gy)	D_{01} (Gy)	D_{02} (Gy)
BPh-IRPL	473 ± 59	1838 ± 260	388 ± 121	1795 ± 400	447 ± 50	1989 ± 350	324 ± 96	1481 ± 220
APh-IRPL	184 ± 19	882 ± 56	195 ± 31	1052 ± 182	227 ± 26	1207 ± 160	253 ± 53	1118 ± 245
$IRSL_{50}$	332 ± 170	1074 ± 570	332 ± 170	1074 ± 570	374 ± 42	1240 ± 220	374 ± 42	1240 ± 220
$pIR_{50}IRPL$	184 ± 19	882 ± 56	195 ± 31	1052 ± 182	269 ±20	1137 ± 140	243 ± 59	1314 ± 510
$pIR_{50,90}IRPL$	184 ± 19	882 ± 56	195 ± 31	1052 ± 182	265 ± 27	1198 ± 215	256 ± 100	891 ± 370

samples. Either three or six aliquots were measured per sample (see in Table 8.5 and 8.6). The recycling ratios are found to be excellent within 10% of unity for both the protocols.

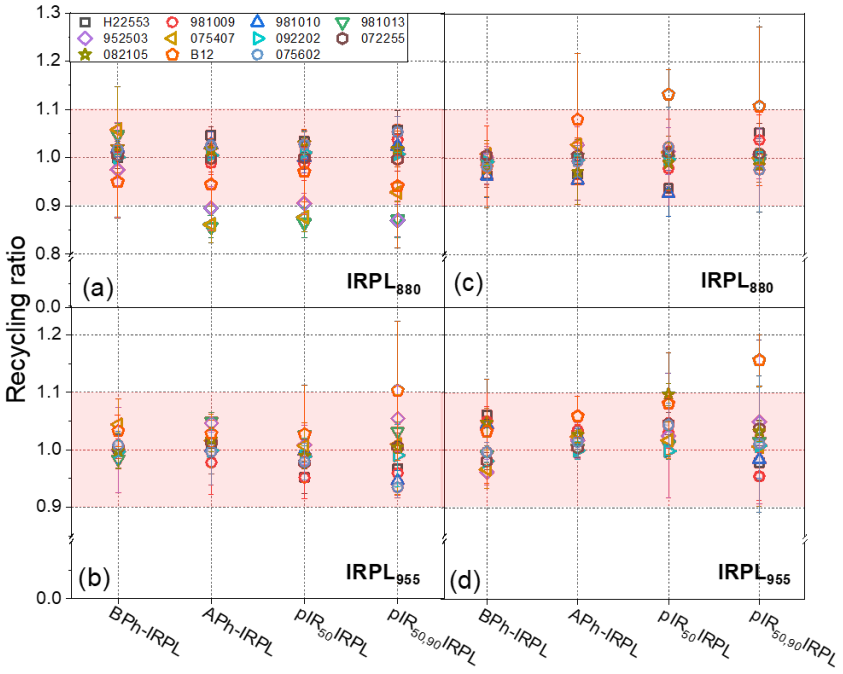

Figure 8.4: *Left column:* (a,b) Recycling ratio of the different $IRPL_{880}$ and $IRPL_{955}$ signals (see Table 8.3) for protocol A. *Right column:* (c,d) Recycling ratio of the different $IRPL_{880}$ and $IRPL_{955}$ signals for protocol B.

Recuperation is the ratio between the L_x/T_x values for the zero dose and the natural dose cycle. Recuperation % is plotted in Figure 8.5. Surprisingly, the IRPL signals before preheat (BPh-IRPL) result in low recuperation (<5%) for all samples. However, the signals after preheat and so on (APh-IRPL, $pIR_{50}IRPL$, and $pIR_{50,90}IRPL$) result in relatively higher recuperation ranging from 5-12% using protocol A (Figures 8.5a and b), and 7-18% using protocol B (Figures 8.5c and d). A closer examination of the zero dose point (data not shown) suggests that there is minor charge transfer during the preheat. But most importantly the clean-out step (Steps 12 and 27; Table 8.3) results in further depletion of

even the zero dose signal resulting in a finite IRPL after the background subtraction. The greater the relative depletion compared to the clean-out at the end of the previous cycle, the higher the apparent recuperation. We observe that this relative depletion is greater for protocol B compared with protocol A, probably because of the lower preheat in Protocol B (260 °C/60s) results in relatively more unstable charge than in protocol A. The reason why this recuperation is less evident in the case of BPh-IRPL can be ascribed to relatively high intensity of this signal (no depletion by heating). In general, we consider these recuperation values as acceptable; the performance of the SAR protocol is further tested using the dose recovery test and D_e estimation of the known-age samples in the next sections.

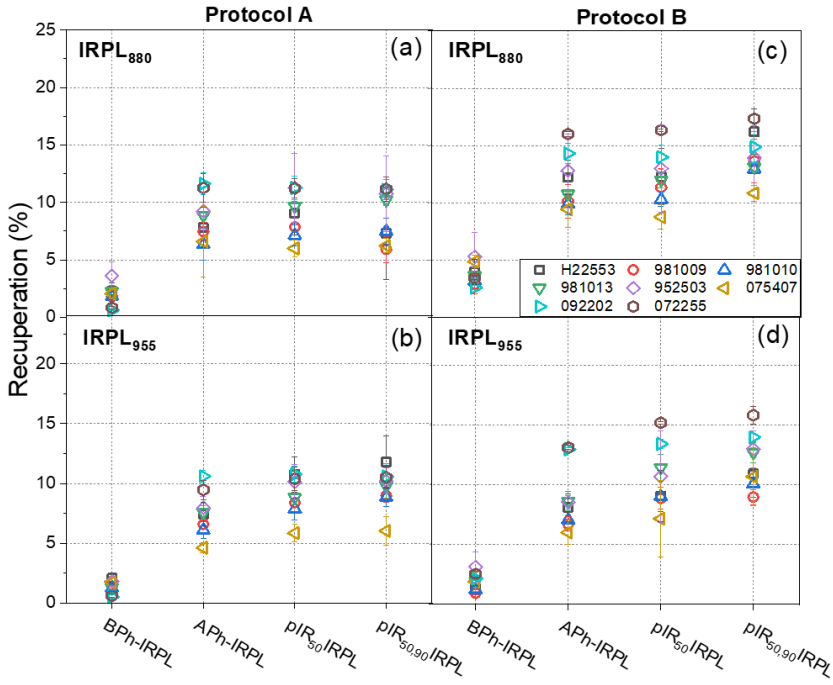

Figure 8.5: *Left column:* (a,b) Percentage recuperation of the different $IRPL_{880}$ and $IRPL_{955}$ signals for protocol A (see Table 8.3). *Right column:* (c,d) Percentage recuperation of the different $IRPL_{880}$ and $IRPL_{955}$ signals for protocol B.

8.5.3 Dose recovery test

A dose recovery test consists of administering a known beta/gamma dose to an unheated modern or laboratory bleached sample and then estimating this dose using the measurement protocol under investigation. If the measured dose minus the residual dose equals the given dose to the sample, then it is inferred that the measurement protocol does not result in any systematic errors. A dose recovery test is commonly used for the SAR protocol as an indicator of the robustness of dose measurement (Wallinga et al., 2000; Murray et al., 2003).

We applied a dose recovery test to one of the modern samples (082105). A set of six aliquots were given a 230 Gy beta dose and another set of six aliquots did not receive any dose. Subsequently, three aliquots from each set were measured using either protocol A or protocol B. Residual dose was measured from the aliquots that did not receive a beta dose. These residual doses were then subtracted from the D_e estimates obtained using the corresponding signals from the aliquots that received 230 Gy. Figure 8.6a shows the D_e obtained using the $IRPL_{880}$ and $IRPL_{955}$ signals for protocol A. Figure 8.6b shows these data using protocol B. Both the protocols result in an acceptable recovery of the given dose (within $\pm 10\%$ of the expected value) for all the IRPL signals examined here. However, interestingly the IRSL and pIR_TIRSL_T signals result in a poor recovery of the given dose, which is not uncommon (Buylaert et. al., 2012b; Kars et al., 2014; Lowick et al., 2012).

8.6 Applying IRPL-IRSL SAR to sediment dating

The coupled IRPL-IRSL SAR protocol was tested on eight known age (20 ka to 128 ka) samples. The obtained equivalent doses (D_e) at different stages of the protocol have been summarized in Table 8.5 for protocol A and Table 8.6 for protocol B.

The D_e values for the six old samples are plotted individually in Figure 8.7. The D_e values for the two relatively younger and three modern samples are plotted individually in Figure 8.8. The left column presents the results for protocol A, and the right column for protocol B. The solid black line denotes the expected dose estimated from the known age and dose rate of each sample. The grey band represents one standard

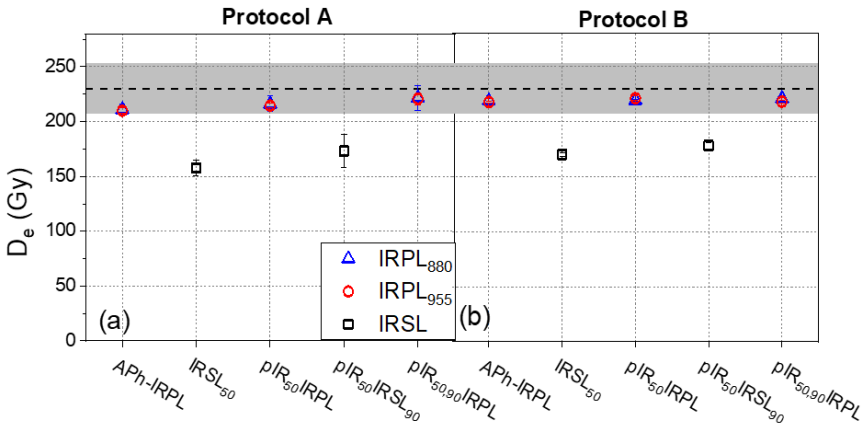

Figure 8.6: Results from the dose recovery test on sample 082105. The measured dose obtained using the different IRPL signals (see Table 8.3 for details) are plotted for (a) protocol A, and (b) protocol B. The grey band represents 10% deviation from the given dose (230 Gy).

deviation (1σ), and the dashed lines represent two standard deviations (2σ) of the expected dose based on the reported uncertainties (Buylaert et al., 2012). The x-axis shows the IRPL and pIR_TIRSL_T signals measured during different stages of the SAR cycle (Table 8.3).

The D_e values for the young/modern samples are plotted in Figure 8.8. Since we do not know the exact ages of the three notionally modern/young samples (B12, 082105 and 075602), their maximum apparent expected dose is defined using the IRSL signals. Moreover, in our three modern/young samples, we see a natural IRSL D_e of less than 5 Gy. The measured IRPL (APh-IRPL) doses in these samples are of the order of 8-40 Gy for the $IRPL_{955}$ and 13-70 Gy for the $IRPL_{880}$ signals. These data suggest that the IRPL bleaches slower than the IRSL in nature.

In general, we observe a fairly good agreement between the IRPL doses at different stages and the expected doses. The extent of agreement varies from sample to sample. The IRSL signals, on the other hand, show a large deviation from the expected answer. A qualitative summary of the results for the old samples (Figures 8.7, and 8.8) is presented in Figures 8.9 and 8.10 for the $IRPL_{880}$ and $IRPL_{955}$, respectively. Here, D_es consistent with the 1σ band are marked as the deep-red cells, D_es outside 1σ but inside 2σ band are marked as red cells, and D_es outside the 2σ band are marked as light-red cells. The purpose of this represen-

Table 8.5: Summary of measured equivalent dose (D_e) values using protocol A.

Sample code	No. of aliquots (n)	D_e, $IRPL_{880}$ (Gy ± se)				D_e, $IRPL_{955}$ (Gy ± se)				Expected D_e (Gy ± se)	Expected D_e, IR-RF (Gy ± se)
		BPh-IRPL	APh-IRPL	pIR_{50} IRPL	$pIR_{50,90}$ IRPL	BPh-IRPL	APh-IRPL	pIR_{50} IRPL	$pIR_{50,90}$ IRPL		
981009	3	293±3	265±4	297±9	325±18	244±3	226±3	279±14	298±14	279±11	229±12
981010	3	306±6	267±7	280±5	309±2	267±2	246±9	282±16	288±6	298±12	218±11
981013	6	289±2	314±3	331±2	348±4	261±5	245±4	296±4	319±7	274±12	193±12
H22553	3	275±23	232±10	248±11	262±16	230±16	205±10	237±10	250±5	209±11	155±4
952503	6	250±10	263±6	288±7	304±8	228±4	226±8	255±6	280±7	262±12	183±7
072255	3	147±4	105±7	103±6	104±6	125±2	94±2	105±4	108±4	97±7	155±4
092202	3	218±10	156±10	159±11	161±13	185±5	146±3	151±4	162±10	158±10	221±12
075407	6	110±3	121±3	129±3	133±4	103±1	104±1	124±3	131±4	103±7	153±7
075602	3	43±2	41±2	45±2	47±4	29±1	32±2	44±2	52±5	Unknown	Unknown
082105	3	13±1	12±1	11±1	11±1	8±1	8±1	10±1	11±2	Unknown	Unknown
B12	3	71±7	68±6	70±4	70±1	33±2	39±1	66±5	72±4	Unknown	Unknown

Table 8.6: Summary of measured equivalent dose (D_e) values using protocol B.

Sample code	No. of aliquots (n)	D_e, $IRPL_{880}$ (Gy ± se)				D_e, $IRPL_{955}$ (Gy ± se)				Expected D_e (Gy ± se)	Expected D_e, IR-RF (Gy ± se)
		BPh-IRPL	APh-IRPL	pIR_{50} IRPL	$pIR_{50,90}$ IRPL	BPh-IRPL	APh-IRPL	pIR_{50} IRPL	$pIR_{50,90}$ IRPL		
981009	3	226±7	220±6	213±7	217±3	243±2	242±1	257±12	260±7	279±11	229±12
981010	3	294±26	260±9	276±23	275±14	267±5	262±3	290±11	282±1	298±12	218±11
981013	3	247±3	248±2	265±5	271±4	216±1	229±3	254±4	236±4	274±12	193±12
H22553	3	197±15	162±20	186±16	198±17	209±14	216±13	247±14	284±14	209±11	155±4
952503	3	228±2	218±17	228±24	250±26	189±2	194±7	224±12	221±4	262±12	183±7
072255	3	134±3	92±3	95±3	95±2	106±1	87±1	93±1	97±1	97±7	155±4
092202	3	202±4	143±2	151±6	152±1	166±1	137±1	148±2	152±1	158±10	221±12
075407	3	101±3	107±3	120±5	126±5	83±2	96±3	106±7	116±13	103±7	153±7
075602	3	32±3	21±1	24±2	27±1	19±1	17±1	22±1	29±1	Unknown	Unknown
082105	3	6±1	3±1	3±1	1±1	6±1	3±1	3±1	4±1	Unknown	Unknown
B12	3	37±4	34±4	34±5	49±8	24±3	24±4	39±6	42±5	Unknown	Unknown

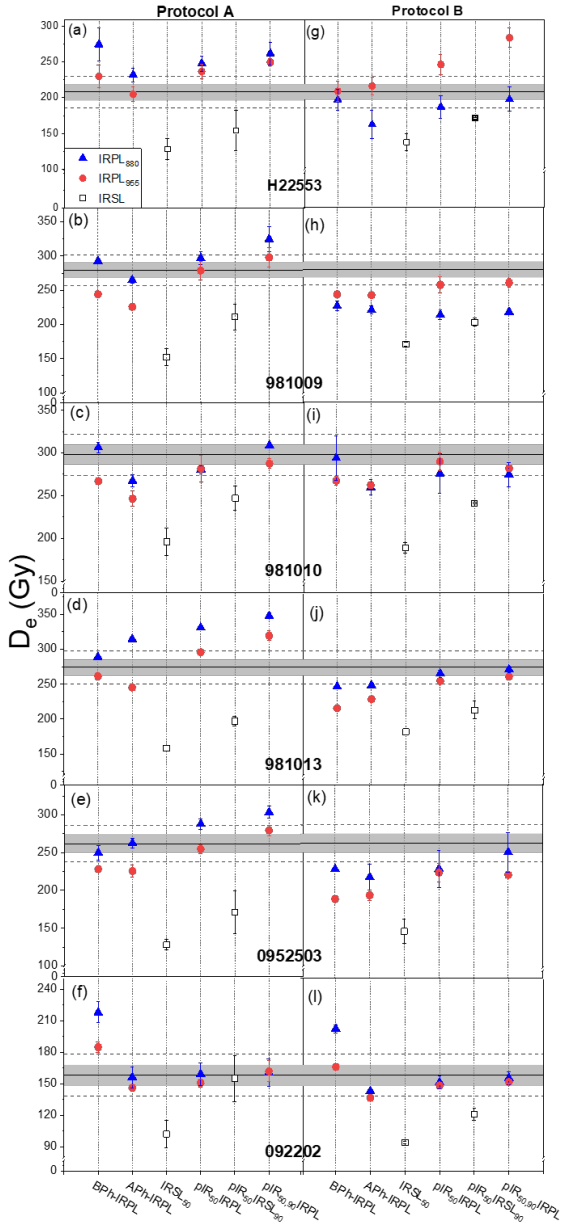

Figure 8.7: (a-f) Measured equivalent doses (D_es) from the 6 known-age samples using protocol A (left column. (g-l) Measured equivalent doses (D_es) from the 6 known-age samples using protocol B (right column). The x-axis shows the different IRPL signals used for D_e estimation (see Table 8.3). The grey band represents 1σ deviation from the expected dose, while the band under dashed line represents 2σ deviation. Blue and red symbols indicate the D_e values obtained for the $IRPL_{880}$ and $IRPL_{955}$ signals, respectively. Hollow black squares represent D_e from the IRSL signals.

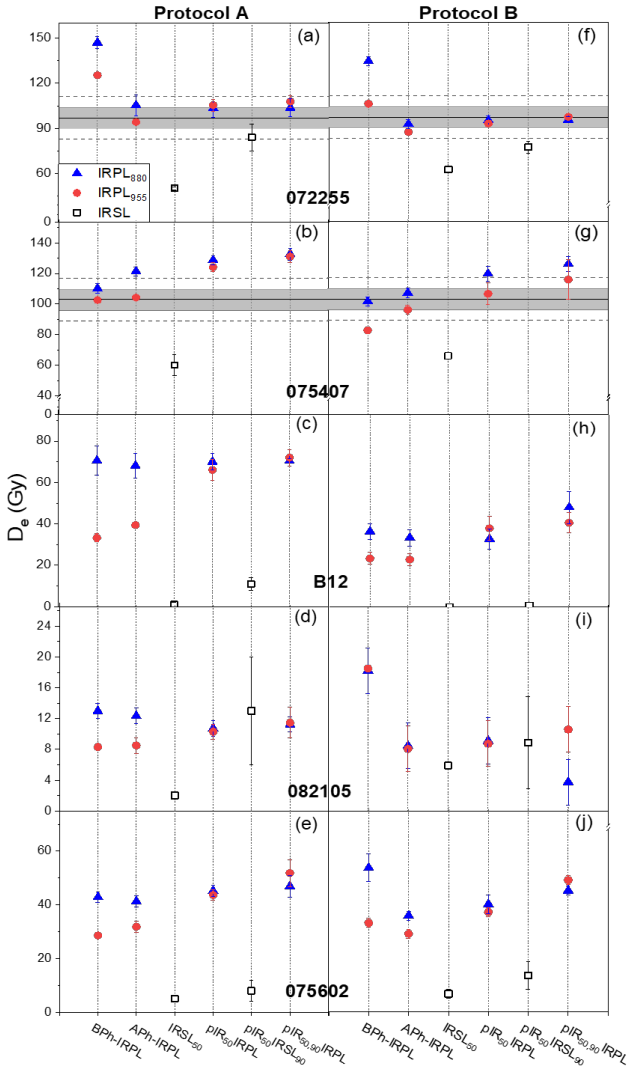

Figure 8.8: (a-e) Measured equivalent doses (D_es) from the 2 known-age and 3 unknown-age samples using protocol A (left column). (f-j) Measured equivalent doses (D_es) from the 2 known-age and 3 unknown-age samples using protocol B (right column). The x-axis shows the different IRPL signals used for D_e estimation (see Table 8.3). The grey band represents 1σ deviation from the expected dose while the dashed lines represent 2σ deviation. Blue and red symbols indicate the D_e values obtained for the $IRPL_{880}$ and $IRPL_{955}$ signals, respectively. Hollow black squares represent D_e from the IRSL signals.

tation is to get a visual overview of the performance of the different signals. For the $IRPL_{955}$ (Figure 8.10), D_es estimates using $pIR_{50}IRPL$ and $pIR_{50,90}IRPL$ signals are generally consistent with the expected doses within 2σ, for both protocol A and B. However, for the $IRPL_{880}$, the $pIR_{50,90}IRPL$ signal using protocol B seems to perform the best (Figure 8.9).

Sample (dose)	Protocol A				Protocol B			
	BPh-IRPL	APh-IRPL	pIR_{50} IRPL	$pIR_{50,90}$ IRPL	BPh-IRPL	APh-IRPL	pIR_{50} IRPL	$pIR_{50,90}$ IRPL
H22553 (209 Gy)								
981009 (279 Gy)								
981010 (298 Gy)								
981013 (274 Gy)								
952503 (262 Gy)								
092202 (158 Gy)								
072255 (97 Gy)								
075407 (103 Gy)								

Figure 8.9: Ranking of D_es obtained using the $IRPL_{880}$ signals at different stages of the protocol. Deep-red cells represent D_es consistent with the 1σ band, red cells represent the D_es outside 1σ but inside 2σ band, light-red cells represent and the D_es outside the 2σ band.

Sample (dose)	Protocol A				Protocol B			
	BPh-IRPL	APh-IRPL	pIR_{50} IRPL	$pIR_{50,90}$ IRPL	BPh-IRPL	APh-IRPL	pIR_{50} IRPL	$pIR_{50,90}$ IRPL
H22553 (209 Gy)								
981009 (279 Gy)								
981010 (298 Gy)								
981013 (274 Gy)								
952503 (262 Gy)								
092202 (158 Gy)								
072255 (97 Gy)								
075407 (103 Gy)								

Figure 8.10: Ranking of D_es obtained using the $IRPL_{955}$ signals at different stages of the protocol. Deep-red cells represent D_es consistent with the 1σ band, red cells represent the D_es outside 1σ but inside 2σ band, light-red cells represent and the D_es outside the 2σ band.

We now examine closely the performance of each signal in recovering the known dose. Figure 8.11 (a-h) and Figure 8.12(a-h), for the $IRPL_{880}$ and the $IRPL_{955}$, respectively, present the summary plots for each IRPL signal measured at different stages of the protocol (Table 8.3). Each subfigure consists of the measured vs. expected dose for the old samples (>20 ka). We do not include young samples since residual doses in young

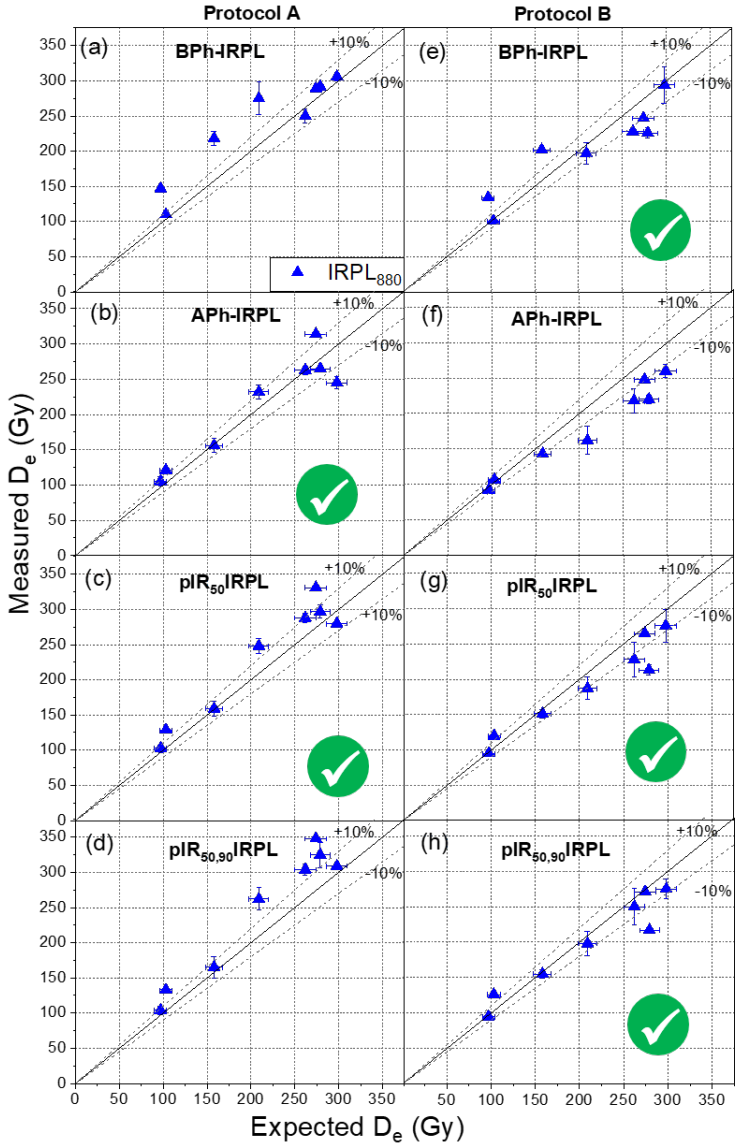

Figure 8.11: Plots of measured equivalent dose (D_e) using the $IRPL_{880}$ signals against the expected dose for the samples with age ∼20 ka. Left column (a-d): data obtained using different IRPL signals from protocol A. Right column (e-h): data obtained using different IRPL signals from protocol B. See Table 8.3 for details. About 3 to 6 aliquots were used for obtaining each data point (see Table 8.5 and 8.6). The checkmark symbol represents a good agreement between the measured and the expected dose.

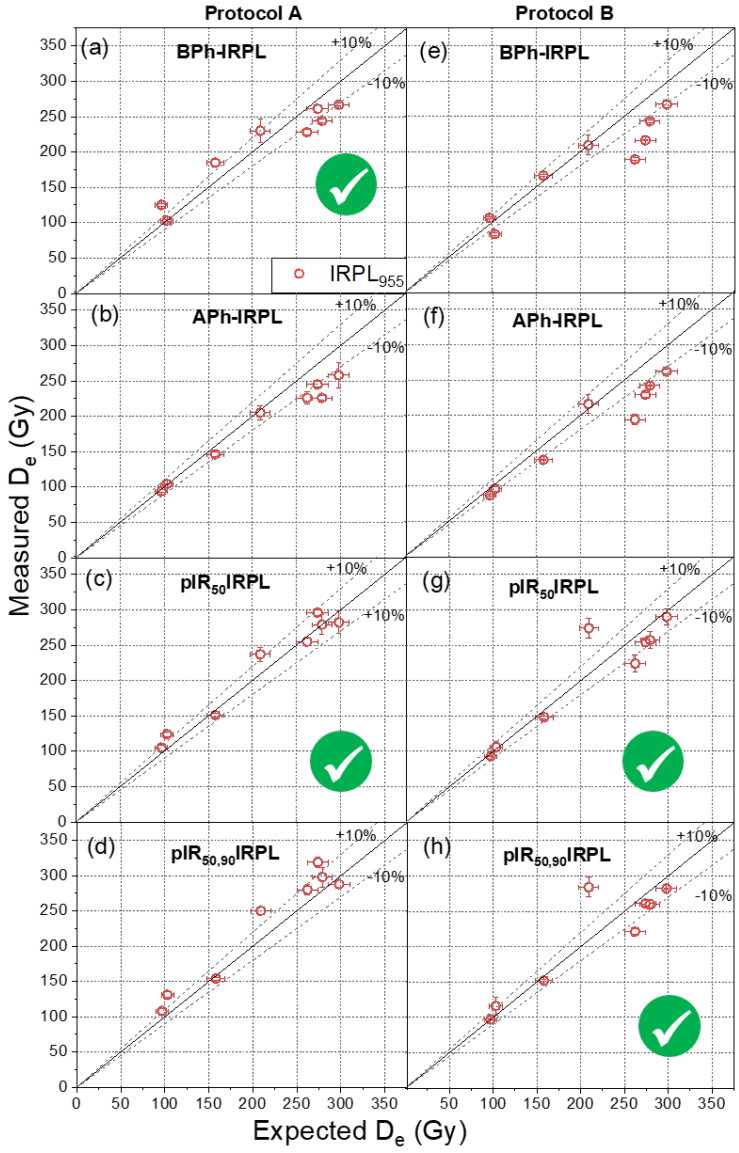

Figure 8.12: Plots of measured equivalent dose (D_e) using the $IRPL_{955}$ signals against the expected dose for the samples with age ∼20 ka. Left column (a-d): data obtained using different IRPL signals from protocol A. Right column (e-h): data obtained using different IRPL signals from protocol B. See Table 8.3 for details. About 3 to 6 aliquots were used for obtaining each data point (see Table 8.5 and 8.6). The checkmark symbol represents a good agreement between the measured and the expected dose.

or modern samples may not necessarily reflect partial bleaching in older samples (Jain et al., 2004). Moreover, feldspar dating using pIR_TIRSL_T or IRPL is mainly interesting for dating old sediments, where correction for anomalous fading (Huntley and Lamothe, 2001; Morthekai et al., 2008) does not apply. The left column presents the results for protocol A, and the right column for protocol B. The solid line represents a ratio of 1:1 (perfect agreement) and the dashed lines show a 10% deviation from this line. Most of the signals are generally able to recover the known dose. However there is tendency for the $IRPL_{955}$ to underestimate at high doses for some IRPL signals (for e.g. Figures 8.12a, and b).

To assess the performance of the dual SAR protocol across the sample of different doses, we perform a paired sample t-test (Kim, 2015; Appendix) to determine which signals universally provide D_es that are consistent with the expected value. For this test, we chose the old samples plotted in Figures 8.11 and 8.12. The results of the t-test are presented in Table 8.7 for protocol A and Table 8.8 for protocol B. The 't' statistic suggests that:

1. Protocol A ($IRPL_{880}$): the IRPL signals after preheat (APh-IRPL) and that after $IRSL_{50}$ ($pIR_{50}IRPL$) are most successful in recovering the known dose. The former performs slightly better than the latter.

2. Protocol A ($IRPL_{955}$): the IRPL signals before preheat (BPh-IRPL) and after $IRSL_{50}$ ($pIR_{50}IRPL$) are most successful in recovering the known dose.

3. Protocol B ($IRPL_{880}$): the IRPL signals before preheat (BPh-IRPL), after $IRSL_{50}$ ($pIR_{50}IRPL$), and after IRSL90 ($pIR_{50,90}IRPL$) are most successful in recovering the known dose.

4. Protocol B ($IRPL_{955}$): the IRPL signals after $IRSL_{50}$ ($pIR_{50}IRPL$), and after IRSL90 ($pIR_{50,90}IRPL$) are most successful in recovering the known dose.

8.7 Discussion

For a set of 8 samples with age control, the comparison of equivalent doses obtained using IRPL with the expected doses suggests that the IRPL

Table 8.7: Calculated t values for protocol A using equation 1 (Appendix). For 5% significance level, t_s =2.365 (degree of freedom: n-1=7). Symbols $*$, $\times$, $+$, and # represent different $IRPL_{880}$ signals. Symbols •, ◇, ♠, and ♣ represent different $IRPL_{955}$ signals. These symbols are shown in Figure A.1 (left) for t distribution to aid visualization.

	Protocol A		
	Signal	**t**	**Comment**
$IRPL_{880}$	BPh-IRPL (*)	-2.553	$t<-t_s$: means are significantly different
	APh-IRPL (x)	-0.26556	$t>-t_s$: means are not significantly different
	$pIR_{50}IRPL$ (+)	-2.3508	$t>-t_s$: means are not significantly different
	$pIR_{50,90}IRPL$ (#)	-3.9104	$t<-t_s$: means are significantly different
$IRPL_{955}$	BPh-IRPL (•)	0.47568	$t<t_s$: means are not significantly different
	APh-IRPL (♦)	3.08711	$t>t_s$: means are significantly different
	$pIR_{50}IRPL$ (♠)	-1.07237	$t>-t_s$: means are not significantly different
	$pIR_{50,90}IRPL$ (♣)	-2.67723	$T<-t_s$: means are significantly different

Table 8.8: Calculated t values for protocol B using equation 1 (Appendix). For 5% significance level, t_s =2.365 (degree of freedom: n-1=7). Symbols $*$, $\times$, $+$, and # represent different $IRPL_{880}$ signals. Symbols •, ◇, ♠, and ♣ represent different $IRPL_{955}$ signals. These symbols are shown on Figures A.1 (right) for t distribution to aid visualization.

	Protocol B		
	Signal	**t**	**Comment**
$IRPL_{880}$	BPh-IRPL (*)	0.5388	$t<t_s$: means are not significantly different
	APh-IRPL (x)	3.6899	$t>t_s$: means are significantly different
	$pIR_{50}IRPL$ (+)	2.0744	$t>t_s$: means are not significantly different
	$pIR_{50,90}IRPL$ (#)	1.3573	$t<t_s$: means are not significantly different
$IRPL_{955}$	BPh-IRPL (•)	2.3420	$t<t_s$: means are not significantly different
	APh-IRPL (♦)	3.1829	$t>t_s$: means are significantly different
	$pIR_{50}IRPL$ (♠)	0.3915	$t>t_s$: means are not significantly different
	$pIR_{50,90}IRPL$ (♣)	0.0719	$T<t_s$: means are not significantly different

can measure natural doses accurately, without any fading correction. In order to test whether IRPL is completely free from fading or not, the methods proposed here should be tested on infinitely old samples (i.e. samples with palaeodose greater than the saturation dose). Similar to the pIR_TIRSL_T signals, the stability of the IRPL may be increased by increasing the temperature of the first IR readout (Buylaert et al., 2012b).

Based on the t-test, both the protocols, A and B, perform satisfactorily in recovering natural dose as well as known laboratory dose. Recycling values are acceptable (within 10%) with both the protocols. However, protocol B results in a relatively higher recuperation for the IRPL signals measured after preheat (APh-IRPL) in comparison to protocol A.

There is a tendency that $IRPL_{955}$ signals show slightly lower doses than $IRPL_{880}$ for BPh-IRPL and APh-IRPL. This may indicate that $IRPL_{955}$ is slightly less stable compared with $IRPL_{880}$. Nonetheless, $IRPL_{955}$ measured after IRSL gives D_e values that agree within 10% of the expected dose. The 't' test for protocol A suggests that $IRPL_{880}$ (APh-IRPL, $pIR_{50}IRPL$) and the $IRPL_{955}$ (BPh-IRPL, $pIR_{50}IRPL$) result in the best agreement with the expected doses. Similarly, the t-test for protocol B suggests that $IRPL_{880}$ (BPh-IRPL, $pIR_{50}IRPL$, and $pIR_{50,90}IRPL$) and the $IRPL_{955}$ ($pIR_{50}IRPL$ and $pIR_{50,90}IRPL$) result in the best agreement with the expected doses.

From the bleaching perspective, $IRPL_{955}$ bleaches faster than the $IRPL_{880}$, both in nature and in laboratory. In the three modern/young samples, residual doses for the $IRPL_{880}$ signal are found to be higher than for the $IRPL_{955}$ signal, especially for the signals before $IRSL_{50}$ (i.e. APh-IRPL and BPh-IRPL). However, signals after $IRSL_{50}$ result in similar residual doses. Based on the bleaching behavior, $IRPL_{955}$ may be preferable over the $IRPL_{880}$ in environments where resetting may be an issue. In this case, the best results will be obtained using protocol A and $pIR_{50}IRPL$ signal (Figure 8.12).

For the same samples studied here, Buylaert et al., (2012a) observed that IRRL D_es underestimated the expected dose. However, we generally observe a good agreement between IRPL and the expected dose (Figures 8.11 and 8.12). Since IRRL and IRPL have been shown to emit from the same trap (Kumar et al., 2018; Chapter 3 in this thesis), the discrepancy between IRRL and IRPL dose is surprising. Buylaert et al. (2012a) attributed the lower estimates using IRRL D_es to the signal instability

(anomalous fading or thermal instability) and possible sensitivity changes between the additive and regenerative dose response curves. They also found IRRL D_es to be quite sensitive to the bleaching level between the additive and regeneration measurements. Since we know that IRPL and IRRL arise from the same traps (Kumar et al., 2018; Chapter 3 in this thesis), and IRPL gives us higher doses than IRRL, we may conclude that the under-estimation in IRRL is likely because of sensitivity changes rather than signal stability. IRPL is more amenable to a SAR protocol because of the possibility of pretreatments (such as preheating, prior IR exposure) and sensitivity correction; this may be the reason why IRPL performs better than the IRRL. New methods such as the improved IRRL or IRRF protocol (IR-RF_{70}; Frouin et al. 2017) are important to test whether IRRL is indeed fully stable or not.

Interestingly, IRPL signals before preheat (BPh-IRPL) in both protocols A and B, also recover known doses within 10-20% of the expected value. This suggests that the majority of the electron trap population is quite stable in these samples; only a small fraction of the principal trap must be close to holes and only these participate in IRSL production. Therefore, IRSL is significantly less stable than IRPL. These IRPL results have important implications for the design of portable OSL instruments for in-situ sediment dating as well as for rock surface dating (e.g. Rades et al., 2018) where uniform heating in the field may not be feasible.

Finally, these results have implications for spatially resolved single-grain dating. Sellwood et al. (2019) have demonstrated that it is possible to do IRPL imaging with a high-spatial resolution because the signal can be measured with very high sensitivity. The fact that IRPL can be used to measure doses accurately, suggests that it should be possible to extend IRPL dating protocols to dating based on microscopic imaging and be able to examine whether different regions of a single grain give same or different doses. Ultimately, this opens the possibility of microdosimetric investigations.

8.8 Conclusions

We have successfully developed a coupled IRPL-IRSL SAR protocol and tested its performance on 11 sedimentary K-feldspar samples. The equivalent doses (D_es) obtained for the IRPL signals are generally in very good

agreement with the independently determined doses. Both protocol A (using 320 °C preheat) and protocol B (using 260 °C preheat) perform satisfactorily in measuring expected doses. Based on a combination of the ability to bleach modern/young samples, and the ability to measure expected dose accurately, it may be suggested that the IRPL signal after preheat (APh-IRPL) for the 880 nm emission and the IRPL signal after $IRSL_{50}$ ($pIR_{50}IRPL$) for the 955 nm emission are the most promising signals for sediment/rock-surface dating. Nonetheless, all the signals presented here in our test samples show encouraging results for dating. Our data confirm that IRPL with appropriate pretreatment allows accessing a stable trapped electron (sub)population. The ability to measure accurate doses using IRPL opens up new possibilities of dating feldspar at the sub-single grain level using microscopic imaging because of very high sensitivity of this signal.

Acknowledgments

We thank Dr. Jan-Pieter Buylaert, Prof. Andrew Murray, and National Luminescence Laboratory (NLL) for sediment samples.

Supplementary Material

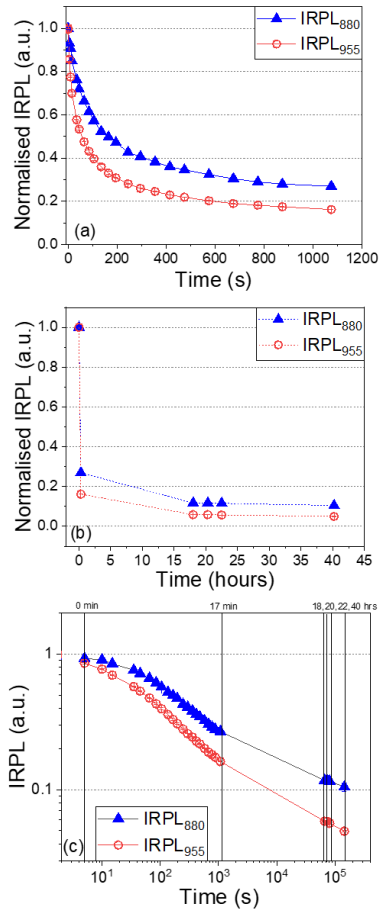

Figure SI 8.1: Bleaching of IRPL signals using solar simulator (a) in 1000 s, and (b) in 40 hours. (c) data from (a) and (b) are shown on the log scale. Sample 981010 (three aliquots) was used for these measurements.

References

Buylaert, J. P., Murray, A. S., Thomsen, K. J., & Jain, M. (2009). Testing the potential of an elevated temperature IRSL signal from K-feldspar. Radiation Measurements, 44(5-6), 560-565.

Buylaert, J. P., Jain, M., Murray, A. S., Thomsen, K. J., & Lapp, T. (2012a). IR-RF dating of sand-sized K-feldspar extracts: a test of accuracy. Radiation Measurements, 47(9), 759-765.

Buylaert, J. P., Jain, M., Murray, A. S., Thomsen, K. J., Thiel, C., & Sohbati, R. (2012b). A robust feldspar luminescence dating method for Middle and Late P leistocene sediments. Boreas, 41(3), 435-451.

Degering, D., & Krbetschek, M. R. (2006). 11. Dating of interglacial sediments by luminescence methods. The Climate of Past Interglacials, 157.

Duller, G. A. T. (1991). Equivalent dose determination using single aliquots. International Journal of Radiation Applications and Instrumentation. Part D. Nuclear Tracks and Radiation Measurements, 18(4), 371-378.

Duller, G. A. T. (1995). Luminescence dating using single aliquots: methods and applications. Radiation Measurements, 24(3), 217-226.

Duller, G. A. T., Bøtter-Jensen, L., Kohsiek, P., & Murray, A. S. (1999). A high-sensitivity optically stimulated luminescence scanning system for measurement of single sand-sized grains. Radiation Protection Dosimetry, 84(1-4), 325-330.

Erfurt, G. (2003). Infrared luminescence of Pb+ centres in potassium-rich feldspars. Physica status solidi (a), 200(2), 429-438.

Erfurt, G., & Krbetschek, M. R. (2003a). Studies on the physics of the infrared radioluminescence of potassium feldspar and on the methodology of its application to sediment dating. Radiation Measurements, 37(4-5), 505-510.

Erfurt, G., & Krbetschek, M. R. (2003b). IRSAR-a single-aliquot regenerative-dose dating protocol applied to the infrared radiofluorescence (IR-RF) of coarse-grain K-feldspar. Ancient TL, 21(1), 35.

Erfurt, G., & R. Krbetschek, M. (2002). A radioluminescence study of spectral and dose characteristics of common luminophors. Radiation protection dosimetry, 100(1-4), 403-406.

Frouin, M., Huot, S., Kreutzer, S., Lahaye, C., Lamothe, M., Philippe, A., & Mercier, N. (2017). An improved radiofluorescence single-aliquot regenerative dose protocol for K-feldspars. Quaternary Geochronology, 38, 13-24.

Huntley, D. J., Godfrey-Smith, D. I., & Thewalt, M. L. (1985). Optical dating of sediments. Nature, 313(5998), 105-107.

Huntley, D. J., & Lamothe, M. (2001). Ubiquity of anomalous fading in K-feldspars and the measurement and correction for it in optical dating. Canadian Journal of Earth Sciences, 38(7), 1093-1106.

Hütt, G., Jaek, I., & Tchonka, J. (1988). Optical dating: K-feldspars optical response stimulation spectra. Quaternary Science Reviews, 7(3-4), 381-385.

Jain, M., Murray, A. S., & Botter-Jensen, L. (2004). Optically stimulated luminescence dating: how significant is incomplete light exposure in fluvial environments? Quaternaire, 15(1), 143-157.

Jain, M., & Ankjærgaard, C. (2011). Towards a non-fading signal in feldspar: insight into charge transport and tunnelling from time-resolved optically stimulated luminescence. Radiation Measurements, 46(3), 292-309.

Jain, M., Guralnik, B., & Andersen, M. T. (2012). Stimulated luminescence emission from localized recombination in randomly distributed defects. Journal of physics: Condensed matter, 24(38), 385402.

Jain, M., Sohbati, R., Guralnik, B., Murray, A.S., Kook, M., Lapp, T.,

Prasad, A.K., Thomsen, K.J. & Buylaert, J.P. (2015a). Kinetics of infrared stimulated luminescence from feldspars. Radiation Measurements, 81, pp.242-250.

Jain, M., Buylaert, J. P., Thomsen, K. J., & Murray, A. S. (2015b). Further investigations on 'non-fading'in K-Feldspar. Quaternary international, 362, 3-7.

Kumar, R., Kook, M., Murray, A. S., & Jain, M. (2018). Towards direct measurement of electrons in metastable states in K-feldspar: Do infrared-photoluminescence and radioluminescence probe the same trap?. Radiation Measurements, 120, 7-13.

Kook, M., Kumar, R., Murray, A. S., Thomsen, K. J., & Jain, M. (2018). Instrumentation for the non-destructive optical measurement of trapped electrons in feldspar. Radiation Measurements, 120, 247-252.

Kim, T. K. (2015). T test as a parametric statistic. Korean journal of anesthesiology, 68(6), 540.

Kars, R. H., Reimann, T., Ankjærgaard, C., & Wallinga, J. (2014). Bleaching of the post-IR IRSL signal: new insights for feldspar luminescence dating. Boreas, 43(4), 780-791.

Li, B., & Li, S. H. (2011). Luminescence dating of K-feldspar from sediments: a protocol without anomalous fading correction. Quaternary Geochronology, 6(5), 468-479.

Lowick, S. E., Trauerstein, M., & Preusser, F. (2012). Testing the application of post IR-IRSL dating to fine grain waterlain sediments. Quaternary Geochronology, 8, 33-40.

Lapp, T., Kook, M., Murray, A. S., Thomsen, K. J., Buylaert, J. P., & Jain, M. (2015). A new luminescence detection and stimulation head for the Risø TL/OSL reader. Radiation Measurements, 81, 178-184.

Murray, A. S., & Wintle, A. G. (2000). Luminescence dating of quartz using an improved single-aliquot regenerative-dose protocol. Radiation

measurements, 32(1), 57-73.

Murray, A. S., & Wintle, A. G. (2003). The single aliquot regenerative dose protocol: potential for improvements in reliability. Radiation measurements, 37(4-5), 377-381.

Morthekai, P., Jain, M., Murray, A. S., Thomsen, K. J., & Bøtter-Jensen, L. (2008). Fading characteristics of martian analogue materials and the applicability of a correction procedure. Radiation Measurements, 43(2-6), 672-678.

Prasad, A. K., Poolton, N. R., Kook, M., & Jain, M. (2017). Optical dating in a new light: A direct, non-destructive probe of trapped electrons. Scientific reports, 7(1), 1-15.

Rades, E. F., Sohbati, R., Lüthgens, C., Jain, M., & Murray, A. S. (2018). First luminescence-depth profiles from boulders from moraine deposits: Insights into glaciation chronology and transport dynamics in Malta valley, Austria. Radiation Measurements, 120, 281-289.

Roberts, H. M. (2012). Testing Post-IR IRSL protocols for minimising fading in feldspars, using Alaskan loess with independent chronological control. Radiation Measurements, 47(9), 716-724.

S. Murray, A., G. Wintle, A., & Wallinga, J. (2002). Dose estimation using quartz OSL in the non-linear region of the growth curve. Radiation Protection Dosimetry, 101(1-4), 371-374.

Sellwood, E.L., Guralnik, B., Kook, M., Prasad, A.K., Sohbati, R., Hippe, K., Wallinga, J. & Jain, M. (2019). optical bleaching front in bedrock revealed by spatially-resolved infrared photoluminescence. Scientific reports, 9(1), pp.1-12.

Thomsen, K. J., Murray, A. S., Jain, M., & Bøtter-Jensen, L. (2008). Laboratory fading rates of various luminescence signals from feldspar-rich sediment extracts. Radiation measurements, 43(9-10), 1474-1486.

Thomsen, K., Murray, A., & Jain, M. (2011). Stability of IRSL signals

from sedimentary K-feldspar samples. Geochronometria, 38(1), 1-13.

Trautmann, T., Krbetschek, M. R., Dietrich, A., & Stolz, W. (1998). Investigations of feldspar radioluminescence: potential for a new dating technique. Radiation Measurements, 29(3-4), 421-425.

Trautmann, T., Krbetschek, M. R., Dietrich, A., & Stolz, W. (2000). The basic principle of radioluminescence dating and a localized transition model. Radiation Measurements, 32(5-6), 487-492.

Trautmann, T., Krbetschek, M. R., Dietrich, A., & Stolz, W. (1999). Feldspar radioluminescence: a new dating method and its physical background. Journal of Luminescence, 85(1-3), 45-58.

Tsukamoto, S., Denby, P. M., Murray, A. S., & Bøtter-Jensen, L. (2006). Time-resolved luminescence from feldspars: new insight into fading. Radiation Measurements, 41(7-8), 790-795.

Tsukamoto, S., Kondo, R., Lauer, T., & Jain, M. (2017). Pulsed IRSL: A stable and fast bleaching luminescence signal from feldspar for dating Quaternary sediments. Quaternary Geochronology, 41, 26-36.

Thiel, C., Buylaert, J. P., Murray, A., Terhorst, B., Hofer, I., Tsukamoto, S., & Frechen, M. (2011). Luminescence dating of the Stratzing loess profile (Austria)–Testing the potential of an elevated temperature post-IR IRSL protocol. Quaternary International, 234(1-2), 23-31.

Wintle, A. G. (1973). Anomalous fading of thermo-luminescence in mineral samples. Nature, 245(5421), 143-144.

Wintle, A. G. (2008). Luminescence dating: where it has been and where it is going. Boreas, 37(4), 471-482.

Wallinga, J., Murray, A., & Duller, G. (2000). Underestimation of equivalent dose in single-aliquot optical dating of feldspars caused by preheating. Radiation measurements, 32(5-6), 691-695.

Wintle, A. G., & Murray, A. S. (2006). A review of quartz optically stim-

ulated luminescence characteristics and their relevance in single-aliquot regeneration dating protocols. Radiation measurements, 41(4), 369-391.

Whitlock, M. C., & Schluter, D. (2009). The analysis of biological data (No. 574.015195 W5).

Yi, S., Buylaert, J. P., Murray, A. S., Lu, H., Thiel, C., & Zeng, L. (2016). A detailed post-IR IRSL dating study of the Niuyangzigou loess site in northeastern China. Boreas, 45(4), 644-657.

CHAPTER 9

SUMMARY AND CONCLUSION

My Ph.D. research has investigated the luminescence processes in feldspar by examining the main dosimetric electron-trapping center (principal trap) using low-temperature, site-selective spectroscopic techniques.

I made the following inquiries and attempted to answer them systematically during the course of my Ph.D.:

1. **Do the two site-selective techniques, infrared radioluminescence (IRRL) and infrared photoluminescence (IRPL), probe the same trap or different traps?**

   This aspect of my research demonstrated that both IRRL and IRPL arise from the same trap (i.e. principal trap). The former reflects the electron trapping process during exposure to ionizing radiation, while the latter is an optical probe of the trapped electrons after irradiation.

2. **Which are the main spectral emissions arising from internal transitions within the principal trap?**

   I demonstrated that there are two dominant emissions at 1.41 eV (880 nm) and 1.30 eV (955 nm) in both IRRL and IRPL using low temperature spectroscopy.

3. **Do the two IRPL emissions (1.41 eV and 1.30 eV) arise**

from the same defect, different defects, or the same defect experiencing different crystal fields?

I used low temperature excitation-emission spectroscopy to answer this question. This work led to the mapping of the energy levels (electronic states) of the two emission centers. I concluded that these centers represent two principal traps (electron traps) in feldspar resulting from the same defect residing in two different environments.

4. **Does the distribution of the two principal traps (1.41 eV and 1.30 eV emission centers) vary spatially within a crystal? Does the spectral distribution of the IRRL depend on the feldspar composition?**

   These questions were addressed using simultaneous cathodoluminescence microscopy and elemental mapping at 6-22 µm resolution. A significant spatial variability even within a single grain, and a correlation between the intensities of the two emission bands and the K-Na-Fe concentrations were observed.

5. **Can we understand the origin of optically stimulated luminescence (OSL) by independently tracking the trapped electron population?**

   This question was examined using coupled IRPL-IRSL measurements. IRPL tracked the trapped electrons, whereas IRSL tracked electron-hole recombination. It was demonstrated that a coupled PL-OSL system is a powerful tool to investigate luminescence physics in feldspar.

6. **Can IRPL be used for dating based on direct measurement of the trapped electron concentration?**

   This question was addressed using several known-age samples. It was concluded that IRPL could measure accurate equivalent doses without any need for fading correction in these samples.

All these investigations are novel and together constitute a major body of work that has pushed luminescence geochronology significantly forward. Brief conclusions and the highlights/impact of my research are discussed in the following sections.

9.1 Conclusions

Chapter 2 to 8 at a glance: Chapter 2 describes the instrumentation, methods, and samples used in this work. Chapter 3 presents the results on the comparison of infrared photoluminescence (IRPL) and infrared radioluminescence (IRRL) signals in K-feldspar samples. Chapter 4 provides details on the development of the IRPL measurement system. Chapter 5 presents the characterization of the principal trap in feldspar using low-temperature photoluminescence excitation-emission spectroscopy. Chapter 6 provides results on the mapping of metastable states using electron-beam induced luminescence microscopy. Chapter 7 exploits the coupled PL-OSL physical system in feldspar to probe the dynamics of the metastable states. Chapter 8 presents the results on sediment dating using IRPL.

IRPL offers a site-selective and non-destructive technique to probe the trapped electrons in the principal trap. Prasad et al. (2017) used an 885 nm laser to excite the trap and measured a Stokes-shifted emission centered at 955 nm (1.30 eV). Chapter 3 reports an additional IRPL emission at 1.41 eV together with the 1.30 eV emission. when using an 830 nm laser excitation. Thus, feldspar shows two Stokes-shifted emission bands, centered at 1.41 eV (880 nm) and 1.30 eV (955 nm). Both these IRPL emissions showed similar x-ray dose-response but different thermal quenching behavior. IRRL showed the same two emissions bands at low temperature and a similar curvature of the dose response curve (characteristic dose) as the IRPL; however, it is to be noted that the IRPL increases with dose whereas the IRRL decreases with dose. Based on the similarity of the spectral emission, and the curvature of the dose response curves, it was concluded that IRPL and IRRL arise from the same trap, i.e. principal trap. Temperature dependence of IRPL and IRRL suggested that the thermalization of electrons from the conduction band into the band-tail states and subsequent retrapping into the principal trap result in IRRL, while IRPL arises due to intra-defect optical transitions after an electron has been captured in the principal trap. This study formed the backbone of my Ph.D. research; in all subsequent investigations, whether using PL or RL, I measured both the near-infrared (NIR) emissions ($\sim$1.30 and $\sim$1.41 eV). The question of the origin of these two emission bands was investigated in both the energy-domain using excitation-emission spectroscopy (Chapter 5), and the spatial-domain using cathodoluminescence microscopy (Chapter 6).

A detailed investigation of the origin of these two NIR emissions (∼1.41 eV and ∼1.30 eV) using PL excitation-emission spectroscopy at low temperature (7 K) confirmed that they arise from two distinct centers and not from different electronic levels of a single center. The two trapping centers have similar electron capture cross-sections and excited-to-ground state relaxation lifetimes, but different trap depths and the excited-state energies (higher electronic levels). The difference in the trap depths reflected in the bleaching speed (under light exposure) and the thermal stability of the 1.41 and 1.30 eV IRPL signals. Overall, these results indicated that the 1.41 eV and 1.30 eV emission centers consist of the same defect experiencing two different crystal fields. In other words, there are two distinct principal traps consisting of the same defect in different environments.

The question on the spatial variability of the two principal traps and their link to feldspar composition was explored using cathodoluminescence (CL) microscopy. Near infrared cathodoluminescence (IRCL) arises from the same process as the IRRL, but sampling is restricted to only up to 4 µm below the sample surface. These investigations suggested that the two NIR emission bands (i.e. the two traps) vary spatially even within a single-grain of feldspar. A correlation between K-Na content and the peak positions of the IRCL emission indicated that the two principal traps vary as a function of alkali-feldspar composition; this observation supports our interpretation of the two different crystal fields around the same defect. A correlation between IRCL peak positions and Fe^{3+} emission peak suggested that Fe competes with the principal trap to capture free electrons resulting in IRCL (i.e., IRRL) quenching.

A link between the NIR emission bands and the OSL phenomenon was also investigated. New quantities were suggested to measure changes in trapped electron and hole populations individually. Tracking the changes in IRPL (i.e. trapped electron population) and IRSL (i.e. electron and hole population) due to different thermal or optical treatments suggested that a) both the principal traps (1.41 eV and 1.30 eV IRPL emission centers) participate in IRSL by acting as electron donors, and b) only a fraction of these principal trap populations participates in the IRSL at a given measurement temperature. A comparison of thermal depletion of IRSL and IRPL suggested that the decrease in IRSL intensity due to preheating results from the depletion of holes; the holes are used up during the TL measurement (i.e. preheat) prior to the IRSL measurement. This

work also suggested that the electron trapping probability in the principal trap is both a function of its electron capture cross-section (a function of coulomb attraction) and its distance to the nearest hole. Based on the variations in the IRSL and IRPL signals due to the measurement temperature, it was inferred that the diffusion-volume dependent probability of finding a hole is an important factor in the IRSL production. These new insights are critical for the development of mathematical models of luminescence phenomena involving metastable states.

Finally, the potential of IRPL as a dose measurement tool was investigated. It was demonstrated that the IRPL can be successfully adapted to a SAR protocol. Accurate equivalent doses from 100 to 300 Gy (age range 20-128 ka) can be obtained using IRPL based SAR protocol without a fading correction.

9.2 Research highlights

My research has provided a new understanding of the luminescence processes and the associated defect system in feldspar. It has resolved some long-standing issues in feldspar luminescence, e.g., single vs. multiple trap origin, and provided many new insights to inspire future research.

The highlights of this Ph.D. research are:

- Discovering a second non-destructive (at 7 K) IRPL emission at 1.41 eV (880 nm) in addition to the 1.30 eV emission reported by Prasad et al. (2017).
- Demonstrating that both IRPL and IRRL show the same spectral emission and arise from the principal trap.
- Demonstrating that there exist two principal traps in feldspar. Both these electron-trapping centers participate in IRSL (i.e., electron-hole recombination), however, the 1.30 eV center contributes relatively more to the IRSL at room temperature than the 1.41 eV center. One can tune the excitation energy to preferentially sample from these centers.
- Making a direct measurement of the optical trap depth and the excited energy levels of the principal trap.

- Demonstrating that feldspar exhibits a coupled PL-OSL physical system, where changes in electron population i.e., change in IRPL (ΔIRPL) due to IRSL, can be monitored. ΔIRPL provides a unique tool to understand luminescence recombination pathways involving the metastable states.
- Providing a first direct experimental support of the localized feldspar model involving a recombination bottleneck. ΔIRPL proves that only a fraction of trapped electron population participates in IRSL at a given measurement temperature.
- Understanding the spatial distribution of the metastable states (principal trap) in feldspar at a micron-scale (6-22 µm) and linking their occurrence to feldspar composition (K or Na). It was observed that that the higher energy emission (1.41 eV) is biased more towards Na-rich feldspars and the lower energy emission (1.30 eV) is biased more towards K-rich feldspars.
- Helping development of a facility for the measurement of infrared photoluminescence (IRPL) for the Risø TL/OSL reader.
- Developing a measurement protocol i.e., coupled IRPL-IRSL SAR protocol, to routinely measure natural doses in feldspar using IRPL.

9.3 Impact of this research

I expect that the techniques used in this thesis will inspire researchers not only from luminescence dating but also from the fields of solid-state dosimetry and luminescent materials for understanding luminescence phenomena involving the metastable states. I believe that my research will have an impact on the following research topics.

- Spectroscopy for routine measurement of the trap depth and the excited energy levels of the principal trap, and understanding the linkages between such parameters and the composition/structure of a feldspar crystal.
- Measurement of trapping of charge at a high resolution (6-22 µm) paves the way for studying microdosimetry and for developing next-generation luminescence dating techniques at the sub-single-grain level.

- Use of dose-dependent excitation-emission spectroscopy to distinguish between the emissions from the excited states of a trap or charge transfer from other traps. This is a simple yet robust technique to map the excited states of a metastable defect in other materials that exhibit complex interactions between the defects (e.g., persistent phosphors).

- Development of a coupled PL-OSL (photoluminescence-optically stimulated luminescence) physical system that allows selective examination of the electron and hole traps. I expect that this will inspire the search for similar coupled systems in other dosimeters to enhance our understanding of the luminescence phenomena.

APPENDIX

Student t test (Paired sample t test)

The t test is done to evaluate if two sample means are different or not (Kim, 2015). It is done by calculating t statistic as,

$$t = \frac{\overline{d} - \mu_d}{S_d/\sqrt{n}} \tag{1}$$

where n= sample size, $\bar{d}$= mean of the difference between paired data points, S_d = standard deviation of the difference between paired data points, and $\mu_d = \mu_1$-μ_d= difference of two means.

If $t>t_s$ or $t<$-t_s, the two mean values are significantly different. Here s represents the significance level.

The μ_1 is always the same since it is the mean of the known D_es for 8 samples. The μ_2 is derived mean of D_es for each IRPL signal under consideration (Chapter 8, Table 8.3). We calculate the t values for all the IRPL signals using equation 1 and compare them with a t_s value for a 5% significance level (obtained from the statistical table; Whitlock and Schluter, 2009). If, $-t_{0.5} < t < t_{0.5}$, means are not significantly different. Otherwise they are statistically different. A graphical representation to show the t values on the t distribution curve is shown in the following Figures A.1 (left: Protocol A, right: Protocol B).

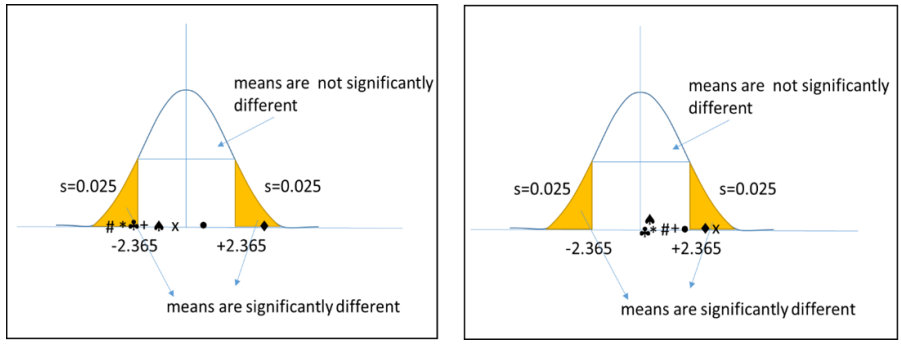

Figure A.1: A graphical representation of the t values for the $IRPL_{880}$ signal (left) and the $IRPL_{955}$ signal (right) at different stages of the protocols (Chapter 8, Table 8.3). Symbols $*$, $\times$, $+$, and $\#$ represent t values for $IRPL_{880}$ signals before preheat (BPh-IRPL), after preheat (APh-IRPL), after $IRSL_{50}$ ($pIR_{50}IRPL$), and after $IRSL_{90}$ ($pIR_{50,90}IRPL$), respectively. Symbols $\bullet$, $\diamond$, $\spadesuit$, and $\clubsuit$ represent t values for $IRPL_{955}$ signal before preheat (BPh-IRPL), after preheat (APh-IRPL), after $IRSL_{50}$ ($pIR_{50}IRPL$), and after $IRSL_{90}$ ($pIR_{50,90}IRPL$). These symbols are put on the t-axis to have better visualization.

———————x———————